University of Southampton

Faculty of Engineering and Physical Sciences
School of Physics & Astronomy

Phonon-Based Quantum Testing Schemes Using BECs for Gravity Modifications in Light of Dark Matter Exploration

by
Hector Antonio Fernandez Melendez
MSc.
ORCiD: 0000-0003-3224-1282

A thesis for the degree of
Doctor of Philosophy

June 2025

University of Southampton

Abstract

Faculty of Engineering and Physical Science
School of Physics & Astronomy

Doctor of Philosophy

Phonon-Based Quantum Testing Schemes Using BECs for Gravity Modifications in Light of Dark Matter Exploration

by Hector Antonio Fernandez Melendez

The nature of dark matter and dark energy remains an open question in modern physics. While dark matter is inferred from astrophysical observations and dark energy accounts for the accelerated expansion of the universe, their fundamental origins remain unknown. This motivates alternative approaches to explain the observed behaviour of the universe by modifying our current theory of gravity. This thesis proposes a novel method for testing such modified theories of gravity by exploiting the dynamics of quantum phononic excitations present in Bose-Einstein Condensates (BECs), which can be realized in tabletop experiments with current technology. Our proposal implements quantum metrology within the physics of the BEC and its phononic excitations, taking advantage of Gaussian states and the tritter operation to prepare highly sensitive phonon states for estimating gravitational parameters. Specifically, we aim to measure the gravitational potential of an oscillating massive sphere by estimating the exerted acceleration on a BEC, inferred through phonon dynamics. We predict an acceleration precision of approximately 10^{-17} m/s^2, allowing us to test deviations from Newtonian gravity. We examine two modified-gravity models: Modified Newtonian Dynamics (MOND) and Lambda-gravity. The precision of our method enables the distinction between MOND and Newtonian gravity under experimentally feasible conditions. For Lambda-gravity, our setup allows us to measure Newton's gravitational constant G with a relative precision of 10^{-7}, improving current measurements by two orders of magnitude. Additionally, it provides an upper bound on the cosmological constant of $\Lambda < 10^{-31}$ m^{-2}, representing the first laboratory-based experimental constraint on Λ. In conclusion, this thesis presents a novel, high-precision method for probing Newtonian gravity while paving the road for future research focused on probing relativistic effects.

Contents

Bibliography

List of Figures

List of Tables

Declaration of Authorship

I declare that this thesis and the work presented in it is my own and has been generated by me as the result of my own original research.

I confirm that:

1. This work was done wholly or mainly while in candidature for a research degree at this University;
2. Where any part of this thesis has previously been submitted for a degree or any other qualification at this University or any other institution, this has been clearly stated;
3. Where I have consulted the published work of others, this is always clearly attributed;
4. Where I have quoted from the work of others, the source is always given. With the exception of such quotations, this thesis is entirely my own work;
5. I have acknowledged all main sources of help;
6. Where the thesis is based on work done by myself jointly with others, I have made clear exactly what was done by others and what I have contributed myself;
7. Parts of this work have been published as:

   H.A. Fernandez-Melendez, A. Belyaev, V. Gurzadyan and I. Fuentes. (2024) 'Probing Modified Gravity with Bose-Einstein Condensate' arXiv:2409.19755 [quant-ph].

   H.A. Fernandez-Melendez, A. Belyaev, X. Hernandez, F. Shankar and I. Fuentes. (2025) 'Testing MOND with a BEC' in progress.

Signed:.. Date:..................

Acknowledgements

Undoubtedly, the mentoring and support of so many persons have been essential not only for the completion of my PhD studies but also for my professional and personal growth. First and foremost, I am deeply grateful to my supervisor, Ivette Fuentes, whose passion has always been a source of inspiration. Her invaluable support and lessons have guided my academic and personal journey. I could not have asked for a better supervisor. Thank you, Ivette! I also extend my sincere thanks to my co-supervisor, Alexander Belyaev, whose curiosity, thoughtful advice, and encouragement have been very significant to me.

This work has greatly benefited from the contributions and collaboration of many colleagues. I sincerely thank Francesco Shankar, Hendrik Ulbricht, Jesus Rogel, Vahe Gurzadyan and Xavier Hernandez for their support, discussions, and involvement in various aspects of this research. Additionally, I am grateful to Chris Westbrook and Carlos Lobo for dedicating their time and expertise to examining this work.

A special mention goes to our research group! I could not have asked for a better team to learn, collaborate, and grow with. Abdul Afzal, Anthony Kull, Balazs Novak, Ethan Campos, Kia Romero and Melanie Bautista, thanks for the interesting and fun discussions, the support and, most importantly, the friendship. It has been a pleasure to be part of this group.

Beyond academia, I am incredibly fortunate to have such amazing friendships. Your support throughout these years has been invaluable. Fernanda Salazar and Erik Mata, thank you for being my home away from home. Marilu Hernandez, thank you for your love and company. And to my lifelong friends back in Mexico, thank you for always believing in me, long before this PhD journey even began.

No words will ever be enough to thank my family. Your unconditional love and support have carried me through every challenge and every success. This achievement is as much yours as it is mine.

Finally, I gratefully acknowledge CONACYT and Ivette Fuentes for funding my studies and making this journey possible.

To my father,
to my family

Que otros se jacten de las páginas que han escrito;
a mí me enorgullecen las que he leído.
...
la tarea que emprendo es ilimitada
y ha de acompañarme hasta el fin,
no menos misteriosa que el universo
y que yo, el aprendiz.

— Jorge Luis Borges, *Un Lector* (1969)

Chapter 1

Introduction

Technological progress has consistently improved our ability to achieve more precise measurements. Nowadays, relativistic corrections are continually taken into account for various applications, such is the case of GPS technology [1]. This progress is also reaching the quantum technologies, exemplified by current plans aiming to take tabletop experiments to space-based setups [2, 3]. However, the effects of motion and gravity on quantum experiments and technologies have remained largely unexplored [4].

Since a complete theory of quantum gravity has not been achieved, the most reliable approach to understanding the interplay between quantum matter and gravity, based on the current theoretical progress, is through quantum field theory (QFT). This theory describes quantum matter within a relativistic framework, respecting principles from special relativity, such as Lorentz invariance. Furthermore, this framework can be extended to curved spacetime, allowing the study of quantum fields in a more general gravitational setting [5].

To understand how motion and gravity affect quantum experiments, we appeal to quantum metrology, the field dedicated to measuring physical parameters with high precision using quantum theory. By employing techniques like laser interferometry, quantum metrology has played a crucial role in achieving major breakthroughs, including the detection of gravitational waves at LIGO [6]. Recently, it has been applied to quantum field theory, leading to the development of a framework for relativistic quantum metrology. This has allowed the estimation of parameters associated with quantum fields evolving under relativistic settings, showing that motion and gravity can enhance or degrade quantum entanglement [7]. It has also been demonstrated that quantum metrology can be employed to measure the Unruh effect [8], estimate the curvature of spacetime [9], and determine the expansion rate of the universe [10].

In particular, quantum metrology has greatly benefited from cold atom systems, such as the Bose-Einstein condensate (BEC). Their high degree of control and low internal noise make them an ideal testing ground [11]. A notable application is BEC-based gravimetry. Current BEC gravimetry relies on atom interferometry, where the wave function of each atom in the BEC is split into two paths and then recombined to measure independent phase differences. However, if one is interested in studying the interplay between quantum matter and gravity, atom interferometry presents certain limitations. On one hand, it is founded in non-relativistic quantum mechanics [12, 13], dismissing effects typical to QFT, such as particle creation [14, 15] or the mixing of field modes [16]. On the other hand, its precision scales with the size of the experiment, requiring larger interferometers to improve the measurement precision, which restricts the capabilities of this approach.

One can take an alternative approach to BEC gravimetry by considering frequency interferometry [17], which takes advantage of the phononic collective oscillations of the atoms in a BEC. This novel method has been proposed to measure gravitational waves [18] and develop gravitational gradiometers [19]. These proposals apply quantum metrology to bosonic quantum fields, modelling the BEC and its phonons as a quantum field evolving over a fixed background spacetime, which is employed to measure gravitational parameters related to the structure of the underlying spacetime. This framework has also been implemented in non-relativistic settings to measure Newtonian gravity. In contrast to atom interferometry, frequency interferometry offers different advantages when applied to BEC gravimetry. Firstly, it allows a relativistic description, which was recently achieved by the theoretical description of the relativistic BEC. Secondly, the measurement precision depends on the lifetimes of the BEC and the phonons, thereby eliminating the need for larger experiments. Therefore, this approach stands as a promising method for measuring not only Newtonian gravity but also for probing relativistic effects in quantum systems.

Beyond the scales of tabletop experiments, important open questions related to gravity arise when studying astrophysics and cosmology. The observation of the universe's accelerated expansion [20, 21] and the anomalous rotation of galaxies [22] have raised questions regarding our understanding of the universe. This has led us to propose the existence of dark matter and dark energy. While dark energy is believed to drive the accelerated expansion of the universe, accounting for approximately 70% of its matter-energy content, dark matter is invoked to explain astronomical observations, which is considered to constitute around 25% of the universe. However, their fundamental nature remains unknown.

Several models have been developed to explain and understand the nature of these phenomena. Dark matter candidates range from weakly interacting massive particles (WIMPs) to fuzzy dark matter and primordial black holes [23]. Experimental research has restricted the parameter space for several of these proposed models, yet no conclusive results or evidence have favoured any of them in particular.

Alternatively, modified theories of gravity offer an approach to dark matter that does not rely on the existence of missing matter to account for astronomical observations. In some cases, this approach could also account for dark energy. For instance, $f(R)$-gravity extends general relativity by generalizing the Einstein-Hilbert action [24]. At the level of Newtonian gravity, models such as Modified Newtonian Dynamics (MOND) and Lambda-gravity change the Newtonian gravitational force.

In this thesis, we take advantage of the progress in quantum metrology to propose a novel method for high-precision gravimetry using BEC phonons. Our approach aims to improve current gravimetry accuracies while offering additional benefits to existing techniques for testing deviations from Newtonian gravity. By applying this method to two specific modified gravity models, which seek to explain the origins of dark matter and dark energy, we aim to constrain their parameter space.

1.1 Thesis Objectives

The main objective of this thesis is to establish a novel experimental proposal for high-precision measurements of gravity by employing BEC phonons within a frequency interferometry framework. Specifically, we focus on the first application of this method for exploring modified theories of gravity—motivated by the dark matter and dark energy problems—by testing deviations from Newtonian gravity.

To this end, we explore two modified gravity models: Modified Newtonian Dynamics (MOND) and Lambda-gravity. For MOND, the objective is to investigate whether the proposed experiment is sensitive enough to distinguish between Newtonian and MOND-like dynamics, thereby contributing to the currently limited Earth-based tests of this model. For Lambda-gravity, the goal is to determine how precisely our method can measure Newton's gravitational constant G and the cosmological constant Λ, two fundamental constants that characterise this model. Additionally, we seek to improve the current precision in determining G and to present the first tabletop experiment designed for constraining Λ.

To enhance the measurement precision of BEC phonons within the frequency interferometry scheme, we also propose the first implementation of the tritter operation applied to measure Newtonian gravity.

In addition to these primary objectives, this thesis also aims to pave the road for extending our experimental proposal to test relativistic modifications of gravity and, more generally, relativistic effects in the weak-gravity regime. Furthermore, another goal is to encourage the realization of a proof-of-principle experiment of our proposal, that is, an initial experimental demonstration of its feasibility, by providing a comprehensive theoretical framework for employing BEC phonons to measure gravity.

Finally, we expect that this proposal will not only contribute to fundamental physics research but also motivate the generation of new technology and lay the groundwork for its potential commercial implementation in high-precision gravimetry.

1.2 Thesis Overview

The structure of the thesis is organized as follows. Chapter 2 lays the groundwork by studying the evolution of bosonic quantum fields confined to a region in Minkowski spacetime from the perspective of both an inertial observer and an accelerated observer. Through the quantization of the field, the Fock space is constructed, and the concept of particles or excitations for each observer is introduced. The connection between the inertial and accelerated observers is established by employing a Bogoliubov transformation. This chapter helps us understand the dynamics of quantum fields, to which we will later return in the context of Bose-Einstein condensation, and prepare the ground for constructing Gaussian states.

In Chapter 3, the focus shifts to describing Gaussian states and Gaussian transformations. We begin by comparing the descriptions of quantum states in Hilbert space and Phase space. In preparation for the rest of the chapter, the formal construction of Fock space is presented. Then, Gaussian states and Gaussian transformations are introduced, with their respective descriptions in Phase space provided through the covariance matrix formalism. We review symplectic geometry, which captures the properties of Gaussian states and transformation in Phase space. Finally, a list of the basic Gaussian states and their physical interpretation is given.

Chapter 4 introduces quantum metrology, the field dedicated to performing high-precision measurements on quantum systems. By employing local estimation theory, we derive the quantum Cramér-Rao bound, which is the quantity that establishes a limit on the precision to estimate a physical parameter driving a change in a quantum state. The quantum Fisher information for Gaussian states, which is required to evaluate such precision, is introduced using the covariance matrix formalism. Then, the notion of a metrological scheme is presented, and we discuss its usefulness in preparing and optimizing parameter estimations. The chapter concludes with a discussion on the application of quantum metrology to relativistic settings and the progress achieved in this direction.

In Chapter 5, we provide a comprehensive review of the study of the Bose-Einstein condensation phenomenon. It first examines the non-interacting Bose gas, identifying a phase transition that occurs below a critical temperature, which is estimated. Then, the weakly interacting Bose gas is investigated by introducing the Bogoliubov theory. The BEC's ground-state energy and thermodynamic equation are derived in the zeroth-order momentum approximation. In the second-order approximation, the excitation spectrum reveals phonon-like elementary excitations. Finally, the study of non-uniform BECs leads to the derivation of the Gross-Pitaevskii equation, which is employed to study small-amplitude perturbations in the BEC. This chapter also investigates the relativistic BEC (RBEC) in flat space by following a similar approach to the non-relativistic case. Using the Bogoliubov approximation, we derive the dispersion relation for small-amplitude perturbations and analyse its limiting cases. For the gapless branch of the low-momentum limit, we identify the acoustic metric, an effective metric governing the RBEC phonon evolution. Lastly, we verify that in the Newtonian limit, the theory consistently recovers the non-relativistic BEC description.

Chapter 6 integrates the material of previous chapters to establish the core idea of this thesis: the experimental proposal for employing the BEC phonons to measure gravity. The chapter begins by discussing the difference between atom interferometry—the currently employed method for BEC-based gravimetry—and frequency interferometry, a novel method on which our proposal is based. Then, the experimental setup proposed for probing gravity using the BEC is detailed.

This involves placing an oscillating massive sphere near the BEC, which acts as a source of gravitational potential. Next, we derive the dynamics of the BEC under the gravitational influence of the oscillating sphere. Assuming the presence of small-amplitude perturbations in the BEC, we obtain the equations of motion for both the condensed atoms and the perturbations, where the dispersion relation allows us to identify these perturbations as phonons. By implementing quantum metrology, we can establish a metrological scheme that is enhanced by using a tritter to estimate a physical parameter related to the induced acceleration on the BEC, which quantifies the effects of the gravitational potential from the oscillating sphere. We derive a formula that bounds the measurement precision, which depends on numerous experimental parameters. We provide a review of the state-of-the-art BEC experiments and discuss the conditions and constraints that the experimental parameters must satisfy. To conclude, we analyse the precision's parameter dependence and compute its explicit value for different sets of experimental parameters.

Building upon this experimental framework, Chapter 7 explores its application for testing deviations from Newtonian gravity. We consider two modified-gravity models: Modified Newtonian Dynamics (MOND), which alters the gravitational force at accelerations below $\sim 10^{-10}$ m/s^2, and Lambda-gravity, which extends Newton's gravitational force by introducing an additional term dependent on the cosmological constant. For both cases, we derive the gravitational potential of the oscillating sphere and the corresponding theoretical prediction for the value of the acceleration amplitude, comparing it to the Newtonian result. In the case of Lambda gravity, we estimate the precision for measuring Newton's gravitational constant G and the cosmological constant Λ, comparing our results with the current state-of-the-art precisions.

Taking a broader perspective, Chapter 8 summarizes an extensive market analysis dedicated to the technological implementation and commercialisation of BEC-based quantum gravimeters as proposed in this thesis. Finally, Chapter 9 summarizes the main results of the thesis and outlines future directions for research.

As supplementary material, Appendix A presents a complete list of the fundamental one-mode and two-mode Gaussian transformations and Gaussian states described employing the covariance matrix formalism. Appendix B indicates the number of particles associated with the basic Gaussian states. In Appendix C, the code used to calculate the expression for the quantum Fisher information in (6.32) is provided. Appendix D contains the code for evaluating the precision in (6.37).

Chapter 2

QFT in Minkowski Space for Confined Bosonic Fields

Quantum field theory (QFT) is the natural generalization of quantum mechanics. It goes beyond the one-particle quantum mechanical description of nature governed by the Schrödinger equation. Furthermore, QFT is a Lorentz-invariant formulation, making it a relativistic description. From the study of QFT, important consequences arise, including the prediction of antimatter's existence and the fact that the particle number is no longer conserved [5]. It represents a semiclassical description, meaning that matter and radiation are quantized and evolve within a fixed classical spacetime.

Usually, QFT is studied assuming flat Minkowski spacetime. However, studying quantum fields on curved spacetime has yielded interesting outcomes. Among the most important results obtained, we can find the Hawking radiation [25, 26] and the cosmological particle creation [27, 28]. In practice, one may consider that spacetime is flat near the Earth, but this is a consequence of our technological limitations in making high-precision measurements. Recent works have pointed out that quantum experiments may be sensitive enough to detect small-magnitude differences in the parameters describing spacetime or non-inertial motion. It is expected that this will be tested in the near future [29]. This opens the possibility to experimentally explore the dynamics of quantum fields under accelerated motion, gravitational fields and curved spacetime.

Since this thesis focuses on the study of the Bose-Einstein condensate and is interested in examining its relation to relativistic effects, a good starting point before tackling these subjects is the study of the evolution of a confined bosonic quantum field in Minkowski spacetime. This approach is helpful in understanding the description and evolution of a quantum field without the complexities associated with BEC physics while simultaneously learning about the description of quantum fields in Minkowski spacetime, the natural framework of special relativity.

In this chapter, we restrict ourselves to studying the evolution of bosonic matter, which is described as a real scalar quantum field with no spin, such as light or the excitations created on a BEC. As we are interested in describing real tabletop experiments, we confine the quantum fields to a cavity. As a first step, we consider the field to be on a flat Minkowski spacetime described from an inertial reference frame. Then, we describe it from the reference frame of an accelerated observer.

This chapter is organized as follows: Section 2.1 discusses the evolution of a confined massive quantum field ϕ in Minkowski spacetime for an inertial observer with coordinates (t, x). The solutions to the equation of motion are derived and quantized through canonical quantization. The resulting Hamiltonian corresponds to an infinite collection of quantum harmonic oscillators, which allow the introduction of particle creation and annihilation operators, as well as the construction of a Fock space. In Section 2.2, a similar procedure is followed for an accelerated observer with coordinates (η, χ), yielding a similar construction that results in a Fock space for a different set of particles. Finally, in Section 2.3, the relationship between the field's descriptions by the inertial and accelerated observers is established using a Bogoliubov transformation. The metric signature $(-,+,+,+)$ is employed, with Greek indices taking the values: 0, 1, 2, 3 and Latin indices running through the spatial coordinates. The summation convention is applied for repeated indices, and natural units where $c = \hbar = 1$ are assumed for this chapter.

2.1 Inertial Cavity

Consider a real scalar field ϕ with mass m on a curved spacetime described by the metric $g_{\mu\nu}$. The classical Lagrangian density of this system is given by

$$\mathcal{L} = \sqrt{-g}\left(-\frac{1}{2}g^{\mu\nu}\nabla_\mu\phi\nabla_\nu\phi - \frac{1}{2}m^2\phi^2\right), \tag{2.1}$$

where $g = \det(g_{\mu\nu})$ and the operator ∇ corresponds to the covariant derivative [5, 30]. Invoking Hamilton's principle, the dynamical evolution of the Lagrangian is set by the Euler-Lagrange equation in curved spacetime [31],

$$\frac{\partial \mathcal{L}}{\partial \phi} - \nabla_\mu \frac{\partial \mathcal{L}}{\partial(\nabla_\mu \phi)} = 0. \tag{2.2}$$

For the massive real scalar field ϕ, this leads to the Klein-Gordon (KG) equation

$$\left(\Box - m^2\right)\phi = 0, \tag{2.3}$$

where $\Box$ is the d'Alembert operator, which has the general form

$$\Box = \frac{1}{\sqrt{-g}}\partial_\mu\left(\sqrt{-g}g^{\mu\nu}\partial_\nu\right). \tag{2.4}$$

Restricting ourselves to the case of flat (1+1)-dimensional Minkowski spacetime, where the metric $\eta_{\mu\nu}$ can be read from the line element $ds^2 = \eta_{\mu\nu}dx^\mu dx^\nu = -dt^2 + dx^2$, the d'Alembert operator is $\Box = \eta^{\mu\nu}\partial_\mu\partial_\nu$. Then, the Lagrangian density reduces to

$$\mathcal{L} = -\frac{1}{2}\eta^{\mu\nu}\partial_\mu\phi\,\partial_\nu\phi - \frac{1}{2}m^2\phi^2, \tag{2.5}$$

and the Klein-Gordon equation takes the form

$$\left(-\partial_t^2 + \partial_x^2 - m^2\right)\phi(t,x) = 0. \tag{2.6}$$

The most general solution is obtained by constructing a complete set of orthonormal modes. Following [30], the pseudo-inner product on the space of solutions to the KG equation in Minkowski spacetime is defined as

$$(\phi_1, \phi_2)_{\text{KG}} := -i\int_{\Sigma_t}(\phi_1\,\partial_t\phi_2^* - \phi_2^*\,\partial_t\phi_1)dx, \tag{2.7}$$

where Σ_t denotes a constant-time hypersurface and * denotes complex conjugation.

To restrict the field inside a cavity, Dirichlet boundary conditions are imposed on the field,

$$\phi(t, x_l) = \phi(t, x_r) = 0, \tag{2.8}$$

where $L := x_r - x_l$, is the length of the cavity. The normalized solutions obtained are

$$\phi_n(t,x) = \frac{1}{\sqrt{\omega_n L}}\sin\left[\frac{n\pi}{L}(x - x_l)\right]e^{-i\omega_n t}, \tag{2.9}$$

where

$$\omega_n = \sqrt{\left(\frac{n\pi}{L}\right)^2 + m^2}, \qquad n \in \mathbb{Z}^+. \tag{2.10}$$

Equation (2.9) describes a single mode solution to the KG equation (2.6) for a massive scalar field inside a cavity of length L, inertially moving through Minkowski spacetime. The modes get a discrete label n, which characterizes the energy of the eigenstates through the eigenvalues given by (2.10).

The solutions can be classified into positive-frequency solutions ϕ_n and negative-frequency solutions ϕ_n^*, where ϕ_n^* denotes the complex conjugate of ϕ_n, according to the following criteria:

$$i\partial_t \phi_n = +\omega_n \phi_n \,, \tag{2.11a}$$

$$i\partial_t \phi_n^* = -\omega_n \phi_n^* \,. \tag{2.11b}$$

This allows us to define a notion of a particle by identifying the positive-frequency excitations of the field as particles.

The full solution to the KG equation can be expanded as

$$\phi(t,x) = \sum_n \left[a_n \phi_n(t,x) + a_n^* \phi_n^*(t,x)\right], \tag{2.12}$$

where the a_n are arbitrary complex functions.

In order to implement the canonical quantization, we need to calculate the Hamiltonian density associated with the Lagrangian density (2.5). The canonically conjugate field is

$$\pi(t,x) = \frac{\partial \mathcal{L}}{\partial \dot{\phi}(t,x)} = \dot{\phi}(t,x), \tag{2.13}$$

where the dot represents temporal derivation. As customary, using a Legendre transformation, the Hamiltonian density is computed as

$$\mathcal{H} = \pi\dot{\phi} - \mathcal{L} = \frac{1}{2}\left(\pi^2 + (\partial_x \phi)^2 + m^2\phi^2\right). \tag{2.14}$$

Now, we promote the classical fields $\phi(t,x)$ and $\pi(t,x)$, to quantum operators satisfying equal-time commutation relations

$$[\hat{\phi}(t,x),\hat{\pi}(t,x')] = i\delta(x-x')\,, \tag{2.15a}$$

$$[\hat{\phi}(t,x),\hat{\phi}(t,x')] = [\hat{\pi}(t,x),\hat{\pi}(t,x')] = 0\,. \tag{2.15b}$$

The Hamiltonian operator is then,

$$\hat{H} = \int \frac{1}{2}\left(\hat{\pi}(t,x)^2 + (\partial_x\hat{\phi}(t,x))^2 + m^2\hat{\phi}(t,x)^2\right) dx. \tag{2.16}$$

Using the commutation relations, we can calculate Hamilton's equations to obtain that

$$\partial_t\,\hat{\phi} = -i[\hat{\phi}(t,x),\hat{H}] = \hat{\pi}(t,x), \tag{2.17a}$$

$$\partial_t\,\hat{\pi} = -i[\hat{\pi}(t,x),\hat{H}] = (\partial_x^2 - m^2)\hat{\phi}(t,x). \tag{2.17b}$$

Therefore, combining the two previous equations, we find that the quantized field operator keeps satisfying the KG equation,

$$\left(-\partial_t^2 + \partial_x^2 - m^2\right)\hat{\phi}(t,x) = 0. \tag{2.18}$$

Then, the solution to the KG equation obtained for the classical case, Eq. (2.12), can be recovered and quantized by promoting the complex functions a_n and a_n^* to quantum operators $\hat{a}_n$ and $\hat{a}_n^\dagger$. The quantum field operator can be expressed as,

$$\hat{\phi}(t,x) = \sum_n \left[\hat{a}_n\phi_n(t,x) + \hat{a}_n^\dagger\phi_n^*(t,x)\right]. \tag{2.19}$$

Using the commutation relations for the field operators, as well as the completeness and orthogonality of the functions (2.9), we can obtain that the operators $\hat{a}_n$ and $\hat{a}_n^\dagger$ satisfy the commutation relations [32, 33]

$$[\hat{a}_m,\hat{a}_n^\dagger] = \delta_{mn}\,, \tag{2.20a}$$

$$[\hat{a}_m,\hat{a}_n] = [\hat{a}_m^\dagger,\hat{a}_n^\dagger] = 0\,. \tag{2.20b}$$

These relations correspond to the ones usually associated with creation and annihilation operators. To make sure of their interpretation, we substitute the expansions of the field operators $\hat{\phi}(t,x)$ and $\hat{\pi}(t,x)$ in terms of $\hat{a}_n$ and $\hat{a}_n^\dagger$ into the Hamiltonian, which results in

$$\hat{H} = \sum_n \omega_n \left(\hat{a}_n^\dagger \hat{a}_n + \frac{1}{2} \right) . \tag{2.21}$$

This Hamiltonian allows us to interpret the field operator $\hat{\phi}$, defined in Minkowski spacetime governed by the Klein-Gordon equation, as an infinite collection of decoupled harmonic oscillators of bosonic nature. The operators $\hat{a}_n^\dagger$ and $\hat{a}_n$, create and annihilate particles described by the functions $\phi_n(t,x)$. These operators can be used to define a basis for the Hilbert space where the basis states correspond to the eigenstates of the number operator $\hat{n}_k = \hat{a}_k^\dagger \hat{a}_k$ for each k-th mode.

Restricting ourselves to the k-th mode, we can define the vacuum state $|0\rangle_k$ through the relation

$$\hat{a}_k |0_k\rangle = 0, \qquad \text{for all } \; k, \tag{2.22}$$

as the state which contains no particles. The state containing n_k particles can be constructed by acting n_k times the operator $\hat{a}_k^\dagger$ on the vacuum state,

$$|n_k\rangle = \frac{1}{\sqrt{n_k!}} (\hat{a}_k^\dagger)^{n_k} |0_k\rangle . \tag{2.23}$$

Considering the rest of the modes and defining the complete vacuum state as $|0\rangle = \otimes_{i=0}^{k} |0_i\rangle$, the most general state up to the k-th mode is given by

$$|n_1, n_2, \cdots, n_k\rangle = \frac{1}{\sqrt{n_1! n_2! \cdots n_k!}} (\hat{a}_1^\dagger)^{n_1} (\hat{a}_2^\dagger)^{n_2} \cdots (\hat{a}_i^\dagger)^{n_k} |0\rangle , \tag{2.24}$$

which contains n_1 particles in the first mode, n_2 particles in the second mode, etc. These states are known as the Fock basis, and they form a basis for the Hilbert space. When constructed this way, the Hilbert space is often called a Fock space.

2.2 Accelerated Cavity

Let us consider the case of a field contained inside an accelerated cavity. To describe the reference frame of a uniformly accelerated observer in a (1+1)-dimensional Minkowski spacetime, we introduce Radar coordinates (η, χ) [5, 30]. These coordinates are defined for the right Rindler wedge, that is, the region where $|t| < x$, by the transformation

$$t = \frac{1}{\alpha} e^{\alpha\chi} \sinh(\alpha\eta), \tag{2.25a}$$

$$x = \frac{1}{\alpha} e^{\alpha\chi} \cosh(\alpha\eta), \tag{2.25b}$$

where the coordinate domain is $0 < \chi < \infty$ and $-\infty < \eta < \infty$, and $\alpha \in \mathbb{R}$ is a parameter related to the observer's proper acceleration. The inverse transformations are given by

$$\eta = \frac{1}{\alpha} \tanh^{-1}\left(\frac{t}{x}\right), \tag{2.26a}$$

$$\chi = \frac{1}{2\alpha} \ln[\alpha^2(x^2 - t^2)]. \tag{2.26b}$$

Under this change of coordinates, the line element for Minkowski spacetime becomes

$$ds^2 = e^{2\alpha\chi}(-d\eta^2 + d\chi^2). \tag{2.27}$$

To verify that Radar coordinates describe a uniformly accelerated observer, notice that Eqs. (2.25) imply the relation

$$x^2 - t^2 = \alpha^{-2} e^{2\alpha\chi}. \tag{2.28}$$

which defines a family of hyperbolas for each constant value of χ. These curves represent time-like worldlines and describe the trajectory of point-like observers experiencing a constant proper acceleration.

From the line element, the proper time along these trajectories is $\tau = e^{\alpha\chi}\eta$ for a fixed χ. The corresponding trajectory, $x^\mu = (t, x)$, is described by Eqs. (2.25) and its the four-acceleration, a^μ, is evaluated as

$$a^\mu = \frac{d^2x^\mu}{d\tau^2} = \alpha e^{-\alpha\chi}(\sinh(\alpha e^{-\alpha\chi}\tau), \cosh(\alpha e^{-\alpha\chi}\tau)), \tag{2.29}$$

whose proper acceleration yields

$$a = \sqrt{a^\mu a_\mu} = \alpha e^{-\alpha\chi}. \tag{2.30}$$

This confirms that an observer described with Radar coordinates for a fixed χ follows hyperbolic trajectories with constant proper acceleration. Figure 2.1 displays a

Rindler chart where trajectories for constant χ and constant η are shown.

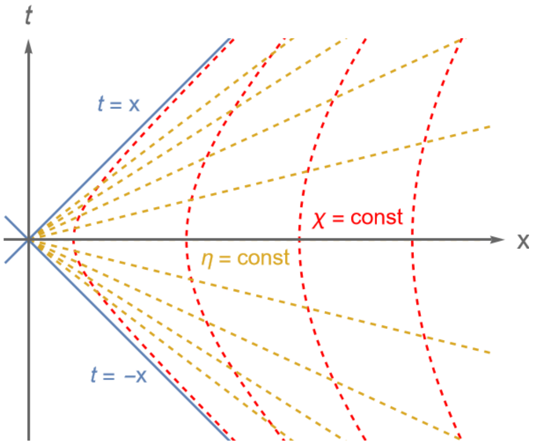

Figure 2.1: Rindler Chart for the Right Rindler Wedge ($|t| < x$). Trajectories for χ =constant (dashed red lines) describe a family of uniformly accelerated point-like observers. Trajectories for η =constant (dashed yellow lines) describe a family of space-like trajectories that correspond to foliations of simultaneity for an accelerated observer at a fixed own proper time. The Rindler horizons (solid blue lines) correspond to $t = x$ and $t = -x$.

Now, let's consider an accelerated cavity in Minkowski spacetime containing a scalar field ψ governed by the KG equation (2.3). In Radar coordinates, the d'Alembert operator takes the form

$$\Box = e^{-2\alpha\chi}(-\partial_\eta^2 + \partial_\chi^2). \tag{2.31}$$

Then, the KG equation describing the evolution of a massive scalar field is

$$(-\partial_\eta^2 + \partial_\chi^2 - e^{2\alpha\chi}m^2)\psi(\eta, \chi) = 0. \tag{2.32}$$

For simplicity, we restrict ourselves to solutions for the massless scalar field case.

The accelerated cavity can be constructed by restricting the field inside a bounded region. We suppose that the left wall of the cavity follows a uniformly accelerated worldline of constant $\chi = \chi_l$, while the right wall will follow another uniformly accelerated worldline given by $\chi = \chi_r$. The length of the cavity as measured by an observer co-moving with the accelerated reference frame, i.e. the proper length, is given by $l = \chi_r - \chi_l$.

To restrict the field to a cavity following a uniformly accelerated trajectory in

Minkowski spacetime, we impose Dirichlet conditions on the field:

$$\psi(\eta, \chi_l) = \psi(\eta, \chi_r) = 0. \tag{2.33}$$

Restricting ourselves to the case of a massless field, the mode solutions to the KG equation in Radar coordinates can be expressed as

$$\psi_n(\eta, \chi) = \frac{1}{\sqrt{\Omega_n l}} \sin[\Omega_n(\chi - \chi_l)] e^{-i\Omega_n \eta}\,, \tag{2.34}$$

where the frequencies of the modes must satisfy the relation

$$\Omega_n = \frac{n\pi}{l}, \qquad n \in \mathbb{Z}^+. \tag{2.35}$$

The solutions can be split into positive frequency solutions ψ_n and negative frequency solutions ψ_n^* according to

$$i\partial_t \psi_n = +\Omega_n \psi_n\,, \tag{2.36a}$$

$$i\partial_t \psi_n^* = -\Omega_n \psi_n^*\,. \tag{2.36b}$$

The full solution to the KG equation can be expanded as

$$\psi(\eta, \chi) = \sum_n \left[A_n \psi_n(\eta, \chi) + A_n^* \psi_n^*(\eta, \chi)\right], \tag{2.37}$$

where A_n is an arbitrary complex function.

The canonical quantization can be implemented following the approach taken for the field inside the inertial cavity. For that, we need to obtain the Hamiltonian associated with the field inside the accelerated cavity. Considering again the general case of a massive scalar field, we use the general definition (2.1) to compute the Lagrangian density,

$$\mathcal{L} = \frac{1}{2}\left((\partial_\eta \psi)^2 - (\partial_\chi \psi)^2 - m^2 \psi^2 e^{2\alpha\chi}\right). \tag{2.38}$$

Then, the canonically conjugate field corresponds to

$$\Pi(\eta, \chi) = \frac{\partial \mathcal{L}}{\partial(\partial_\eta \psi(\eta, \chi))} = \partial_\eta \psi(\eta, \chi), \tag{2.39}$$

therefore, through the usual Legendre transformation, we get that the Hamiltonian density reads

$$\mathcal{H} = \frac{1}{2}\left(\Pi^2 + (\partial_\chi \psi)^2 + e^{2\alpha\chi} m^2 \psi^2\right). \tag{2.40}$$

The classical fields $\psi(t,x)$ and $\Pi(t,x)$ get promoted to quantum operators satisfying equal-time commutation relations

$$[\hat{\psi}(\eta,\chi), \hat{\Pi}(\eta,\chi')] = i\delta(\chi-\chi')\,, \tag{2.41a}$$

$$[\hat{\psi}(\eta,\chi), \hat{\psi}(\eta,\chi')] = [\hat{\Pi}(\eta,\chi), \hat{\Pi}(\eta,\chi')] = 0\,, \tag{2.41b}$$

so we can write the Hamiltonian operator as

$$\hat{H} = \int \frac{1}{2}\left(\hat{\Pi}(\eta,\chi)^2 + (\partial_\chi \hat{\psi}(\eta,\chi))^2 + e^{2\alpha\chi} m^2 \hat{\psi}(\eta,\chi)^2\right) d\chi. \tag{2.42}$$

In analogy with the case of the inertial cavity, calculating Hamilton's equations yields $\partial_\eta \hat{\psi}(\eta,\chi) = \hat{\Pi}(\eta,\chi)$ and $\partial_\eta \hat{\Pi}(\eta,\chi) = (\partial_\chi^2 - e^{2\alpha\chi} m^2)\hat{\psi}(\eta,\chi)$, which together imply that the quantized field also fulfils the same KG equation as the classical field,

$$(-\partial_\eta^2 + \partial_\chi^2 - e^{2\alpha\chi} m^2)\hat{\psi}(\eta,\chi) = 0. \tag{2.43}$$

Returning the case of a massless quantum field, we recover the classical solution for the quantized field by promoting the complex functions A_n and A_n^* to quantum operators $\hat{A}_n$ and $\hat{A}_n^\dagger$. Then, the quantum field operator is

$$\hat{\psi}(\eta,\chi) = \sum_n \left[\hat{A}_n \psi_n(\eta,\chi) + \hat{A}_n^\dagger \psi_n^*(\eta,\chi)\right], \tag{2.44}$$

where we find that the operators $\hat{A}_n$ and $\hat{A}_n^\dagger$ satisfy the commutation relations

$$[\hat{A}_m, \hat{A}_n^\dagger] = \delta_{mn}\,, \tag{2.45a}$$

$$[\hat{A}_m, \hat{A}_n] = [\hat{A}_m^\dagger, \hat{A}_n^\dagger] = 0\,. \tag{2.45b}$$

Using the expansion of the quantum field operator in terms of the $\hat{A}_n$, $\hat{A}_n^\dagger$ operators, the Hamiltonian operator for the field inside the accelerated cavity is

$$\hat{H} = \sum_n \Omega_n \left(\hat{A}_n^\dagger \hat{A}_n + \frac{1}{2}\right). \tag{2.46}$$

Again, we have an infinite sum of decoupled harmonic oscillators where the operators

$\hat{A}_n^\dagger$ and $\hat{A}_n$ can be related to the creation and annihilation of particles described by the functions $\psi_n(\eta,\chi)$.

The Hilbert space can be constructed from the eigenstates of the number operator $\hat{N}_k = \hat{A}_k^\dagger \hat{A}_k$ for the mode k. We can define the vacuum state $|0'_k\rangle$ for the k-th mode, which is the state containing no particles, as

$$\hat{A}_k\,|0'_k\rangle = 0 \qquad \text{for all } \; k, \tag{2.47}$$

and so on, for the rest of the modes. A Fock state containing N_1 particles in the first mode, N_2 particles in the second mode, etc., can be built as

$$|N_1, N_2, \cdots, N_k\rangle = \frac{1}{\sqrt{N_1!N_2!\cdots N_k!}}(\hat{A}_1^\dagger)^{N_1}(\hat{A}_2^\dagger)^{N_2}\cdots(\hat{A}_i^\dagger)^{N_k}\,|0'\rangle\,, \tag{2.48}$$

where the complete vacuum state is $|0'\rangle = \otimes_{i=0}^{k}|0'_i\rangle$.These states then constitute the basis for the Fock space of the accelerated cavity containing a quantum field in Minkowski spacetime.

2.3 Bogoliubov Transformations

As we can see, the choice of a complete basis of solutions to the Klein-Gordon equation in flat spacetime is not unique. However, the set of field mode solutions detected by the inertial observer $\{\phi_n(t,x),\phi_n^*(t,x)\}_{n\in\mathbb{Z}^+}$ and those detected by the accelerated observer $\{\psi_n(\eta,\chi),\psi_n^*(\eta,\chi)\}_{n\in\mathbb{Z}^+}$ can be related to each other by a Bogoliubov transformation. A Bogoliubov transformation is a change of basis from one set of mode solutions to another that preserves the commutation relations of the field operators, that is, a unitary transformation. The relation between the field solutions measured by the inertial and accelerated observers is given as

$$\psi_m(t,x) = \sum_n \left[\alpha_{mn}\,\phi_n(t,x) + \beta_{mn}\,\phi_n^*(t,x)\right], \tag{2.49a}$$

$$\psi_m^*(t,x) = \sum_n \left[\alpha_{mn}^*\,\phi_n^*(t,x) + \beta_{mn}^*\,\phi_n(t,x)\right]. \tag{2.49b}$$

The matrices α_{ij} and β_{ij} implementing the transformation correspond to the Bogoliubov coefficients. Using the orthonormality of the mode functions and the inner product (2.7), they can be expressed as

$$\alpha_{mn} = (\psi_m, \phi_n)_{\mathrm{KG}}\,, \tag{2.50a}$$

$$\beta_{mn} = -\,(\psi_m, \phi_n^*)_{\mathrm{KG}}\,. \tag{2.50b}$$

We can find the relation between the mode solutions that we have obtained. To achieve this, we parameterize the cavity geometry using the dimensionless small parameter

$$h \equiv a_c L\,, \tag{2.51}$$

where a_c is the acceleration at the centre of the cavity and L, as before, is the length of the cavity from the rest frame. Performing a perturbative analysis for $h \ll 1$, we get

$$\alpha_{nn} = 1 - \frac{1}{240}\pi^2 n^2 h^2 + O(h^4)\,, \tag{2.52a}$$

$$\alpha_{mn} = \sqrt{mn}\,\frac{(-1 + (-1)^{m-n})}{\pi^2 (m-n)^3} h + O(h^2)\,, \tag{2.52b}$$

$$\beta_{mn} = \sqrt{mn}\,\frac{(1 - (-1)^{m-n})}{\pi^2 (m+n)^3} h + O(h^2)\,. \tag{2.52c}$$

These expressions allow us to relate the field solutions between an inertial and an accelerated observer.

Overall, Bogoliubov transformations are very important as they can be used to model the time evolution of quantum fields. Such transformations arise, for example, when considering changes in coordinate systems (such as Lorentz boosts or transformations between observers) or as a result of spacetime dynamics [16]. They also arise, for instance, in the evolution of a phonon field inside a BEC when it is perturbed by the passing of a gravitational wave, as in [18].

Bogoliubov transformations carry deep physical meaning related to the particle content in a quantum state as seen by different observers [5]. This can be seen by considering the Bogoliubov transformation in terms of the annihilation and creation operators:

$$\hat{A}_m = \sum_n (\alpha_{mn}^*\,\hat{a}_n - \beta_{mn}^*\,\hat{a}_n^\dagger)\,. \tag{2.53}$$

A positive frequency excitation, as described by one observer, will be a superposition of both positive and negative frequencies as described by a different observer.

Therefore, in QFT, there is no such thing as a universal notion of a particle. In particular, transformations where $\beta = 0$, which preserve the number of particles, are called passive transformations, whereas transformations where $\beta \neq 0$, which create or annihilate particles, are called active transformations.

It is worth noticing that an important property is satisfied by the Bogoliubov coefficients. As the Bogoliubov transformation is unitary, it must preserve the field's commutation relations. This forces the coefficients to satisfy the relations

$$\alpha\alpha^\dagger - \beta\beta^\dagger = \mathbb{I}, \tag{2.54a}$$

$$\alpha\beta^T = \beta\alpha^T, \tag{2.54b}$$

known as the Bogoliubov identities [5, 30].

In conclusion, Chapter 2 has provided the framework for understanding the behaviour of bosonic scalar fields confined to a region in Minkowski spacetime from the perspectives of both an inertial and an accelerated observer. The quantization of the scalar fields was performed using canonical quantization, which allowed us to express each field as an infinite sum of quantum harmonic oscillators. This subsequently led us to the construction of a Fock space for each observer, where the natural states correspond to the particle states. By employing Bogoliubov transformations, we have demonstrated the relationship between the fields and particle content for each observer. This chapter laid the groundwork for the study of Gaussian states, a particular family of states that can be generated from the vacuum state of any Fock space and that will prove to have a useful implementation for metrology. These states will be the main focus of the next chapter.

Chapter 3

Gaussian States and the Covariance Matrix Formalism

In the previous chapter, we studied a quantum field contained inside a cavity travelling with an inertial or an accelerated motion through a (1+1)-dimensional Minkowski spacetime. The analysis allowed us to understand the field in both cases as an infinite sum of quantum harmonic oscillators, which, at the same time, can be viewed as a decomposition of the quantum field in terms of bosonic quantum modes. The natural description for this system involves Fock states, which specify the number of particles in each of the modes of the field. Using the Fock basis, we can construct a special family of states known as Gaussian states.

Gaussian states can be identified because their characteristic function has a Gaussian form. They originate from Hamiltonians that are at most quadratic in the canonical operators[1], such as the creation and annihilation operators of the harmonic oscillator or the position and momentum operators in quantum mechanics. Although the condition of a quadratic Hamiltonian might seem restrictive, it is commonly satisfied in many experimental settings in areas such as quantum optics, optomechanics, trapped ions and atomic ensembles [34].

For example, Gaussian states naturally emerge as ground or thermal states of bosonic systems, such as light fields, the vibrational modes in solids, or Bose-Einstein condensates [35]. They have been extensively studied in the context of quantum optics and have become a central theme in the area of continuous-variable quantum information. Moreover, Gaussian transformations—the transformations that pre-

---

[1] Operators following canonical commutation relations.

serve the Gaussianity of a state—are associated with typical experimental operations such as beam splitters and phase shifters. These features make Gaussian states rather straightforward to generate and manipulate, making them easy to implement experimentally [36, 37, 38].

From a theoretical standpoint, it is very convenient to work with Gaussian states. Despite living in an infinite-dimensional Hilbert space inherited from their continuous-variable nature, they can be completely described simply by their first and second statistical moments using the covariance matrix formalism (CMF) [37]. Briefly speaking, the CMF provides a description for Gaussian states and Gaussian transformations in Phase space [39], which is equivalent to the conventional description in Hilbert space but benefits from making calculations more tractable. For instance, it can facilitate the evaluation of the entropy of a quantum state.

The chapter is organized as follows. In Section 3.1, the difference between Hilbert space and Phase space, along with their implications for quantum states and transformations, is discussed. Section 3.2 reviews the formal construction of Fock space for a bosonic system. Gaussian states and its Phase space description, known as the covariance matrix formalism, are introduced in Section 3.3. The description for Gaussian transformation in Phase space is given in Section 3.4, where the explicit relation between the Hilbert space and Phase space formalism for Gaussian states and transformations is provided. Next, Section 3.5 discusses the mathematical structure followed by Gaussian states and transformations in Phase space, that is, the symplectic geometry. Section 3.6 presents Williamson's theorem, which is a tool that permits the factorization of Gaussian states in terms of symplectic matrices. Finally, Section 3.7 provides a list of the basic Gaussian states expressed in terms of the covariance matrix formalism.

3.1 Quantum Continuous-Variable Systems: Hilbert space vs Phase space

Quantum continuous variable systems are quantum systems whose degrees of freedom are associated with canonical operators that have a continuous spectrum [37]. The eigenstates of these operators define an infinite-dimensional basis for the Hilbert space of the system. A classic example of a quantum continuous variable system is a quantized bosonic field, which can be modelled as a collection of non-interacting quantum harmonic oscillators with different frequencies. Continuous variable quantum systems play a relevant role in quantum communication and for quantum sensing, detection, and imaging techniques [35].

Working with an infinite-dimensional Hilbert space can present some difficulties, for instance, when studying the dynamics of the system. Restricting exclusively to Gaussian states is a good strategy to make quantum continuous variable systems more tractable since, in Phase space, Gaussian states can be completely described by a finite number of degrees of freedom.

Usually, quantum states are described in Hilbert space by a positive semi-defined operator known as the density matrix $\hat{\rho}$. On the contrary, in Phase space, quantum states are represented by a characteristic function, for example, the Wigner function. Another comparison arises when considering transformations. In particular, Gaussian transformations in Hilbert space are driven by unitary transformations, while in Phase space, they are represented by symplectic matrices.

Continuous variable systems are usually associated with the dynamical degrees of freedom of non-relativistic particles (first quantization) or bosonic quantum fields (second quantization). In any case, the formalism used to describe the Gaussian states in Phase space is equivalent for both cases. In the next section, we construct the Fock space for a bosonic system in preparation for defining and describing Gaussian states.

3.2 Fock Space of a Bosonic System

In quantum field theory, a bosonic field is a quantum field composed of bosons. Bosons are integer-spin particles that are characterized for obeying canonical commutation relations and, consequently, they follow the Bose-Einstein statistics[2]. A key property derived from the statistics reveals that bosons are not subject to the Pauli exclusion principle. Therefore, an arbitrary number of identical bosons can occupy the same quantum state.

Examples of bosonic fields include scalar fields, which give rise to spin-0 bosons such as the Higgs boson, and gauge fields, which correspond to spin-1 bosons like the photon. Bosons can also exist in the form of composite bosons, where bound states of fermions combine to behave effectively as a boson. Examples include Cooper pairs in superconductors, atomic bosons like helium-4 atoms or Bose-Einstein condensates.

---

[2] In contrast, fermionic systems follow canonical anti-commutation relations and obey the Fermi-Dirac statistics.

Fields in the context of quantum field theory correspond to systems with a varying number of particles. To mathematically represent such systems, we use the Fock space, an algebraic structure that is constructed from the single-particle Hilbert space to represent multi-particle states. The Fock space is the sum of the Hilbert spaces representing zero-particle states, one-particle states, two-particle states, and so forth.

More technically, if we denote as $\mathcal{H}$ the one-particle Hilbert space, then the bosonic Fock space $\mathcal{F}(\mathcal{H})$ is the direct sum of symmetric tensor powers of $\mathcal{H}$ [40]

$$\mathcal{F}(\mathcal{H}) = \bigoplus_{n=0}^{\infty} \mathrm{Sym}(\mathcal{H}^{\otimes n}), \tag{3.1}$$

where $\mathrm{Sym}(\cdot)$ is the symmetrization operator that ensures the tensor product states are symmetric under particle exchanges and

$$\mathcal{H}^{\otimes n} = \underbrace{\mathcal{H} \otimes \cdots \otimes \mathcal{H}}_{n\text{-times}}\,, \tag{3.2}$$

is the n-particle Hilbert space.

The Fock basis can be constructed explicitly as follows. Consider a bosonic system composed of a discrete number N of modes described by the following Hamiltonian,

$$\hat{H} = \sum_{k=1}^{N} \hat{H}_k, \qquad \hat{H}_k = \hbar\omega_k \left(\hat{a}_k^{\dagger}\hat{a}_k + \frac{1}{2} \right), \tag{3.3}$$

which, for instance, could originate from the quantization of the electromagnetic field inside a cavity [41]. The infinite sum of quantum harmonic oscillators has a straightforward interpretation in terms of bosonic particles. The Hamiltonian (3.3) describes the total energy of a collection of bosonic particles, which are created and annihilated by the operators $\hat{a}_k^{\dagger}$ and $\hat{a}_k$, respectively. Each particle has an energy $\hbar\omega_k$. These operators satisfy the standard canonical commutation relations,

$$[\hat{a}_k, \hat{a}_l^{\dagger}] = \delta_{kl}, \qquad [\hat{a}_k, \hat{a}_l] = [\hat{a}_k^{\dagger}, \hat{a}_l^{\dagger}] = 0. \tag{3.4}$$

The total particle number operator is defined as

$$\hat{n}_{tot} = \sum_k \hat{n}_k = \sum_k \hat{a}_k^{\dagger}\hat{a}_k, \tag{3.5}$$

where $\hat{n}_k$ is the particle number operator for the mode k. It is relevant to notice that these operators commute with each other for different modes

$$[\hat{n}_k, \hat{n}_l] = 0, \quad \text{for } k \neq l. \tag{3.6}$$

Therefore, the operator $\hat{n}_{tot}$ commutes with the Hamiltonian $\hat{H}$, implying that it is possible to find a common set of eigenstates for both operators. These eigenstates can be fully characterized by the action of the operators $\hat{n}_k$ on them,

$$\hat{n}_k \left| n_1, n_2, \ldots, n_k, \ldots \right\rangle = n_k \left| n_1, n_2, \ldots, n_k, \ldots \right\rangle, \tag{3.7}$$

yielding the eigenvalues n_k that correspond to the number of particles in the mode k. The eigenstates $\left| n_1, n_2, \ldots \right\rangle$ form an orthonormal basis for the Fock space that is usually called the 'particle-number representation'. The inner product in Fock space is defined as

$$\left\langle n_1', n_2', \ldots \middle| n_1, n_2, \ldots \right\rangle = \delta_{n_1', n_1} \delta_{n_2', n_2} \cdots . \tag{3.8}$$

The total number of particles n is found by applying the operator $\hat{n}_{tot}$ to the eigenstates:

$$\hat{n}_{tot} \left| n_1, n_2, \ldots \right\rangle = \sum_k \hat{n}_k \left| n_1, n_2, \ldots \right\rangle = n \left| n_1, n_2, \ldots \right\rangle . \tag{3.9}$$

The application of the operators $\hat{a}_k^\dagger$ and $\hat{a}_k$ on the state $\left| n_1, n_2, \ldots \right\rangle$ produces a new state. The particle number of these new states can be calculated, and it is obtained that

$$\hat{n}_{tot}\, \hat{a}_k^\dagger \left| n_1, n_2, \ldots \right\rangle = (n+1) \hat{a}_k^\dagger \left| n_1, n_2, \ldots \right\rangle, \tag{3.10a}$$

$$\hat{n}_{tot}\, \hat{a}_k \left| n_1, n_2, \ldots \right\rangle = (n-1) \hat{a}_k \left| n_1, n_2, \ldots \right\rangle . \tag{3.10b}$$

The action of the operators on the Fock basis translates into the increase or decrease of the particle number by adding or subtracting a particle in the mode k. This confirms the interpretation of $\hat{a}_k^\dagger$ and $\hat{a}_k$ as creation and annihilation operators. Since the operator $\hat{n}_{tot}$ is a positive operator[3], it must be bounded from below. This implies that a state $|0\rangle = \bigotimes_{k=1}^{N} |0_k\rangle$ must exist, such that

---

[3] Given a Hilbert space $\mathcal{H}$, a linear operator $\hat{A} : \mathcal{H} \to \mathcal{H}$ is called positive semi-definite $\hat{A} \geq 0$ if, for every $|x\rangle \in \mathcal{H}$, $\langle x | \hat{A} x \rangle \geq 0$, [42].

$$\hat{a}_k \left|0\right\rangle = 0, \tag{3.11}$$

for every mode k. The state $\left|0\right\rangle$, called the vacuum, is the state that does not contain any particles. The rest of the Fock states are built by repeatedly applying the creation operators onto the vacuum state. In this way, the state containing n_1 particles in the first mode, n_2 particles in the second mode, and so on, is created as

$$\left|n_1, n_2, \cdots\right\rangle = \frac{1}{\sqrt{n_1! n_2! \cdots}} (\hat{a}_1^\dagger)^{n_1} (\hat{a}_2^\dagger)^{n_2} \cdots \left|0\right\rangle, \tag{3.12}$$

where the states have already been normalized.

Finally, the explicit action of the creation and annihilation operators on the Fock states is given by,

$$\hat{a}_k^\dagger \left|n_1, \ldots, n_k, \ldots\right\rangle = \sqrt{n_k + 1} \left|n_1, \ldots, n_k + 1, \ldots\right\rangle, \qquad \text{for } n_k \geq 0, \tag{3.13a}$$

$$\hat{a}_k \left|n_1, \ldots, n_k, \ldots\right\rangle = \sqrt{n_k} \left|n_1, \ldots, n_k - 1, \ldots\right\rangle, \qquad \text{for } n_k \geq 1. \tag{3.13b}$$

In summary, the Fock space representation of the Hilbert space provides a natural description for bosonic quantum fields, which correspond to systems with a varying number of particles. The Fock states encapsulate the behaviour of the field by specifying the field's particle content. An example where this representation is well-suited is found in Chapter 2, where we describe the motion through spacetime of a cavity-confined quantum field. The Fock space will again become relevant in Chapter 5, where we discuss the phonons of the Bose-Einstein condensate.

3.3 Gaussian States in Phase Space

All the physical information about a quantum system is contained in its quantum state. In Hilbert space, quantum states are represented by a density matrix $\hat{\rho}$. The density matrix is a positive-definite, self-adjoint operator of trace one that acts on the Hilbert space of the system. In the case of a bosonic system, we have that $\hat{\rho} : \mathcal{H}^{\otimes n} \to \mathcal{H}^{\otimes n}$. When the state of the system is pure, which follows whenever $\hat{\rho}^2 = \hat{\rho}$ is satisfied, the density matrix can be expressed as $\hat{\rho} = |\varphi\rangle\langle\varphi|$, for all $|\varphi\rangle \in \mathcal{H}^{\otimes n}$. Any density matrix has an equivalent representation in Phase space in terms of a characteristic function.

The defining feature of Gaussian states is that their associated characteristic function has a Gaussian form, which is completely determined by the first and second statistical moments of the canonical operators. The Phase space description of Gaussian states and Gaussian transformations is known as the *covariance matrix formalism* [36, 37]. Notice that the covariance matrix formalism corresponds to a subspace of the Phase space description of a quantum system with the restriction to Gaussian states.

The representation of the covariance matrix formalism, however, is not unique. The selection of the Hilbert space basis affects the definition of the statistical moments, leading us to at least two different representations of the covariance matrix formalism. If the statistical moments are defined in terms of the creation and annihilation operators, $\hat{a}$ and $\hat{a}^\dagger$, we obtain the complex representation. However, if they are defined in terms of the generalized position and momentum operators, $\hat{x}$ and $\hat{p}$, we get the real representation [43]. In this work, we will exclusively employ the complex representation.

To start constructing the covariance matrix formalism, let us consider the bosonic creation and annihilation operators $\hat{a}_k$, $\hat{a}_k^\dagger$ for a bosonic system of N modes. All the operators for each of the modes in the N-dimensional Fock space can be collected into a $2N$-dimensional vector

$$\hat{\boldsymbol{A}} = (\hat{a}_1, \ldots, \hat{a}_N; \hat{a}_1^\dagger, \ldots, \hat{a}_N^\dagger)^T \,. \tag{3.14}$$

The canonical commutation relations obeyed by the operators can be written compactly by the use of the symplectic form K

$$[\hat{\boldsymbol{A}}_i, \hat{\boldsymbol{A}}_j^\dagger] = K_{ij}, \qquad \text{with} \;\; K = \begin{pmatrix} 1 & 0 \\ 0 & -1 \end{pmatrix} \otimes \mathbb{I}_N \,, \tag{3.15}$$

where $\mathbb{I}_N$ is the $N \times N$ identity matrix. The symplectic form K is a matrix that is Hermitian $K = K^\dagger$ and unitary $K^{-1} = K^\dagger$, that additionally satisfies the relation $K^2 = \mathbb{I}_{2N}$.

Given a quantum state described by the density matrix $\hat{\rho}$, the symmetric characteristic function associated with the state is defined as [34],

$$\chi(\boldsymbol{\xi}) = \mathrm{Tr}[\hat{\rho}\hat{D}(\boldsymbol{\xi})] \tag{3.16}$$

where $\hat{D}(\boldsymbol{\xi}) = e^{\hat{\boldsymbol{A}}^\dagger K \boldsymbol{\xi}}$ is the Weyl displacement operator, $\boldsymbol{\xi}$ is a $2N$-dimensional complex vector of the form $\boldsymbol{\xi} = (\boldsymbol{\gamma}, \boldsymbol{\gamma}^*)^T$ and $\boldsymbol{\gamma} \in \mathbb{C}^N$. For Gaussian states, the characteristic function becomes [44],

$$\chi(\boldsymbol{\xi}) = e^{-\frac{1}{4}\boldsymbol{\xi}^\dagger \Gamma \boldsymbol{\xi} - i\boldsymbol{d}^\dagger K \boldsymbol{\xi}}, \tag{3.17}$$

which we can see, is completely determined by the first statistical moment $\boldsymbol{d}$, also called the displacement vector, and the second statistical moment Γ, also called the covariance matrix. They are respectively defined as:

$$\boldsymbol{d} = \langle \hat{\boldsymbol{A}} \rangle \,, \tag{3.18a}$$

$$\Gamma_{ij} = \langle \hat{\boldsymbol{A}}_i \hat{\boldsymbol{A}}_j^\dagger + \hat{\boldsymbol{A}}_j^\dagger \hat{\boldsymbol{A}}_i \rangle - 2 \langle \hat{\boldsymbol{A}}_i \rangle \langle \hat{\boldsymbol{A}}_j^\dagger \rangle \,, \tag{3.18b}$$

where $\langle \hat{\boldsymbol{A}} \rangle$ denotes the expectation value of $\hat{\boldsymbol{A}}$ in the state $\hat{\rho}$, which is defined as

$$\langle \hat{\boldsymbol{A}} \rangle := \mathrm{Tr}(\hat{\boldsymbol{A}}\hat{\rho}) := (\mathrm{Tr}(\hat{a}_1\hat{\rho}), \mathrm{Tr}(\hat{a}_2\hat{\rho}), ...)^T \,, \tag{3.19}$$

with $\mathrm{Tr}(\cdot)$ indicating the trace. The covariance matrix Γ is a positive semi-definite matrix that carries the most relevant properties of the state. Then, working with the entire characteristic function is no longer necessary. The state of the system is completely described by $\boldsymbol{d}$ and Γ.

From their definition, the displacement vector and the covariance matrix carry the following structure,

$$\boldsymbol{d} = \begin{pmatrix} \tilde{\boldsymbol{d}} \\ \tilde{\boldsymbol{d}}^* \end{pmatrix}, \qquad \Gamma = \begin{pmatrix} X & Y \\ Y^* & X^* \end{pmatrix}, \tag{3.20}$$

where $\tilde{\boldsymbol{d}}$ is an N-dimensional complex vector, $\tilde{\boldsymbol{d}}^*$ its complex conjugate and X, Y are $N \times N$ matrices with complex entries. The Hermiticity of the covariance matrix, $\Gamma = \Gamma^\dagger$, imply that $X^\dagger = X$ and $Y^T = Y$.

In the standard formulation of Hilbert space, the density matrix represents a physical state if and only if it is a positive semi-definite operator. That is, it must fulfil $\hat{\rho} \geq 0$. In Phase space, this condition, along with the canonical commutation relations (3.15), is reflected by the inequality

$$\Gamma + K \geq 0 \,. \tag{3.21}$$

This is a necessary and sufficient condition for the covariance matrix to describe a physical state. The condition considers Gaussian states, but it also must be followed by any covariance matrix associated with a more general non-Gaussian, continuous variable state [34, 37].

3.4 Gaussian Transformations in Phase Space

Gaussian transformations are defined as the set of transformations that map Gaussian states into Gaussian states. In Hilbert space, Gaussian transformations are performed by unitary transformations $\hat{U}$ that act onto a quantum state as $\hat{\rho}' = \hat{U}\hat{\rho}\hat{U}^{\dagger}$. These transformations can be generated via an exponential map where the argument is at most quadratic in the annihilation and creation operators,

$$\hat{U} = e^{\frac{i}{2}\hat{\boldsymbol{A}}^{\dagger} W \hat{\boldsymbol{A}} + \hat{\boldsymbol{A}}^{\dagger} K \boldsymbol{\gamma}}, \tag{3.22}$$

where $\boldsymbol{\gamma}$ is a $2N$- dimensional complex vector and W is a Hermitian matrix, both possessing the same structure as the displacement vector $\boldsymbol{d}$ and the covariance matrix Γ, established in (3.20).

In Phase space, Gaussian transformations are carried by symplectic transformations. Under the transformation represented by $\hat{U}$, it can be shown [44, 45] that the first and second statistical moments transform according to

$$\boldsymbol{d}' = S\boldsymbol{d} + \boldsymbol{b}, \qquad \Gamma' = S\,\Gamma S^{\dagger}, \tag{3.23}$$

with

$$S = e^{iKW}, \qquad \boldsymbol{b} = \left(\int_0^1 e^{iKWt} dt\right)\gamma\,, \tag{3.24}$$

where S corresponds to a $2N$-dimensional symplectic matrix and $\boldsymbol{b} \in \mathbb{C}^{2N}$. The relationship between the unitary transformations (3.22) and the symplectic transformations (3.23) mediated through (3.24) is of great relevance for describing Gaussian states. It constitutes the recipe that allows us to move between the density matrix formalism in Hilbert space and the covariance matrix formalism in Phase space.

We can obtain different Gaussian transformations depending on the specific selection for W and γ. For instance, setting $W = 0$ corresponds to the Weyl displacement operator, which is the transformation that generates a coherent state. Setting $\gamma = 0$ can lead us to the phase-changing operator, the squeezing operator, or the mode-mixing operator, depending on the particular form of W. In Appendix A, we give the most general parameterization for the matrix W accounting for all the 1-mode and 2-mode Gaussian transformations.

We mentioned the symplectic nature related to the matrix S and the Gaussian transformations in Phase space; however, it has not been formally established. In the next section, we introduce the definition of the symplectic group, which connects the Phase space formalism for Gaussian states and transformation with the symplectic geometry.

3.5 Symplectic Geometry

Symplectic geometry focuses on the study of symplectic manifolds. Its inception goes back to the Hamiltonian formulation of classical mechanics, where it was found that the Phase space associated with certain classical systems exhibited the structure of a symplectic manifold. A symplectic manifold (M, K) corresponds to a smooth manifold M equipped with a closed, nondegenerate 2-form K, called the symplectic form [46]. Symplectic geometry provides a natural mathematical framework for Hamiltonian systems and also has applications to quantum mechanics and quantum optics [47].

Returning to the transformation matrix S, let us investigate its algebraic properties. From the results obtained in (3.24), we can notice two properties. First, the matrix S has the same structure as the covariance matrix and, second, it leaves invariant the symplectic form K introduced in (3.15), which can be expressed as

$$S = \begin{pmatrix} \alpha & \beta \\ \beta^* & \alpha^* \end{pmatrix}, \qquad SKS^\dagger = K\,. \tag{3.25}$$

These properties precisely define the complex representation of the real symplectic group in $2N$ dimensions $Sp(2N, \mathbb{R})$. This group corresponds to the set of all $2N \times 2N$ complex matrices that preserve the symplectic form K,

$$Sp(2N, \mathbb{R}) = \big\{ S | SKS^\dagger = K \big\}. \tag{3.26}$$

Therefore, we identify S as a symplectic matrix. An important remark is that this is not a complexification of the group. Rather, it corresponds to a change of basis that involves a transformation from the set of operators $\{\hat{x}_j, \hat{p}_j\}$, which constitutes the real representation of the covariance matrix formalism, to the set of mode operators

$\{\hat{a}_j, \hat{a}_j^\dagger\}$, which constitutes the complex representation [37, 43].

The symplectic group can alternatively be understood as the set of all real linear canonical transformations of a $2N$-dimensional vector space, where one can find that there exists a one-to-one correspondence between these linear transformations and the symplectic matrices [43, 47]. Then, the physical interpretation for the symplectic matrices is that they are transformations that preserve the commutation relations of the operators.

The Lie algebra associated with the symplectic group will be very useful when describing quantum metrology on Gaussian states. The symplectic group $Sp(2N, \mathbb{R})$ is generated through the exponential map of the Lie algebra

$$\mathfrak{sp}(2N, \mathbb{R}) = \big\{ KW_j | W_j^\dagger = W_j \big\}, \tag{3.27}$$

where W_j define a set of Hermitian, $2N \times 2N$, linearly independent basis matrices. The matrices KW_j are the infinitesimal generators of $Sp(2N, \mathbb{R})$, as can be seen from Eqs. (3.22) and (3.24), and are associated with Hamiltonians that are quadratic in the canonical operators [37, 43]. In Appendix A, we set the most general parameterization for W that generates all the Gaussian transformations for the one-mode and two-mode cases.

Before closing this section, an important final remark needs to be made. The defining properties of the symplectic group given by (3.25) can be rewritten as

$$\alpha\alpha^\dagger - \beta\beta^\dagger = \mathbb{I}, \tag{3.28a}$$

$$\alpha\beta^T = \beta\alpha^T. \tag{3.28b}$$

These relations turn out to coincide exactly with the identities satisfied by the coefficients of a Bogoliubov transformation, as obtained in (2.54). It can be concluded then that Bogoliubov transformations are, in fact, symplectic matrices and thus correspond to Gaussian transformations [44].

In general, the symplectic transformations driven by the matrix S can be classified in two ways: passive transformations and active transformations. Passive transformations, characterized by the condition $\beta = 0$, correspond to transformations that preserve the number of particles and the energy of the system, like phase shiftings or beam splitters. Active transformations, identified by the condition $\beta \neq 0$, do not preserve the number of particles or the energy of the system, such is the case of the squeezing. In the next section, we will introduce the complete set of fundamental Gaussian states for one-mode and two-mode systems.

3.6 Williamson's Theorem

In this section, we introduce a theorem of great relevance for the study of Gaussian states of multimode bosonic systems. Williamson's theorem [48] provides a powerful mathematical tool to factorize a Gaussian state.

Williamson's theorem. For any $2N \times 2N$ positive definite matrix σ, there exists a symplectic transformation $S \in \mathrm{Sp}(2N, \mathbb{R})$ that diagonalises σ as

$$\sigma = S \bigoplus_{k=1}^{N} \begin{pmatrix} \lambda_k & 0 \\ 0 & \lambda_k \end{pmatrix} S^\dagger = SDS^\dagger. \tag{3.29}$$

where λ_k corresponds to the symplectic eigenvalues of the matrix σ, and $D = \mathrm{diag}(\lambda_1, \ldots, \lambda_N, \lambda_1, \ldots, \lambda_N)$ is a $2N \times 2N$ diagonal matrix.

A proof of the theorem can be found on [34]. The relevance of this theorem relies on its application to the covariance matrices, demonstrating that any covariance matrix can be diagonalized through symplectic transformations. Given their correspondence to the covariance matrices, this fact directly translates into Gaussian states. That is, every Gaussian state can be decomposed as the product of symplectic matrices with a diagonal eigenbasis matrix D. In the next section, we will see that D can be identified with the thermal and vacuum states of a bosonic system.

The symplectic eigenvalues λ_k of the matrix σ are determined by solving the eigenvalue problem [37, 44]

$$D = \mathrm{Eig}_+(K\sigma), \tag{3.30}$$

where K corresponds to the symplectic form used throughout this chapter. If σ represents a covariance matrix, then it corresponds to a physical state if the eigenvalues satisfy the condition $\lambda_k \geq 1$ for all k. This constraint is equivalent to the condition given by (3.21).

In practical applications, it is often convenient to consider only a subsystem of a Gaussian state. In Hilbert space, this is done by tracing out all the modes or states that are not of interest. In Phase space, partial tracing using the covariance matrix formalism is very easy to compute. We just need to remove from the covariance matrix the rows and columns corresponding to the unobserved modes, as well as the elements from the displacement vector related to those dismissed modes.

3.7 List of Gaussian States in the CMF

In this section, we present the basic Gaussian states. The number of elementary Gaussian states that can be generated from a quadratic Hamiltonian can be characterized by a finite number. These fundamental states can be obtained by considering only one-mode and two-mode systems, where the generalization to a higher number of modes is straightforward. Their physical meaning can be easily understood in analogy with their interpretation within quantum optics [49]. This section is complemented by Appendix B, which presents the number of particles associated with each Gaussian state.

3.7.1 Thermal State

Let's consider a system composed of N non-interacting bosonic modes, each mode described by a state $|\psi_k\rangle$ with an energy E_k. Assuming that each mode is thermally populated, the number of particles per mode follows the thermal distribution:

$$\hat{\rho}^k_{\text{th}} = \frac{1}{Z}\exp\left(-\frac{E_k}{k_B T}\hat{n}_k\right), \qquad Z = \text{Tr}\left[\exp\left(-\frac{E_k}{k_B T}\hat{n}_k\right)\right], \tag{3.31}$$

where Z is the partition function, $\hat{n}_k$ is the number operator for the mode k and k_B is the Boltzmann constant. In Hilbert space, the complete thermal state of the system corresponds to the tensor product of the states of each of the modes $\hat{\rho}_{\text{th}} = \hat{\rho}^1_{\text{th}} \otimes \cdots \otimes \hat{\rho}^N_{\text{th}}$. In Phase space, the state is represented as

$$\boldsymbol{d}_{\text{th}} = 0, \qquad \Gamma_{\text{th}} = \bigoplus_{k=1}^{N} \begin{pmatrix} \lambda_k & 0 \\ 0 & \lambda_k \end{pmatrix}, \tag{3.32}$$

where $\lambda_k = \coth(\frac{E_k}{2k_B T})$. We find that the covariance matrix of a thermal state corresponds precisely to the diagonal matrix of symplectic eigenvalues introduced in the previous section [34, 35]. In connection with Williamson's theorem, we conclude that every Gaussian state can be generated starting from a thermal state. In this sense, the most fundamental Gaussian state is the thermal state.

The symplectic eigenvalues increase with higher temperatures and with lower energies. In the limit as $T \to 0$, the eigenvalues approach $\lambda_k \to 1$, thus satisfying the constraint $\lambda_k \geq 1$ required for the covariance matrix to represent a physical state.

3.7.2 Vacuum State

A special case from the thermal state is the vacuum state $|0\rangle$, corresponding to the case when $T = 0$. In this state, where there are no particles, the first moment of the system vanishes $\boldsymbol{d}_{\text{vac}} = 0$. Considering an N-mode system, the covariance matrix representing the vacuum state simply is

$$\Gamma_{\text{vac}} = \mathbb{I}_{2N}\,. \tag{3.33}$$

Consequently, any state Γ generated by applying a transformation S to the vacuum state can be calculated simply as $\Gamma = S\,S^{\dagger}$.

Thermal states are mixed states. However, when the temperature of the system drops to zero, we end with the vacuum state, which is a pure state. The purity μ_ρ of a Gaussian state $\hat{\rho}$ can be determined in terms of the covariance matrix as

$$\mu_\rho = \frac{1}{\sqrt{\det(\Gamma)}} = \prod_{k=1}^{N} \lambda_k^{-1}. \tag{3.34}$$

3.7.3 Coherent State

The coherent state $|\alpha\rangle$ can be obtained by applying the Weyl displacement operator $\hat{D}_k(\alpha)$ to the vacuum state,

$$|\alpha\rangle = \hat{D}_k(\alpha)\,|0\rangle = e^{\alpha\hat{a}_k^{\dagger} - \alpha^{*}\hat{a}_k}\,|0\rangle\,, \tag{3.35}$$

where $\alpha \in \mathbb{C}$ and the Weyl displacement operator is an operator generated from a linear Hamiltonian. Coherent states are eigenstates of the annihilation operator $\hat{a}_k\,|\alpha\rangle = \alpha\,|\alpha\rangle$. In the Heisenberg picture, the annihilation operator gets transformed as $\hat{a} \to \hat{a} + \alpha$. Coherent states constitute an overcomplete basis for the Hilbert space since they are non-orthogonal states. In terms of the Fock basis, they can be expanded as

$$|\alpha\rangle = e^{-\frac{1}{2}|\alpha|^2} \sum_{n=0}^{\infty} \frac{\alpha^n}{\sqrt{n!}} |n\rangle \,. \tag{3.36}$$

Coherent states are usually described as being the states that most closely resemble the behaviour of a classical harmonic oscillator. The expectation values of the position and momentum operators in a coherent state follow the dynamics of the classical harmonic oscillator. Furthermore, coherent states minimize the Heisenberg uncertainty principle in a balanced way:

$$\Delta\hat{x} = \Delta\hat{p} = \sqrt{\frac{\hbar}{2}} \qquad \Rightarrow \qquad \Delta\hat{x}\Delta\hat{p} = \frac{\hbar}{2}. \tag{3.37}$$

Physical realizations of coherent states can be found in the light emitted from lasers and in the ground state of Bose-Einstein condensates, superconductors and superfluids, which can be approximated by coherent states.

In Phase space, a coherent state is represented by

$$\mathbf{d}_\alpha = (\alpha,\, \alpha^*)^T \,, \qquad \Gamma_\alpha = \mathbb{I}_{2N} \,. \tag{3.38}$$

3.7.4 Squeezed State

Squeezed states $|s_k\rangle$ are obtained by applying the squeezing operator to the vacuum state. The squeezing operator can be classified into two categories: single-mode squeezing and two-mode squeezing. In the single-mode case, the squeezing operator is given by

$$\hat{S}^k_{\text{1-sq}} = e^{-\frac{r}{2}(\hat{a}^{\dagger 2} - \hat{a}^2)} \,, \tag{3.39}$$

where $r \in \mathbb{R}$ is known as the squeezing parameter. The two-mode squeezing operator is introduced in Appendix A. The single-mode squeezed vacuum state is obtained as

$$|s_{\text{1-sq}}\rangle = \hat{S}^k_{\text{1-sq}} |0\rangle \,. \tag{3.40}$$

The squeezing operators are generated from quadratic Hamiltonians of the form $\hat{H} \propto (\hat{a}^\dagger)^2 + h.c.$ in the single-mode case and $\hat{H} \propto \hat{a}^\dagger \hat{b}^\dagger + h.c.$ in the two-mode case. In the Heisenberg picture, the annihilation operator transforms as $\hat{a} \to (\cosh r)\hat{a} - (\sinh r)\hat{a}^\dagger$. In Hilbert space, the single-mode squeezed state in terms of the Fock basis can be expressed as

$$|s_{\text{1-sq}}\rangle = \frac{1}{\sqrt{\cosh r}} \sum_{n=0}^{\infty} (\tanh r)^n \frac{\sqrt{(2n)!}}{2^n n!} |2n\rangle \,. \tag{3.41}$$

Squeezed states, like coherent states, minimize the Heisenberg uncertainty principle. However, the uncertainties for the canonical conjugated variables are not balanced, that is, $\Delta x \neq \Delta p$; rather, they follow

$$\Delta\hat{x} = \sqrt{\frac{\hbar}{2}} e^{-r}, \; \Delta\hat{p} = \sqrt{\frac{\hbar}{2}} e^{r}, \qquad \Rightarrow \qquad \Delta\hat{x}\Delta\hat{p} = \frac{\hbar}{2}. \tag{3.42}$$

This implies that in squeezed states, the uncertainty of one of the canonical variables is reduced at the expense of increasing the uncertainty of the other.

The asymmetry of the uncertainties has been conveniently applied to enhance the measurement precision in different experiments. For instance, it has been used in the LIGO experiment for gravitational wave detection [6] and in spin-squeezed states of light to improve the precision of atomic clocks [50, 51].

The two-mode squeezed state is the paradigmatic example of entanglement for Gaussian states and, generally, for continuous-variable quantum systems. This state can be produced, for example, using non-linear optical crystals via a process known as parametric down-conversion. Squeezed states have also been achieved on phonon states in crystal lattices, spin states in neutral atom ensembles, and ion traps.

In Phase space, the first moment of the state vanishes $\boldsymbol{d}_{\text{1-sq}} = 0$. Consequently, the state is completely characterized by its covariance matrix

$$\Gamma_{\text{1-sq}} = \begin{pmatrix} \cosh 2s_k & -\sinh 2s_k \\ -\sinh 2s_k & \cosh 2s_k \end{pmatrix} . \tag{3.43}$$

3.7.5 Mode-mixed State

The mode-mixed state arises in the context of multi-mode systems, where at least two modes are necessary. It is created by the mode-mixing transformation, which is also famously known as a beam splitter. This transformation is the simplest example of an interferometer. The transformation is defined by

$$\hat{B}(\theta) = e^{\theta(\hat{a}^\dagger \hat{b} - \hat{a}\hat{b}^\dagger)}, \tag{3.44}$$

where $\theta \in \mathbb{R}$ is a parameter that characterizes the transmissivity τ of the beam splitter. The transmissivity is defined as $\tau = \cos^2\theta \in [0,1]$, and we say that the beam splitter is balanced when $\tau = 1/2$. In the Heisenberg picture, the annihilation operators $\hat{a}$ and $\hat{b}$ are transformed as

$$\begin{pmatrix} \hat{a} \\ \hat{b} \end{pmatrix} \to \begin{pmatrix} \sqrt{\tau} & \sqrt{1-\tau} \\ \sqrt{1-\tau} & \sqrt{\tau} \end{pmatrix} \begin{pmatrix} \hat{a} \\ \hat{b} \end{pmatrix}. \tag{3.45}$$

Before concluding the chapter, two interesting remarks can be made. Firstly, for Gaussian states, measurements are straightforward to implement in practice and typically yield precisions close to the optimized bound. Furthermore, the states themselves can be easily produced in any quantum optics laboratory through optical operations (e.g. coherent states and thermal states or squeezed operations or mode-mixing operations) and have shown to be experimentally convenient when working with bosonic fields [38]. The second remark is that phononic excitations in a BEC can be used for various purposes in analogy to photons, particularly for quantum metrology. For instance, see [18], where Gaussian states constructed with the phonons of a BEC were employed to develop a strategy for measuring gravitational waves.

To conclude, this chapter has introduced the covariance matrix formalism and employed it to establish the description of Gaussian states and Gaussian transformations in Phase space, which represent the chapter's core idea. To support this, we briefly discussed the differences between Hilbert space and Phase space and derived the construction of Fock space, which is essential for generating Gaussian states. Furthermore, we introduced symplectic geometry and Williamson's theorem, two crucial mathematical tools for a formal understanding of Gaussian states and Gaussian transformations in Phase space. We ended by enlisting the basic Gaussian states in terms of the covariance matrix formalism. In the next chapter, we introduce quantum metrology and demonstrate how to implement this tool to Gaussian states to estimate physical parameters driving the evolution of a quantum state.

Chapter 4

Quantum Metrology for Gaussian States

Science relies fundamentally on the measuring process. Without a clear understanding of measurements, experiments would not be possible, and science as we know it would not exist. Metrology is the branch of science dedicated to the study of measurements, and it plays a fundamental role in ensuring precision, reliability and consistency across science. Its main objectives include defining measurement units, establishing standardized methods for reproducing measurements, quantifying measurement uncertainties and improving measuring techniques. By providing a rigorous study of measurements, metrology establishes an essential link between basic scientific research and its practical application.

Quantum mechanics is essential for understanding the dynamics of small systems, like those at the scale of atoms and elementary particles. As systems become smaller in size, more precise measurements are required to study their behaviour. Quantum metrology is the area of physics that focuses on the practical measurements of quantum systems[1]. In particular, it takes advantage of quantum effects to facilitate more precise measurements.

A key component of quantum metrology is the quantum phenomenon of entanglement. In quantum mechanics, entangled particles exhibit stronger correlations than those observed in classical systems. This phenomenon has driven the development and improvement of high-precision technologies currently in use. Significant examples include the use of entangled photons in optical coherence tomography for

---

[1] Do not confuse this with the 'measurement problem' in quantum mechanics.

medical imaging [52], entangled atomic clouds for quantum-enhanced magnetometry to measure magnetic fields [53], and squeezed states of light in the LIGO experiment for gravitational wave detection [54]. By exploiting the unique properties of quantum systems, quantum metrology has become one of the most promising areas of technological development.

Since this thesis aims to propose a quantum tabletop experiment for measuring a gravitational field—or, more precisely, for estimating a physical parameter characterizing a gravitational field—quantum metrology is the appropriate field of study.

This chapter is organized as follows. Section 4.1 reviews the fundamental ideas and concepts of quantum metrology. Following this, Section 4.2 introduces estimation theory to establish the definition of the quantum Cramér-Rao bound, which quantifies the parameter estimation precision. In Section 4.3, the quantum Fisher information for Gaussian states is presented using the covariance matrix formalism. This quantity is crucial for evaluating the quantum Cramér-Rao bound. Section 4.4 describes the metrological schemes, which summarize the preparation and optimization of the estimation process. Finally, Section 4.5 discussed the progress of quantum metrology when considering relativistic effects.

4.1 Quantum Metrology's Overview

Quantum metrology focuses on studying high-resolution and high-sensitive measurements of physical quantities using quantum theory, particularly exploiting quantum entanglement and quantum squeezing. The main goal of this research field is to provide techniques that enable the precise estimation of physical parameters encoded within a quantum state. By taking advantage of quantum resources, the application of quantum metrology can outperform the precision and accuracy of measurements performed with classical strategies [55, 56].

The study of quantum metrology can be broadly classified into two main categories depending on the nature of the degrees of freedom of the quantum system: discrete and continuous. In discrete-variable systems, the Hilbert space is finite-dimensional, and it is spanned by a discrete set of eigenstates. In this context, quantum metrology focuses on discriminating between states using an appropriate measurement basis. The paradigmatic example is the qubit, a two-level system with two distinguishable states. In contrast, continuous-variable systems have an infinite-dimensional Hilbert space characterized by a continuous eigenbasis, with the quantum harmonic oscillator being the classical example. In this case, quantum metrology aims to estimate parameters encoded in a quantum state.

In the context of quantum metrology for continuous systems, estimation theory provides the mathematical framework for studying parameter estimation [57, 58]. Estimation theory is the branch of statistics concerned with estimating the value of a parameter based on the measurement of empirical data that contains random components. The parameter in question characterizes the underlying physical state of the system in such a way that its value influences the measured data distribution.

In general, estimation theory can be divided into two classes: global and local. Global estimation theory assumes no a priori knowledge about the data distribution of the parameter's possible values. Conversely, local estimation theory works under the assumption that the parameter is approximately located around a certain value.

Assuming that a physical parameter is known to be localized around a certain approximate value, local estimation theory provides an optimal measurement that helps us estimate the parameter in the shortest amount of time or with minimal resources. The central figure of merit when estimating an unknown parameter corresponds to the quantum Cramér-Rao bound. This bound sets a limit on the optimal measurement precision and is closely related to another important quantity, the quantum Fisher information. In the next section, we provide a basic derivation of these two quantities and elaborate on their physical interpretation.

4.2 Continuous-Variable Quantum Systems and Local Estimation Theory

Consider a continuous-variable quantum system in a state represented by the density matrix $\hat{\rho}_\epsilon$, which depends on some real physical parameter ϵ. In order to estimate ϵ, we conduct an experiment involving the measurement of an observable. Each measurement yields an outcome x that depends on the value of ϵ. Due to the presence of errors and uncertainties in the measurement process, the relation between ϵ and the measurement outcome x is governed by an unknown probability distribution $p(\epsilon|x)$.

Since we only have access to the measurement outcomes x, the experiment can be modelled using the state of the system $\hat{\rho}_\epsilon$ and a positive operator-valued measure (POVM) $\{\hat{E}_x\}$, which characterizes the measurement process on the system.

The Born rule establishes the connection between the measurement outcomes x and the parameter ϵ as

$$p(x|\epsilon) = \mathrm{Tr}\big[\hat{E}_x \hat{\rho}_\epsilon\big], \tag{4.1}$$

where the POVM $\{\hat{E}_x\}$ is defined as a set of positive semi-definite operators satisfying the completeness relation $\int dx\, \hat{E}_x = \hat{\mathbb{I}}$, with $\hat{\mathbb{I}}$ denoting the identity operator. The uncertainties of the measurement process are contained in the POVM, while the uncertainties related to the state preparation are captured by $\hat{\rho}_\epsilon$.

Through Bayes' theorem, the conditional probability $p(\epsilon|x)$ representing the likelihood of having the value ϵ given the experimental data x, can be expressed as

$$p(\epsilon|x) = \frac{p(x|\epsilon)p(\epsilon)}{p(x)}, \tag{4.2}$$

where $p(\epsilon)$ and $p(x)$ are the unconditional probabilities of observing ϵ and x, respectively, and are assumed to be known or that can be inferred.

To estimate the value of ϵ from the data x, an estimator $T(x)$ is defined. This corresponds to a function that maps the measurement data into a value of ϵ. If the experiment is repeated N times, resulting in the measurement outcomes $(x_1, \ldots, x_N)$, the estimator T acts as

$$T:\ (x_1, \ldots, x_N) \mapsto T(x_1, \ldots, x_N), \tag{4.3}$$

mapping an N-tuple in $\mathbb{R}^N$ to a real number. For a single measurement outcome x, the mean value of the estimator is given by

$$\langle T \rangle_\epsilon = \int dx\, p(x|\epsilon)\, T(x). \tag{4.4}$$

An estimator is *consistent* if it asymptotically converges to the true value of ϵ as the number of measurements N tends to infinity. The estimator is *unbiased* if $\langle T \rangle_\epsilon = \epsilon$, that is, if its mean value coincides with the true value of the parameter [55]. For N independent measurement outcomes, the mean value for any estimator reads

$$\langle T \rangle_\epsilon = \int dx_1 \ldots dx_N\ p(x_1|\epsilon) \ldots p(x_N|\epsilon) T(x_1, \ldots, x_N). \tag{4.5}$$

A crucial quantity for the analysis of uncertainties in parameter estimation is the Fisher information [59, 60], defined as

$$F(\epsilon) \equiv \int dx \; p(x|\epsilon) \left(\frac{\partial}{\partial \epsilon} \ln p(x|\epsilon) \right)^2 = \int dx \; \frac{1}{p(x|\epsilon)} \left(\frac{\partial}{\partial \epsilon} p(x|\epsilon) \right)^2 . \tag{4.6}$$

The Fisher information $F(\epsilon)$ measures the amount of information that the experimental setup reveals from the value of ϵ through the probability distribution $p(x|\epsilon)$. Since the experimental setup consists of the state $\hat{\rho}_\epsilon$ and the POVM $\{\hat{E}_x\}$, the Fisher information heavily depends on both the state of the system and the choice of the measurement.

Given that $F(\epsilon)$ is proportional to the derivative with respect to ϵ of the outcome probabilities $p(x|\epsilon)$, it quantifies the system's response to changes in ϵ. Expressed more intuitively, this means that bigger variations of the outcome probabilities imply larger amounts of information extracted from the system. This is again discussed at the end of this section.

To quantify the precision of the estimation process, the mean square error (MSE) for the parameter ϵ is defined as:

$$\langle (\Delta\epsilon)^2 \rangle \equiv \int d\boldsymbol{x} \; \left(T(\boldsymbol{x}) - \langle T \rangle_\epsilon \right)^2 p(\boldsymbol{x}|\epsilon), \tag{4.7}$$

where the joint probability distribution for independent measurements can be written as

$$p(\boldsymbol{x}|\epsilon) = \prod_{i=1}^{N} p(x_i|\epsilon), \tag{4.8}$$

with $\boldsymbol{x} = (x_1, \ldots, x_N)$ representing a vector that collects the measurement outcomes.

A lower bound on the mean square error in estimating ϵ can be derived at this point. The outcome corresponds to the Cramér-Rao bound [61]

$$\langle (\Delta\epsilon)^2 \rangle \geq \frac{1}{N F(\epsilon)}, \tag{4.9}$$

valid for any estimator given a fixed number N of independent measurements. This bound defines a fundamental limit to the minimal value of the error in estimating ϵ. The formal derivation of this result can be found in [59, 60]. The precision in the estimation improves when the Fisher information increases. Therefore, designing experiments that maximize the Fisher information is crucial for an optimal parameter estimation. This optimization involves the careful construction of quantum states

$\hat{\rho}_\epsilon$ and the selection of appropriate observables through the POVM $\{\hat{E}_x\}$.

Let us revisit the Fisher information. Previously, it was used to obtain the Cramér-Rao bound, which sets a limit on the precision of estimating a parameter by optimizing for all possible estimators. However, we can go a step further and optimize $F(\epsilon)$ also for all possible measurements. The quantum Fisher information $F_Q(\epsilon)$ is then defined as the maximum of the classical Fisher information $F(\epsilon)$ over all possible POVM $\{\hat{E}_x\}$

$$F_Q(\epsilon) = \sup_{\{\hat{E}_x\}} F(\epsilon), \tag{4.10}$$

where $\sup_{\{\hat{E}_x\}}$ denotes the supremum over the set of all possible POVMs. By construction, the definition ensures $F_Q(\epsilon) \geq F(\epsilon)$. This leads to the definition of the quantum Cramér-Rao bound

$$\langle (\Delta\epsilon)^2 \rangle \geq \frac{1}{N F_Q(\epsilon)}\,, \tag{4.11}$$

which states that, on average, the estimation for ϵ cannot be closer to its real value than the inverse of the quantum Fisher information times the number of measurements N performed. The quantum counterpart of the Cramér-Rao bound establishes a lower bound to the precision of the estimation that is independent of the measurement procedure as it is optimized for all quantum measurements [55, 62].

There is an alternative way to understand the quantum Cramér-Rao bound and the quantum Fisher information that provides valuable insight into their physical interpretation. Particularly, the quantum Fisher information is closely related to the Bures distance ds_B^2, a measure that quantifies the distinguishability between two quantum states $\hat{\rho}_1$ and $\hat{\rho}_2$. The Bures distance [63] is defined as

$$ds_B^2(\hat{\rho}_1, \hat{\rho}_2) = 2\left[1 - \sqrt{\mathcal{F}(\hat{\rho}_1, \hat{\rho}_2)}\right], \tag{4.12}$$

where $\mathcal{F}(\hat{\rho}_1, \hat{\rho}_2)$ denotes the Uhlman fidelity [64], given by

$$\mathcal{F}(\hat{\rho}_1, \hat{\rho}_2) = \mathrm{Tr}\left(\sqrt{\sqrt{\hat{\rho}_1}\,\hat{\rho}_2\,\sqrt{\hat{\rho}_1}}\right)^2. \tag{4.13}$$

The fidelity measures the overlap between two quantum states. For identical states the overlap is perfect, $\mathcal{F}(\hat{\rho}, \hat{\rho}) = 1$, and for orthogonal states the overlap is zero, $\mathcal{F}(\hat{\rho}, \hat{\rho}_\perp) = 0$.

Now consider the state $\hat{\rho}_\epsilon$ characterized by a parameter ϵ. If the parameter undergoes an infinitesimal change $d\epsilon$, the distinguishability between the states $\hat{\rho}_\epsilon$ and $\hat{\rho}_{\epsilon+d\epsilon}$ is related to the quantum Fisher information through [44, 55, 60, 65]

$$F_Q(\epsilon) = \frac{8}{d\epsilon^2}\left[1 - \sqrt{\mathcal{F}(\hat{\rho}_{\epsilon+d\epsilon}, \hat{\rho}_\epsilon)}\right]. \tag{4.14}$$

This equation reveals a connection between state distinguishability and parameter estimation. The right-hand side quantifies the distance between the states $\hat{\rho}_\epsilon$ and $\hat{\rho}_{\epsilon+d\epsilon}$, while in the left-hand side the quantum Fisher information $F_Q(\epsilon)$ is key to determine the precision of estimating ϵ. Therefore, the more distinguishable the states are under a small change in ϵ, the higher the quantum Fisher information becomes, which means a better precision to estimate ϵ. This geometric perspective reinforces the importance of optimizing the quantum states $\hat{\rho}_\epsilon$ to maximize the Fisher information.

4.3 Quantum Fisher Information for Gaussian States

Quantum metrology can be conveniently applied to Gaussian states, resulting in a powerful tool. In this section, we take advantage of the covariance matrix formalism to express the quantum Fisher information in terms of the displacement vector and the covariance matrix.

Notice from the previous section that the quantum Fisher information was written in terms of the density matrix $\hat{\rho}$. When restricting ourselves exclusively to Gaussian states, the quantum state $\hat{\rho}$ can be fully described by the displacement vector $\boldsymbol{d}$ and the covariance matrix Γ. Therefore, the quantum Fisher information can be re-expressed in terms of these two quantities. A careful derivation can be found in [44, 66].

Consider a quantum system described by a Gaussian state with initial displacement vector $\boldsymbol{d}_0$ and covariance matrix Γ_0. Suppose the state undergoes an evolution driven by a symplectic transformation $S(\epsilon)$ characterized by a parameter ϵ. The change in the state will be described according to Eq. (3.23) as

$$\boldsymbol{d}(\epsilon) = S(\epsilon)\boldsymbol{d}_0, \quad \Gamma(\epsilon) = S(\epsilon)\Gamma_0 S^\dagger(\epsilon). \tag{4.15}$$

The goal is to estimate the parameter ϵ encoded in the state by the transformation $S(\epsilon)$. For a single-parameter estimation of a multi-mode pure state, the quantum Fisher information is given by [44]

$$F_Q(\epsilon) = \sum_{k,l=1}^{N} 2\,\mathrm{Re}[Q^*_{kl}(\epsilon)Q_{kl}(\epsilon)] + 2\dot{\boldsymbol{d}}^\dagger(\epsilon)\Gamma^{-1}(\epsilon)\dot{\boldsymbol{d}}(\epsilon)\,, \tag{4.16}$$

where N is the number of modes of the state, $\mathrm{Re}[\cdot]$ denotes the real part of the argument and the matrix Q is defined through

$$P(\epsilon) = S^{-1}(\epsilon)\partial_\epsilon S(\epsilon), \tag{4.17}$$

where ∂_ϵ denotes partial differentiation with respect to ϵ. The matrix $P(\epsilon)$ naturally follows the algebra (3.25) of the symplectic group,

$$P = \begin{pmatrix} R & Q \\ Q^* & R^* \end{pmatrix}, \qquad PK + KP^\dagger = 0, \tag{4.18}$$

where K corresponds to the symplectic form. Equation (4.16) will play a central role in Chapter 6 to determine the precision to estimate gravitational parameters.

In more general cases, we can account for the thermal effects. In particular, we can consider a special class of thermal states, the *isothermal states*, whose symplectic eigenvalues are all identical, $\lambda_1 = \ldots = \lambda_N = \lambda$.[2]

The single-parameter estimation for a multi-mode isothermal state undergoing the same symplectic transformation $S(\epsilon)$, the quantum Fisher information generalizes to [67, 68]

$$F_Q(\epsilon) = \frac{1}{2}\frac{\lambda^2}{1+\lambda^2}\mathrm{Tr}\left[\left(\Gamma(\epsilon)^{-1}\dot{\Gamma}(\epsilon)\right)^2\right] + 2\dot{\boldsymbol{d}}^\dagger(\epsilon)\Gamma^{-1}(\epsilon)\dot{\boldsymbol{d}}(\epsilon)\,, \tag{4.19}$$

where the dot represents the derivative with respect to ϵ, and λ is the symplectic eigenvalue of the isothermal state. This expression is particularly relevant considering that, strictly speaking, it is impossible to generate a perfect vacuum state and, likewise, to generate perfect pure states where the thermal component is non-negligible.

Nonetheless, studies such as [69], which explores the effects of finite temperature in a BEC-based gravitational wave detector very similar to the proposal in this thesis, indicate that the thermal contributions have a negligible impact on the measurement precision, showing the robustness of the BEC-based detector.

---

[2] Recall that the symplectic eigenvalues were previously defined in equation (3.29).

It is worth highlighting that implementing the covariance matrix formalism in quantum metrology has some advantages from the mathematical perspective. First, the density matrix of Gaussian states is usually written as a Taylor series in operators. In the covariance matrix formalism, states are represented only by one vector and one matrix. Another advantage arises when considering a subsystem, as there is no need to take infinite-dimensional traces over all the quantum states. The irrelevant modes can be traced out from the covariance matrix by simply removing their rows and columns.

4.4 Metrological Schemes

One of the most promising applications of quantum metrology lies in the development of quantum technologies. In the previous sections, we established how quantum metrology provides a method to determine the precision with which a parameter can be measured when it is not a direct observable of the system. In this section, we describe a systematic scheme for implementing quantum metrology. The main strategy for implementing quantum metrology focuses on finding optimal initial states and selecting optimal measurements that maximize the precision of parameter estimation [70].

The estimation process comprises a number of steps, starting with the selection and preparation of a convenient initial state for the quantum system, often called the *probe state*. The probe state should be selected according to how sensitive it is to variations of the unknown parameter ϵ. Next, ϵ gets encoded into the probe state by a unitary transformation, which physically corresponds to the interaction of the probe state with an external system driving the transformation. The information about ϵ is then extracted by an appropriately chosen POVM. Finally, an estimator processes the complete sequence of measurement outcomes to estimate the value of the parameter. This procedure is known as the *metrological scheme*.

Figure 4.1 provides a schematic representation of the metrological scheme, which can be summarized as follows:

1) Selection and preparation of the probe state $\hat{\rho}_0$.

2) Encoding of ϵ into $\hat{\rho}_0$ through the transformation $\hat{U}(\epsilon)$ representing the interaction of the probe with an external system, yielding the state $\hat{\rho}_\epsilon$.

3) Extraction of the parameter information by selecting a suitable measurement basis given by a POVM.

4) Estimation of the parameter based on the measurement outcomes $\{x_i\}$ after N independent measurements.

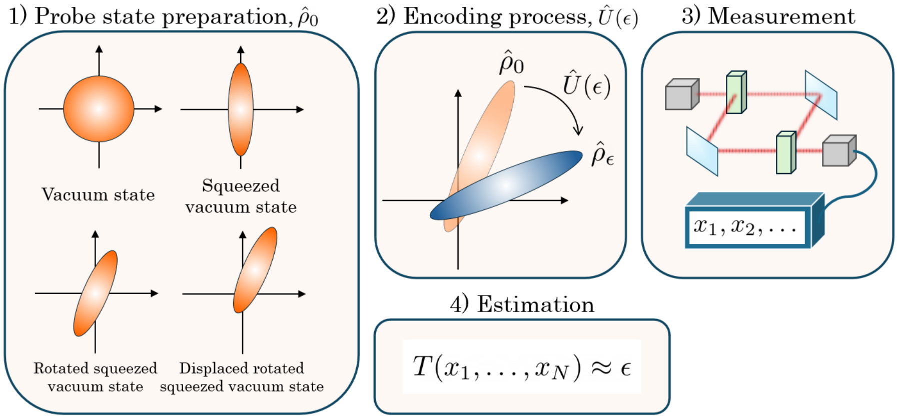

Figure 4.1: Metrological Scheme for the Parameter Estimation Procedure. The probe state is prepared in a state $\hat{\rho}_0$. Then, the probe state undergoes an evolution driven by a transformation $\hat{U}(\epsilon)$ that encodes the parameter ϵ. The resulting state $\hat{\rho}_\epsilon$ gets measured by a POVM that generates an outcome x_i. After N independent measurements, an estimator maps the outcomes to an estimation for the value of ϵ.

This procedure applies to any quantum system described by a probe state $\hat{\rho}_0$ undergoing any unitary transformation $\hat{U}(\epsilon)$. In the case of Gaussian states, the probe state is fully described by the pair $(\boldsymbol{d}_0, \Gamma_0)$, and the parameter ϵ gets encoded by the symplectic transformation $S(\epsilon)$. The resulting state to be measured is given by $(\boldsymbol{d}(\epsilon), \Gamma(\epsilon))$.

From the metrological scheme, it follows that quantum metrology focuses on undertaking three main duties to optimize the parameter estimation process. The first is to identify an optimal probe state that is the most sensitive to the changes induced by $\hat{U}(\epsilon)$, meaning that it maximizes the quantum Fisher information. The second task is to select optimal measurements that ensure the classical Fisher information from the measurement saturates the quantum Fisher information, therefore minimizing the mean squared estimation error. The third and final task is to choose an appropriate estimator that most effectively generates an estimate for the real value of ϵ.

Before concluding this section, let us discuss the scaling limits associated with the estimation precision $\Delta\epsilon$ derived from the quantum Crámer-Rao bound.

Consider N identical copies of the state $\hat{\rho}_\epsilon$, which depends on the unknown parameter ϵ. Let's assume that the state is associated with a single-particle system. Then, performing N independent measurements of the state is equivalent to performing a single measurement of a collection of N classically correlated (non-entangled) particles in the state $\hat{\rho}_\epsilon$. By the central limit theorem, the precision of the parameter estimation scales as $\Delta\epsilon \propto 1/\sqrt{N}$. This statistical bound is known as the standard quantum limit [70].

However, this limit can be improved by considering quantum effects. If the collection of N particles is entangled, the central limit theorem does not apply anymore, and the precision of the parameter estimation scales as $\Delta\epsilon \propto 1/N$. This quantum-enhanced limit is known as the Heisenberg limit and represents the ultimate limit on the estimation precision.

Hence, the end goal of quantum metrology is to exploit quantum effects, such as entanglement, to outperform classical methods and achieve the Heisenberg limit, which is the optimal scaling rate for estimation precision given the energy stored in a probe state.

4.5 Relativistic Quantum Metrology

Quantum metrology has been successfully applied to design quantum technology for high-precision measurements. However, typical setups do not consider the effects of relativity on quantum properties, which is surprising given the fruitful efforts to combine quantum and relativistic theories.

The prime example is the standard model of particles, formulated in terms of quantum field theory, which is a quantum theory that incorporates special relativity. Another successful instance comes from the study of quantum field theory in curved spacetime for predicting particular effects such as Hawking radiation [25, 26] or the cosmological particle creation [27, 28].

One of the most compelling ideas and recent achievements is the application of quantum metrology to quantum field theory. As quantum metrology provides the limits on the precision for estimating a parameter, it can be employed to validate predictions in quantum field theory within curved spacetime and to demonstrate whether measuring spacetime parameters is achievable with current and future technology.

In this spirit, quantum metrology has recently seen a wide range of theoretical applications that consider relativistic effects, thereby establishing the field of relativistic quantum metrology. A particular relativistic framework for quantum metrology has been developed by applying metrology techniques to estimate parameters of quantum fields that undergo relativistic transformations [4]. These techniques can be applied to estimate spacetime parameters such as proper times, gravitational field strengths, accelerations or small perturbations induced by changes in the spacetime curvature.

Among the progress made, we can highlight the study of entanglement and its generation due to either gravity or non-inertial motion [7], the development of relativistic quantum accelerometers [4], the study of the precision of quantum clocks [71], the determination of relativistic parameters such as the Schwarzschild radius [72] or the development of a gravitational wave detector using Bose-Einstein condensates [18].

In conclusion, this chapter has presented the material required to understand the figure of merit in quantum metrology: the quantum Crámer-Rao bound, which establishes the precision for estimating a physical parameter. To achieve this, a review of local estimation theory was required. The quantum Fisher information, essential for evaluating the quantum Crámer-Rao bound, was introduced using the covariance matrix formalism. Later, we discussed the concept of a metrological scheme and its importance in establishing and optimizing the estimation process of a physical parameter. Therefore, implementing the material presented in this chapter will allow us to link the idea of parameter estimation to a system such as the BEC.

In the next chapter, a comprehensive study of the physics of Bose-Einstein condensates is presented. This represents the final piece needed before establishing how to employ the phonons in the BEC to measure gravity, which will be the focus of Chapter 6.

Chapter 5

Bose-Einstein Condensate

A Bose-Einstein condensate (BEC) is a special state of matter that emerges when a low-density gas of bosonic particles is cooled down to temperatures close to the absolute zero of temperature. Under these conditions, a large fraction of the bosons transition into their lowest-energy state, so the gas of bosons is collectively taken into the same quantum state. In consequence, quantum effects not only determine the system's dynamics at the microscopic scale but also determine its macroscopic behaviour.

Bose-Einstein condensation differs notably from more familiar states of matter such as gases, liquids and solids. One way to gain some intuition behind the Bose-Einstein condensation is by illustrating some of these differences. For instance, the typical atomic density at the centre of a BEC is about 10^{13}–10^{15} cm^{-3}. In contrast, the molecular density of air at room temperature and atmospheric pressure is of the order of 10^{19} cm^{-3}, while the atomic density in liquids and solids is approximately 10^{22} cm^{-3} and the nuclear density in the atomic nuclei is around 10^{38} cm^{-3}. The extremely low densities of BECs imply that the temperature required to observe quantum effects is of the order of 10^{-5} K or less. In comparison, quantum phenomena manifest below the Fermi temperature for the electrons in metals, which normally corresponds to 10^4–10^5 K, and below the Debye temperature for phonons in solids, which is typically around 10^2 K. For liquid helium, quantum effects arise below 1 K temperatures, while for atomic nuclei they arise for temperatures about 10^{11} K.

From the experimental perspective, clouds of cold atomic gases represent a highly convenient venue for studying quantum phenomena. First, BECs can be appropriately described using mean-field theory as a first approximation because almost all the atoms in the system occupy the same quantum state. Second, the interactions within a BEC, which play a fundamental role by giving rise to the collective phenomena, can be experimentally fine-tuned by using different atomic species, exploiting the Feshbach resonances, or modifying the strength of the magnetic or electric trapping fields. Finally, given the low densities of the system, the microscopic structure of the condensate can be directly probed by optical methods [73].

The original idea behind Bose-Einstein condensation dates back to 1924 when S. N. Bose published a work dedicated to the statistical description of photons [74]. A year later, based on Bose's paper, A. Einstein predicted that a gas of non-interacting bosonic atoms would undergo a phase transition below a specific critical temperature. Due to the bosonic quantum statistics, the atoms would condense to the lowest energy state [75].

Over the next decades, Einstein's prediction remained experimentally unexplored. However, during that time, important theoretical contributions surrounding his idea were developed. In 1938, F. London conjectured that Bose-Einstein condensation was the mechanism responsible for the superfluidity in ^{4}He [76]. Later, in 1941, L. Landau was responsible for developing the theory of superfluids [77]. In 1947, N. Bogoliubov conceived the first microscopic theory of weakly interacting Bose gases based on the Bose-Einstein condensation concept [78]. In the 1950s, the concept of nondiagonal long-range order was introduced, revealing how Bose-Einstein condensation could give rise to quantum coherence over macroscopic distances [79, 80, 81]. In 1961, the Gross-Pitaevskii equation was derived, which describes the non-uniform weakly interacting Bose gas [82, 83].

Experimental research on dilute atomic gases was generated much later. Leveraging the technical progress in atomic physics, the 1970s saw the development of magnetic and optical trapping techniques and progress in cooling mechanisms. In the 1980s, further improvement was reached in laser-based techniques, such as magneto-optical trapping and laser cooling, to control neutral atoms. These efforts culminated in 1995, when the first gaseous BECs were successfully produced. First, E. Cornell and C. Wieman achieved Bose-Einstein condensation by cooling a gas of ^{87}Rb atoms down to 170 nK [84]. Shortly after, W. Ketterle produced a BEC using ^{23}Na atoms [85]. For their groundbreaking achievements, they were awarded the 2001 Nobel Prize in Physics. Since then, BECs have been produced using numerous atomic species and, interestingly, other bosonic constituents such as photons, molecules, polaritons and other quasi-particles.

In this chapter, we provide a thorough overview of the theoretical framework behind Bose-Einstein condensation, following closely the treatment found in Pitaevskii & Stingari's textbook [86]. The structure of the chapter is as follows:

Section 5.1 starts by presenting the ideal Bose gas, which captures some of the fundamental properties of Bose-Einstein condensation, such as the appearence of a phase transition. Next, Section 5.2 describes the weakly interacting Bose gas by using the Bogoliubov theory from which the energy spectrum of the system can be derived. Later, Section 5.3 considers the non-uniform Bose gas and introduces the basic equation for describing a BEC, the Gross-Pitaevskii equation. Finally, Section 5.4 presents the description of the relativistic BEC in flat spacetime in analogy to the one presented for the non-relativistic BEC. At the end of the section, the Newtonian limit of the relativistic BEC is taken to ensure the consistency between both approaches.

5.1 The Ideal Bose Gas

The ideal Bose gas represents the simplest example of Bose-Einstein condensation, describing a uniform, non-interacting gas of bosonic particles. By studying this model, one can correctly predict important characteristic properties of an actual BEC, including the appearance of a critical temperature determining the condensation of the bosonic gas. This section provides the quantum statistical description of the Bose gas using the grand canonical ensemble.

The grand canonical ensemble represents the possible states for a collection of particles in thermodynamic equilibrium with a reservoir that can exchange both energy and particles. In this ensemble, the probability of finding a state composed of N' particles, each in a state $|k\rangle$ with energy E_k is

$$P_{N'}(E_k) = e^{\beta(\mu N' - E_k)}, \tag{5.1}$$

where $\beta = 1/k_B T$, k_B is the Boltzmann constant, and μ corresponds to the chemical potential of the reservoir in thermal equilibrium with the system.

In statistical mechanics, the description of the system can be completely determined by knowing the partition function of the ensemble. For the present case, the grand canonical partition function is given by

$$Z(\beta,\mu)=\sum_{N'=0}^{\infty}\sum_{k}P_{N'}(E_k)=\sum_{N'=0}^{\infty}e^{\beta\mu N'}\sum_{k}e^{-\beta E_k}, \tag{5.2}$$

where the sum $\sum_k$ ranges over a complete set of eigenstates of the Hamiltonian with eigenenergy E_k. The thermodynamic variables of the grand canonical ensemble are the chemical potential μ and the temperature T. Other variables, like the volume or the oscillation frequency of a harmonic trap, may be involved in the system only through the eigenenergies of the Hamiltonian.

From the grand canonical partition function, we can define the grand canonical potential,

$$\Omega=-k_BT\ln Z\,, \tag{5.3}$$

from which we can straightforwardly calculate the thermodynamical properties of the system, such as the entropy, the average energy or the average pressure. For example, the total number of particles can be expressed as

$$N=-\frac{\partial\Omega}{\partial\mu}. \tag{5.4}$$

Let us consider the Hamiltonian of the ideal gas, described by a collection of non-interacting single particles,

$$\hat{H}=\sum_i\hat{H}_i^{(1)}, \tag{5.5}$$

where the eigenstates $|k\rangle$ are defined by the set $\{n_i\}$ of microscopic occupation numbers n_i of the single-particle states, which can be obtained from solving the Schrödinger equation

$$\hat{H}_i^{(1)}\varphi_i(\vec{r})=\varepsilon_i\varphi_i(\vec{r}). \tag{5.6}$$

In the Fock representation (see Chapter 3.2), the many-body eigenstate of the Hamiltonian is

$$|k\rangle=(\hat{a}_0^{\dagger})^{n_0}\,(\hat{a}_1^{\dagger})^{n_1}\ldots|0\rangle\,, \tag{5.7}$$

where $\hat{a}_i$ and $\hat{a}_i^{\dagger}$ are the creation and annihilation operators for to the i-th single-particle state, satisfying bosonic commutation relations $[\hat{a}_i,\hat{a}_j^{\dagger}]=\delta_{ij}$ and $[\hat{a}_i,\hat{a}_j]=$

$[\hat{a}_i^\dagger, \hat{a}_j^\dagger] = 0$. The vacuum is defined as $\hat{a}_i |0\rangle = 0$.

Under fixed energy and particle number, the system can be depicted as a gaseous system of N' non-interacting indistinguishable particles confined to a volume V, with total energy E_k. However, in the grand canonical ensemble, the number of particles and the energy are not constant but are constrained by the following conditions

$$N' = \sum_i n_i, \qquad E_k = \sum_i n_i \varepsilon_i. \tag{5.8}$$

By inserting these conditions into the grand canonical partition function (5.2) and summing over all possible values of N', we obtain

$$Z(T,\mu) = \prod_i \sum_{n_i} e^{\beta(\mu-\varepsilon_i)n_i}, \tag{5.9}$$

where the sum extends over $n_i = 0, 1, 2, \ldots$ for the case of bosonic particles[1].

Using the grand canonical partition function, the total number of particles (5.4) can be evaluated via the grand canonical potential, which yields

$$N = \sum_i \frac{1}{e^{\beta(\varepsilon_i-\mu)} - 1} \equiv \sum_i \bar{n}_i \,, \tag{5.10}$$

where $\bar{n}_i$ is defined as the average occupation number of the single-particle state with eigenenergy ε_i. This result implies an important constraint for the chemical potential, bounding it from above as $\mu < \varepsilon_0$ by the lowest eigenvalue of $\hat{H}^{(1)}$. Breaking this inequality would generate unphysical states with a negative occupation number and energy smaller than μ.

The total number of particles can be separated into the ground-state and excited-state contributions:

$$N = \bar{n}_0 + \sum_{i\neq 0} \bar{n}_i \equiv N_0 + N_T, \tag{5.11}$$

with

$$N_0(T,\mu) = \frac{1}{e^{\beta(\varepsilon_0-\mu)} - 1}, \qquad N_T(T,\mu) = \sum_{i=1}^{\infty} \frac{1}{e^{\beta(\varepsilon_i-\mu)} - 1}. \tag{5.12}$$

---

[1] For fermionic particles, the sum is limited to $n = 0, 1$ by the Pauli exclusion principle.

In the limit when $\mu \to \varepsilon_0$, the number of particles in the lowest-energy state N_0 grows arbitrarily large, while the number of particles in the exited states N_T becomes increasingly smaller.

Precisely, this limit determines the mechanism at the origin of the Bose-Einstein condensation. We can identify N_0 as the number of condensed particles, that is, the number of particles in the ground state. Meanwhile, N_T corresponds to the number of exited particles, i.e., the particles out of the condensate, which is also called the thermal component of the gas [86].

Considering a fixed value T for the temperature, Figure 5.1 illustrates the behaviour of N_0 and N_T as a function of the chemical potential. The actual value of μ is fixed by the normalization condition $N = N_0 + N_T$. First, notice that N_0 is of order 1 except when μ gets closer to ε_0, where N_0 diverges. In contrast, N_T has a smooth behaviour as a function of μ and reaches its maximum, N_c, when $\mu = \varepsilon_0$.

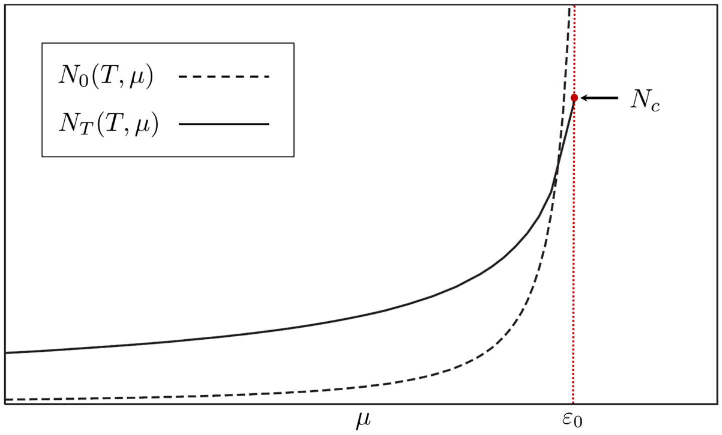

Figure 5.1: Ideal Gas Model. The number of condensed particles N_0 (dashed line) and the number of particles out of the condensate N_T (solid line) as a function of the chemical potential μ for a fixed temperature T. In the limit $\mu \to \varepsilon_0$, N_0 diverges and N_T reaches a constant value $N_T(T, \varepsilon_0) = N_c$.

Since N_c is an increasing function of the temperature, $N_c(T) = N_T(T, \varepsilon_0)$, we can always look for a temperature in which $N_c > N$ is satisfied. Let us define the critical temperature T_c at which

$$N_T(T_c, \varepsilon_0) = N. \tag{5.13}$$

For $T > T_c$, the condition $N_c > N$ is satisfied and implies that μ remains below ε_0, meaning that the ground-state occupation N_0 is negligible in comparison to N. In contrast, for $T < T_c$, the condition $N_c < N$ is followed, the value of μ approaches ε_0, and the contribution of N_0 becomes dominant.

Therefore, the critical temperature T_c locates the threshold that determines the occurrence of the phase transition originating the phenomenon of the Bose-Einstein condensation.

The Ideal Bose Gas in a Box

Let us consider an ideal Bose gas confined to a box of volume V. In this case, the single particle Hamiltonian of the system takes the free particle form

$$\hat{H}^{(1)} = \frac{p^2}{2m}. \tag{5.14}$$

The eigenstates φ of the system, considering the boundary condition $\varphi(x, y, z) = \varphi(x + L, y, z)$ for $L = V^{1/3}$, correspond to plane wave solutions

$$\varphi_{\boldsymbol{p}} = \frac{1}{\sqrt{V}} e^{-i\boldsymbol{p}\cdot\boldsymbol{r}/\hbar}, \tag{5.15}$$

with energy $\epsilon = p^2/2m$ and the momentum $\boldsymbol{p} = 2\pi\hbar\boldsymbol{n}/L$, where the components of the vector $\boldsymbol{n}$ correspond to integer numbers. The chemical potential must be negative since the lowest energy state has eigenvalue $\epsilon_0 = 0$.

The number of excited particles N_T can be evaluated by making the replacement $\sum_{\boldsymbol{p}} \to V/(2\pi h^3) \int d\boldsymbol{p}$ in equation (5.12). Using the change of variable $p^2 = 2mk_BTx$, we get

$$N_T = \sum_{\boldsymbol{p}\neq 0} \frac{1}{e^{\beta(p^2/2m-\mu)} - 1} = \frac{V}{\lambda_T^3} g_{3/2}(e^{\beta\mu}), \tag{5.16}$$

where the thermal wavelength λ_T is given by

$$\lambda_T = \sqrt{\frac{2\pi\hbar^2}{mk_BT}}, \tag{5.17}$$

and

$$g_{3/2}(z) = \frac{1}{\Gamma(3/2)} \int_0^\infty \frac{1}{z^{-1}e^x - 1} x^{1/2} dx \tag{5.18}$$

is a special case of the Bose functions, where $\Gamma(s)$ is the factorial function $(s-1)!$.

Notice that the number of excited atoms N_T is independent of the total number of atoms in the gas but depends on the volume V of confinement. This is an important fact, implying that if we add more atoms to the system, then the number of condensed atoms N_0 will increase, but the number of excited atoms will remain the same. This saturation property predicted by the ideal Bose gas trapped in a box has been experimentally confirmed and is also present in the case of harmonic trappings [86].

To derive the critical temperature T_c, the condition (5.13) is used, yielding

$$k_B T_c = \frac{2\pi\hbar^2}{m}\left(\frac{n}{g_{3/2}(1)}\right)^{2/3}, \tag{5.19}$$

which is completely determined by the particle density $n = N/V$ and the mass of the particles of the Bose gas. The critical temperature predicted by the ideal Bose gas model provides valuable experimental guidance for reaching the Bose-Einstein condensation in the laboratory.

5.2 Weakly Interacting Bose Gas

While the ideal Bose gas model successfully captures some of the properties of Bose-Einstein condensation, such as the appearance of a purely quantum-statistical phase transition, it importantly neglects the interactions between particles. In reality, particle interactions are always present, even for very dilute samples where interactions are weak. Therefore, even in the weak interaction limit, interactions play an essential role in the system's dynamics, being responsible for the collective behaviour exhibited in BECs.

The theoretical framework used to describe the weakly interacting Bose gas is given by the Bogoliubov theory [78], and it represents the modern approach to studying the Bose-Einstein condensation in dilute gases. Established in 1947 by N. Bogoliubov, the theory allowed the calculation of the excitation spectrum and the thermodynamic properties of the weakly interacting Bose gas. This section is dedicated to presenting the basic construction behind the Bogoliubov theory.

5.2.1 Dilute Gases

In a dilute gas, the range r_0 of interatomic forces is much smaller than the average distance d between particles. Consequently, particles only interact when their distance is of the order of r_0, which is rarely the case. Then, the condition

$$r_0 \ll d, \tag{5.20}$$

constitutes the defining requirement for a dilute gas. This approximation allows us to consider exclusively interactions between pairs of particles while safely neglecting the rest of the interactions. The large separation between pairs of particles also justifies using an asymptotic expression for the two-particle wave function, which is fixed by the scattering amplitude.

In addition, the temperature T of the dilute gas is assumed to be low enough that the particle's momentum distribution for the thermal components $p^2/2m \sim k_B T$ remains much smaller than the particle's characteristic momentum $p_c = \hbar/r_0$. This yields the condition

$$T \ll \frac{\hbar^2}{2mk_B r_0^2}, \tag{5.21}$$

where m is the mass of the particles. Similarly, this condition implies that $pr_0/\hbar \ll 1$. At such momenta, the scattering amplitude becomes independent of the particle energy and the scattering angle. Then, in accordance with the standard scattering theory, the scattering amplitude is completely determined by the s-wave scattering length a_s. This means that a single parameter, the scattering length, characterizes the effects of the interactions on the properties of the gas.

In terms of the scattering length, the requirement for dilute and weakly interacting gases can be expressed as

$$|a_s| \ll n^{-1/3}, \tag{5.22}$$

where $n = N/V$ is the density of the gas, N is total number of particles and V is the gas volume. Satisfying this inequality ensures that the Bogoliubov theory remains valid.

5.2.2 Bogoliubov Theory

The Hamiltonian describing a cloud of bosonic particles is given by

$$\hat{H} = \int \left(\frac{\hbar^2}{2m} \nabla \hat{\Psi}^\dagger \nabla \hat{\Psi} \right) d\boldsymbol{r} + \frac{1}{2} \int \hat{\Psi}^\dagger \hat{\Psi}^{\dagger\prime} U(\boldsymbol{r}' - \boldsymbol{r}) \hat{\Psi} \hat{\Psi}' d\boldsymbol{r}' d\boldsymbol{r}, \tag{5.23}$$

where $\hat{\Psi}$ corresponds to the quantum field operator, $U(\boldsymbol{r}' - \boldsymbol{r})$ is the two-body interaction potential and m is the mass of the particles. The first term corresponds to the kinetic energy of the particles, and the second term represents the two-particle interactions, where any external potentials have been left out for the moment.

Considering a uniform gas of volume V, the field operators can be written as a plane-wave expansion

$$\hat{\Psi}(\boldsymbol{r}) = \sum_{\boldsymbol{p}} \hat{a}_{\boldsymbol{p}} \frac{1}{\sqrt{V}} e^{i\boldsymbol{p}\cdot\boldsymbol{r}/\hbar}, \tag{5.24}$$

where $\hat{a}_{\boldsymbol{p}}$ and $\hat{a}_{\boldsymbol{p}}$ are, respectively, the annihilation and creation operators associated with the single-particle state of a plane wave with momentum $\boldsymbol{p}$. The operators satisfy the commutation relations $[\hat{a}_{\boldsymbol{p}}, \hat{a}^{\dagger}_{\boldsymbol{p'}}] = \delta_{\boldsymbol{pp'}}$.

If we explicitly consider the potential $U(\boldsymbol{r'} - \boldsymbol{r})$, solving the many-body Schrodinger equation at the microscopic level represents an arduous challenge. However, for a sufficiently dilute and cold gas, it can be concluded that the precise functional form of the two-particle interaction potential is not required to describe the macroscopic properties of the system as far as the potential reproduces the correct value for the scattering length.

Thus, to implement the many-body formalism, we replace the microscopic potential $U(\boldsymbol{r'} - \boldsymbol{r})$ with an effective, soft potential $U_{\text{eff}}(\boldsymbol{r})$. Since the macroscopic properties of the system depend only on the scattering length, this method will represent an appropriate approach to the many-body problem as far as we restrict ourselves to the study of the macroscopic behaviour. Then, we define the effective two-particle interaction potential as

$$U_0 = \int U_{\text{eff}}(\boldsymbol{r}) d\boldsymbol{r}. \tag{5.25}$$

Inserting the plane wave expansion and the effective potential into (5.23), the Hamiltonian acquires the form

$$\hat{H} = \sum_{\boldsymbol{p}} \frac{p^2}{2m} \hat{a}^{\dagger}_{\boldsymbol{p}} \hat{a}_{\boldsymbol{p}} + \frac{1}{2V} U_0 \sum_{\boldsymbol{p}_1, \boldsymbol{p}_2, \boldsymbol{q}} \hat{a}^{\dagger}_{\boldsymbol{p}_1 + \boldsymbol{q}} \hat{a}^{\dagger}_{\boldsymbol{p}_2 - \boldsymbol{q}} \hat{a}_{\boldsymbol{p}_1} \hat{a}_{\boldsymbol{p}_2}. \tag{5.26}$$

Bogoliubov Approximation

A crucial step in the Bogoliubov theory is the implementation of the so-called *Bogoliubov approximation.* The approximation is equivalent to assuming the macroscopic occupation of the ground state of the field operator $\hat{\Psi}$, which consequently gets treated as a classical field. In practice, it consists of making the replacement of the operator $\hat{a}_0$ with a complex number:

$$\hat{a}_0 \to \sqrt{N_0}. \tag{5.27}$$

The physical meaning of this strategy can be understood more clearly by explicitly rewriting the field operator expansion

$$\hat{\Psi}(\boldsymbol{r}) = \frac{1}{\sqrt{V}} \left(\hat{a}_0 + \sum_{\boldsymbol{p} \neq 0} \hat{a}_{\boldsymbol{p}} e^{i\boldsymbol{p}\cdot\boldsymbol{r}/\hbar} \right) \approx \frac{1}{\sqrt{V}} \left(\sqrt{N_0} + \sum_{\boldsymbol{p} \neq 0} \hat{a}_{\boldsymbol{p}} e^{i\boldsymbol{p}\cdot\boldsymbol{r}/\hbar} \right).$$

The substitution of the ground state operator $\hat{a}_0$ with the square root of the total number of condensed particles N_0 reflects the macroscopical occupation of the ground state. The substitution is justified when the ground-state occupation number N_0 is very large because losing or gaining one particle, $N_0 - 1$ or $N_0 + 1$, represents a negligible fluctuation for the dynamics of the system.

By neglecting the quantum fluctuations of the macroscopically populated ground state, the first term of the $\hat{\Psi}(\boldsymbol{r})$ expansion loses its quantum nature, and the Bogoliubov approximation implies that a classical mean-field $\psi(\boldsymbol{r})$ will describe the condensed fraction of particles of the Bose gas, whereas the non-condensed, excited fraction of particles of the Bose gas will keep being described by a quantum field operator $\delta\hat{\psi}$

$$\hat{\Psi}(\boldsymbol{r}) = \psi(\boldsymbol{r}) + \delta\hat{\psi}(\boldsymbol{r}), \tag{5.28}$$

where it is assumed by construction that $\delta\hat{\psi}$ corresponds to a small perturbation.

The Bogoliubov approximation represents an accurate approach for soft potentials whose perturbations remain small at all distances. It will represent a poor description at short length scales of the same order as the interatomic forces r_0 and smaller than the average distance d between particles, where the potential is strong and quantum correlations become relevant.

5.2.3 Zeroth-Order Approximation

Ground-State Energy

In the ideal gas, when the temperature goes down to $T = 0$, all the particles are condensed and $N = N_0$. By contrast, in a dilute Bose gas, the occupation number of the excited states ($\boldsymbol{p} \neq 0$) is finite but small at $T = 0$. Therefore, to a zeroth order approximation, one can neglect in the Hamiltonian (5.26) all the terms proportional to $\hat{a}_{\boldsymbol{p}}^{\dagger}$ and $\hat{a}_{\boldsymbol{p}}$ for $\boldsymbol{p} \neq 0$. In this case, given that $N_0 \sim N$, one can make the substitution $\hat{a}_0 \to \sqrt{N}$.

At the same order of approximation, the effective two-particle interaction potential U_0 (5.25) can be written in terms of the scattering length by applying the Born approximation, which yields

$$U_0 = \frac{4\pi\hbar^2 a_s}{m}. \tag{5.29}$$

The Born approximation assumes that the scattering process with a potential does not significantly modify the total wave function or field of the system. Let us introduce the interaction coupling constant

$$g = \frac{4\pi\hbar^2 a_s}{m}, \tag{5.30}$$

which captures the role of the interactions through the scattering length a_s. Under the taken approximations, the ground-state energy becomes

$$E_0 = \frac{1}{2} N n g, \tag{5.31}$$

where n is the density of the gas. The expressions obtained for the ground-state energy E_0 and the coupling constant g are valid for arbitrary interactions, as discussed in the previous section, as long as the potential reproduces the correct value for the scattering length. However, the result (5.29) for the effective potential U_0 holds as long as the first-order Born approximation is valid.

Thermodynamic Equation of State

Unlike the ideal gas, whose pressure vanishes when the temperature drops down to $T = 0$ when it is confined to a box potential, the weakly interacting Bose gas possesses a nonzero pressure:

$$P = -\frac{\partial E_0}{\partial V} = \frac{gn^2}{2}. \tag{5.32}$$

From this, one can evaluate the compressibility of the gas, $\partial n/\partial P$. By invoking the hydrodynamic relation,

$$\frac{\partial n}{\partial P} = \frac{1}{mc_s^2}, \tag{5.33}$$

the sound velocity c_s, which is an important parameter that characterizes the dynamics of the gas, is obtained to be

$$c_s = \sqrt{\frac{gn}{m}}. \tag{5.34}$$

The thermodynamic stability of the system requires the compressibility to be positive. This imposes that the scattering length must be positive, i.e., $a_s > 0$. Therefore, the Bose-Einstein condensation for a dilute uniform gas is only possible for positive values of the scattering length.

Finally, the chemical potential can be calculated via $\mu = \partial E_0/\partial N$. In terms of the sound velocity, the chemical potential reads

$$\mu = mc_s^2. \tag{5.35}$$

This result is valid for diluted Bose gases. The relation between μ and the sound velocity, for a temperature $T = 0$, is dictated by the formula $mc^2 = n\partial\mu/\partial n$.

5.2.4 Second-Order Approximation

In the Hamiltonian (5.26), the first-order approximation is missing because there are no terms containing only one particle operator, $\hat{a}_{\boldsymbol{p}}$ or $\hat{a}^\dagger_{\boldsymbol{p}}$. This fact is consistent with the momentum conservation principle. Otherwise, the appearance of these terms would imply that the Hamiltonian creates or annihilates a particle without conserving the energy of the system.

Moving to the second-order approximation, we retain in the Hamiltonian all the quadratic terms in the particle operators. Separating the ground-state operators $\hat{a}_0$ and $\hat{a}^\dagger_0$ from the excited-states operators $\hat{a}_{\boldsymbol{p}}$ and $\hat{a}^\dagger_{\boldsymbol{p}}$ ($\boldsymbol{p} \neq 0$), yields

$$\hat{H} = \sum_{\boldsymbol{p}} \frac{p^2}{2m} \hat{a}^\dagger_{\boldsymbol{p}} \hat{a}_{\boldsymbol{p}} + \frac{U_0}{2V} \hat{a}^\dagger_0 \hat{a}^\dagger_0 \hat{a}_0 \hat{a}_0 + \frac{U_0}{2V} \sum_{\boldsymbol{p}\neq 0} (4\hat{a}^\dagger_0 \hat{a}^\dagger_{\boldsymbol{p}} \hat{a}_0 \hat{a}_{\boldsymbol{p}} + \hat{a}^\dagger_{\boldsymbol{p}} \hat{a}^\dagger_{-\boldsymbol{p}} \hat{a}_0 \hat{a}_0 + \hat{a}^\dagger_0 \hat{a}^\dagger_0 \hat{a}_{\boldsymbol{p}} \hat{a}_{-\boldsymbol{p}}). \tag{5.36}$$

Next, the Bogoliubov approximation is again invoked. In the third term of the Hamiltonian, we can safely replace $\hat{a}_0$ and $\hat{a}^\dagger_0$ with $\sqrt{N}$. However, in the second term, the approximation should be taken with higher accuracy, which is achieved by considering the normalization relation

$$\hat{a}^\dagger_0 \hat{a}_0 + \sum_{\boldsymbol{p}\neq 0} \hat{a}^\dagger_{\boldsymbol{p}} \hat{a}_{\boldsymbol{p}} = N. \tag{5.37}$$

Also the potential U_0 has to be considered beyond the lowest-order Born approximation. This correction to U_0 can be incorporated using high-order perturbation theory, which reads [87]

$$U_0 = g\left(1 + \frac{g}{V} \sum_{\boldsymbol{p}\neq 0} \frac{m}{p^2}\right), \tag{5.38}$$

where the relation of g with respect to the scattering length is still given by (5.30). Substituting the normalization relation and the effective two-particle interaction potential U_0 into (5.36), we get that

$$\hat{H} = \frac{1}{2} gnN + \sum_{\boldsymbol{p}} \frac{p^2}{2m} \hat{a}^\dagger_{\boldsymbol{p}} \hat{a}_{\boldsymbol{p}} + \frac{1}{2} gn \sum_{\boldsymbol{p}\neq 0} \left(2\hat{a}^\dagger_{\boldsymbol{p}} \hat{a}_{\boldsymbol{p}} + \hat{a}^\dagger_{\boldsymbol{p}} \hat{a}^\dagger_{-\boldsymbol{p}} + \hat{a}_{\boldsymbol{p}} \hat{a}_{-\boldsymbol{p}}\right), \tag{5.39}$$

which, interestingly, is uniquely fixed by the coupling constant g. Reading the terms in the Hamiltonian, the first one is a constant term that does not contribute to the dynamics, the second term corresponds to the kinetic energy of the particles, and the third one describes the two-particle interactions. Within the interaction term, the first sub-term represents the self-energy interaction of the excited states; the other two sub-terms represent, respectively, the simultaneous creation and annihilation of excited states of momenta $\boldsymbol{p}$ and $-\boldsymbol{p}$.

Diagonalized Hamiltonian and the Bogoliubov Transformation

The Hamiltonian, being quadratic in the particle operators, can be diagonalized via a Bogoliubov transformation

$$\hat{a}_{\boldsymbol{p}} = u_{\boldsymbol{p}}\hat{b}_{\boldsymbol{p}} + v^*_{-\boldsymbol{p}}\hat{b}^\dagger_{-\boldsymbol{p}}, \qquad \hat{a}^\dagger_{\boldsymbol{p}} = u^*_{\boldsymbol{p}}\hat{b}^\dagger_{\boldsymbol{p}} + v_{-\boldsymbol{p}}\hat{b}_{-\boldsymbol{p}}, \tag{5.40}$$

which introduces a new set of quantum operators $\hat{b}_{\boldsymbol{p}}$ and $\hat{b}^\dagger_{\boldsymbol{p}}$ satisfying bosonic commutation relations $[\hat{b}_{\boldsymbol{p}}, \hat{b}^\dagger_{\boldsymbol{p}'}] = \delta_{\boldsymbol{p}\boldsymbol{p}'}$. The parameters $u_{\boldsymbol{p}}$ and $v_{\boldsymbol{p}}$ correspond to complex coefficients constrained by the condition

$$|u_{\boldsymbol{p}}|^2 - |v_{-\boldsymbol{p}}|^2 = 1, \tag{5.41}$$

which guarantees that the commutation relations are satisfied. The condition implies that the coefficients have the form

$$u_{\boldsymbol{p}} = \cosh\alpha_{\boldsymbol{p}}, \qquad v_{\boldsymbol{p}} = \sinh\alpha_{\boldsymbol{p}}. \tag{5.42}$$

The parameter $\alpha_{\boldsymbol{p}}$ is selected accordingly to cancel the off-diagonal terms of the Hamiltonian.

After applying the Bogoliubov transformation and determining the coefficients $u_{\boldsymbol{p}}$ and $v_{\boldsymbol{p}}$, one obtains the diagonalized form of the Hamiltonian:

$$\hat{H} = E_0 + \sum_{\boldsymbol{p}\neq 0} \epsilon(p)\hat{b}^\dagger_{\boldsymbol{p}}\hat{b}_{\boldsymbol{p}}, \tag{5.43}$$

where

$$E_0 = g\frac{N^2}{2V} + \frac{1}{2}\sum_{\boldsymbol{p}\neq 0}\left[\epsilon(p) - gn - \frac{p^2}{2m} + \frac{m(gn)^2}{p^2}\right], \tag{5.44}$$

is the higher-order approximation of the ground-state energy and

$$\epsilon(p) = \sqrt{\frac{gn}{m}p^2 + \left(\frac{p^2}{2m}\right)^2}, \tag{5.45}$$

is the Bogoliubov dispersion relation for the system's elementary excitations generated by the operators $\hat{b}_{\boldsymbol{p}}$ and $\hat{b}^\dagger_{\boldsymbol{p}}$. The explicit form of the coefficients $u_{\boldsymbol{p}}$ and $v_{\boldsymbol{p}}$ is given by

$$u_{\boldsymbol{p}}, v_{\boldsymbol{p}} = \pm\sqrt{\frac{p^2/2m + gn}{2\epsilon(p)} \pm \frac{1}{2}}. \tag{5.46}$$

The conclusions that can be extracted from equations (5.43)-(5.45) carry a deep physical meaning. The original system consisting of a gas of weakly interacting particles, associated with the operators $\hat{a}_{\boldsymbol{p}}$ and $\hat{a}^\dagger_{\boldsymbol{p}}$, has an equivalent description in terms of a system of non-interacting quasi-particles, with creation and annihilation operators $\hat{b}_{\boldsymbol{p}}$ and $\hat{b}^\dagger_{\boldsymbol{p}}$, of energy $\epsilon(p)$.

Following the Bogoliubov transformation (5.40), in this picture, a real particle $\hat{a}^\dagger_{\boldsymbol{p}}$, e.g. the atoms composing the Bose gas, is described as the mode superposition of the forward propagating quasi-particles $u^*_{\boldsymbol{p}}\hat{b}^\dagger_{\boldsymbol{p}}$ and the backward propagating quasi-particles $u_{-\boldsymbol{p}}\hat{b}_{-\boldsymbol{p}}$.

The ground state of the weakly interacting Bose gas at $T = 0$, now corresponds to the vacuum state for the Bogoliubov quasi-particles:

$$\hat{b}_{\boldsymbol{p}} \left|0\right\rangle = 0 \qquad \text{for } \boldsymbol{p} \neq 0. \tag{5.47}$$

Finally, it is worth discussing the experimental validity of the ground states described by equations (5.31) and (5.44). In general, the ground state of most physical systems that present interactions through interatomic potentials corresponds to a solid rather than a gas. In these systems, the gas phase is a metastable configuration, and it is expected that three-body collisions will eventually take the system into the solid configuration. The Bogoliubov theory presented in this section is valid only for those metastable phases, which may compromise its utility. However, experiments conducted for multiple atomic species have proven that the quantum gas phase remains stable for a sufficiently long time, allowing systematic measurements to confirm the predictions of the Bogoliubov theory.

5.2.5 Particles and Elementary Excitations

Let us recall the dispersion relation (5.45) followed by the gas of non-interacting quasi-particles. Analysing its behaviour under different momentum regimes offers valuable insight into how the system transitions from collective to single-particle excitations.

For low momenta $p \ll mc_s$, the dispersion relation reduce to a linear form

$$\epsilon(p) = c_s p, \tag{5.48}$$

indicating that the quasi-particles behave as phonons. Therefore, the Bogoliubov theory predicts that for a weakly interacting Bose gas, the low-momentum (long-wavelength) excitations are described by travelling sound waves with speed c_s. In this regime, the Bogoliubov coefficients satisfy $|u^*_{\boldsymbol{p}}| \simeq |v_{-\boldsymbol{p}}| \gg 1$, so the Bogoliubov transformation becomes approximately

$$\hat{a}^\dagger_{\boldsymbol{p}} \sim u_p(\hat{b}^\dagger_{\boldsymbol{p}} + \hat{b}_{-\boldsymbol{p}}).$$

Conversely, in the high-momenta (short-wavelength) limit, $p \gg mc_s$, the dispersion relation approaches the free particle behaviour

$$\epsilon(p) \approx \frac{p^2}{2m} + gn, \tag{5.49}$$

and the coefficients satisfy $|u^*_{\boldsymbol{p}}| \simeq 1$ and $|v_{-\boldsymbol{p}}| \simeq 0$. Thus, a quasi-particle $\hat{b}^\dagger_{\boldsymbol{p}}$ becomes indistinguishable from a real particle $\hat{a}^\dagger_{\boldsymbol{p}}$, implying

$$\hat{a}^\dagger_{\boldsymbol{p}} \sim \hat{b}^\dagger_{\boldsymbol{p}}.$$

The transition between the *phonon regime* and the *particle regime* takes place roughly when the kinetic energy $p^2/2m$ matches the interaction energy gn. Setting $p^2/2m = gn$ and writing $p = \hbar/\xi$, we can define the so-called *healing length*

$$\xi = \frac{1}{\sqrt{2}} \frac{\hbar}{mc_s}, \tag{5.50}$$

that defines the characteristic interaction length of the weakly interacting bosonic gas, which also can be interpreted as the shortest distance over which the wave function changes.

The thermodynamic behaviour of the system can be derived by analogously following the steps taken for the ideal gas. The energy of the elementary excitations is given by the dispersion relation (5.45). At sufficiently low temperatures, where the quasi-particles do not interact, the chemical potential for these excitations is effectively equal to zero. From equation (5.10), the average occupation number N_b of the quasi-particles of momentum $\boldsymbol{p}$ can be expressed as

$$N_b = \langle \hat{b}^\dagger_{\boldsymbol{p}} \hat{b}_{\boldsymbol{p}} \rangle = \frac{1}{e^{\beta\epsilon(p)} - 1}. \tag{5.51}$$

This quantity should not be confused with the average occupation number of real particles $N_a = \langle \hat{a}^\dagger_{\boldsymbol{p}} \hat{a}_{\boldsymbol{p}} \rangle$, for $\boldsymbol{p} \neq 0$, which can be easily calculated via the Bogoliubov transformation relating the particles and the excitations. This yields the useful relation

$$N_a = |v_{-\boldsymbol{p}}|^2 + |u_{\boldsymbol{p}}|^2 \langle \hat{b}^\dagger_{\boldsymbol{p}} \hat{b}_{\boldsymbol{p}} \rangle + |v_{-\boldsymbol{p}}|^2 \langle \hat{b}^\dagger_{-\boldsymbol{p}} \hat{b}_{-\boldsymbol{p}} \rangle \,. \tag{5.52}$$

Validity of Bogoliubov Theory

To conclude Section 5.2, let us briefly review the applicability of the Bogoliubov theory presented here. The fundamental assumption is that most of the atoms in the gas are condensed, that is, $N_0 \approx N$. This clearly follows for low temperatures. For temperatures of the order of the chemical potential, the condensate depletion is also small, which is guaranteed by the diluteness condition, $|a_s| \ll n^{-1/3}$. This condition also represents a fundamental requirement that must be fulfilled. Finally, provided that the temperature of the system lies below the critical temperature, $T \ll T_c$, both the phonon regime $k_B T \ll m c_s^2$ and the particle regime $k_B T \gg m c_s^2$ are compatible with the Bogoliubov procedure.

5.3 Non-Uniform Bose Gas

The development of the theory for non-uniform dilute Bose gases is crucial for at least two reasons. First, the experimental realization of Bose-Einstein condensation almost always involves the presence of external trapping potentials—the most common of which is the harmonic or quadratic trap—that normally produce spatially inhomogeneous systems. Second, non-uniformity is the source of new quantum phenomena and effects that are absent in uniform gases. The theoretical framework used to study non-uniform condensates is well-suited for both stationary and non-stationary configurations, allowing the research of a diverse class of physical problems.

5.3.1 Gross-Pitaevskii Equation

To study the non-uniform interacting gas, the Bogoliubov theory must be generalized. One of the key ideas of the theory is to divide the field operator of the gas into two terms: the condensed fraction and the excited fraction, as established by (5.28). This separation remains valid for non-uniform gases. At low temperatures and to the lowest-order approximation, the Bogoliubov approximation is performed by replacing the operator $\hat{\Psi}(\boldsymbol{r},t)$ with the classical field $\Psi_0(\boldsymbol{r},t)$, which will be called the order parameter and corresponds to the wave function of the condensate. This replacement is analogous to the transition from quantum electrodynamics to classical electromagnetism, and it is justified by the presence of a large number of particles in a single state, e.g., a large number of atoms in the ground state of an atomic gas.

However, we have not yet specified the equation of motion that describes the system. This equation can be derived in the Heisenberg picture by employing the Heisenberg equation $i\hbar\,\partial_t\hat{\Psi}(\boldsymbol{r},t) = [\hat{\Psi}(\boldsymbol{r},t), \hat{H}]$. Using the Hamiltonian (5.23) and the commutation relations for the field operator, we obtain

$$i\hbar\frac{\partial}{\partial t}\hat{\Psi}(\boldsymbol{r},t) = \left(-\frac{\hbar^2\nabla^2}{2m} + V_{\text{ext}}(\boldsymbol{r},t) + \int \hat{\Psi}^{\dagger}(\boldsymbol{r}',t')\,U(\boldsymbol{r}'-\boldsymbol{r})\hat{\Psi}(\boldsymbol{r}',t)d\boldsymbol{r}'\right)\hat{\Psi}(\boldsymbol{r},t). \tag{5.53}$$

Following the arguments used in the previous section for the uniform Bose gas, we are allowed to make the replacement $\hat{\Psi}(\boldsymbol{r},t) \to \Psi_0(\boldsymbol{r},t)$ as long as an effective soft potential U_{eff} is used and the Born approximation is applicable. By assuming that the function $\Psi_0(\boldsymbol{r},t)$ varies slowly at distances of the order of the interatomic force, one can set $\boldsymbol{r}'$ to be approximately equal to $\boldsymbol{r}$ in the integrand, yielding the Gross-Pitaevskii (GP) equation:

$$i\hbar\frac{\partial}{\partial t}\Psi_0(\boldsymbol{r},t) = \left(-\frac{\hbar^2\nabla^2}{2m} + V_{\text{ext}}(\boldsymbol{r},t) + g|\Psi_0(\boldsymbol{r},t)|^2\right)\Psi_0(\boldsymbol{r},t), \tag{5.54}$$

where

$$g = \int V_{\text{ext}}(\boldsymbol{r})d\boldsymbol{r},$$

is the interaction coupling constant. This equation represents the main theoretical tool for studying non-uniform dilute Bose gases at low temperatures. One of the main features of the equation is its non-linearity. The expression (5.30) for the interaction coupling constant can be recovered by expressing the integral of $V_{\text{ext}}(\boldsymbol{r})$ in terms of the scattering length a_s,

$$g = \frac{4\pi\hbar^2 a_s}{m}. \tag{5.55}$$

In analogy with the discussion in the previous section, equations (5.54) and (5.55) are valid for arbitrary forces, not being restricted by the use of soft potentials. The energy of the system is obtained to be

$$E = \int \left(\frac{\hbar^2}{2m}|\nabla\Psi|^2 + V_{\text{ext}}(\boldsymbol{r})|\Psi|^2 + \frac{g}{2}|\Psi|^4 \right) d\boldsymbol{r}. \tag{5.56}$$

It was mentioned that the field operator $\hat{\Psi}$ and the order parameter Ψ_0 play an analogous role in relation to the quantum electrodynamics to classical electrodynamics transition. Unlike Maxwell equations, the Gross-Pitaevskii equation explicitly contains $\hbar$. The reason for this difference lies in the fact that the photon's classical dispersion relation, $\omega = ck$, does not depend on $\hbar$, while the atomic dispersion relation, $\omega = \hbar k^2/2m$, is $\hbar$-dependent. The presence of $\hbar$ implies the presence of coherent phenomena like interference.

Another feature from (5.54) is its nonlinearity due to the particle interactions. Thus, the Gross-Pitaevskii equation is helpful for studying coherence and interaction effects, making the physics of Bose-Einstein condensation a rich field for theoretical and experimental research.

It is important to establish the conditions of applicability of the GP equation.

1. **Large particle number.** The condensate must contain many atoms, allowing $\hat{\Psi}$ to be approximated by the classical field Ψ_0.
2. **Diluteness.** The diluteness condition, $|a_s| \ll n^{-1/3}$, must be satisfied to keep the particle collisions weak.
3. **Low temperatures.** Both quantum and thermal depletion of the condensate must remain low. In practice, $T \ll T_c$ ensures the system is mostly condensed.
4. **Length Scale.** Effects involving distances smaller than the scattering length a_s lie outside the applicability of the GP equation.

Under these requirements, the density of the condensed particles $|\Psi_0(\boldsymbol{r})|^2$ coincides with the total density of the gas $n(\boldsymbol{r})$, which impies the normalization condition

$$\int |\Psi_0|^2 d\boldsymbol{r} = N. \tag{5.57}$$

Stationary Gross-Pitaevskii equation

The Gross-Pitaevskii equation takes a simple form in the case of stationary solutions. When the external potential $V_{\text{ext}}(\boldsymbol{r}, t)$ does not depend on time, one can look for stationary solutions of the form

$$\Psi_0(\boldsymbol{r}, t) = \Psi_0(\boldsymbol{r}) e^{-i\mu t/\hbar}. \tag{5.58}$$

The temporal dependence is determined by the chemical potential, which can be calculated via

$$\mu = \frac{\partial E}{\partial N}. \tag{5.59}$$

Substituting the ansatz (5.58) into the GP equation, one obtains its time-independent version known as the stationary Gross-Pitaevskii equation

$$\left(-\frac{\hbar^2 \nabla^2}{2m} + V_{\text{ext}}(\boldsymbol{r}) + g|\Psi_0(\boldsymbol{r})|^2 \right) \Psi_0(\boldsymbol{r}) = \mu \Psi_0(\boldsymbol{r}), \tag{5.60}$$

where the value of μ gets fixed by the normalization condition $\int |\Psi_0|^2 d\boldsymbol{r} = N$. For a uniform gas in the absence of an external potential, the chemical potential of the ideal gas gets recovered $\mu = g|\Psi_0|^2 = gn$.

5.3.2 Small-Amplitude Perturbations

The Gross-Pitaevskii equation admits an important family of time-dependent solutions constructed from small-amplitude perturbations around the stationary configuration of the system. Here, the spatial and temporal changes of the order parameter are assumed to be small with respect to the stationary solutions, and the new solutions obtained reflect the collective behaviour of the interacting Bose gases. The small-amplitude perturbations can be interpreted as elementary excitations, or pseudo-particles, of the system, whose behaviour can admit both a classical or a quantum description. In this subsection, we focus on the quantum case.

Let Ψ_0 be a stationary solution of the Gross-Pitaevskii equation with chemical potential μ. We consider small deviations from Ψ_0 by writing the field operator as

$$\hat{\Psi}(\boldsymbol{r},t) = [\Psi_0(\boldsymbol{r}) + \hat{\vartheta}(\boldsymbol{r},t)]e^{i\mu t/\hbar}, \tag{5.61}$$

where $\hat{\vartheta}(\boldsymbol{r},t)$ is a small quantum perturbation. This perturbation can be expanded as an infinite sum of elementary modes or excitations

$$\hat{\vartheta}(\boldsymbol{r},t) = \sum_i [u_i(\boldsymbol{r})\hat{b}_i e^{-i\omega_i t} + v_i^*(\boldsymbol{r})\hat{b}_i^\dagger e^{i\omega_i t}]. \tag{5.62}$$

Here, the index i labels the discrete modes, ω_i is the oscillation frequency of the perturbation and the opertors $\hat{b}_i^\dagger$ and $\hat{b}_i$ respectively create and annihilate the i-th elementary excitation. The operators satisfy the bosonic commutation relations $[\hat{b}_i, \hat{b}_j^\dagger] = \delta_{ij}$. The complex functions $u_i(\boldsymbol{r})$ and $v_i(\boldsymbol{r})$ are determined by solving the Gross-Pitaevskii equation in the linear limit.

Inserting (5.61) into the Gross-Pitaevskii equation and keeping the terms up to the first order in $\hat{\vartheta}$ yields the pair of coupled differential equations known as the Bogoliubov-de Gennes (BdG) equations:

$$\begin{aligned} \hbar\omega_i u_i(\boldsymbol{r}) &= [\hat{H}_0 - \mu + 2gn(\boldsymbol{r})]u_i(\boldsymbol{r}) + g[\Psi_0(\boldsymbol{r})]^2 v_i(\boldsymbol{r}), \\ -\hbar\omega_i v_i(\boldsymbol{r}) &= [\hat{H}_0 - \mu + 2gn(\boldsymbol{r})]v_i(\boldsymbol{r}) + g[\Psi_0(\boldsymbol{r})]^2 u_i(\boldsymbol{r}), \end{aligned} \tag{5.63}$$

where

$$\hat{H}_0 = \frac{\hbar^2\nabla^2}{2m} + V_{\text{ext}}(\boldsymbol{r}). \tag{5.64}$$

The operator $\hat{H}_0$ represents the single-particle Hamiltonian free of particle interactions, and $n(\boldsymbol{r}) = |\Psi_0(\boldsymbol{r})|^2$ is the condensate density where the term $gn(\boldsymbol{r})$ in the BdG equations arises from the interactions in the mean-field approximation.

The solutions of the Bogoliubov-de Gennes equations determine the eigenfrequencies ω_i and the amplitudes u_i and v_i of the normal modes of the system generated by the operators $\hat{b}_i^\dagger$ and $\hat{b}_i$. In general, the solutions must be computed numerically. However, analytic expressions exist for collective oscillations around the ground state of the uniform gas.

For a pair of mode functions (u_i, v_i) representing a normal mode of the system associated with an elementary perturbation, the orthonormalization condition of the solutions is given by

$$\int [u_i^*(\boldsymbol{r})u_j(\boldsymbol{r}) - v_i^*(\boldsymbol{r})u_j(\boldsymbol{r})]d\boldsymbol{r} = \delta_{ij}. \tag{5.65}$$

This concludes the review of the study of Bose-Einstein condensation as considered in the standard setting of a laboratory on Earth, which we will also refer to as the non-relativistic BEC. The next section focuses on generalising this phenomenon to a relativistic setting, where the constituents of the BEC are considered to have a relativistic nature; for instance, we can consider a Bose gas of relativistic particles.

5.4 The Relativistic Bose-Einstein Condensate in Spacetime

One can consider the phenomenon of Bose-Einstein condensation not only for non-relativistic bosons but also for their relativistic counterpart. The relativistic description of a BEC moving over a general spacetime metric has been achieved. The foundational work behind the development of the relativistic BEC can be found in [88], where the Bogoliubov theory was successfully applied to a quantum field in flat spacetime. Later, the generalization to curved spacetime was accomplished by the authors in [89].

We are interested in describing a BEC located on a general spacetime metric to investigate the behaviour of its quantum perturbations in curved spacetime and take advantage of their dynamics to estimate physical parameters containing information about the spacetime, such as the strength of the gravitational field or any parameter characterizing its curvature. Since BECs are extremely small compared to the scales found in the theory of relativity, one may think that the influence of spacetime on the dynamics of the BEC is too small to be detected. Interestingly, amplification effects produced by the slow propagation of excitations on the BEC make the effects, in principle, observable [18].

This relativistic formalism will not be implemented in this work. Nevertheless, the aim is to didactically prepare the stage for generalizing the ideas presented in this thesis for gravity exploration using BECs in a relativistic setting, which is more natural for gravity. Furthermore, we want to encourage research in this direction, both from the theoretical and experimental perspective, by demonstrating the potential and versatility of this proposal. If the reader is not interested in exploring this direction, this section can be safely skipped to continue reading Chapter 6.

The relativistic Bose-Einstein condensate (RBEC) presents significant differences from the non-relativistic BEC. For example, we can highlight the appearance of a different energy spectrum for the perturbations or the presence of relativistic bosons and anti-bosons.

This section is organized as follows. In Section 5.4.1, the RBEC in flat spacetime is examined through an analogous analysis to that of the non-relativistic BEC. First, the ideal Bose gas case is studied to then consider weak interactions between the particles of the Bose gas. By applying the Bogoliubov approximation to the weakly interacting Bose gas while considering small-amplitude perturbations, we derive the equation of motion for the condensate and the perturbations in Section 5.4.2. Section 5.4.3 obtains the perturbation's dispersion relation and analyses the high-momentum and low-momentum limiting cases, with the latter subdividing into gapped and gapless excitations. Section 5.4.4 considers the gapless-excitation case to analyse the phonon dynamics, finding out that they evolve over an effective metric, which is denoted as the acoustic metric. Finally, Section 5.4.5 takes the Newtonian limit of the RBEC to demonstrate consistency between the relativistic and non-relativistic BECs and to show how modifications of general relativity could be inherited at the Newtonian level.

5.4.1 Condensate's Non-Linear Klein-Gordon Equation

We begin by considering the Lagrangian density describing an interacting relativistic scalar Bose field $\hat{\Phi}(x^\mu)$ with coordinates $x^\mu = (t, \boldsymbol{x})$ in flat spacetime,

$$\hat{\mathcal{L}} = \frac{1}{c^2}\frac{\partial \hat{\Phi}^\dagger}{\partial t}\frac{\partial \hat{\Phi}}{\partial t} - \nabla\hat{\Phi}^\dagger \cdot \nabla\hat{\Phi} - \left(\frac{m^2c^2}{\hbar^2} + V_{\text{ext}}(x^\mu)\right)\hat{\Phi}^\dagger\hat{\Phi} - U(\hat{\Phi}^\dagger\hat{\Phi};\lambda_i), \tag{5.66}$$

where m corresponds to the mass of the bosons, $V(x^\mu)$ is an external potential, and U is a self-interaction with coupling constants $\lambda_i(x^\mu)$, which can be expanded as

$$U(\hat{\Phi}^\dagger\hat{\Phi};\lambda_i) = \frac{\lambda_2}{2}(\hat{\Phi}^\dagger\hat{\Phi})^2 + \frac{\lambda_3}{6}(\hat{\Phi}^\dagger\hat{\Phi})^3 + \cdots . \tag{5.67}$$

The first term of the expansion corresponds to the two-particle interaction with coupling constant λ_2, the second one is the three-particle interaction with coupling constant λ_3, and so forth.

Since the Lagrangian density is invariant under global phases, corresponding to a global $U(1)$ symmetry, there exists an associated Noether charge and current that are conserved. The first corresponds to the quantity $N - \bar{N}$, denoting the difference between the number of bosons N and the number of anti-bosons $\bar{N}$, which will appear later.

Ideal Bose Gas

In the ideal Bose gas, the interaction term U and the external potential V vanish. For an ideal gas of temperature T and chemical potential μ, we have

$$N - \bar{N} = \sum_k [n_k(T,\mu) - \bar{n}_k(T,\mu)], \tag{5.68}$$

with n_k and $\bar{n}_k$ respectively denoting the average number of bosons and anti-bosons in the state of energy $|E_k|$,

$$n_k(T,\mu) = \frac{1}{e^{\beta(|E_k|-\mu)} - 1}, \qquad \bar{n}_k(T,\mu) = \frac{1}{e^{\beta(|E_k|+\mu)} - 1}, \tag{5.69}$$

where $\beta = 1/k_B T$ and $E_k^2 = \hbar^2 k^2 c^2 + m^2 c^4$. Defining the number density $n = (N - \bar{N})/\Omega$, where Ω is the volume of the gas, the relation between the critical temperature T_c and the density n is

$$n = \frac{1}{4\pi^{3/2}\Gamma(3/2)} \int_0^\infty \frac{\sinh(\beta_c mc^2)}{\cosh(\beta_c|E_k|) - \cosh(\beta_c mc^2)} k^2 dk, \tag{5.70}$$

where $\Gamma(z)$ is the factorial function $(z-1)!$ and $\beta_c := \beta(T_c)$. In the non-relativistic limit, $k_B T \ll mc^2$, the contribution of the anti-bosons can be neglected, and we recover the relation (5.19) for the critical temperature for the non-relativistic BEC.

Bogoliubov Approximation

In the low-temperature regime $T \ll T_c$, where most relativistic bosons transition into the ground state and Bose-Einstein condensation is realised, the field can be approximated using a classical mean-field by making the substitution $\hat{\Phi} \to \Phi$, in an analogous fashion as performed in (5.54). The classical mean-field Φ is regarded as the order parameter, or wave function, describing the dynamics of the condensate.

The equation of motion for $\hat{\Phi}$ can be derived using the Euler-Lagrange equation

$$\frac{\partial \mathcal{L}}{\partial \Phi} - \nabla \frac{\partial \mathcal{L}}{\partial(\nabla\Phi)} - \frac{\partial}{\partial t}\frac{\partial \mathcal{L}}{\partial \dot{\Phi}} = 0, \tag{5.71}$$

where the dot represents derivation with respect to the time coordinate t. Introducing the d'Alembert operator in flat spacetime $\Box = \eta^{\mu\nu}\partial_\mu\partial_\nu$, the dynamics of the system is given by the non-linear Klein-Gordon equation

$$\Box\Phi - \left(\frac{m^2c^2}{\hbar^2} + V(x^\mu)\right)\Phi - U'(\rho;\lambda_i)\Phi = 0, \tag{5.72}$$

where $\rho = \Phi^*\Phi$ corresponds to the density of the condensate, and the prime $'$ denotes derivation with respect to ρ. In the non-relativistic limit $c \to \infty$, the Gross-Pitaevskii equation (5.54) is recovered.

5.4.2 Small-Amplitude Perturbations

Similar to the small-amplitude perturbations analysis carried out for the non-relativistic BEC in Section 5.3.2, we can study the behaviour followed by quantum perturbations around the condensate's wave function Φ. In a similar spirit to (5.28), we decompose the field operator $\hat{\Phi}$ as the classical mean-field Φ describing the condensate plus a perturbation of quantum nature:

$$\hat{\Phi} = \Phi(1 + \hat{\vartheta}). \tag{5.73}$$

For convenience, the Mandelung representation for the complex mean-field ϕ is adopted. In this representation, Φ is factorized into two real fields corresponding to its modulus $\sqrt{\rho(x^\mu)}$ and its phase $\theta(x^\mu)$,

$$\Phi = \sqrt{\rho}e^{i\theta}. \tag{5.74}$$

Additionally, the following quantities are defined:

$$u^\mu = \frac{\hbar}{m}\eta^{\mu\nu}\partial_\nu\theta, \tag{5.75a}$$

$$c_0^2 = \frac{\hbar^2}{2m^2}\rho U''(\rho;\lambda_i), \tag{5.75b}$$

$$T_\rho = \frac{\hbar^2}{2m}[\Box + \eta^{\mu\nu}\partial_\mu(\ln\rho\,\partial_\nu)] = -\frac{\hbar^2}{2m\rho}\eta^{\mu\nu}\partial_\mu(\rho\partial_\nu), \tag{5.75c}$$

where u^μ is a four-velocity vector related to the conserved current $j^\mu = \rho m u^\mu/\hbar$ associated with the $U(1)$ symmetry, c_0 indicates the RBEC's self-interaction strength and has units of velocity, and T_ρ is the generalized kinetic operator which reduces to the standard kinetic operator $-\hbar^2\nabla^2/2m$ in the non-relativistic limit.

Condensate's Equation of Motion

To derive the equations of motion of the system, consisting of the condensate and the quantum perturbations, the decomposition (5.73) and the Madelung representation are implemented in the non-linear Klein-Gordon equation. Then, the condensate's classical wave function evolves according to

$$\frac{1}{\sqrt{\rho}}\sqrt{\rho} - \partial^\mu\theta\partial_\mu\theta - \left(\frac{m^2c^2}{\hbar^2} + V\right) - U' + i\,\frac{1}{\rho}\partial_\mu(\rho\partial^\mu\theta) = 0. \tag{5.76}$$

Further implementing the quantities defined in (5.75), the equations of motion of the condensate read

$$\partial_\mu(\rho u^\mu) = 0, \tag{5.77a}$$

$$-u_\mu u^\mu = c^2 + \frac{\hbar^2}{m^2}\left[V(x^\mu) + U'(\rho;\lambda_i) - \frac{\Box\sqrt{\rho}}{\sqrt{\rho}}\right]. \tag{5.77b}$$

The first equation corresponds to the continuity equation, establishing the conservation of the current j^μ. In analogy with the Gross-Pitaevskii equation, the second equation determines the chemical potential of the condensate, which corresponds to the temporal component of the four-velocity u^μ.

Perturbation's Equation of Motion

The equation of motion governing the quantum perturbations, considering the Madelung representation, is obtained to be

$$\Box\hat{\vartheta} + 2\eta^{\mu\nu}\left(\frac{1}{2}\partial_\mu \ln\rho + i\partial_\mu\theta\right)\partial_\nu\hat{\vartheta} - \rho U''(\rho;\lambda_i)(\hat{\vartheta} + \hat{\vartheta}^\dagger) = 0. \tag{5.78}$$

Using the definitions (5.75), the equation for the perturbations of a relativistic BEC can be expressed as

$$\left(i\hbar u^\mu\partial_\mu - T_\rho - mc_0^2\right)\hat{\vartheta} = mc_0\,\hat{\vartheta}^\dagger. \tag{5.79}$$

This equation involves two perturbation associated field operators, $\hat{\vartheta}$ and $\hat{\vartheta}^\dagger$. Taking its Hermitian conjugate, we can eliminate one of the fields and get a single equation for the other, thus obtaining for $\hat{\vartheta}$

$$\left[(i\hbar u^\mu\partial_\mu + T_\rho)\frac{1}{c_0^2}(-i\hbar u^\mu\partial_\mu + T_\rho) - \frac{\hbar^2}{\rho}\eta^{\mu\nu}\partial_\mu\rho\,\partial_\nu\right]\hat{\vartheta} = 0. \tag{5.80}$$

This equation describes the propagation of linearized perturbations over the relativistic condensate, whose description is given by (5.77), and it represents a generalization to the equations obtained in Section 5.3.2 for the non-relativistic BEC. An important fact to remark on is that the information of (5.80) is contained in (5.79), but the opposite implication is not true.

5.4.3 Dispersion Relation

The dispersion relation characterizing the propagation of the RBEC's perturbations carries important physical insight for understanding their behaviour. For the derivation of the dispersion relation, let us assume that the speed of the fluid in the RBEC $\boldsymbol{u}$, the chemical potential μ, the density of the RBEC ρ and the self-interaction strength c_0 are constant both in space and in time. For simplicity, consider the case when the background fluid is at rest, $\boldsymbol{u} = 0$. Under these assumptions, Eq. (5.80) is reduced to

$$\left[\left(i\frac{u^0}{c}\partial_t - \frac{\hbar}{2m}\Box\right)\left(-i\frac{u^0}{c}\partial_t - \frac{\hbar}{2m}\Box\right) - c_0^2\Box\right]\hat{\vartheta} = 0. \tag{5.81}$$

The equation can be solved analytically by making the ansatz

$$\hat{\vartheta}(t, \boldsymbol{x}) = e^{-i\omega t + i\boldsymbol{k}\cdot\boldsymbol{x}}, \tag{5.82}$$

using Fourier modes, which yields

$$\left(\frac{u^0}{c}\omega - \frac{\hbar}{2mc^2}\omega^2 + \frac{\hbar}{2m}k^2\right)\left(-\frac{u^0}{c}\omega - \frac{\hbar}{2mc^2}\omega^2 + \frac{\hbar}{2m}k^2\right) - \left(\frac{c_0}{c}\right)^2\omega^2 + c_0^2 k^2 = 0, \tag{5.83}$$

whose solution is fulfilled for

$$\omega_\pm^2 = c^2\left\{k^2 + 2\left(\frac{mu^0}{\hbar}\right)^2\left[1 + \left(\frac{c_0}{u^0}\right)^2\right] \pm \left(\frac{2mu^0}{\hbar}\right)\sqrt{k^2 + \left(\frac{mu^0}{\hbar}\right)^2\left[1 + \left(\frac{c_0}{u^0}\right)^2\right]^2}\right\}. \tag{5.84}$$

This equation establishes the dispersion relation describing the perturbation propagation in an RBEC and generalizes the Bogoliubov dispersion relation (5.45) from the non-relativistic BEC.

Associated with the RBEC dispersion relation, different regimes for the perturbations can be found. This depends on the relative strength of the first two terms in (5.84), the second of them being absent for the non-relativistic BEC case. Below, a brief overview of the dispersion relation regimes is presented, to later focus, in the next subsection, on the one relevant to this work. The complete overview of the regimes is summarized in Table 5.1. For convenience, we introduce the dimensionless parameter

$$b := \left(\frac{c_0}{u^0}\right)^2, \tag{5.85}$$

where temporal component u^0 of the four-velocity u^μ determines the rate of the passage of time.

Low-Momentum Regime

The low momentum limit of the dispersion relation is characterized by,

$$|k| \ll \frac{mu^0}{\hbar}(1+b). \tag{5.86}$$

Making a Taylor expansion of (5.84) for small k, up to the fourth order, the dispersion relation takes the form

$$\omega_\pm^2 \approx c^2 \left[k^2 + 2(1\pm 1)\left(\frac{mu^0}{\hbar}\right)^2(1+b) \pm \frac{k^2}{1+b} \mp \left(\frac{\hbar}{mu^0}\right)^2 \frac{k^4}{4(1+b)^3}\right]. \tag{5.87}$$

From this expression, several cases bifurcate, which can be broadly separated into two types of perturbations: gapless excitations and gapped excitations. Let us analyse these cases.

Gapless Excitations.
Let us focus on the branch associated with the negative sign ω_-, for which the dispersion relation is reduced to

$$\omega_-^2 \approx c^2 \left[\frac{b}{1+b}k^2 + \left(\frac{\hbar}{mu^0}\right)^2 \frac{1}{4(1+b)^3}k^4\right]. \tag{5.88}$$

In this case, the perturbations correspond to massless quasi-particles. Notice that the dispersion relation has the same functional form as the Bogoliubov dispersion relation (5.45) of the non-relativistic BEC. A further sub-regime can be obtained by

RBEC's Dispersion Relation
$\omega_{\pm}^2 = c^2 \left\{ k^2 + 2\left(\frac{mu^0}{\hbar}\right)^2 (1+b) \pm 2\left(\frac{mu^0}{\hbar}\right)\sqrt{k^2 + \left(\frac{mu^0}{\hbar}\right)^2 (1+b)^2} \right\}$

High Momentum Regime
∘ Condition: $\lvert k\rvert \gg \frac{mu^0}{\hbar}(1+b)$ $\Downarrow$ Massless field propagating at c: $\omega_{\pm}^2 = c^2k^2$

<table>
<tr><th colspan="7">Low Momentum Regime</th></tr>
<tr><td colspan="7">∘ Condition: $\lvert k\rvert \ll \frac{mu^0}{\hbar}(1+b) \quad (*)$
$\Downarrow$
$\omega_{\pm}^2 \approx c^2 \left\{ k^2 + 2(1\pm 1)\left(\frac{mu^0}{\hbar}\right)^2 (1+b) \pm \frac{k^2}{1+b} \mp \left(\frac{\hbar}{mu^0}\right)^2 \frac{k^4}{4(1+b)^3} \right\}$</td></tr>
<tr><th colspan="4">Gapless Excitations</th><th colspan="3">Gapped Excitations</th></tr>
<tr><td colspan="4">$\omega_{-}^2 \approx c^2 \left\{ \frac{b}{1+b}k^2 + \left(\frac{\hbar}{mu^0}\right)^2 \frac{1}{4(1+b)^3}k^4 \right\}$
NRL: $\omega_{-}^2 \approx c_0^2 \left[k^2 + \left(\frac{\hbar}{2mc_0}\right)^2 k^4 \right]$</td><td colspan="3">$\omega_{+}^2 \approx c^2 \Big\{ 4(1+b)\left(\frac{mu^0}{\hbar}\right)^2 + \frac{2+b}{1+b}k^2$
$+ \left(\frac{\hbar}{mu^0}\right)^2 \frac{1}{4(1+b)^3}k^4 \Big\}$
Only allowed case: $k^2 \gg k^4$
$\Downarrow$
$\omega_{+}^2 \approx m_{\text{eff}}^2 c_{s,\text{gap}}^4/\hbar^2 + c_{s,\text{gap}}^2 k^2$</td></tr>
<tr><td colspan="4">Sub-regimes</td><td colspan="3">Sub-regimes</td></tr>
<tr><th colspan="2">Phononic (IR)</th><th colspan="2">Particle (UV)</th><td rowspan="2">$b \ll 1$
$\Downarrow$
$\omega_{+}^2 \approx \frac{m_{\text{eff}}^2 c_{s,\text{gap}}^4}{\hbar^2}$
Non-relativistic
massive particle</td><td rowspan="2">$b \gg 1$
$\Downarrow$
$\omega_{+}^2 \approx \frac{m_{\text{eff}}^2 c_{s,\text{gap}}^4}{\hbar^2}$
$+c_{s,\text{gap}}^2 k^2$</td><td rowspan="2">$\frac{2(1+b)}{\sqrt{1+b}} \ll \frac{\hbar\lvert k\rvert}{mu^0}$,
$1+b \gg \frac{\hbar\lvert k\rvert}{mu^0}$
$\Downarrow$
$\omega_{+}^2 \approx c_{s,\text{gap}}^2 k^2$</td></tr>
<tr><td colspan="2">∘ Condition:
$\lvert k\rvert \ll \frac{2mc_0}{\hbar}(1+b)$
Always compatible with $(*)$</td><td colspan="2">∘ Condition:
$\lvert k\rvert \gg \frac{2mc_0}{\hbar}(1+b)$
Compatible with $(*)$ if:
$\frac{mc_0}{\hbar} \ll \lvert k\rvert \ll \frac{mu^0}{\hbar}$</td></tr>
<tr><td>$b \gg 1$
$\Downarrow$
$\omega_{-}^2 \approx c_s^2 k^2$
NRL:
$c_s^2 \to c_0^2$</td><td>$b \ll 1$
$\Downarrow$
$\omega_{-}^2 \approx c_0^2 k^2$
Already in NRL</td><td>$b \gg 1$
$\Downarrow$
Not compatible</td><td>$b \ll 1$
$\Downarrow$
$\hbar\omega_{-} = \frac{(\hbar k)^2}{2\mu/c^2}$
NRL:
$\hbar\omega_{-} = \frac{\hbar^2 k^2}{2m}$</td><td colspan="3">Vanishes at NRL</td></tr>
</table>

Non-Relativistic Limit (NRL) ∘ Conditions: 1) $c \to \infty \Leftrightarrow u^0 \to c$, 2) $b \ll 1 \Leftrightarrow c_0 \ll c$.

Table 5.1: Dispersion Relation Diagram. The dispersion relation of an RBEC is schematically summarized. First, the two main regimes, the high-momentum and low-momentum regimes, are displayed along with their defining conditions. Then, in the low momentum regime, the excitations are divided into two different classes: gapless and gapped excitations, each having sub-regimes depending on the behaviour of b, where $b = (c_0/u^0)^2$.

comparing the relative size of the k^2 and k^4 terms and studying the cases in which one term dominates over the other and vice versa.

Phononic Regime (Infrared Relativistic).
The quadratic term k^2 dominates whenever the condition

$$|k| \ll \frac{2mc_0}{\hbar}(1+b), \tag{5.89}$$

is satisfied, which is always compatible with the low-momentum condition (5.86). In this limit, the dispersion relation matches that corresponding to phonon-like perturbations

$$\omega_-^2 = c_s^2 k^2, \tag{5.90}$$

travelling at the speed of sound c_s, defined by

$$c_s^2 := \frac{(c\,c_0/u^0)^2}{1+(c_0/u^0)^2} = \frac{c^2 b}{1+b}. \tag{5.91}$$

In this case, the perturbations correspond to relativistic phonons.

To consider the non-relativistic limit, two conditions are required: first, the interactions must be weak and second, we must take the limit $c \to \infty$. Recall from the definition (5.75) that c_0 indicates the self-interaction strength of the RBEC. Thus, the first condition requires that $c_0 \ll c$, which can be equivalently stated as $b \ll 1$. The second condition can also be established by the limit $u^0 \to c$, which implies that the BEC flows with a velocity $\boldsymbol{u}$ much smaller than the speed of light (recall that the four-velocity follows the normalization $\eta_{\mu\nu}u^\mu u^\nu = -c^2$). Therefore, in the non-relativistic limit, we have that $c_s \to c_0$ and the dispersion relation becomes

$$\omega_-^2 = c_0^2 k^2, \tag{5.92}$$

corresponding to the phononic perturbations present in the non-relativistic BEC, which matches (5.48). Notice that c_0 corresponds to the speed of sound in the non-relativistic BEC[2]. Generally, c_s will differ from c_0, coinciding only in the non-relativistic limit.

This regime becomes relevant when describing the evolution of phononic perturbations on an RBEC for low-energy gravitational settings and in trying to connect

---

[2] Denoted c_s throughout Section 5.2.

this theoretical framework to actual experiments. We will return to it in the next subsection to derive the acoustic metric.

Particle Regime (Ultraviolet).
The opposite regime, where the k^4 term dominates, is determined by the condition

$$|k| \gg \frac{2mc_0}{\hbar}(1+b), \tag{5.93}$$

which is compatible with the condition (5.86) only in the low-coupling case $b \ll 1$. These two conditions together can be summarized as

$$\frac{mc_0}{\hbar} \ll |k| \ll \frac{mu^0}{\hbar}, \tag{5.94}$$

yielding the dispersion relation

$$\hbar\omega_- = \frac{(\hbar k)^2}{2\mu/c^2}. \tag{5.95}$$

This implies that the perturbations correspond to massive relativistic particles with an effective mass $mu^0/c = \mu/c^2$, and coincides with the non-relativistic BEC's result indicating that decreasing the wavelength of the perturbation (or increasing its momentum) puts in evidence the atomic structure of the condensate, e.g., see (5.49).

In the non-relativistic limit, when $u^0 \to c$, we recover the dispersion relation corresponding to particles of mass m

$$\hbar\omega_- = \frac{\hbar^2 k^2}{2m}, \tag{5.96}$$

revealing the atomic structure in the non-relativistic BEC.

Gapped Excitations.
In the branch associated with the positive sign, the dispersion relation reads

$$\omega_+^2 \approx c^2\left[4(1+b)\left(\frac{mu^0}{\hbar}\right)^2 + \frac{2+b}{1+b}k^2 + \left(\frac{\hbar}{mu^0}\right)^2 \frac{1}{4(1+b)^3}k^4\right]. \tag{5.97}$$

Depending on the relative weight of the three terms appearing in the dispersion relation, different cases for the perturbations arise. Concerning the k-dependent terms, given that (5.86) is satisfied, the only allowed regime is when the k^2 term dominates over the k^4 term. In such a limit, the dispersion relation simplifies as

$$\omega_+^2 = \frac{m_{\text{eff}}^2 c_{s,\text{gap}}^4}{\hbar^2} + c_{s,\text{gap}}^2 k^2, \tag{5.98}$$

where the speed $c_{s,\text{gap}}$ and the effective mass m_{eff} are defined as

$$c_{s,\text{gap}} := \frac{2+b}{1+b}c^2, \qquad m_{\text{eff}} := \frac{(1+b)^{3/2}}{2+b}\frac{u^0}{c}m. \tag{5.99}$$

In this case, the perturbations result in massive relativistic particles with an effective mass propagating at a speed $c_{s,\text{gap}}$. In the limit when $b \ll 1$, the mass term dominates the k^2 term, and the perturbations become non-relativistic particles of mass m_{eff}. In the opposite limit, $b \gg 1$, both terms are of the same order of magnitude. Finally, the k^2 term dominates when

$$\frac{mu^0}{\hbar}\frac{2(1+b)}{\sqrt{1+b}} \ll |k| \ll \frac{mu^0}{\hbar}(1+b). \tag{5.100}$$

Let us look closer at what happens in the $b \ll 1$ limit. Since the mass term dominates in this limit, assuming a comoving reference frame where $u^0 = c$ and that b can be neglected, the frequency of the perturbations simplifies to $\omega_+ \approx \pm 2mc^2/\hbar$. A gap, $\Delta\hbar\omega_+ \approx 2mc^2$, arises between the energy levels involving a massive factor of $2m$. This mass gap indicates that the lowest energy excitation of this mode requires the creation of a boson–anti-boson pair. The presence of anti-bosons is one of the main differences compared to the non-relativistic BEC.

Finally, in the non-relativistic limit, the dispersion relation of the gapped perturbations vanishes when taking the limit $c \to \infty$. This is because the energy required to excite these modes is much larger than the typical energy scales found in non-relativistic configurations. Thus, boson–anti-boson pairs cannot be created, so the modes cannot be excited.

High-Momentum Regime

The regime where the momenta is high arises when

$$|k| \gg \frac{mu^0}{\hbar}(1+b), \tag{5.101}$$

where it is straightforward to get that the dispersion relation is reduced to $\omega_\pm^2 = c^2k^2$. This corresponds to the standard dispersion relation of a massless field travelling at the speed of light c, where the energy of the perturbation has become much larger than the chemical potential of the RBEC.

5.4.4 Acoustic Metric

Since the aim is to describe the propagation of phonon-like perturbations in an RBEC considered in a context close to an actual experiment, the gapless branch ω_- of the low-momentum regime is the appropriate case to consider. Following [88], the propagation of phonons can be described as a quantum field evolving over a fixed curved spacetime background only in the case when the relativistic kinetic operator T_ρ can be neglected. This condition is the relativistic analogue of neglecting the quantum pressure term in the Gross-Pitaevskii equation in a non-relativistic BEC, as is done, for instance, when considering the Thomas-Fermi limit.

Neglecting the operator T_ρ, similar to the non-relativistic BEC case, involves making an eikonal approximation. This corresponds to the assumption that the variation of all the background quantities with respect to space and time is small compared to the scales set by the wavelength and the period of the perturbations, respectively. The eikonal approximation mathematically states that

$$\left|\frac{\partial_t\,\rho}{\rho}\right| \ll \omega_-, \qquad \left|\frac{\partial_t\,c_0}{c_0}\right| \ll \omega_-, \qquad \left|\frac{\partial_t\,u_\mu}{u_\mu}\right| \ll \omega_-, \tag{5.102}$$

in addition to the corresponding relations for the spatial variations. Also, recall that the phononic regime of the gapless excitations requires conditions (5.86) and (5.89) to be fulfilled. Combining these assumptions, the equation describing the perturbations, (5.80), simplifies to

$$\left[\frac{\rho}{c_0^2}u^\mu\partial_\mu(u^\nu\partial_\nu) - \eta^{\mu\nu}\partial_\mu(\rho\partial_\nu)\right]\hat{\vartheta} = 0. \tag{5.103}$$

Using the continuity equation (5.77a), we notice that ρu^μ is a conserved quantity in the system. Thus, we can rewrite the previous equation as

$$\partial_\mu(f^{\mu\nu}\partial_\nu)\hat{\vartheta} = 0, \tag{5.104}$$

where

$$f^{\mu\nu} := \frac{\rho}{c_0^2}u^\mu u^\nu - \rho\eta^{\mu\nu}, \tag{5.105}$$

can be identified as the metric density $f^{\mu\nu} = \sqrt{-g}g^{\mu\nu}$ associated with a metric $g^{\mu\nu}$. From the definition of $f^{\mu\nu}$, it can be obtained that

$$g_{\mu\nu} = \frac{\rho}{\sqrt{1 - u_\sigma u^\sigma / c_0^2}} \left[\eta_{\mu\nu} \left(1 - \frac{u_\sigma u^\sigma}{c_0^2} \right) + \frac{u_\mu u_\nu}{c_0^2} \right], \tag{5.106}$$

where coordinates $x^\mu = (ct, \boldsymbol{x})$ were used. Defining the four-velocity

$$v^\mu := \frac{c}{\|u\|} u^\mu, \qquad \text{with} \quad \|u\| = \sqrt{-u_\sigma u^\sigma}, \tag{5.107}$$

the speed of sound c_s, defined in (5.91), can be generalised to the case when the spatial components of u^μ are different from zero:

$$c_s^2 = \frac{c^2 c_0^2 / \|u\|^2}{1 + c_0^2 / \|u\|^2}, \tag{5.108}$$

which can be used to rewrite the metric as

$$g_{\mu\nu} = \rho \frac{c}{c_s} \left[\eta_{\mu\nu} + \left(1 - \frac{c_s^2}{c^2} \right) \frac{v_\mu v_\nu}{c^2} \right], \tag{5.109}$$

where $\eta_{\mu\nu}$ is the Minkowski metric in flatspacetime. Finally, recalling the d'Alembertian operator in curved spacetime

$$\Box = \frac{1}{\sqrt{-g}} \partial_\mu \left(\sqrt{-g} g^{\mu\nu} \partial_\nu \right), \tag{5.110}$$

the equation of motion describing the propagation of phonons in an RBEC reduces to the massless Klein-Gordon equation

$$\Box \hat{\vartheta} = 0, \tag{5.111}$$

where the quantum field $\hat{\vartheta}$ associated with the phononic perturbations evolves over the so-called *acoustic metric* $g_{\mu\nu}$, which is composed of two terms. The first term corresponds to the real spacetime metric $\eta_{\mu\nu}$, while the second term corresponds to an effective metric originated on the RBEC itself. Notice how the second term depends on the four-velocity v^ν of the fluid and on the RBEC's self-interaction strength c_0. Additionally, notice the presence of the conformal factor that depends on the density $\rho = \Phi^* \Phi$ and, again, on c_0. The acoustic metric was also derived in [90] using a different approach based on fluid dynamics for the perturbations in a relativistic, barotropic and irrotational fluid flow. The generalisation to a curved real spacetime metric was achieved in [89].

As an example, let us consider the acoustic metric experienced by the quantum perturbations $\hat{\vartheta}$ when the real background spacetime corresponds to flat Minkowski spacetime for the case of a comoving reference frame, $v_\mu = (c, 0, 0, 0)$. Here, the acoustic metric reads

$$g_{\mu\nu} = \rho \frac{c}{c_s} \begin{pmatrix} -c_s^2/c^2 & 0 & 0 & 0 \\ 0 & 1 & 0 & 0 \\ 0 & 0 & 1 & 0 \\ 0 & 0 & 0 & 1 \end{pmatrix} . \tag{5.112}$$

This means that even though the phononic perturbations $\hat{\vartheta}$ live on a flat Minkowski spacetime, the presence of the condensed part of the RBEC, given by the wave function Φ in (5.73), plays a role in the phonon propagation. In this case, it causes time to flow more slowly.

To summarize, the RBEC can be described by a mean-field classical background Φ, describing the condensed part of the system, plus quantum perturbations $\hat{\vartheta}$. In the low-momentum regime and whenever the kinetic operator T_ρ can be neglected, these fluctuations behave like a phononic quantum field evolving over a fixed background curved spacetime for length scales larger than the so-called healing length, where the change of the condensate is small compared to spatial and temporal scales set by the perturbations.

5.4.5 Newtonian Limit

In this subsection, the Newtonian limit of the RBEC Lagrangian is directly taken without going through the derivation of the equations of motion of the system. On the one hand, this procedure allows the tracking of corrections coming from modifications of gravity at the level of GR that may still be present at a Newtonian level[3], which can be explored using Earth-based experiments. On the other hand, it shows the consistency and potential of the approach presented in this work. For instance, under careful consideration and depending on the experiment in mind, we could stay at the weak-gravity limit and use the BEC to study the relativistic effects of linearized gravity without making the complete jump to Newtonian gravity. Examples of this approach can be found in [89], where the acoustic metric was used

---

[3] Consider, for example, the geodesic followed by a particle in a Schwarzschild spacetime. There, an effective gravitational potential at a Newtonian level can be derived, containing three terms: the Newtonian gravitational potential energy ($\propto r^{-1}$), the standard centrifugal potential energy ($\propto r^{-2}$) and extra contribution coming exclusively from GR ($\propto r^{-3}$). See Section 5.4 in [30].

to study the entanglement in BECs, or in [91], where the passage of a gravitational wave was simulated in a BEC.

As it was established in the previous subsection, the full effects of gravity on a BEC can be studied through its relativistic formulation [88, 89, 91]. Considering an arbitrary curved spacetime, the RBEC will be described by the Lagrangian density,

$$\hat{\mathcal{L}} = -\sqrt{-g}\left[g^{\mu\nu}\partial_\mu\hat{\Phi}^\dagger\partial_\nu\hat{\Phi} + \left(\frac{m^2c^2}{\hbar^2} + \frac{2m}{\hbar^2}V_{\text{tr}}\right)\hat{\Phi}^\dagger\hat{\Phi} + \frac{1}{2}\lambda\hat{\Phi}^\dagger\hat{\Phi}^\dagger\hat{\Phi}\hat{\Phi}\right], \tag{5.113}$$

where the BEC's wavefunction is described by a relativistic scalar field $\hat{\Phi}$ whose evolution happens over a fixed background curved spacetime with metric $g_{\mu\nu}$. The first term corresponds to the kinetic term. The second one considers an external trapping potential V_{tr} and a relativistic correction proportional to the second power of m, the mass of the atoms in the BEC. The last term corresponds to the two-atom interaction via the potential $\hat{\Phi}^4$ and the coupling constant λ, which depends on the scattering length.

To achieve the Newtonian limit from the theory of general relativity, three requirements must be fulfilled [30]:

1. **Slow particles.** Test particles should be moving slowly with respect to the speed of light.
2. **Weak gravity.** Gravity should be weak, such that its effects represent just a perturbation with respect to flat spacetime.
3. **Static gravitational fields.** The gravitational field should be static or have negligible changes with time, such that the spacetime is fixed.

Basically, the Newtonian limit consists of a non-relativistic weak gravity limit of general relativity. We shall apply these criteria to the BEC's relativistic formulation. For this, we must first consider the consequences imposed by the Newtonian limit on the spacetime metric.

Consider that the BEC corresponds to an inertial observer. In general relativity, free-falling particles, or inertial observers, move along trajectories given by the geodesic equation,

$$\frac{d^2x^\mu}{du^2} + \Gamma^\mu_{\alpha\beta}\frac{dx^\alpha}{du}\frac{dx^\beta}{du} = 0, \tag{5.114}$$

where u is a scalar that parameterizes the particle's trajectory with coordinates $x^\mu = (ct, x^i)$, and

$$\Gamma^\mu_{\alpha\beta} = \frac{1}{2}g^{\mu\rho}(\partial_\alpha g_{\beta\rho} + \partial_\beta g_{\rho\alpha} - \partial_\rho g_{\alpha\beta}), \tag{5.115}$$

corresponds to the Christoffel connection. In the non-relativistic limit, requiring the particles to move slowly compared to the speed of light is translated into

$$\frac{dx^i}{d\tau} \ll \frac{dx^0}{d\tau}, \tag{5.116}$$

where $\tau = ct$ is the proper time of the particle. Under this condition, the geodesic equation becomes

$$\frac{d^2x^\mu}{du^2} + \Gamma^\mu_{00}\left(\frac{cdt}{d\tau}\right)^2 = 0, \tag{5.117}$$

and the Christoffel symbol simplifies as

$$\Gamma^\mu_{00} = -\frac{1}{2}g^{\mu\rho}\partial_\rho g_{00}. \tag{5.118}$$

Now, let us assume the case when the BEC is subjected to weak gravitational forces. When gravitational forces are weak, the spacetime metric can be linearized as

$$g_{\mu\nu} = \eta_{\mu\nu} + h_{\mu\nu}, \tag{5.119}$$

where $\eta_{\mu\nu}$ is the flat spacetime metric and $h_{\mu\nu}$ is a small perturbation such that $|h_{\mu\nu}| \ll 1$. From the nondegeneracy condition of the metric, which allows the definition of the inverse metric $g^{\mu\rho}g_{\rho\nu} = \delta^\mu_\nu$, we find that to first order in $h_{\mu\nu}$, the inverse metric is $g^{\mu\nu} = \eta^{\mu\nu} - h^{\mu\nu}$. In this order of approximation, the geodesic equation becomes

$$\frac{d^2x^\mu}{d\tau^2} = -\frac{1}{2}\eta^{\mu\rho}\partial_\rho h_{00}\left(\frac{dt}{d\tau}\right)^2. \tag{5.120}$$

Further, requiring the gravitational field to be static implies the condition

$$\partial_0 g_{\mu\nu} = 0. \tag{5.121}$$

Then, using the coordinate time t, the particle's acceleration is [30]

$$\frac{d^2x^i}{dt^2} = \frac{1}{2}\partial_i h_{00}. \tag{5.122}$$

Typically, in the non-relativistic weak-gravity limit of general relativity, the perturbation h_{00} is associated with the Newtonian gravitational potential ϕ of a massive source of gravity by making the identification

$$h_{00} = -2\phi, \tag{5.123}$$

which constitutes the derivation of Newtonian gravity from general relativity. Therefore, in the Newtonian limit, the only contribution of the metric to the Lagrangian density comes from the temporal part of the perturbation

$$g_{00} = -1 + \frac{h_{00}}{c^2}, \qquad \text{with} \quad \sqrt{-g} = 1 - \frac{h_{00}}{2c^2}. \tag{5.124}$$

The BEC's Lagrangian density gets reduced to

$$\begin{aligned}\mathcal{L} = &-\left(1-\frac{h_{00}}{2c^2}\right)\left[\partial_i\hat{\Phi}^\dagger\partial^i\hat{\Phi} + \left(\frac{m^2c^2}{\hbar^2} + \frac{2m}{\hbar^2}V_{\text{tr}}\right)\hat{\Phi}^\dagger\hat{\Phi} + \lambda\hat{\Phi}^\dagger\hat{\Phi}^\dagger\hat{\Phi}\hat{\Phi}\right] \\ &+\left(1+\frac{h_{00}}{2c^2}\right)\partial_0\hat{\Phi}^\dagger\partial_0\hat{\Phi}.\end{aligned} \tag{5.125}$$

Now, we must also take the Newtonian limit for the field operator $\hat{\Phi}$. The time dependence of $\hat{\Phi}$ can be factorized into two terms, taking the form

$$\hat{\Phi}(\boldsymbol{r},t) = \frac{\hbar}{\sqrt{2m}}\hat{\Psi}(\boldsymbol{r},t)e^{-imc^2t/\hbar}, \tag{5.126}$$

where $\hat{\Psi}$ contains the kinetic energy E' of the field, and the other factor considers the rest mass energy. Considering the total energy E of the field, the kinetic energy is written as $E' = E - mc^2$. In the non-relativistic limit, where the field moves slowly compared to c, it is required that $E' \ll mc^2$. This implies the condition [88, 91]

$$i\hbar|\partial_t\hat{\Psi}| \ll mc^2\hat{\Psi}, \tag{5.127}$$

which yields

$$\begin{aligned}\mathcal{L} = &-\left(1-\frac{h_{00}}{2c^2}\right)\left[\frac{\hbar^2}{2m}\left(\partial_i\hat{\Psi}^\dagger\partial^i\hat{\Psi} + g\,\hat{\Psi}^\dagger\hat{\Psi}^\dagger\hat{\Psi}\hat{\Psi}\right) + V_{\text{tr}}\hat{\Psi}^\dagger\hat{\Psi}\right]\\ &+\left(1+\frac{h_{00}}{2c^2}\right)\frac{i\hbar}{2}\left(\hat{\Psi}^\dagger\partial_t\hat{\Psi} - \partial_t\hat{\Psi}^\dagger\hat{\Psi}\right) + \frac{1}{2}mh_{00}\hat{\Psi}^\dagger\hat{\Psi},\end{aligned} \tag{5.128}$$

where $g := \hbar^2\lambda/2m$ is the self-interaction coupling constant. Taking the limit $c \to \infty$, the BEC's Lagrangian density in the Newtonian approximation is obtained, which further simplifies to

$$\begin{aligned}\mathcal{L} =&\frac{i\hbar}{2}\left(\hat{\Psi}^\dagger\partial_t\hat{\Psi} - \partial_t\hat{\Psi}^\dagger\hat{\Psi}\right) - \frac{\hbar^2}{2m}\partial_i\hat{\Psi}^\dagger\partial^i\hat{\Psi} - \left(V_{\text{tr}} - \frac{1}{2}mh_{00}\right)\hat{\Psi}^\dagger\hat{\Psi}\\ &-\frac{1}{2}g\hat{\Psi}^\dagger\hat{\Psi}^\dagger\hat{\Psi}\hat{\Psi}.\end{aligned} \tag{5.129}$$

Since we have arrived at a non-relativistic system of quantum nature, it is more convenient to work within the Hamiltonian formalism. The associated Hamiltonian density can be evaluated using the Legendre transformation

$$\mathcal{H} = \frac{\partial\mathcal{L}}{\partial(\partial_t\hat{\Psi})}\partial_t\hat{\Psi} + \partial_t\hat{\Psi}^\dagger\frac{\partial\mathcal{L}}{\partial(\partial_t\hat{\Psi}^\dagger)} - \mathcal{L}, \tag{5.130}$$

obtaining that

$$\mathcal{H} = \frac{\hbar^2}{2m}\nabla\hat{\Psi}^\dagger\nabla\hat{\Psi} + V_{\text{tr}}\hat{\Psi}^\dagger\hat{\Psi} - \frac{1}{2}mh_{00}\hat{\Psi}^\dagger\hat{\Psi} + \frac{1}{2}g\hat{\Psi}^\dagger\hat{\Psi}^\dagger\hat{\Psi}\hat{\Psi}. \tag{5.131}$$

Therefore, the Hamiltonian describing a BEC in the non-relativistic weak gravity limit can be written as,

$$\hat{H} = \int_{\mathcal{V}} \hat{\Psi}^{\dagger} \left(-\frac{\hbar^2}{2m} \nabla^2 + V_{\mathrm{tr}} - \frac{1}{2} m h_{00} + \frac{g}{2} \hat{\Psi}^{\dagger} \hat{\Psi} \right) \hat{\Psi} \, d\boldsymbol{r}, \tag{5.132}$$

where $\mathcal{V} = L\mathcal{A}$ is the volume of the BEC, and the coupling constant can be rewritten as $g = 4\pi\hbar^2 a_s/m$ in terms of the scattering length a_s. If we dismiss the presence of the external gravitational force, represented by the term proportional to h_{00}, we recover the standard textbook BEC Hamiltonian (5.53), under the pertinent assumptions on the two-body interaction potential.

Connecting this limit to the relativistic description of the BEC highlights the versatility of our scheme for investigating modifications of gravity that could be examined at a low-energy relativistic level, as demonstrated in the examples [89, 91] mentioned at the beginning of this subsection. In the Newtonian limit, this approach coincides with the usual treatment for studying BECs.

In summary, this chapter presented a comprehensive overview of the phenomenon of Bose-Einstein condensation. First, we examined the non-interacting Bose gas, where we observed the emergence of a phase transition below a critical temperature whose value was estimated. Next, we investigated the weakly interacting Bose gas, where the Bogoliubov theory was introduced. We derived the ground-state energy and the thermodynamic equation for the zeroth-order approximation in the momentum of the gas atoms. In the second-order approximation, we derived the excitation spectrum, which revealed the presence of phonon-like elementary excitations. Finally, the study of the non-uniform BEC was established with the derivation of the Gross-Pitaevskii equation and its application to the analysis of small-amplitude perturbations.

Additionally, we studied the RBEC in flat space, following a similar analysis to that conducted for the non-relativistic BEC. By employing the Bogoliubov approximation, we derived the dispersion relation associated with small-amplitude perturbations. We analysed the different limiting cases of the dispersion relation. For the gapless branch of the low-momentum limit, we derived the acoustic metric, an effective metric over which the phonons in the RBEC evolve. Finally, we considered the Newtonian limit of the RBEC, consistently recovering the non-relativistic BEC.

In the next chapter, we revisit the description of the BEC, taking into account the presence of an external gravitational potential. We will assume an oscillating massive sphere serves as the source of this external gravitational potential. By combining this scenario with quantum metrology, we derive the precision for estimating a physical parameter characterizing the gravitational potential of the oscillating sphere.

Chapter 6

Testing Gravity with a BEC

In previous chapters, we explored various areas of physics. In Chapter 2, we studied the theoretical treatment of bosonic quantum fields. Gaussian states and their description in terms of the covariance matrix formalism were discussed in Chapter 3, along with quantum metrology and the estimation of physical parameters in Chapter 4 and the physics of the Bose-Einstein condensate in Chapter 5. Now, everything can be combined to construct a consistent framework for performing high-precision measurements with the BEC's elementary excitations by exploiting quantum metrology and the benefits of Gaussian states. The aim is to present a *detector concept* for measuring gravitational parameters to explore modified theories of gravity in the light of dark matter and dark energy problems.

The structure of this chapter is as follows. Section 6.1 discusses the difference between the conventional implementation of BECs for gravimetry: atom interferometry and the method proposed in this thesis: frequency interferometry. In Section 6.2, we explain the experimental setup proposed for employing the BEC to probe gravity. This is achieved using the gravitational potential of an oscillating massive sphere. Next, Section 6.3 provides a detailed description of a BEC influenced by the gravitational potential of the oscillating sphere. By assuming the presence of small-amplitude perturbations in the BEC, we derive the equations of motion for the condensed atoms and the perturbations. The dispersion relation of the perturbations identifies them as phonons, and their temporal evolution is obtained. In Section 6.4, quantum metrology is implemented for estimating a parameter that quantifies the gravitational potential of the oscillating sphere, which is related to the induced acceleration on the BEC. By establishing the metrological scheme, enhanced with the implementation of a tritter, we determine the precision for estimating this parameter. Finally, Section 6.5 discusses the experimental parameters involved in determining the precision of the experiment. A review of the state-of-the-art BEC experiments is provided, along with a discussion on the conditions and constraints that the experimental parameters must follow. To close the chapter, we discuss the parameter dependence of the precision for estimating the amplitude acceleration and compute its value for different sets of parameters.

6.1 Atom Interferometry vs Frequency Interferometry

Our proposal for employing the phonons of the BEC to measure gravity relies on the implementation of frequency interferometry. In contrast, the current experimental approach to BEC gravimetry employs atom interferometry. This section introduces both types of interferometry and provides a comparison between them.

6.1.1 Atom Interferometry

The interesting properties of BECs have been implemented to make high-precision measurements. Atom interferometry is the most widely used technique that has exploited Bose-Einstein condensation for metrological purposes [92, 93]. In general, this technique has become an essential tool for fundamental physics research and the development of practical applications. Commonly, atom interferometry is performed by coherently splitting a system of cold atoms into two parts travelling on different spatial trajectories. Later, the trajectories are recombined, making the atoms interfere. If a parameter of interest interacts differently for each of the trajectories followed by the system, a relative phase difference accumulates, which can be measured to estimate the parameter [94, 95]. BECs have been extensively implemented for atom interferometry, leading to experiments to make precision measurements of physical quantities that include rotations [96, 97], accelerations [98], energy differences [99], and magnetic gradients [100], in addition to the creation of atomic clocks [101] and proposals for testing the equivalence principle or detecting gravitational waves [102]. Also, several different features of the BEC have been exploited to perform atom interferometry: BEC's solitons [103], BEC's spin-squeezed states [104], and BEC ring potentials [105].

In particular, BEC-based atom interferometry commonly implements an atomic Mach-Zehnder (MZ) scheme for gravimetry, which is displayed in Figure 6.1. This type of experiment places a BEC in free fall. Then, a sequence of optical pulses acting as a beam splitter put each atom in the cloud in a superposition of two wave packets with different momenta in analogy with the arms of the MZ interferometer. The wave packets spatially separate vertically, providing the distance needed for gravimetry. The wave packets are redirected towards each other with subsequent optical pulses that act as mirrors. Finally, another beam splitter combines the wave packets, allowing them to interfere. For N uncorrelated atoms, a relative phase difference allows the estimation of a uniform gravitational acceleration [102, 106].

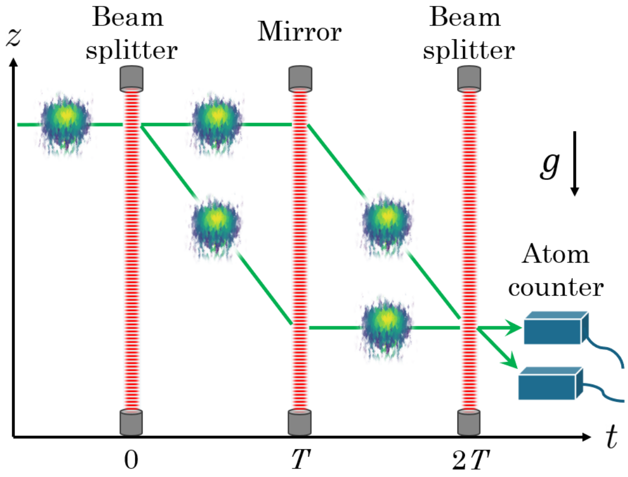

Figure 6.1: Mach-Zehnder-type Atom Interferometry. A cloud of cold atoms in free fall is split into two different spatial trajectories at different heights using a sequence of optical pulses, which play the role of a beam-splitter. Subsequent sequences of optical pulses act, first, like mirrors that redirect the trajectories of the atoms and, later, like a second beam-splitter that recombines the atoms, making them interfere. Finally, a relative phase accounting for any gravitational difference between the two trajectories is measured.

The special quantum properties of Bose-Einstein condensation present an opportunity to enhance the precision of atom interferometers beyond the standard quantum limit. However, the interatomic interactions occurring in the BEC are regarded as an unwanted hindrance that degrades precision. Furthermore, gravimetry based on atom interferometry exhibits a precision that scales with the space-time enclosed area, which is proportional to $2nkT^2$, where n is an integer number, k is the wave number of the optical pulses, and T is the interrogation time [98, 102, 106]. Therefore, precision is improved by increasing this area, which implies extending the free-falling time of the cloud of atoms or increasing the interferometer size.

This fundamental limit has pushed this research area to consider performing experiments where BECs are in microgravity to increase the precision [93]. In Earth-based experiments, the focus has relied on the construction of big towers to increase the free-falling distance. For instance, we can mention the 146 m tall ZARM drop tower in Bremen, which has been able to perform microgravity experiments using BEC-based atom interferometry presenting drop times of 4.7 s [107], and the Einstein Elevator in Hanover, which provides 4 s of microgravity experiments [108]. Space-based experiments have been carried out to increase the free-falling time, and there are plans to keep this research area active. For instance, the MAIUS-I sounding rocket mission accomplished the first BEC in space [109], the Cold Atom Laboratory (CAL) experiment in the International Space Station (ISS) created the first BEC on an Earth-orbiting platform [110], and the Bose-Einstein Condensate and Cold Atom Lab (BECCAL) is the next project planned to expand the experimental and scientific capabilities of the CAL experiment in the ISS [93].

Despite the great efforts and progress achieved by BEC-based atom interferometry experiments, the limitations imposed by the free-falling times on these types of experiments represent a major challenge that requires further technological progress and economic investment in infrastructure. Under this scheme, the best current precision for determining Earth's acceleration, for instance, is around $\Delta g/g = 1.45 \times 10^{-9}$ [95, 111]. Furthermore, from a theoretical point of view, the formalism used in atom interferometry fundamentally depends on the Schrödinger equation, which considers time as an absolute parameter common to all reference frames. Dismissing the frame-dependence of time prevents the correct description or prediction of any relativistic effect in the system.

6.1.2 Frequency Interferometry

In contrast, a different proposal for using Bose-Einstein condensation for metrological purposes is based on a particular physical feature of BECs: their collective oscillations. Instead of performing spatial interferometry with the atoms of a BEC, the idea is to perform interferometry with the frequency modes of the BEC's collective oscillations [17]. This method does not require the BEC to free-fall to capture information about external phenomena. Rather, the BEC's collective oscillations are affected by external potentials or effects while they are being held by a trapping potential. Here, the precision scales with the lifetimes of the BEC and the collective oscillations.

The origin of the idea can be traced back to the study of the evolution of confined quantum fields under accelerated motion [112] and the theoretical realization that acceleration produced observable effects in BECs [89]. Soon, these ideas were combined to set the foundations for a theoretical framework for relativistic quantum metrology focused on estimating spacetime parameters [4, 113]. Since then, the framework has consistently been developed and refined, leading to the proposal of several metrological experiments using the BEC's collective oscillations. Examples of such proposals include gravitational-wave detection [18], gravitational potential measurements [114], screened scalar fields measurements to constrain dark energy [11, 115], and the development of a patent for gravimetry and gradiometry [19, 116].

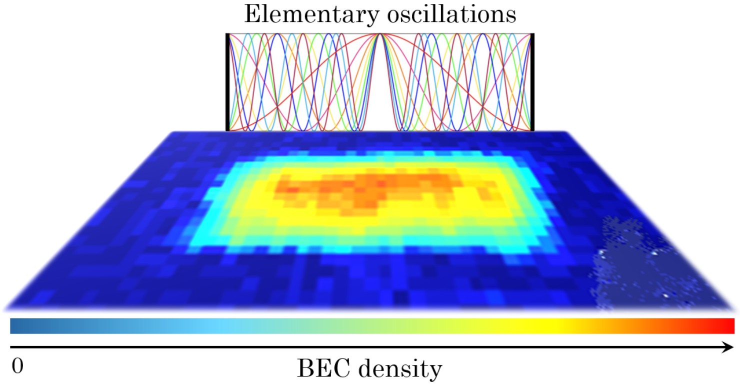

Figure 6.2: Quantum Frequency Interferometry. Depiction of a BEC held by a uniform box potential and its frequency modes, or phonons. The phonon frequencies are determined by the length of the BEC. In this scheme, phonon states are prepared, which can later be mixed or squeezed, for instance.

The basis of this framework for relativistic quantum metrology is rooted in quantum field theory, so it is well-suited for the study of relativistic effects. Moreover, important progress has been made in this direction. For instance, the authors of [117, 118] have developed a method for computing the evolution of confined quantum scalar fields over a general curved spacetime metric restricted to a synchronous frame of reference. Connecting this with the achievement of the relativistic description of the BEC from Section 5.4—where the evolution of the BEC's collective modes, or perturbations, over spacetime was studied—allows the application of the relativistic quantum metrology framework to the physics of the BEC, therefore taking the theoretical progress to actual experiments that can be performed with current technology.

This thesis aims to prepare the ground for future research into relativistic approaches that further advance the applications of the relativistic quantum metrology framework and to encourage the experimental realisation of our proposal by demonstrating its potential and versatility; thus, the relativistic framework has been introduced. However, in this thesis, we apply the quantum metrology framework to the BEC at a Newtonian, non-relativistic level, as this treatment is enough to explore modifications of Newtonian gravity. Interestingly, it was shown in [119] that the effect of a gravitational wave passing through a small detector, like a BEC, can be mimicked with a system of non-relativistic oscillating masses. Therefore, the Newtonian limit is interesting enough by itself for testing gravity and for gravitational parameter estimation.

The work presented in [114] demonstrates that changes in an external gravitational potential lead to measurable phonon creation and phonon transitions on a BEC placed nearby, which implies the BEC's potential to probe gravitational fields. In light of these results and motivated by the exploration of dark matter and dark energy—two important open questions of gravitational nature—in this thesis, we propose an experiment to carry out high-precision measurements to probe the gravitational potential. A further and more in-depth discussion of how dark matter and dark energy exploration motivated this project is presented in the next chapter.

In the next section, we will describe the experimental setup proposed in this thesis to test gravity. It comprises a BEC positioned near a massive gravitational source in the form of an oscillating sphere. The aim of the following sections is to examine the gravitational influence of the massive sphere on the collective oscillations of the BEC.

6.2 Experimental Setup

As a tabletop experiment to test gravity, in this thesis, we propose to study the interaction between a BEC and an oscillating massive sphere, accounting for a source of gravity. In particular, we propose to study the evolution of the collective modes of a BEC in the presence of the massive sphere oscillating in resonance with the frequency of the BEC's collective modes, which will turn out to correspond to phonons. The experimental setup is the following.

Let us consider an oscillating sphere with mass M and frequency Ω, which generates a time-dependent gravitational field. Placed next to it, we find a BEC of length L held by a uniform box trap potential [120], aligned with the direction of the oscillation, as depicted in 6.3. The length of the BEC is assumed to be much smaller than the size of the sphere, which allows the restriction to one spatial dimension indicated by the x-axis. Let $R(t)$ denote the distance between the BEC's centre and the sphere's centre.

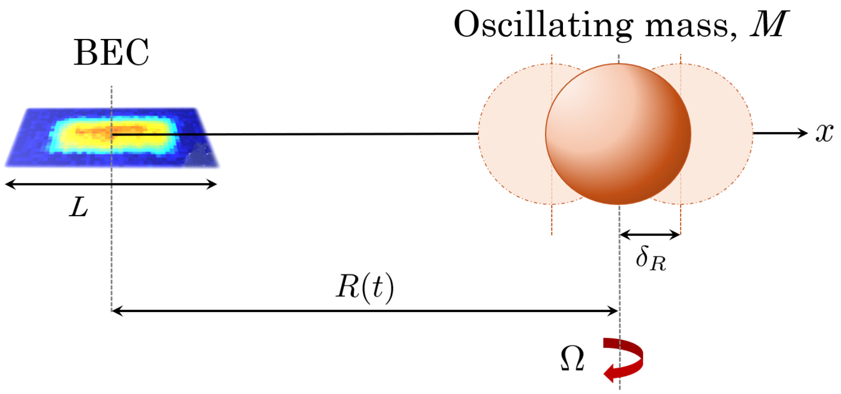

Figure 6.3: Sketch of the Experimental Setup. An oscillating sphere of mass M with frequency Ω and oscillation amplitude δ_R (on the right) is placed at a distance $R(t)$ from a BEC of length L (on the left).

The sphere is assumed to have a sinusoidal displacement $R(t) = R_0 + \delta_R \sin(\Omega t)$ about a fixed position R_0, where δ_R denotes the oscillation's amplitude. In general, for sufficiently small BECs, $L \ll R$, and small oscillation amplitudes, $\delta_R \ll R_0$, we can expand the sphere's gravitational potential ϕ inside the BEC up to first-order both in x/R and in δ_R/R_0, where $x \in [-L/2, L/2]$ is a coordinate denoting the position inside the BEC. The expansion yields

$$\phi(x,t) \approx \phi_0(t) + a(t)x, \tag{6.1}$$

where $\phi_0(t)$ and $a(t)$ are, respectively, the gravitational potential and the acceleration exerted by the sphere at the BEC.

6.2.1 Example: Newtonian gravity

To illustrate this expansion explicitly, take the standard case when the gravitational potential of the oscillating sphere is given by Newtonian gravity

$$\phi(r) = -\frac{GM}{r}.$$

Using the small BEC approximation $x/R \ll 1$, firstly, we expand the gravitational potential around the BEC's centre at $r(t) = R(t) - x$, with $x \in [-L/2, L/2]$. A first-order Taylor expansion in x/R gives,

$$\phi(x,t) = -\frac{GM}{R(t)} - \frac{GM}{R(t)^2}\, x \ + \mathcal{O}(x^2).$$

Notice that although the expansion is in the spatial coordinate, the distance between the BEC and the sphere, $R(t)$, and the gravitational potential itself, are time-dependent. This does not represent a problem for the expansion since we can expand the potential as a spatial function around $R(t)$ at each instant t. Then, we can consider the time evolution of the expansion as $R(t)$ changes.

Now, using the sinusoidal movement of the sphere, $R(t) = R_0 + \delta_R \sin(\Omega t)$, and taking the small oscillation amplitude approximation $\delta_R \ll R_0$, we Taylor expand up to first order in δ_R/R_0, obtaining

$$\phi(x,t) = -\underbrace{\frac{GM}{R_0}\left(1 - \frac{\delta_R}{R_0}\sin(\Omega t)\right)}_{\phi_0(t)} - \underbrace{\frac{GM}{R_0^2}\left(1 - \frac{2\delta_R}{R_0}\sin(\Omega t)\right)}_{a(t)} x \ + \mathcal{O}(x^2). \quad (6.2)$$

The acceleration $a(t)$ thus consists of two components: a static and a time-dependent term. The amplitude of the time-oscillating term for Newtonian gravity is defined as

$$a_\Omega := \frac{2GM\delta_R}{R_0^3}. \quad (6.3)$$

Importantly, it can be shown that in general $\phi_0(t)$ does not contribute to the dynamics of the BEC's phonons. Furthermore, as shown in [114], the static part of the acceleration $a(t)$ has a negligible contribution to the phonon's dynamics. The physical interpretation of the latter is connected to the fact that the BEC's phonons are affected only by effects that resonate with their frequency. Therefore, only the time-dependent part of the acceleration plays a relevant role in the dynamics, and, as we will see in Section 6.4, the value of acceleration amplitude a_Ω can be estimated using quantum metrology techniques applied to the BEC's phonon states.

The practical implementation of an oscillating massive sphere will be discussed in Section 6.5.3. Anticipating that discussion, let us estimate the magnitude of a_Ω for realistic parameters. Consider we perform an experiment using a sphere with mass $M = 200$ g, oscillation amplitude $\delta_R = 1$ mm placed at a distance $R_0 = 1$ cm from the BEC. These values yield that

$$a_\Omega \approx 2.7 \times 10^{-8} \text{ m/s}^2. \tag{6.4}$$

Naturally, when considering modifications of Newtonian gravity, the explicit functional form of the acceleration $a(t)$ exerted on the BEC will be uniquely determined by the specific gravitational model considered. The goal of the proposed experiment is to measure a_Ω and compare it against the theoretical predictions given by the different gravity models. In Chapter 7, we return to this question by deriving the functional form of $a(t)$ for the two modified gravity models considered in this thesis: MOND and Lambda-gravity.

The following section is dedicated to the description of the BEC and its collective excitations, considering the presence of an external gravitational field.

6.3 Description of a BEC

6.3.1 Hamiltonian Formalism and Field Decomposition

The description of the BEC under an external gravitational potential $\phi(x,t)$ follows in analogy with the procedure established in Chapter 5. Let us consider the Hamiltonian (5.23) describing a Bose gas of particles with two-particle interactions

$$\hat{H} = \int_{\mathcal{V}} \hat{\Psi}^\dagger \left(-\frac{\hbar^2}{2m} \nabla^2 + V_{\text{tr}} + m\, \phi(x,t) + \frac{g}{2} \hat{\Psi}^\dagger \hat{\Psi} \right) \hat{\Psi}\, d\boldsymbol{r}, \tag{6.5}$$

where $\mathcal{V} = L\mathcal{A}$ is the BEC's volume with L and $\mathcal{A}$ respectively corresponding to the BEC's length and cross-section, m is the mass of the BEC's atoms, V_{trap} is the trapping potential, and the two-particle coupling constant is $g = 4\pi\hbar^2 a/m$ as established in (5.30) for an effective interaction potential.

Assuming that the temperature T of the Bose gas is much lower than the critical temperature for condensation, the ground state becomes macroscopically occupied by a large collective coherent state populated by a large number of atoms, achieving the Bose-Einstein condensation. In this case, it is helpful to expand the field operator as

$$\hat{\Psi}(\boldsymbol{r},t) = \left(\hat{\Psi}_0(\boldsymbol{r}) + \hat{\vartheta}(\boldsymbol{r},t)\right) e^{-\frac{i}{\hbar}[\mu t - \int_0^t \delta\mu(t')dt']}, \tag{6.6}$$

with

$$\hat{\Psi}_0(\mathbf{r}) := \psi_0(\mathbf{r})\, \hat{a}_0, \tag{6.7a}$$

$$\hat{\vartheta}(\mathbf{r},t) := \sum_{n\neq 0} \psi_n(\mathbf{r})\, \hat{a}_n(t), \tag{6.7b}$$

where $\hat{\Psi}_0(\mathbf{r})$ describes the atoms in the ground state, and $\hat{\vartheta}(\mathbf{r},t)$ corresponds to the excited atoms of the Bose gas. The atom creation and annihilation operators, $\hat{a}_n^\dagger$ and $\hat{a}_n$, satisfy the canonical commutation relations $[\hat{a}_n, \hat{a}_m^\dagger] = \delta_{nm}$, μ denotes the chemical potential of the gas, and $\delta\mu$ is the time-dependent energy shift of the ground state.

The Bose-Einstein condensation is formally performed by making the *Bogoliubov approximation*, which replaces the operators $\hat{a}_0$ and $\hat{a}_0^\dagger$ with the complex number $\sqrt{N_a}$,

$$\hat{\Psi}_0 \to \Psi_0 = \sqrt{N_a}\psi_0, \tag{6.8}$$

where N_a corresponds to the number of atoms in the ground state of the BEC, and $\psi_0 = \mathcal{V}^{-1/2}$.

Then, under the Bogoliubov approximation, the expansion (6.6) decomposes the BEC into two parts. The *condensed part*, which describes the atoms on the ground state with a classical field $\Psi_0(\boldsymbol{r})$ satisfying the stationary Gross-Pitaevskii equation, plus the *excited* part, which describes the excited atoms in the BEC with the quantum operator $\hat{\vartheta}(\boldsymbol{r},t)$. Similarly to Section 5.3.2, we assume $\hat{\vartheta}$ corresponds to small-amplitude perturbations, then $\hat{\Psi}(\boldsymbol{r},t)$ can be considered to be very close to the stationary solution of the Gross-Pitaevskii equation.

Substituting the expansion (6.6) into the Hamiltonian (6.5) while applying the Bogoliubov approximation results in a Hamiltonian composed of three terms

$$\hat{H} = \hat{H}^{(0)} + \hat{H}^{(2)} + \hat{H}^{(\mathrm{int})}, \tag{6.9}$$

where we have discarded the higher-order terms $\mathcal{O}(\hat{\vartheta}^3)$. The first term corresponds to the ground state energy

$$\hat{H}^{(0)} = E^{(0)} = \frac{gN_a^2}{2}\int_{\mathcal{V}} |\psi_0|^4\, d\boldsymbol{r}, \tag{6.10}$$

which matches accordingly with the energy of the ideal gas (5.31). The second term is the Bogoliubov Hamiltonian

$$\hat{H}^{(2)} = :\int_{\mathcal{V}} \left[\hat{\vartheta}^{\dagger}\left(-\frac{\hbar^2\nabla^2}{2m} - \mu + 2gN_a|\psi_0|^2\right)\hat{\vartheta} + \frac{gN_a}{2}(\hat{\vartheta}^{\dagger 2}\psi_0^2 + \text{c.c.})\right] d\boldsymbol{r} :, \quad (6.11)$$

where $:\hat{O}:$ denotes the normal ordering of operators[1], and μ is the stationary eigensolution determined by the stationary GP equation, (5.60). The remaining terms are collected into the interaction Hamiltonian

$$\hat{H}^{(\text{int})} = \sqrt{\rho_0}\int_{\mathcal{V}} [\delta a(t) - \delta\mu(t)]\left(\hat{\vartheta} + \hat{\vartheta}^{\dagger}\right) d\boldsymbol{r} + \int_{\mathcal{V}} \hat{\vartheta}^{\dagger}[\delta a(t) - \delta\mu(t)]\,\hat{\vartheta}\, d\boldsymbol{r}, \quad (6.12)$$

where $\rho_0 = N_a/\mathcal{V}$ corresponds to the number density of condensed atoms in the BEC, and defining $\delta a(t) := m a_{\Omega}\sin(\Omega t)x$, which determines the ground state energy shift via $\delta\mu(t) = \int \psi_0^*\,\delta a(t)\,\psi_0\, d\boldsymbol{r}$.

6.3.2 Description of the Perturbations

A *Bogoliubov transformation* can be applied to the operators of the excited atoms, $\hat{a}_{n\neq 0}$, which allows us to express the field operator of the perturbations as the mode decomposition [86]

$$\hat{\vartheta}(\boldsymbol{r}, t) = \sum_n \left(u_n(\boldsymbol{r})\hat{b}_n e^{-i\omega_n t} + v_n(\boldsymbol{r})\hat{b}_n^{\dagger} e^{i\omega_n t}\right), \quad (6.13)$$

where $\hat{b}_n^{\dagger}$ and $\hat{b}_n$ are the collective modes creation and annihilation operators following canonical commutation relations $[\hat{b}_n, \hat{b}_m^{\dagger}] = \delta_{nm}$, and ω_n is the mode frequency. The evolution of the mode functions $u_n(\boldsymbol{r})$, $v_n(\boldsymbol{r})$ can be derived by using the Heisenberg equation $i\hbar\,\partial_t\hat{\Psi}(\boldsymbol{r}, t) = [\hat{\Psi}(\boldsymbol{r}, t), \hat{H}]$ and the stationary solution of the GP equation.

We assume the BEC is confined using a box-like uniform trapping potential [120], where Earth's gravity is cancelled and the effective potential inside the trap is approximately zero, $V_{\text{trap}} = 0$. While such traps can provide a nearly uniform density profile for the condensed atoms, they also introduce problems due to the

---

[1] Normal ordering places all creation operators to the left of all annihilation operators whenever a product between these happens.

hard-wall boundary conditions. In particular, the condensate density drops abruptly to zero at the walls, creating strong gradients which invalidate the local density approximation near the walls. However, this phenomenon is present at length scales smaller than the healing length [73], discussed in (5.50). By working in the phonon regime, where excitation wavelengths are much larger than the healing length, we avoid these short-scale features.

Therefore, considering a BEC confined to a uniform trapping potential, the evolution of the mode functions $u_n(\boldsymbol{r})$, $v_n(\boldsymbol{r})$ is governed by the stationary Bogoliubov-de Gennes (BdG) equations

$$\omega_n u_n(\boldsymbol{r}) = \frac{\hbar}{2m}\left[\left(-\nabla^2 + \frac{1}{\xi^2}\right)u_n(\boldsymbol{r}) + \frac{1}{\xi^2}v_n(\boldsymbol{r})\right], \tag{6.14a}$$

$$-\omega_n v_n(\boldsymbol{r}) = \frac{\hbar}{2m}\left[\left(-\nabla^2 + \frac{1}{\xi^2}\right)v_n(\boldsymbol{r}) + \frac{1}{\xi^2}u_n(\boldsymbol{r})\right], \tag{6.14b}$$

where ξ corresponds to the BEC's healing length and the contribution from the gravitational potential can be discarded as shown in [114].

The mode functions satisfy Neumann boundary conditions at the potential walls [114]. Since the perturbations describe density fluctuations, this boundary condition ensures that the atom current flow vanishes at the walls of the box-like trapping potential. The mode functions are normalized with respect to the inner product

$$\int_{\mathcal{V}} [u_n^*(\boldsymbol{r})u_m(\boldsymbol{r}) - v_n^*(\boldsymbol{r})v_m(\boldsymbol{r})]\, d\boldsymbol{r} = \delta_{nm}. \tag{6.15}$$

We assume that the width and height of the BEC are much smaller than its length L, leading to an effective reduction of the phonon dynamics to one dimension. This 3D-to-1D transition in the phonon propagation has been previously studied for BECs in harmonic trapping potentials [121], where radial confinement suppresses the transverse excitations, leaving only longitudinal phonon modes. This dimensional reduction occurs when the phonon wavelength becomes larger than the transverse radius of the condensate.

In a uniform box-like trap, we expect a similar behaviour. As the transverse BEC dimensions fall below the characteristic phonon wavelength of the system, the phonons get effectively constrained to propagate along the longitudinal spatial direction. However, unlike harmonic traps, uniform box traps impose hard-wall boundary conditions in all directions [120]. To keep a well-defined region in the condensate where the local density approximation remains valid, the width and height of the BEC must be larger than the healing length ξ.

Under the 3D-to-1D transition, the atom-atom interaction strength g becomes effectively renormalized due to the restricted transverse motion of the atoms. This renormalization has been derived for both harmonic [122] and box-like trapping potentials [123], and leads to a modified effective 1D coupling constant $g_{1\text{D}} \sim g_{1\text{D}}/A_{\perp}$, where $A_{\perp}$ is the transverse cross-sectional area of the BEC. As a consequence, the healing length ξ, which depends on the interaction strength, is adjusted. These modifications must be taken into consideration since this renormalization may influence the quantum fluctuations of the collective excitations, including phonon number fluctuations (see Eq. (6.48)).

Assuming the 3D-to-1D transition, we restrict our analysis to excitations along the x-direction, aligned with the direction of the sphere's gravitational potential. Under these conditions, the set of real solutions to the BdG equation is

$$u_n(x) = \sqrt{\frac{1}{\mathcal{V}}\left(\frac{1}{\sqrt{2}\xi k_n}+1\right)}\cos\left[k_n\left(x+\tfrac{L}{2}\right)\right], \tag{6.16a}$$

$$v_n(x) = -\sqrt{\frac{1}{\mathcal{V}}\left(\frac{1}{\sqrt{2}\xi k_n}-1\right)}\cos\left[k_n\left(x+\tfrac{L}{2}\right)\right], \tag{6.16b}$$

where $k_n = n\pi/L$ and n is a positive integer number.

Returning to the Hamiltonian of the system, the Bogoliubov Hamiltonian, $\hat{H}^{(2)}$, can be diagonalized by the mode decomposition (6.13). Discarding the terms of third and fourth order in $\hat{b}_n^{\dagger}$ and $\hat{b}_n$, and using the normalization condition of the mode functions (6.15), we obtain that

$$\hat{H}^{(2)} =: \sum_n \hbar\omega_n \hat{b}_n^{\dagger}\hat{b}_n : \;. \tag{6.17}$$

The energy spectrum is given by the dispersion relation

$$(\hbar\omega_n)^2 = (c_s\hbar k_n)^2 + (\hbar^2 k_n^2/2m)^2, \tag{6.18}$$

where $c_s = \sqrt{g\rho_0/m}$ corresponds to the speed of sound in the BEC.

Considering the low-energy (low-momentum) limit $\hbar\omega_n \ll mc_s^2$, which can be rewritten in terms of the healing length as the limit $\xi\, k_n \ll 1$, can be interpreted as restricting ourselves to work with the modes of lower energy or the modes with wavelength much larger than the healing length. In this limit, the dispersion relation reads

$$\omega_n = c_s k_n. \tag{6.19}$$

This relation is equivalent to (5.48), which corresponds to the dispersion relation associated with phonons travelling at speed c_s. Therefore, in the low-energy limit, the operators $\hat{b}_n^\dagger$ and $\hat{b}_n$ create and annihilate *phonons* in the BEC.

As discussed in Section 5.2.4, and in analogy with (5.43), the Hamiltonian (6.17) tells us that the original system of interacting atoms, associated with the operators $\hat{a}_n$ and $\hat{a}_n^\dagger$, can be equivalently described as a system of non-interactive phonons, associated with the operators $\hat{a}_n$ and $\hat{a}_n^\dagger$, of energy $\hbar\omega_n$. In the low-energy limit, the Bogoliubov transformation that relates them takes the form

$$\hat{a}_n \sim u_n(\hat{b}_n e^{-i\omega_n t} - \hat{b}_n^\dagger e^{i\omega_n t}). \tag{6.20}$$

Moving back to the interaction Hamiltonian, we substitute on it the mode decomposition (6.13), and by using the rotating wave approximation to discard the fast time-oscillating terms, we obtain

$$\begin{aligned}\hat{H}^{(\text{int})} &= \sum_n \mathcal{M}_{0n}\left(\hat{b}_n e^{-i(\omega_n-\Omega)t} - \hat{b}_n^\dagger e^{i(\omega_n-\Omega)t}\right)\\ &+ \sum_{l,n} \mathcal{M}_{ln}\left(\hat{b}_l\hat{b}_n e^{-i(\omega_n+\omega_l-\Omega)t} - \hat{b}_l^\dagger\hat{b}_n^\dagger e^{i(\omega_n+\omega_l-\Omega)t}\right)\\ &- \sum_{l>n}(\mathcal{A}_{ln}+\mathcal{B}_{ln})\left(\hat{b}_l^\dagger\hat{b}_n e^{i(\omega_l-\omega_n-\Omega)t} - \hat{b}_l\hat{b}_n^\dagger e^{-i(\omega_l-\omega_n-\Omega)t}\right),\end{aligned} \tag{6.21}$$

where the transition amplitudes are given as

$$\begin{aligned}\mathcal{M}_{0n} &= -\frac{ima_\Omega}{2}\sqrt{\frac{N_a\mathcal{A}}{L}}\int_{-L/2}^{L/2} x[u_n(x)+v_n(x)]\,dx,\\ \mathcal{M}_{ln} &= -\frac{i\mathcal{A}ma_\Omega}{2}\int_{-L/2}^{L/2} x\,u_l(x)v_n(x)\,dx,\\ \mathcal{A}_{ln} &= -\frac{i\mathcal{A}ma_\Omega}{2}\int_{-L/2}^{L/2} x\,u_l(x)u_n(x)\,dx,\\ \mathcal{B}_{ln} &= -\frac{i\mathcal{A}ma_\Omega}{2}\int_{-L/2}^{L/2} x\,v_l(x)v_n(x)\,dx.\end{aligned}$$

Using the properties of solutions for the BdG equations and taking the approximation $k_n\xi \ll 1$, the amplitudes take the final form

$$\mathcal{M}_{0n} \approx im\sqrt{\frac{LN_a\xi}{(\sqrt{2}n\pi)^3}}(1-(-1)^n)\,a_\Omega, \tag{6.22a}$$

$$\mathcal{M}_{ln} \approx -\frac{imL^2(l^2+n^2)}{2\sqrt{2nl}(l^2-n^2)^2\pi^3\xi}(1-(-1)^{l+n})\,a_\Omega, \quad \text{for} \quad l \neq n, \tag{6.22b}$$

$$\mathcal{M}_{nn} \approx -\mathcal{A}_{nn} \approx -\mathcal{B}_{nn} \approx 0. \tag{6.22c}$$

where $\mathcal{M}_{ln} \approx -\mathcal{A}_{ln} \approx -\mathcal{B}_{ln}$ and a_Ω corresponds to the experimental parameter to be measured, as will be shown in Section 6.4 by implementing quantum metrology. In Chapter 7, this parameter will be explicitly calculated according to the predictions done by MOND (a_M) and Lambda-Gravity (a_Λ).

6.3.3 Time-Evolution Operator

The temporal evolution of the phonons is given by the time-evolution operator $\hat{U}(t) = \exp(-i\int \hat{H}^{(int)}dt/\hbar)$. Considering only processes on resonance with the oscillating massive sphere, such that its oscillating frequency Ω matches the frequency of the phonons, the temporal dependence of $\hat{H}^{(int)}$ is lost and it also implies the existence of a mode number $n_\Omega := L\Omega/(\pi c_s)$ which must be an odd integer. Then, the evolution of the phonons under the influence of the oscillating sphere, considering only resonant processes, is given by the time evolution operator

$$\begin{aligned} \hat{U}(t) = &\ \exp\left[a_\Omega M_{0n_\Omega}\left(\hat{b}^\dagger_{n_\Omega} - \hat{b}_{n_\Omega}\right)t/\hbar\right] \\ \times &\ \exp\left[\sum_{l<n_\Omega} a_\Omega M_{l,n_\Omega-l}\left(\hat{b}^\dagger_l\hat{b}^\dagger_{n_\Omega-l} - \hat{b}_l\hat{b}_{n_\Omega-l}\right)t/\hbar\right] \\ \times &\ \exp\left[\sum_{l>n_\Omega} 2a_\Omega M_{l,l-n_\Omega}\left(\hat{b}^\dagger_l\hat{b}_{l-n_\Omega} - \hat{b}^\dagger_{l-n_\Omega}\hat{b}_l\right)t/\hbar\right], \end{aligned} \tag{6.23}$$

where we defined the quantities

$$M_{0n} = 2m\sqrt{\frac{LN_a\xi}{(\sqrt{2}n\pi)^3}}, \qquad M_{ln} = \frac{mL^2(l^2+n^2)}{\sqrt{2nl}(l^2-n^2)^2\pi^3\xi}. \tag{6.24}$$

Let us discuss and explain the physical meaning of the three exponentials appearing in the time evolution operator. Their interpretation is closely related to the Gaussian transformations described in Chapter 3.

The first exponential, with argument proportional to $(\hat{b}^\dagger_{n_\Omega} - \hat{b}_{n_\Omega})$, corresponds to the Weyl displacement operator introduced by Eq. (3.35). Its resonant condition requires $\omega_n = \Omega$, which is equivalent to taking the mode $n = n_\Omega$. This operator creates a coherent state when applied to the vacuum state. If we dismiss the rest of the operators in $\hat{U}(t)$, the average number of phonons N_p created by the displacement operator is given as $N_p = |a_\Omega M_{0 n_\Omega}\, t/\hbar|^2$, as established by (B.4) in Appendix B.

The second exponential, with argument $\sim (\hat{b}^\dagger_l \hat{b}^\dagger_{n_\Omega - l} - \hat{b}_l \hat{b}_{n_\Omega - l})$, corresponds to the two-mode squeezing operator defined by (A.27) in Appendix A. Under the resonant condition $\omega_l + \omega_n = \Omega$, which is equivalent to taking the modes l and $n_\Omega - l$ that satisfy $l + n = n_\Omega$, this operator generates a pair of squeezed phonons with frequencies ω_l and ω_n. As discussed in Section 3.7.4, a squeezed state corresponds to a Gaussian state exhibiting entanglement, which minimizes the Heisenberg uncertainty principle. Suppose we dismiss the rest of the operators in $\hat{U}(t)$. In that case, this operator creates squeezed states of phonons thanks to the resonant effect of gravity created by the oscillating sphere, creating an average number of phonons corresponding to $N_p = 2\sinh^2(a_\Omega\, M_{l, n_\Omega - l} t/\hbar)$, as established in Appendix B.

The last exponential, whose argument is proportional to $(\hat{b}^\dagger_l \hat{b}_{l - n_\Omega} - \hat{b}^\dagger_{l - n_\Omega} \hat{b}_l)$, corresponds to the mode-mixing operator, which acts as a beam-splitter mixing a pair of phonons with frequencies ω_l and ω_n. This process is resonant given the condition $\omega_l - \omega_n = \Omega$, which is equivalent to taking the modes l and $l - n_\Omega$ that satisfy $l - n = n_\Omega$. The mode-mixing operator is a mode-coupling process that does not change the number of phonons.

6.4 Quantum Metrology

Quantum metrology is now employed to detect the change in the BEC's phonons induced by the gravitational influence of the oscillating sphere. The strategy is to estimate the physical parameter responsible for phonon generation, in this case, the acceleration amplitude a_Ω of the oscillating gravitational field. This parameter is imprinted onto the phonon states through the displacing, squeezing, and mode-mixing operators as established by the time evolution operator $\hat{U}(t)$ derived in the previous section. By measuring the resulting phonon state, or the BEC's phonon content, the value of a_Ω can be estimated.

As discussed in Section 4.4, to optimize the precision of the estimation, the strategy is to find optimal initial states and optimal measurement bases for the final state. It was shown in [45, 124] that the optimal estimation of a parameter via Gaussian processes—either for any of the states studied in Chapter 3, including the evolution driven by $\hat{U}(t)$—is obtained when the probe state corresponds to a squeezed state.

Additionally, a frequency interferometry strategy can be performed with a single BEC in a pumped-up $SU(1,1)$ scheme [125], which enhances the estimation precision [17]. In this case, the condensate atoms act as the pump, and two phonon modes can be used as the side modes.

6.4.1 Metrological Scheme

A three-mode frequency interferometry scheme [17] is implemented, involving the BEC's ground state and two phonon modes coming from (6.17). We focus on the modes l, n that satisfy the resonance condition $\Omega = \omega_l + \omega_n$ with the oscillation frequency Ω of the sphere, where $l+n$ is an odd integer. The full scheme is illustrated in Figure 6.4.

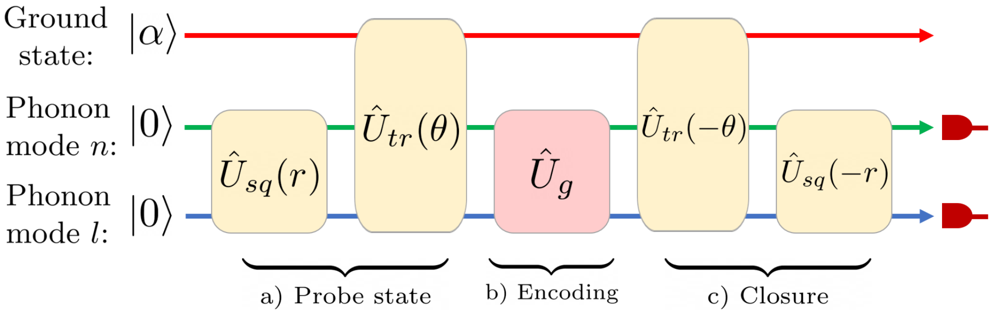

Figure 6.4: Frequency Interferometry Scheme. **a)** The probe state is prepared by applying the transformation $\hat{U}_{\text{sq}}(r)$ on two vacuum phonon modes (green and blue) to then mix them with the BEC ground state (red) through the tritter $\hat{U}_{\text{tr}}(\theta)$. **b)** The acceleration amplitude is encoded by $\hat{U}_g(a_\Omega)$. **c)** To close the circuit, the probe state is reversed. Finally, the number of phonons is counted at the output.

a) Probe State Preparation

The scheme begins with the preparation of the probe state, priorly to the involvement of the oscillating sphere. First, studies show that in general the ground state of a BEC is well approximated by a coherent state $|\alpha\rangle$ [126, 127], satisfying $\hat{a}_0 |\alpha\rangle = \alpha_0 |\alpha\rangle$, where α_0 is a complex number related to the number of atoms in the ground state, N_a (see Section 3.7).

Next, we take two phonon modes l and n in the vacuum. When working with Gaussian states, squeezed states are known to be optimal probe states [45, 124]. Therefore, a two-mode squeezing transformation is applied to the phonon modes l and n,

$$\hat{U}^{ln}_{\mathrm{sq}}(r, \vartheta_{\mathrm{sq}}) = e^{r(e^{i\vartheta_{\mathrm{sq}}}\hat{b}_l^\dagger \hat{b}_n^\dagger - e^{-i\vartheta_{\mathrm{sq}}}\hat{b}_l \hat{b}_n)}, \tag{6.25}$$

where r is the squeezing parameter and $\vartheta_{\mathrm{sq}} \in \mathbb{R}$ is the squeezing phase. This transformation parametrically populates the modes, and its experimental implementation can be achieved by the sinusoidal modulation of the trapping potential at a fixed frequency, i.e., by the periodical change of the BEC's length [128, 129, 17]. The frequency of the trapping potential modulation is selected in accordance with the frequency of the oscillating sphere that squeezes the phonon modes l and n.

To further optimize the probe state, the BEC's ground state gets coupled with the squeezed phonon state using a tritter transformation $\hat{U}_{\mathrm{tr}}(\theta, \vartheta)$. This transformation is generated from the Hamiltonian [125]

$$\hat{H}^{ln}_{\mathrm{tr}}(\theta, \vartheta) = \frac{\hbar\theta}{\sqrt{2}} \left[e^{i\vartheta}\hat{a}_0^\dagger(\hat{b}_l + \hat{b}_n) + e^{-i\vartheta}\hat{a}_0(\hat{b}_l^\dagger + \hat{b}_n^\dagger) \right], \tag{6.26}$$

where $\theta \in \mathbb{R}$ is the coupling strength and $\vartheta \in \mathbb{R}$ is a phase. The explicit form of the tritter is shown in Appendix C. Recall that $\hat{a}_0^\dagger$ is the creation operator associated with the atoms in the ground state, that is, the condensed atoms of the BEC. Therefore, the tritter transformation can be understood in analogy to the beam splitting transformation (see Eq. (3.44)) as the mixing of ground-state atoms with phonon modes l and n, as depicted in Figure 6.5.

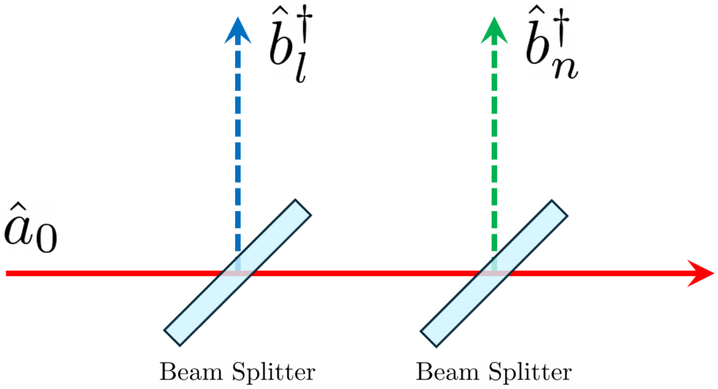

Figure 6.5: Tritter Transformation Diagram. Ground-state atoms (solid red line) sequentially decay into phonon modes l and n (dotted blue and green lines, respectively) in a process analogous to the beam-splitting, or mode-mixing, transformation. Simultaneously, phonon modes l and n decay into ground-state atoms, illustrating both processes given by the two terms in Eq. (6.26).

The tritter transformation is inspired by a beam splitter-like coupling between different modes in the BEC. This could be implemented through a suitable modulation of the trapping potential or by using Bragg diffraction [130, 131, 132], where applying two electromagnetic fields tuned to the excitation energies of the phonon modes could impart the required momentum to excite the ground state, or conversely, supply the energy to return excitations to the ground state. The tritter concludes the preparation of the probe state before the involvement of the gravitational effects of the oscillating sphere.

In the Bogolibov approximation, $\hat{a}_0$ is replaced by $\sqrt{N_a}$. We assume that the number of condensed atoms is fairly undepleted by the squeezing transformation and remains in a coherent state $|\alpha\rangle$, implying that $N_a = |\alpha_0^2|$. It is also assumed that N_a will remain reasonably undepleted after the tritter transformation, which requires that the coupling θ driving the tritter cannot be too large.

b) Parameter Encoding

After the probe state is ready, the gravitational interaction with the BEC's phonon states is started by activating the oscillation of the massive sphere. As discussed in Section 6.3.3, the sphere's oscillation frequency Ω can be tuned to resonate with the phonons of the BEC using the relation

$$\Omega = \frac{n_\Omega \pi c_s}{L}, \tag{6.27}$$

determined by the speed of sound c_s in the BEC and its length L. The integer number n_Ω is a free parameter whose value will determine which phonon modes are stimulated by the massive sphere, as established by Eq. (6.23). Focusing exclusively on the two-mode squeezing induced by the oscillating sphere, resonant when $\Omega = \omega_n + \omega_l$ (or equivalently, $l + n = n_\Omega$, with n_Ω an odd integer), we find that the phonon evolution is given by

$$\hat{U}_g(t) = e^{\sum_{l,n} r_{ln}(t)\left(\hat{b}_l^\dagger \hat{b}_n^\dagger - \hat{b}_l \hat{b}_n\right)}, \tag{6.28}$$

with squeezing parameter

$$r_{ln}(t) = \frac{a_\Omega M_{l,n} t}{\hbar}. \tag{6.29}$$

In principle, the operator $\hat{U}_g(t)$ squeezes all phonon modes pairs satisfying $l+n = n_\Omega$ an odd integer. However, as we discuss below in Section 6.5.1, we will focus on low mode numbers, which effectively restrict the dynamics. In particular, selecting $n_\Omega = 3$ unambiguously squeezes exclusively the phonon modes $l = 1$ and $n = 2$.

The activation of the oscillation of the massive sphere is not expected to stimulate unwanted phonon modes, given that we are working with resonant processes and that we are stimulating the lowest phonon modes. First, as the frequency ramps up, it won't spend enough time near any resonant mode to induce phonon stimulation. Second, targeting low-frequency modes avoids stimulating higher-frequency modes, as this requires a higher frequency than the one being used.

The change produced in the phonon states by the gravitational interaction is quantified by magnitude of the squeezing parameter r_{ln}, which depends on the acceleration amplitude a_Ω exerted on the BEC by the oscillating sphere, the mode overlap $M_{l,n}$ as given by Eq. (6.24), and the interaction time t as shown in Eq. (6.29). To estimate the amount of squeezing, we use the value $a_\Omega \approx 2.7 \times 10^{-8}$ m/s^2 derived in Eq. (6.4) considering Newtonian gravity. Anticipating the discussion in Section 6.5.1 on the value of the experimental parameters, we can consider the parameters listed in Table 6.2. Considering, for example, a BEC of length $L = 1000$ μm with speed of sound $c_s = 1.02$ mm/s, the squeezing parameter evaluates to

$$r_{ln} \approx 0.65, \tag{6.30}$$

corresponding to approximately one phonon generated, or a signal strength of roughly -0.13 dB.

c) Interferometer Closure and Measurement

To close the frequency interferometry scheme, we apply the inverse transformations $\hat{U}_{\mathrm{sq}}(-r)$ and $\hat{U}_{\mathrm{tr}}(-\theta)$. Although less commonly examined in the literature, inverse squeezing (or antisqueezing) has been studied theoretically and implemented experimentally in systems such as spinor Bose–Einstein condensates [133] and trapped atomic ions [134]. The inverse squeezing can be achieved by reversing the nonlinear evolution, thereby effectively recovering the initial state. In the case of phonons, such a reversal could be implemented by inverting the phase of modulation of the trapping potential. The inverse tritter could, in principle, be implemented by applying the same operation but with a π phase shift, analogous to reversing a beam splitter by changing the relative phase. While experimental demonstrations of mode-mixing operations are available, the inverse operation is less commonly reported.

The metrological scheme ends by measuring the final phonon state. Since the scheme can be implemented independently of the specific measuring protocol, we assume that some feasible protocol exists which can reach or approximate single-phonon sensitivity. To support this assumption, we consider recent developments in phonon detection in BECs. For example, in Ref. [128], single-atom detectors were used after releasing the trap to estimate the number of phonons by measuring the momentum distribution of the atoms. To approximate single-phonon detections, one can adiabatically manipulate the system during the interaction and measurement stages to ensure a one-to-one correspondence between atoms and phonons, thereby suppressing unwanted fluctuations. Although current experiments may resolve only tens of phonons [135, 136], further progress in detection technology may soon enable single-phonon resolution.

While this is one possible method, alternative measurement strategies may also achieve comparable sensitivity. For instance, Ref. [114] discusses homodyne and heterodyne detection schemes, which offer optimal and suboptimal yet practical measurements that estimate the phonon number, or related observables, with high precision [137, 138].

In our metrological scheme, thermal and laser noise are potential sources of fluctuations in the number of condensed atoms. Previous studies have shown that the scheme is robust against thermal noise, and that the presence of initial thermal fluctuations does not significantly affect the phonon states [69]. However, laser noise can influence the number of condensed atoms by reducing the cooling efficiency and trap stability. Therefore, it is crucial to minimize these effects by implementing laser stabilization techniques to ensure the reliability of precision measurements [139, 140].

Since the precision of our proposal scales with the total number of condensed atoms N_a (see Eq. (6.37)), we must ensure the relative fluctuations $\delta N_a/N_a$ to remain small. The key point relies on preventing fluctuations δN_a from introducing significant uncertainties in the phonon population that could compromise the precision for detecting gravitational effects.

6.4.2 Quantum Cramér-Rao Bound & Quantum Fisher Information

From the material studied in Chapter 4, we know that the optimal precision to estimate the parameter a_Ω characterizing the gravitational influence on the BEC's phonons by the oscillating sphere is given by the quantum Cramér-Rao bound, introduced in (4.11),

$$\Delta a_\Omega \geq \frac{1}{\sqrt{N_m F_Q(a_\Omega)}}\,, \tag{6.31}$$

which depends on the number of measurements N_m and on the quantum Fisher information F_Q, defined in (4.16).

The QCRB optimizes all positive-operator-valued measurement schemes and can be saturated for $N_m \to \infty$. When the measurement saturating the bound cannot be experimentally implemented, suboptimal viable measurements, such as heterodyne detection, can be carried out [70].

To determine the precision in estimating the gravitational parameter a_Ω, the quantum Fisher information must be evaluated first. Following the material presented in Section 4.3, the probe state of the system $(\boldsymbol{d}_0, \Gamma_0)$ and the symplectic transformation $S(\epsilon)$ driving its evolution need to be expressed in terms of the covariance matrix formalism. The transformation $S(\epsilon)$ imprints the parameter ϵ in the probe state, resulting in the state $(\boldsymbol{d}, \Gamma)$. Considering the metrological scheme described in the previous subsection, let us determine the probe state, the transformation and the resulting state using the covariance matrix formalism language[2].

Initially, the BEC's ground state is considered to be a coherent state, and we take two phonon modes, l and n, which are assumed to be in the vacuum. The initial state is described by the pair $(\boldsymbol{d}_{\text{coh}}, \Gamma_{\text{vac}})$. To prepare the probe state, both phonon modes are squeezed using the symplectic matrix $S_{\text{sq}}(r, \vartheta_{\text{sq}})$ associated with the transformation $\hat{U}_{\text{sq}}(r, \vartheta_{\text{sq}})$, and then they are mixed with the BEC's ground state using the tritter $S_{\text{tr}}(\theta, \vartheta)$ associated to $\hat{U}_{\text{tr}}(\theta, \vartheta)$. Then, the probe state can be expressed by the pair $\boldsymbol{d}_0 = S_{\text{tr}} S_{\text{sq}} \boldsymbol{d}_{\text{coh}}$ and $\Gamma_0 = (S_{\text{tr}} S_{\text{sq}}) \Gamma_{\text{vac}} (S_{\text{tr}} S_{\text{sq}})^\dagger$.

The oscillating sphere interacts gravitationally with the BEC through the symplectic transformation $S_g(a_\Omega)$ associated with the two-mode squeezing transformation $\hat{U}_g$, which imprints the acceleration amplitude a_Ω on the phonon evolution. This results in the state given by the pair $\boldsymbol{d} = S_g \boldsymbol{d}_0 = S_g S_{\text{tr}} S_{\text{sq}} \boldsymbol{d}_{\text{coh}}$ and $\Gamma = S_g \Gamma_0 S_g^\dagger = (S_g S_{\text{tr}} S_{\text{sq}}) \Gamma_{\text{vac}} (S_g S_{\text{tr}} S_{\text{sq}})^\dagger$. Since the QFI is independent of the measurement performed, the interferometric scheme does not need to be closed to evaluate the QFI. It is enough to consider the system's state until gravity starts acting on the BEC, that is, $(\boldsymbol{d}, \Gamma)$.

The explicit evaluation of the quantum Fisher information can be found in Appendix C, performed using Wolfram Mathematica for convenience. The result obtained for the quantum Fisher information, (4.16), related to the estimation of a_Ω under the metrological scheme followed reads

$$\begin{aligned} F_Q(a_\Omega) = (M_{ln}\, t/\hbar)^2 \big\{ & 4 + \sin^2(2\theta) \sinh^2 r + 2(1 + \cos^4\theta) \sin^2(\vartheta_{\text{sq}}) \sinh 2r \\ & + |\alpha_0|^2 \left(4 \sin^4\theta + [\cos(2\vartheta - \vartheta_{\text{sq}}) \sinh 2r + \cosh 2r] \sin^2 2\theta \right) \big\} . \end{aligned} \tag{6.32}$$

Undepleted Approximation

During the experimental preparation of the probe state, the ground state of the BEC is assumed to remain reasonably undepleted by the squeezing transformation and the tritter, thus staying in a coherent state $|\alpha\rangle$.

First, the conservation of the number of atoms after the action of S_{sq} requires the relation $N_a = \bar{N} - N_{\text{exc}}$ to hold, where $N_a = |\alpha_0^2|$ represents the number of condensed atoms, $\bar{N} = |\alpha|^2$ is the number of initially condensed atoms and N_{exc} is

---

[2] The relationship between symplectic transformations and their associated Gaussian unitary transformations is derived and enlisted in Appendix A.

the number of atoms excited by the squeezing transformation, which is proportional but greater than the number of produced phonons, $N_p = 2\sinh^2 r$. The relation between these two quantities is later provided by Eq. (6.43).

To maximize the QFI, the optimal phase values for S_{sq} and S_{tr} can be experimentally implemented, with values corresponding respectively to $\vartheta_{\mathrm{sq}} = \frac{\pi}{2}$, $\vartheta = \frac{\pi}{4}$. Assuming that the ground state remains relatively undepleted under S_{sq}, implying $\bar{N} \gg N_{\mathrm{exc}}$, and additionally considering that $\bar{N} \gg 1$, $N \gg 1$ and $r \gg 1$, the QFI simplifies to

$$F_Q(a_\Omega) \approx 2(M_{ln}t/\hbar)^2 \sin^2(2\theta)\bar{N}N_p. \tag{6.33}$$

To further assume that the BEC's ground state remains reasonably undepleted after the tritter transformation, it follows that θ must be small. After the application of the tritter, the number of ground-state and excited atoms is:

$$N_a(\theta) = N_a\cos^2\theta + \frac{1}{2}N_{\mathrm{exc}}\sin^2\theta, \tag{6.34a}$$

$$N_{\mathrm{exc}}(\theta) = N_a\sin^2\theta + \frac{1}{2}N_{\mathrm{exc}}(1+\cos^2\theta). \tag{6.34b}$$

Introducing $\gamma, \delta \in \mathbb{R}$, the ground state can be assumed to remain fairly undepleted if we require that $N_{\mathrm{exc}} = \gamma N_a$ and $N_{\mathrm{exc}}(\theta) = \delta N_a(\theta)$ for $\gamma \ll 1$ and $\delta \ll 1$. Then, θ corresponds to a small parameter if it satisfies the relation

$$\theta \leq \frac{1}{2}\arccos\left(\frac{\delta\gamma + 2\delta - 3\gamma - 2}{\delta\gamma + 2\delta + \gamma - 2}\right). \tag{6.35}$$

For instance, setting $\delta = 0.05$ and taking the limit when $\gamma \to 0$, results in a value $\theta \approx 0.21$. Then, in the fully undepleted approximation, the QFI becomes

$$F_Q(a_\Omega) \approx 8(M_{ln}t/\hbar)^2\theta^2 N_a N_p. \tag{6.36}$$

It is interesting to note that the quantum Fisher information for estimating a_Ω is independent of the parameter itself. This is due to linear dependence on a_Ω of the squeezing parameter r_{ln} driving the gravitational-induced phonon evolution, as can be checked from (6.29).

6.4.3 Measurement Precision Formula

To determine the precision Δa_Ω for measuring the acceleration amplitude a_Ω exerted on the BEC by the oscillating mass, the results from equations (6.24) and (6.36) are substituted into the Cramér-Rao bound (6.31).

$$\Delta a_\Omega \geq \frac{\alpha \hbar \pi^3 \sqrt{2nl}(l^2 - n^2)^2}{16 m N_a \theta \sqrt{L a_s \tau t N_p}(l^2 + n^2)}. \tag{6.37}$$

The number of measurements appearing in (6.31) is determined as $N_m = \tau/t$, where τ indicates the integration time of the complete experiment and t is the duration of a single measurement. Also, the cross-section of the BEC is assumed to be approximately circular $\mathcal{A} = \pi(\alpha L)^2$, where the BEC's radius is determined with respect to the BEC's length L by the dimensionless number α that represents the BEC's length-to-radius ratio.

The precision for estimating a_Ω depends on several parameters, which contain information about the geometry and density of the BEC or the experimental capacities related to the realization of Bose-Eintein condensation. The summary of the set of parameters involved in the expression for the precision is specified in Table 6.1. The value of these quantities is discussed in the next section.

6.5 Experimental Parameters

This section is divided into three parts. The first part reviews the current experimental progress on the Bose-Einstein realisation relevant to this work. Following this review of the experimental state of the art, we determine the potential numerical values of the experimental parameters involved in estimating a_Ω. In the second part, the set of constraints that must be fulfilled for the realisation of our proposal is enlisted and reviewed. Here, we focus on two aspects: first, making sure that the numerical values of the experimental parameters satisfy all the necessary constraints required to achieve our experimental proposal, and second, demonstrating that our proposal is realisable with the current technology and experimental progress. Finally, in the third part, we explicitly evaluate the precision for measuring a_Ω and discuss the behaviour of Δa_Ω with respect to the most relevant experimental parameters, such as the BEC's length or the number of condensed atoms.

Precision Experimental Parameters	
Parameter	Symbol
Length	L
BEC length-to-radius ratio	α
Number of condensed atoms	N_a
Number of phonons	N_p
Mode numbers	l, n
Single-measurement time	t
Time of experiment	τ
^{87}Rb mass	m
^{87}Rb scattering length	a_s
Tritter coupling	θ
BEC density	ρ_0
Speed of sound	c_s

Table 6.1: Precision Experimental Parameters. Parameter dependence of the precision considering a ^{87}Rb BEC and other relevant derived parameters.

6.5.1 State-of-the-art Experimental Parameters

This proposal considers a Bose-Einstein condensate composed of ^{87}Rb atoms. Although other atomic species, such as ^{23}Na or ^{7}L, could be used to create a BEC, ^{87}Rb has been chosen as a representative example since no atomic species offers a clear advantage for this work compared to the others. The ^{87}Rb atoms have a mass of $m = 1.44 \times 10^{-25}$ kg and a reported scattering length of $a_s = 99\, r_B$ [141], where $r_B \simeq 5.29 \times 10^{-11}$ m is the Bohr radius.

First, let us focus on the geometry required for our experiment. Our proposal assumes a one-dimensional BEC trapped by a uniform potential. This configuration has been successfully achieved by [120], which created an atomic BEC held in a uniform three-dimensional potential with cylindrical geometry. Typically, BECs are created using harmonic trap potentials, which exhibit a cigar-shaped geometry. Interestingly, the authors of [121] discovered a 3D-to-1D transition in the phonon dispersion relation for cigar-shaped BECs, where we estimated a length-to-radius ratio $\alpha \simeq 0.1$ in their experiment from the ratio of axial to radial frequencies. This finding is particularly significant since there is no Bose-Einstein condensation mechanism for a strictly one-dimensional Bose gas. Instead, 3D-to-1D transitions can lead to quasi-1D BECs where the Gross–Pitaevskii equation is approximately one-dimensional. Therefore, a length-to-radius ratio $\alpha \leq 0.1$ is assumed for this work.

Another important parameter related to the BEC's shape is its size. The typical lengths reported for BECs have a wide range, going from approximately 50 μm to 1000 μm [142, 143].

Next, let us consider the number of condensed atoms N_a. Due to the tritter implementation, the precision for measuring a_Ω scales as $1/\sqrt{N_p N_a}$ instead of the $1/N_p$ dependence that would have been obtained had the tritter not been applied, where $N_p \ll N_a$. Therefore, a larger N_a will improve our proposal's precision. The reported number of condensed atoms ranges from 1.6×10^3 to 1.1×10^9 atoms [144, 145, 146].

To determine the duration of a single measurement, we must consider the half-life of both the BEC and the phonons. It has been demonstrated in [73, 147] that three-body recombination processes primarily determine the BEC's half-life, that is, three-atom collisions occurring within the BEC. These processes result in a decay rate for the BEC's density given by

$$\frac{d\rho_0(t)}{dt} = -D\rho_0^3(t), \tag{6.38}$$

where D is the decay constant. From this expression, the half-life of the BEC is determined as

$$t_{\mathrm{hl}} = \frac{3}{2D\rho_0^2}. \tag{6.39}$$

For ^{87}Rb atoms, it has been reported that $D = 5.8 \times 10^{-30}$ cm^6 s^{-1} [148]. Assuming a density within the typical order of magnitude for rubidium BEC experiments, $\rho_0 = 10^{14}$ cm^{-3}, leads to a BEC half-life of $t_{\mathrm{hl}} \approx 10$ s.

The phonon's half-life is governed by two-body decay processes, which include the Landau and Beliaev dampings [149, 150, 151]. Considering a uniform BEC at temperatures $k_B T \ll \hbar\omega_n$, the dominant effect is the Beliaev damping, where a phonon scatters into two lower-energy phonons. Conversely, at temperatures such that $k_B T \gg \hbar\omega_n$, the dominating process is the Landau damping, corresponding to a two-phonon interaction that results in a single higher-energy phonon. The relevant temperature regime for our case is when the thermal energy of the BEC is smaller than the BEC's chemical potential, $k_B T \ll \mu$, ensuring the thermal energy does not generate fluctuations in the number of atoms of the BEC. In this temperature regime, the Landau damping rate for the n phonon mode is given by

$$\gamma_n^{\mathrm{La}} = \frac{3\pi^3}{40} \frac{(k_B T)^4 \omega_n}{m \rho_0 \hbar^3 c_s^5}, \tag{6.40}$$

where k_B is the Boltzmann constant. Assuming a temperature $T = 1$ nK and the experimental parameters considered in this work, γ_n^{La} is of the order of magnitude of $\sim 10^{-6}$ s^{-1}. The Beliaev damping rate is found to be even smaller. In accordance with previous work, [152], we notice that the three-body recombination drives the main decay process and gives an upper bound for the time of the experiment.

Taking into account the phonon's mode numbers, the functional dependence of Δa_Ω in (6.37) indicates that smaller mode numbers enhance the precision. Moreover, larger mode numbers may be challenging to populate and resolve in a single direct measurement due to the short phonon lifetimes. Therefore, it is convenient to consider small mode numbers; specifically, the values $l = 2$ and $n = 1$ are chosen.

The number of squeezed phonons is set to $N_p = 1100$, following the analysis conducted in [153], which corresponds to a squeezing factor of $r \approx 3.8$ (~ 30.4 dB). While squeezing is well-established for photons in quantum optics [70, 154] and for phonons in quantum optomechanical systems [155, 156], the controlled creation and precise measurement of squeezed phonons in BECs remains under research [128, 129]. Phonons in BECs can be experimentally generated and squeezed by changing the atom-atom interactions or by periodically moving the trap boundaries, using an atomic version of the dynamical Casimir effect [128, 153] and, theoretically, high levels of phonon squeezing are possible [153, 157, 158]. Work carried out in [159] reports achieving a phonon squeezing factor of $r \approx 1.33$ (~ 8 dB) for spin-squeezed states in a BEC, therefore, further research is necessary to reproduce these levels consistently in the laboratory.

A separate comment must be made regarding the experimental parameters of the oscillating mass, as the precision in estimating the acceleration amplitude is independent of these parameters. This can be explained by the fact that the BEC phonons respond to the acceleration they experience, regardless of the details of the gravitational source that induces such acceleration. Therefore, we defer the discussion of the value of the oscillating mass's parameters to the end of Section 6.5.3.

6.5.2 Conditions and Constraints

Throughout the derivations for the evolution of the BEC's phonons, resulting in (6.23), and for the precision to measure a_Ω, yielding (6.31), several conditions and constraints have been assumed and imposed on the system. These have been carefully considered when selecting the experimental parameters to ensure Bose-Einstein condensation and consistency with theoretical and experimental requirements [86]. A summary of these concerns is provided here.

1) To achieve the Bose-Einstein condensation, the Bose gas must remain in the dilute regime

$$\rho_0|a_s|^3 \ll 1, \tag{6.41}$$

2) and the Bogoliubov approximation must be satisfied

$$N_{\mathrm{exc}} \ll N_a, \tag{6.42}$$

where the number of excited atoms related to the phonon mode n can be approximated as

$$N_{\mathrm{exc}} \approx (mc_s^2/\hbar\omega_n)N_p. \tag{6.43}$$

3) The modes l, n must fulfil the relation

$$\hbar\omega_{l,n} \ll mc_s^2. \tag{6.44}$$

to guarantee that the excitations are within the phonon regime,

4) and the sum $l+n$ must be odd, following the resonance condition $\omega_l+\omega_n = \Omega$.

5) The condition for the low-temperature regime,

$$k_B T \ll \mu, \tag{6.45}$$

should be satisfied. This is the case for typical experiments, where temperatures can reach down to 0.5 nK for ^{87}Rb BECs [136].

6) The BEC's density must be sufficiently low to maximize the BEC's half-life,

$$t_{\mathrm{hl}} = \frac{3}{2D\rho_0}. \tag{6.46}$$

7) The length-to-radius ratio α must be sufficiently low, ensuring that the shape of the BEC remains within the one-dimensional approximation. The ratio can be expressed as

$$\alpha = \sqrt{\frac{N_a}{\pi \rho_0 L^3}}. \tag{6.47}$$

Taking into account the results in [121], values $\alpha < 0.1$ are considered.

8) The tritter angle must satisfy the inequality

$$\theta \leq \frac{1}{2} \arccos\left(\frac{\delta\gamma + 2\delta - 3\gamma - 2}{\delta\gamma + 2\delta + \gamma - 2}\right). \tag{6.48}$$

For instance, taking $\delta = 0.1$ and the limit $\gamma \to 0$, the value $\theta = 0.31$ is obtained.

In this thesis, we do not aim to optimize the values of the experimental parameters to maximize the precision. This is expected to be achieved by using specialized numerical methods in later works. In the Appendix D, a Wolfram Mathematica program is provided, where the precision Δa_Ω is numerically evaluated, and the conditions and constraints are numerically verified.

6.5.3 Precision: Parameter Dependence and Evaluation

Now that we have established the possible values for the set of parameters determining the precision Δa_Ω, displayed in Table 6.1, by first considering the current experimental progress and second the conditions and constraints required by the assumptions of the proposal, we next turn to analyse the behaviour of the precision with respect to key parameters such as the length of the BEC or the number of condensed atoms.

First, let us consider the parameters that cannot be tuned in the experiment. The mass of the atoms m and the scattering length a_s are determined by the selection of the atom species. While the scattering length can be altered through magnetic and optical tuning of Feshbach resonances [160], this changes the density of the condensate and involves the manipulation of magnetic and optical fields, which can affect other properties of the BEC, thereby complicating the control of the experimental constraints and conditions. This issue lies outside the scope of this thesis, so we will consider the default scattering length value for ^{87}Rb. Additionally, the tritter's coupling constant θ, limited by (6.48) to a small value that cannot be significantly optimized, gets fixed by selecting the value of δ in that bound. Finally, the length-to-radius ratio α gets fixed by the number of condensed atoms and by the BEC's density and length, as established by (6.47). Therefore, these quantities contribute negligibly to the final value of Δa_Ω.

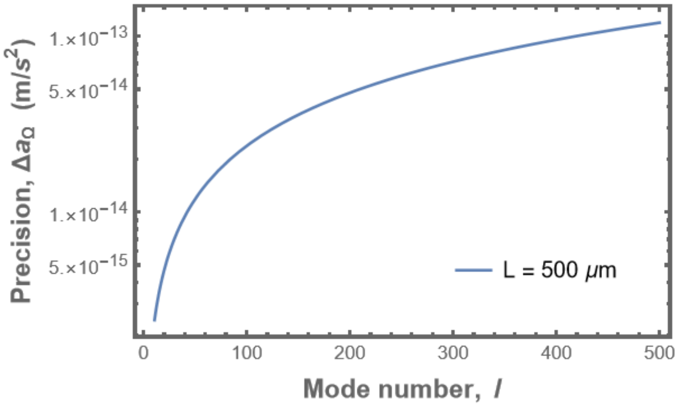

Figure 6.6: Precision vs. Mode Number. Precision Δa_Ω as a function of the phonon mode number l. Lower mode numbers improve the precision. Example presented: BEC with length $L = 500\ \mu$m, number of condensed atoms $N_0 = 10^8$, density $\rho_0 = 10^{14}\ \text{cm}^{-3}$. The rest of the parameters are fixed accordingly with Table 6.2.

We now proceed to examine the parameters that make a significant contribution. The precision is enhanced as the time taken for a single experiment t and the total duration of the experiment τ increase. The aim is then to encourage the experimental improvement of the lifetimes of the BEC and phonons to achieve longer experimental durations. The precision dependence with respect to the mode number is displayed in Figure 6.6. For a BEC of length $L = 500\mu$m, number of condensed atoms $N_a = 10^8$, and density $\rho_0 = 10^{14}\ \text{cm}^{-3}$, the plot indicates that the precision is better for lower phonon mode numbers. Thus, selecting the mode numbers $l = 2$ and $n = 1$ represents the optimal choice.

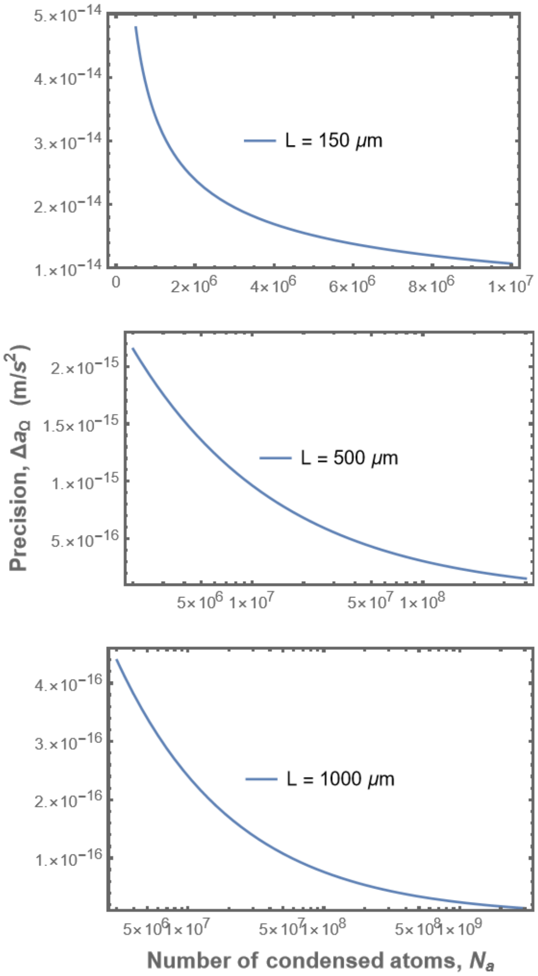

Figure 6.7: Precision vs. Number of Condensed Atoms. Precision Δa_Ω as a function of the number of condensed atoms for three different BEC's lengths: 150 μm, 500 μm, 1000 μm. The density is set to $\rho_0 = 10^{14}$ cm^{-3}, with the remaining parameters following Table 6.2.

The precision of the BEC in measuring the acceleration amplitude a_Ω as a function of the number of condensed atoms N_a is illustrated in Figure 6.7. In this plot, we considered three different lengths for the BEC (150 μm, 500 μm, 1000 μm). The results indicate that the precision is enhanced for longer BECs, which provide a larger interaction region. Similarly, the precision improves with a greater number of condensed atoms. The tritter transformation is crucial for this, as it mixes the condensed atoms with the phonon states, involving a significantly large number of atoms in the experiment that strengthens the correlation in the phonon states.

In Figure 6.8, we present a logarithmic surface plot of the precision Δa_Ω as a function of both the BEC's length and the number of condensed atoms. From Figure 6.7 and Figure 6.8, we can see that the precision improves simultaneously for larger BECs and a greater number of condensed atoms in all cases. However, these two parameters cannot be increased independently due to the various conditions and constraints previously discussed. This indicates that if we wish to increase the number of condensed atoms, we must also increase the size of the BEC in accordance with the constraints required by the system, such as remaining within the dilute regime or the one-dimensional regime of the BEC.

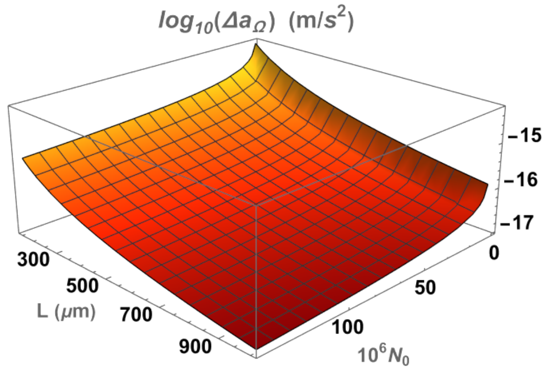

Figure 6.8: Logaritmic 3D plot of precision Δa_Ω as a function of BEC's length L and the number of condensed atoms N_a. The density is fixed at $\rho_0 = 10^{14}$ cm^{-3}, with the rest of the parameters following Table 6.2.

The degree of freedom exhibited by some of the parameters, along with the relevant conditions and constraints, suggests the existence of an optimal set of values for these parameters that maximizes the precision. Such optimization, likely requiring specialized numerical methods, lies beyond the scope of this thesis and is reserved for future research.

Now we turn to evaluate explicitly the precision to measure the acceleration amplitude a_Ω with our proposal for several cases. We can select a conservative set of values for the parameters that lie within the typical values found in BEC experiments. Let us consider a BEC with $L = 200$ μm, $N_a = 10^6$, $\rho_0 = 10^{14}$ cm^{-3}, for an initial phonon number of $N_p = 100$ and a single-expertiment time of $t = 0.1$ s, where the rest of the parameters follow Table 6.2. Explicit evaluation yields a precision of 6.3×10^{-14} m/s^2, which already enables our proposal to compete with current leading experiments like the Eöt-Wash WEP torsion balance, reporting precisions up to 5×10^{-14} m/s^2 [161, 162, 163].

Conversely, an optimistic set of values can be chosen, which still lies within the values found in BEC experiments, except for the number of phonons. Consider a BEC with parameters $L = 1000\ \mu$m, $N_a = 10^9$, $\rho_0 = 10^{14}$ cm^{-3}, $N_p = 1100$ and $t = 1$ s, where the rest of the parameters follow Table 6.2. Evaluating the precision, we obtain that $\Delta a_\Omega = 7.6 \times 10^{-18}$ m/s^2, which represents a very promising result that, if reproduced in the laboratory, would significantly improve current precisions for measuring accelerations.

In Table 6.2, we present a broad value range for the experimental parameters determining the precision of the experiment, showing how the parameter selection affects the value of the precision. All the results displayed there are consistent with the conditions and constraints established in Section 6.5.2.

Experimental Parameter Ranges							
Parameter	L	N_a	α	t	c_s	Ω	Δa_Ω
Units	μm			s	mm/s	Hz	m/s^2
$\rho_0 = 3 \times 10^{13}$ cm^{-3}	150	10^6	0.05	1	1.02	64.6	1.9×10^{-14}
	500	10^7	0.02	1	1.02	19.4	5.5×10^{-16}
	1000	10^8	0.03	1	1.02	9.7	4.3×10^{-17}
$\rho_0 = 10^{14}$ cm^{-3}	150	10^7	0.097	0.1	1.8	118.1	1×10^{-14}
	500	10^8	0.05	0.1	1.8	35.4	3×10^{-16}
	1000	10^8	0.017	0.1	1.8	17.7	7.6×10^{-17}
$\rho_0 = 10^{15}$ cm^{-3}	150	10^8	0.097	0.01	5.9	373.5	3.3×10^{-15}
	500	10^8	0.015	0.01	5.9	112	3×10^{-16}
	1000	10^8	0.005	0.01	5.9	56	7.6×10^{-17}

Table 6.2: Precision Δa_Ω for measuring the acceleration amplitude induced by an oscillating sphere on a ^{87}Rb BEC. Fixed parameters: experiment duration $\tau = 30$ days, mode numbers $n = 1$, $l = 2$, number of phonons $N_p = 1100$, tritter angle $\theta = 0.31$ and a scattering length $a = 99 r_B$, where r_B is the Bohr radius. The ratio α is determined by Eq. (6.47), and $\Omega = \omega_l + \omega_n$ is the resonant frequency between the phonons and the oscillating sphere.

To better understand the role of the two-mode squeezing and the tritter transformation in the preparation of the probe state (cf. Section 6.4.1) for enhancing the parameter estimation, we compare the resulting precision Δa_Ω for three scenarios: i) the full protocol including two-mode squeezing and tritter transformation, ii) a partial protocol dismissing the tritter and considering only the two-mode squeezing transformation given by Eq. (6.25), and iii) the case where both the tritter and the two-mode squeezing transformations are dismissed, i.e., considering only two vacuum phonon modes directly interacting with the gravitational potential.

Let us consider a representative set of parameters from Table 6.2, for example, a BEC with density $\rho_0 = 10^{14}$ cm^{-3} and length $L = 500$ μm, for $N_a = 10^8$ condensed atoms. We find that i) the full protocol yields a precision of $\Delta a_\Omega \sim 10^{-16}$ m/s^2, which follows from Eq. (6.37). The precision Δa_Ω can be derived using Appendix C or starting from Eq. (6.32) for ii) the partial protocol by taking $\theta = 0$ to take out the tritter transformation, to obtain

$$\Delta a_\Omega \geq \frac{\alpha\hbar\pi^3\sqrt{nl}(l^2-n^2)^2}{4m(N_p+1)\sqrt{La_s\tau t N_a}(l^2+n^2)}, \tag{6.49}$$

yielding $\Delta a_\Omega \sim 10^{-14}$ m/s^2. In contrast, the case iii) dismisses the squeezing and the tritter by taking $r = 0$ and $\theta = 0$ in Eq. (6.32), which subsequently leads to

$$\Delta a_\Omega \geq \frac{\alpha\hbar\pi^3\sqrt{nl}(l^2-n^2)^2}{2m\sqrt{La_s\tau t N_a}(l^2+n^2)}, \tag{6.50}$$

yielding a much less favorable precision of $\Delta a_\Omega \sim 10^{-10}$ m/s^2. This comparison highlights the critical enhancement achieved by the appropriate selection of the probe state. By incorporating the two-mode squeezing and tritter operations, the full protocol achieves a six-order-of-magnitude improvement in Δa_Ω over the vacuum phonon modes case.

Before concluding this chapter, let us consider the experimental realization of the oscillating mass. Notice that the nature of the oscillating sphere does not influence or affect the precision Δa_Ω. It is experimentally possible to accelerate a mass with an exact sinusoidal dependence on time, similar to that outlined in Section 6.2. Let us consider two specific examples to illustrate values that can be found in current experiments.

First, we refer to the work presented in [164], which discusses a levitating magnetic sphere of mass $M = 4$ mg and radius $r = 0.5$ mm that oscillates with an amplitude $\delta_R = 0.5$ mm and frequency $\Omega = 30$ Hz. Additionally, we can consider the proposal presented in [114] for a tungsten or gold sphere of mass $M = 200$ g, radius $r = 14$ mm, and an oscillation amplitude of $\delta_R = 2$ mm. Related to the experimental realization of the oscillating mass, the most important parameter is the capacity of matching the frequency that resonates with the phonons. From Table 6.2, we can see that the required frequencies range from a few to hundreds of Hz, which lie within the typical ranges achieved by oscillating massive spheres.

In the next chapter, we explore the oscillating sphere's gravitational potential outside the framework of Newtonian gravity. Instead, we consider two alternative models that modify gravity in the Newtonian regime: MOND and Lambda gravity.

Chapter 7

Testing Modified Theories of Gravity

Having established in Chapter 6 our experimental proposal for estimating the gravitational potential of the oscillating sphere—encoded in the acceleration amplitude—employing the phonons in the BEC, this chapter focuses on implementing the experiment to test deviations from Newtonian gravity. Specifically, we assume that the gravitational potential of the oscillating sphere is fundamentally described by a modified gravity framework, considering two cases: Modified Newtonian Dynamics (MOND) and Lambda-gravity.

This chapter is organized as follows. In Section 7.1, we motivate the origin and exploration of modified theories of gravity, primarily driven by the 'missing mass problem', commonly known as the dark matter problem. Section 7.2 introduces Modified Newtonian Dynamics (MOND), a framework that suggests a change to the Newtonian gravitational force effective for accelerations below the $\sim 10^{-10}$ m/s^2 threshold. Following MOND, we derive the gravitational potential of the oscillating sphere and the theoretical prediction for the value of the acceleration amplitude, which is then compared to the Newtonian prediction. Section 7.3 presents Lambda-gravity, an extension to Newtonian gravity that, supported by the Gurzadyan theorem, incorporates an additional term that depends on the cosmological constant. In accordance with Lambda-gravity, the gravitational potential of the oscillating sphere and the predicted value of the acceleration amplitude are derived. To test this prediction, we estimate the precision for measuring Newton's gravitational constant G and the cosmological constant Λ, both of which determine the strength of the two terms in the modified gravitational force. Finally, these precisions are compared with the current state-of-the-art experimental accuracies.

7.1 Motivation for Modified Theories of Gravity

7.1.1 Dark Matter

Numerous astrophysical and cosmological observations pose an important challenge to our understanding of the Universe. When the observational data gathered by our telescopes is compared with the theoretical predictions of General Relativity, including its Newtonian limit, discrepancies arise. The measurements of the rotation curves of galaxies [165, 166] and the velocity dispersion profiles of galaxy clusters [167] exhibit a behaviour that differs from the curves predicted by theoretical models based on the observed mass distributions. The data collected via gravitational lensing of galaxies and galaxy clusters, as well as data characterizing the large-scale structure of the universe [168, 169], assuming General Relativity, imply a matter content and distribution which differs from the observed one. Additionally, the origin of the acoustic peaks observed in the cosmic microwave background (CMB) angular power spectrum [170, 171] and the baryonic vs non-baryonic matter density—the baryonic abundance—observed in the universe [172] cannot be explained without making extra assumptions. The conflict between these observations and the theoretical predictions is broadly known as the 'missing mass problem'.

The simplest solution to the problem is to postulate the existence of missing matter: dark matter. Another possible solution is to assume that the current theories of gravity need to be modified. The answer seems to lie within this non-necessarily exclusive dichotomy [173]. The community has favoured the proposal of the existence of dark matter. However, no conclusive evidence has been found pointing out its precise nature and features, and "its existence remains hypothetical" [174, 175].

Since its conception, one of the leading proposals for modified gravity at the non-relativistic, low-velocity limit has been Milgrom's Modified Newtonian Dynamics (MOND) [176]. Based on the phenomenology of galaxy rotations, MOND proposes a modification of Newtonian gravity, which is valid for small accelerations in the regime $a \lesssim 10^{-10}$ m/s^2. Several astronomical observations are consistent with MOND and confirm some of its predictions at galactic scales. Such observations include the details of galactic rotation curves across galactic types and masses, galactic disk stability, and the Tully-Fisher relation [174, 177, 178]. Conversely, MOND struggles to reproduce the dynamics of galaxy clusters and is not applicable for cosmological or lensing problems which require a covariant treatment [179, 180]. More recently, the internal dynamics of wide binary stars observed by the *Gaia* satellite demonstrate consistency with MOND predictions [181, 182]. Interestingly, hybrid theories such as dark matter superfluid have been developed, which match the ΛCDM model at cosmological scales and reproduce MOND phenomenology at galactic scales [183, 184].

The search for empirical evidence of MOND has focused on astronomical and cosmological scales. However, some Earth-bound tests have also been conducted. Torsion pendulum experiments have confirmed Newton's second law down to 10^{-14} m/s^2 for torque restoring induced accelerations [162] and down to 10^{-12} m/s^2 for gravitational induced accelerations [163]. These results do not contradict MOND, as the acceleration dependence of the theory implies a violation of the strong equivalence principle. Even for free-falling observers in the presence of an external field, its behaviour is expected to depend on both the system's internal acceleration and any external gravitational field. This effect is known as the *external field effect* (EFE). It suggests that when an external field larger than the a_0 scale is present, modifications to Newtonian expectations are significantly suppressed, particularly in Earth-bound experiments [176]. In addition to the torsion pendulum experiments, recent work proposes to test the isolated system limit of MOND using the gravitational attraction between two levitating magnets [164], expecting to probe MOND at accelerations as low as 10^{-13} m/s^2.

Quantum technologies present a great opportunity for tabletop experiments thanks to the development of ultra-high-precision quantum sensors [92]. This progress has significantly impacted the search for dark matter, which has inspired exploration proposals that take advantage of optomechanical systems [185], atom interferometry [186], and Bose-Einstein Condensates [17]. Despite these advances, efforts to test MOND in tabletop experiments remain limited.

Our proposal contributes to filling that gap by proposing a frequency interferometric scheme to test gravity at a_0 scales with accuracy levels not explored before and search for evidence of MOND.

7.1.2 Dark Energy

The ΛCDM model represents the current standard cosmological model due to its outstanding agreement with the cosmological observations [187]. One of the main components of the model is the cosmological constant Λ, often associated with the dark energy content of the universe.

The role of the cosmological constant is well established within the ΛCDM model. This model assumes the cosmological principle and describes the universe by considering a Friedmann–Lemaître–Robertson–Walker metric. The evolution of the universe is characterised by an expanding universe whose expansion is driven, in its simplest form, by the cosmological constant. Observations analysing the rate of expansion of the universe estimate that the value of the cosmological constant is $\Lambda = (1.09 \pm 0.028) \times 10^{-52}$ m^{-2}, as reported by the Planck experiment [188]. Although the value of Λ is well established for astrophysical and cosmological observations, there are currently no Earth-based experiments aimed at measuring the value of Λ in a laboratory setting.

The physical interpretation of Λ can be extended beyond the role of a parameter in the ΛCDM model. In the light of Gurzadyan theorem [189], it can be considered a fundamental constant of nature. This theorem generalises the Newtonian gravitational force into a model known as Lambda-gravity by adding an extra term to Newtonian gravity, which is proportional to the cosmological constant. In this way, the model concludes that two terms determine Newtonian gravity, each proportional to a fundamental constant, G and Λ.

We propose to measure the gravitational force established by Lambda-gravity by estimating the values of the G and Λ terms. Our proposal represents the first Earth-based tabletop experiment to bound the value of Λ. Its measurement would serve as a confirmation of its role as a fundamental constant and as the main source of the dark energy driving the expansion of the universe. Additionally, studies indicate that dark matter could also be explained by using Lambda-gravity [190].

In the following sections, we provide a brief introduction to MOND and Lambda-gravity and derive the implications these models have on the gravitational potential of the oscillating sphere based on the experiment proposed in Section 6.2.

7.2 Modified Newtonian Dynamics

Modified Newtonian dynamics (MOND) [191] is a hypothesis that proposes a modification of Newtonian gravity at extremely small accelerations, below $\sim 10^{-10}$ m/s^2, characteristic of galactic systems and the universe at large scales. Introduced in 1983 by M. Milgrom [176], its original motivation was to explain the velocity distribution of stars observed in galaxies, which could not be reproduced solely with Newton's theory. This discrepancy—which is one of the many included in the 'missing mass problem'—leads to at least one of the following conclusions:

1) There exist in galaxies large quantities of unseen matter which boost the velocities of the stars.
2) Newton's laws do not apply to galaxies.

Milgrom noted that the discrepancy could be solved if the gravitational force experienced by a star in the outer regions of a galaxy was proportional to the square of its centripetal acceleration. In MOND, violation of Newton's laws occurs at extremely small accelerations, which is characteristic of galactic systems and the universe at large.

The basic premise of MOND is that Newton's laws—extensively tested in high-acceleration environments on the Earth and in the Solar System—have not been verified for objects with extremely low accelerations, such as the stars in the outer part of galaxies. This premise leads to the keystone of MOND: the postulation of a new phenomenologically oriented effective gravitational law, chosen to reproduce the Newtonian result at high acceleration but leading to different behaviour at low acceleration. MOND proposes that, for isolated systems, the force is given by,

$$F_{\mathrm{N}} = m\mu\left(\frac{a}{a_0}\right)a, \tag{7.1}$$

where F_{N} denotes the Newtonian force, m and a are the object's (gravitational) mass and acceleration, and μ is an interpolating function. MOND introduces a new fundamental constant, $a_0 \approx 1.2 \times 10^{-10}$ m/s^2, that marks the transition between the Newtonian regime ($a \gg a_0$) and the deep-MOND regime ($a \ll a_0$) and whose value is set by astronomical observations.

The interpolating function is required to satisfy

$$\mu\left(\frac{a}{a_0}\right) \to 1 \qquad \text{for} \qquad a \gg a_0, \tag{7.2}$$

to agree with Newtonian mechanics at high accelerations. On the other hand, its consistency with astronomical observations at low accelerations requires

$$\mu\left(\frac{a}{a_0}\right) \to \frac{a}{a_0} \qquad \text{for} \qquad a \ll a_0. \tag{7.3}$$

The functional form of μ is not specified by the theory; rather, it is constrained through fits by observational data. The most common functional forms [192] tested for the interpolating function are the 'simple' form

$$\mu\left(\frac{a}{a_0}\right) = \frac{1}{1+\frac{a_0}{a}}, \tag{7.4}$$

and the 'standard' form

$$\mu\left(\frac{a}{a_0}\right) = \frac{1}{\sqrt{1+\left(\frac{a_0}{a}\right)^2}}, \tag{7.5}$$

often parameterized as $\mu(z) = 1/(1+z^{-n})^{1/n}$ for an effective index n, which is determined within the acceleration range and external field effect regime of a particular observation. However, additional alternative functional forms for μ exist.

Therefore, in the Newtonian regime, $a \gg a_0$, Newton's second law is recovered, and in the deep-MOND regime, $a \ll a_0$, we have

$$F_{\mathrm{N}} = m\frac{a^2}{a_0}. \tag{7.6}$$

Since the dynamics established by MOND are non-linear in the acceleration, in this model, subsystems cannot be decoupled from their environment, leading to the external field effect (EFE). Let us consider a system with internal acceleration $a < a_0$, which is embedded in the presence of an external acceleration field a_e. If the external acceleration is considerably larger than a_0, then MOND effects are expected to be suppressed by a factor $(a_0/a_e)^n$ [176, 192]. The isolated MOND limit assumes the system under study is free from any external acceleration field.

In the following subsection, we derive the predictions for our experiment in the isolated MOND limit and discuss the direct detection of MOND while considering the EFE.

7.2.1 Predictions

We propose to experimentally explore MOND by studying the gravitational effects on the phonons of a BEC produced by a nearby oscillating massive sphere. In particular, we examine how MOND modifies the gravitational potential of the oscillating sphere and compare MOND's predictions with those made by Newtonian gravity. By incorporating the tritter operation, we enhance the sensitivity to measure accelerations by two orders of magnitude compared to [114]. As demonstrated in Section 6.5.3, this scheme allows us to probe gravity at a_0 scales with an accuracy level of 10^{-17} m/s^2. Although the EFE might suggest that, for Earth-bound experiments, the leading variants of MOND lie beyond this accuracy, the experiment would provide constraints on any gravity theory at a_0 scales, significantly improving the precision at which this regime has been measured.

In the case of the isolated system limit in MOND, the gravitational force exerted by the oscillating sphere on the BEC is modified according to Eq. (7.1). From it, we can calculate the MOND gravitational potential ϕ_M as

$$\phi_\mathrm{M} = \frac{1}{m}\int \vec{F}\cdot d\vec{r}, \tag{7.7}$$

where m is the mass of the BEC. Recalling the experimental setup established in Section 6.2, we now derive the oscillating sphere's gravitational potential predicted by MOND. Given the small BEC approximation, $L \ll R$, and the small oscillation amplitude approximation, $\delta_R \ll R_0$, considered on the experimental setup, the induced acceleration $a(t)$ on the BEC by the oscillating sphere is only a time-dependent quantity, as shown in (6.1). Therefore, under these approximations, we assume that the interpolating function becomes independent of the position. This implies that (7.7) can be simply integrated, yielding that the MOND gravitational potential ϕ_M is proportional to the Newtonian gravitational potential, $\phi_\mathrm{M}(x,t) = \mu(a/a_0)\,\phi(x,t)$. For the small BEC approximation, $x/R \ll 1$, we obtain that

$$\phi_\mathrm{M}(x,t) \approx -\frac{GM}{\mu\left(\frac{a}{a_0}\right)R(t)} + \frac{GM}{\mu\left(\frac{a}{a_0}\right)R(t)^2}\,x, \tag{7.8}$$

where M is the mass of the sphere and G is Newton's gravitational constant. Recall the sphere is assumed to move sinusoidally, $R(t) = R_0 + \delta_R\sin(\Omega t)$. Then, under the small oscillation amplitude approximation, $\delta_R/R_0 \ll 1$, the induced acceleration on the BEC predicted by MOND can be written as

$$a(t) = \frac{GM}{\mu\left(\frac{a}{a_0}\right)R_0^2} - \frac{2GM}{\mu\left(\frac{a}{a_0}\right)R_0^2}\cdot\frac{\delta_R}{R_0}\sin(\Omega t), \tag{7.9}$$

where the amplitude of the time-oscillating term of the induced acceleration predicted by MOND can be identified as

$$a_{\mathrm{M}} = \frac{2GM\delta_R}{\mu\left(\frac{a}{a_0}\right)R_0^3}. \tag{7.10}$$

Deviations from standard Newtonian gravity originating from MOND must be reflected in the experimental measurement of the acceleration amplitude a_Ω, which should match the value a_{M} predicted by MOND.

7.2.2 Results

Consider the experimental setup described in Section 6.2. To evaluate the performance of our estimation procedure, we generate data that emulate experimental measurements a_Ω^{exp} of the acceleration amplitude induced on the BEC by the oscillating mass. For a set of distances R_0, we first compute the theoretical predictions a_M^{th} for the acceleration amplitude assuming MOND, taking the 'simple' form of the interpolating function μ in the isolated system limit. Then, we add Gaussian-distributed noise to each of these theoretical values to mimic the experimental uncertainty. The magnitude of the noise is determined by the theoretical sensitivity Δa_Ω, obtained from our scheme. Specifically, the standard deviation of the added noise is equal to Δa_Ω, which represents the minimal detectable change in the acceleration amplitude under our scheme.

These simulated data allow us to evaluate the robustness of our fitting procedure and to test whether the gravitational signal predicted by MOND could be distinguished from a purely Newtonian prediction. For comparison, we also generate simulated data assuming the dynamics remain Newtonian.

The top panel of Figure 7.1 presents the results of six independent measurements of a_Ω at varying distances. Each yellow dot represents a simulated measurement based on MOND dynamics, while blue dots correspond to Newtonian gravity. To obtain these simulated measurements, we took into account the theoretical predictions of each gravity model and added noise equal to the experimental precision Δa_Ω. We interpret the resulting quantity as the measured acceleration amplitude a_Ω^{exp}. The solid lines represent fitted curves to the individual measurements for both theories.

The middle panel of Figure 7.1 illustrates the relative deviation of the simulated measurement, a_Ω^{exp}, with respect to the MOND theoretical prediction, a_M^{th}, represented by the yellow dots. This is compared to the relative precision, $\Delta a_\Omega / a_M^{th}$, for estimating the acceleration amplitude predicted by MOND, indicated by the yellow dashed line. The bottom panel of Figure 7.1 presents a similar analysis of the Newtonian prediction of the acceleration amplitude, a_N^{th}.

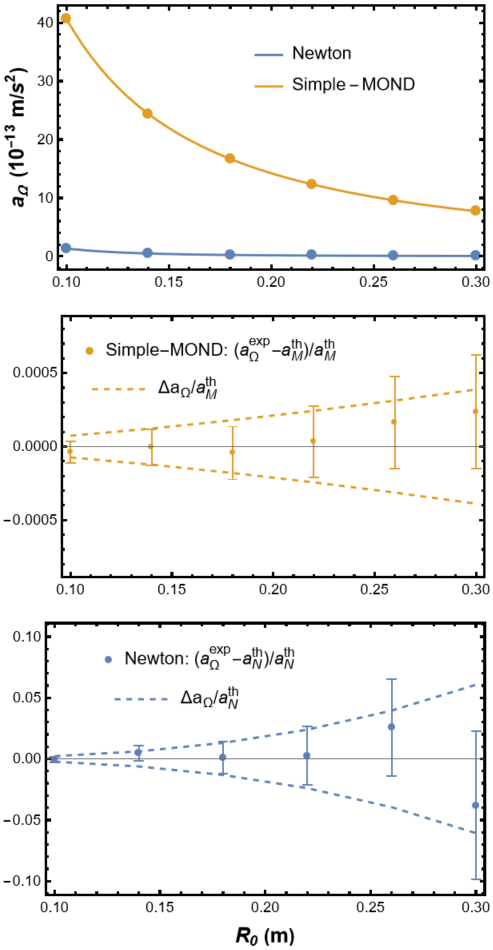

Figure 7.1: Simulated Experiment to Test MOND. Top: Simulated experimental measurements of a_Ω as a function of R_0 following the MOND prediction (yellow dots) and the Newtonian prediction (blue dots). The solid lines correspond to the fitted acceleration curves. Middle and Bottom: Relative deviation (dots) of the simulated experimental acceleration amplitude measurements a_Ω^{exp} from the theoretical prediction a^{th}, and relative precision $\Delta a_\Omega / a^{\text{th}}$ (dashed lines) for MOND (yellow) and Newton (blue). We assume $\Delta a_\Omega = 3 \times 10^{-16}$ m/s^2, and a sphere of mass $M = 1$ g, with an oscillating amplitude $\delta_R = 1$ mm.

From these results, we observe that the relative precision $\Delta a_\Omega / a_\Omega^{\text{th}}$ degrades as the distance between the BEC and the oscillating sphere increases. This is because gravity gets weaker, and the value of a_Ω^{th} decreases. Across the range of explored distances, between 10 cm to 30 cm, we achieve relative precisions of the order of magnitude of $\sim 10^{-4}$ to determine MOND and $\sim 10^{-2}$ to determine Newton. These levels of precision allow us to explore deviations from Newtonian gravity within acceleration regimes where MOND is expected to depart from standard Newtonian dynamics. By varying the separation R_0 between the BEC and the oscillating sphere, we can fit the acceleration curves to distinguish between Newtonian gravity and MOND in the isolated limit.

The results in Figure 7.1 also reveal a difference of approximately two orders of magnitude between the acceleration amplitudes predicted by MOND and Newtonian gravity. This difference arises from the nature of the MOND modification. In the deep-MOND regime, where the acceleration of the system is well below the characteristic MOND acceleration $a_0 \sim 10^{-10}$ m/s^2, the gravitational force transitions from a Newtonian scaling $\propto 1/R_0^2$ to a MOND scaling $\propto 1/R_0$, resulting in a slower decay with the distance[1]. Since the experiment operates in the low-acceleration regime and assumes the ‘simple’ form of the interpolating function, the gravitational signal gets effectively amplified. Therefore, MOND predicts a larger value of a_Ω compared to Newtonian gravity.

The enhanced gravitational signal predicted by MOND in our setup is conceptually analogous to MOND’s explanation for the behaviour observed in galactic rotation curves. In galaxies, the outer stars rotate faster than expected based on the visible mass distribution and the assumption of Newtonian gravity. While Newtonian dynamics predict that the orbital velocities decrease with the distance from the galactic centre, observations show that these velocities remain roughly constant, indicating a stronger gravitational pull than what Newtonian predictions suggest. MOND addresses this by modifying the gravitational force law in regimes below the MOND characteristic acceleration a_0, which results in a stronger gravitational interaction compared to Newtonian gravity. This effectively provides the additional gravitational strength required to explain the galactic dynamics without invoking dark matter. In our laboratory setting, the same theoretical framework applies since the experiment is designed to operate within the low-acceleration regime. Here, MOND induces an enhancement of the gravitational strength experienced by the BEC, analogous to that inferred from stellar motion in galaxies.

---

[1] The MOND scaling in the deep-MOND regime can be derived by solving Eq. (7.7) for a, where on the left-hand side of the equation corresponds to the standard Newtonain gravitational force.

As discussed in Section 7.1.1, the most accurate Earth-based tests of MOND to date have reached precisions up to 10^{-14} m/s^2 [162]. In comparison, our proposal significantly enhances this precision by up to three orders of magnitude by reaching precisions up to 10^{-17} m/s^2. This degree of precision opens up new possibilities for testing MOND in tabletop experiments.

It was previously noted that in the presence of the EFE, deviations between Newtonian and MOND dynamics scale as $a_0(a_0/a_e)^n$, where the parameter n is typically constrained by astrophysical observations. Since no definitive theory for MOND has been developed, there is currently no robust prediction of how the EFE might operate at the scales of Earth-bound experiments. However, our results indicate that the precision achieved by our setup enables us to detect MOND signatures even in the presence of external accelerations for values of $n \lesssim 0.7$. Additionally, alternative interpretations of MOND based on 'modified inertia' —as opposed to the standard modified gravity framework—may further suppress the EFE, making deviations from Newtonian gravity easier to detect in our setup.

Our analysis demonstrates the great potential of employing BEC phonons as a high-precision probe for testing MOND in controlled laboratory conditions. The achieved precisions represent a considerable improvement over current Earth-based experimental constraints, enabling us to explore MOND predictions in regimes where deviations from Newtonian gravity become significant. Furthermore, our findings indicate that even in the presence of external accelerations, the proposed experiment could still detect MOND effects.

7.3 Lambda-Gravity

Lambda-gravity arises as a natural generalization of the Newtonian gravitational force based on the Gurzadyan theorem [189], and its main conclusion is that gravity is described by two fundamental constants: Newton's gravitational constant G and the cosmological constant Λ.

The Gurzadyan theorem establishes the most general function satisfying the first statement of Isaac Newton's shell theorem, the equivalence of the gravitational forces produced by a spherical mass distribution and a point mass located in its centre while dismissing the second statement, the absence of gravitational forces inside a hollowed massive spherical shell. This leads to the appearance of an extra term in the gravitational force, which involves the cosmological constant Λ within the weak-gravity limit of General Relativity [189]

$$F = -\frac{GMm}{r^2} + \frac{c^2 \Lambda m r}{3} \ , \tag{7.11}$$

corresponding to the metric [193, 194]

$$g_{00} = -1 + \frac{2GM}{c^2 r} + \frac{\Lambda r^2}{3}, \tag{7.12}$$

where G is Newton's gravitational constant and c is the speed of light. The second term of the metric is related to the usual Newtonian gravitational potential, and the third one corresponds to the cosmological constant term from general relativity and the McCrea-Milne cosmology [195].

Then, from the Gurzadyan theorem, Λ arises as a second fundamental gravitational constant along with Newton's gravitational constant, which is not coupled to matter and is dimension-independent [194]. The implications of considering Λ as a fundamental constant of nature were investigated in [196].

Experimentally, the Λ term is well supported by cosmological data in the context of the standard ΛCDM cosmological model. Additionally, it was shown that it fits observational data on the local Universe [193, 194], describes the dynamics of groups and clusters of galaxies [190, 197], and offers an explanation for the Hubble tension [198, 199, 200] by proving the existence of a local and a global Hubble flow [197, 201, 202]. The theorem's prediction of the existence of a force at the centre of a hollowed spherical distribution of mass also fits the observational data on determining the structure of spiral galaxy disks by the spherical galactic halos [203].

Studies have suggested that Lambda-gravity can be used to describe dark matter in galactic systems, ranging from pairs to clusters of galaxies, finding support in observations coming from gravitational lensing and the Plack satellite [190].

7.3.1 Predictions

Similarly to the MOND exploration, we propose to study the gravitational effects on the phonons of a BEC produced by a nearby oscillating massive sphere to experimentally explore Lambda-gravity. In particular, we propose to measure the presence of both terms appearing in (7.11) by estimating the value of G and Λ from the experiment.

Considering the experimental setup established in Section 6.2, the gravitational potential predicted from Lambda-gravity ϕ_Λ associated with the oscillating sphere can be straightforwardly derived from the basic equation established by Lambda-gravity, Eq. (7.11). In the small BEC approximation, $L \ll R$, the potential ϕ_Λ reads

$$\phi_\Lambda(x,t) \approx -\frac{GM}{R(t)} - \frac{c^2 \Lambda R(t)^2}{6} + \left[\frac{GM}{R(t)^2} - \frac{c^2 \Lambda R(t)}{3}\right] x, \tag{7.13}$$

where M is the mass of the sphere, G is Newton's gravitational constant and Λ is the cosmological constant. The sphere is assumed to be moving sinusoidally, $R(t) = R_0 + \delta_R \sin(\Omega t)$. Considering the small oscillation amplitude approximation, $\delta_R/R_0 \ll 1$, the induced acceleration on the BEC predicted by Lambda-gravity is expressed as

$$a(t) = \frac{GM}{R_0} - \frac{c^2 R_0 \Lambda}{3} - \left(\frac{2GM}{R_0^2} + \frac{c^2 R_0 \Lambda}{3}\right) \frac{\delta_R}{R_0} \sin(\Omega t), \tag{7.14}$$

where the amplitude of the time-oscillating term of the induced acceleration is determined as

$$a_\Lambda = \frac{2\delta_R M G}{R_0^3} + \frac{c^2 \delta_R \Lambda}{3}. \tag{7.15}$$

By measuring a_Λ, the values for G and Λ can be estimated. Detecting the presence of the Λ term would demonstrate the Gurzadyan theorem. However, the value of the cosmological constant is minute, of the order of $\Lambda \sim 10^{-52}$ m^{-2} as determined by the Planck satellite [188]. Then, in practice, an upper bound can be placed for the value of Λ with our experimental proposal. The first estimation of Λ from an Earth-based experiment.

7.3.2 Results

Following the approach outlined in Section 7.2.2 for the MOND case, we generate simulated data to emulate measurements of the acceleration amplitude a_Ω induced on the BEC by the oscillating mass. As before, we evaluate the theoretical predictions at a set of distances R_0 and add Gaussian-distributed noise with standard deviation equal to the theoretical sensitivity Δa_Ω to mimic the experimental uncertainty.

However, in this case, we assume the gravitational interaction is governed by Lambda-gravity and use the simulated data to estimate both Newton's gravitational constant G and the cosmological constant Λ through statistical fitting. Unlike the MOND analysis, where we compared two competing models, here we focus on testing whether the experimental setup could determine the presence of a nonzero Λ. A successful estimation of Λ would provide direct evidence supporting the fundamental nature of Lambda-gravity.

The precision for estimating G and Λ can be derived by connecting Eq. (7.15) with the quantum Cramér-Rao bound (6.37), yielding

$$\Delta G = \frac{R_0^3}{2\delta_R M}\,\Delta a_\Omega, \qquad \Delta\Lambda = \frac{3}{c^2\delta_R}\,\Delta a_\Omega \ . \tag{7.16}$$

Let us consider an oscillating sphere of mass $M = 100$ g and oscillation amplitude $\delta_R = 1$ mm. Assuming a precision $\Delta a_\Omega = 4.3\times10^{-17}$ m/s^2, we obtain a relative precision for measuring Newton's gravitational constant of $\Delta G/G = 3\times10^{-6}$. Compared to the current best measurements of G, which exhibit a relative precision of $\Delta G/G \simeq 10^{-5}$ [204], our results suggest that the BEC-based experiment proposed in this thesis represents a potential improvement over existing G measurements.

This precision can be further enhanced by experimentally probing the functional dependence of a_Ω on the distance R_0 and fitting the measurements obtained. We conduct a set of simulated experiments representing the measurement of a_Ω at varying distances R_0. Then, the results are fitted using Eq. (7.15), which provides the Lambda-gravity theoretical prediction. The measurements are simulated by adding noise of size Δa_Ω to the theoretical prediction a_Λ^{th}, resulting in the measured acceleration amplitude a_Ω^{exp}. Figure 7.2 illustrates this analysis.

The top panel of Figure 7.2 displays the results of six independent measurements of a_Ω, represented by blue circles, with the corresponding fit depicted by the solid blue line. The estimated value and uncertainty for G, along with the upper limit on Λ, are also displayed. The bottom panel displays the relative deviation of the simulated measurements a_Ω^{exp} from the Lambda-gravity theoretical prediction a_Λ^{th}, indicated by the blue dots. The blue dashed line represents the relative precision $\Delta a_\Omega/a_\Lambda^{\mathrm{th}}$. The experimental error on a^{exp} is not visible in the top panel since its relative error is approximately $\sim 10^{-6}$.

After performing the statistical fit, we observe an improvement in the precision for estimating G, achieving a relative precision of $\Delta G/G = 8.3\times10^{-7}$. Additionally, we establish an upper limit on the cosmological constant $\Lambda < 1.8\times10^{-31}$ m^{-2}.

These results demonstrate that measuring the acceleration amplitude a_Ω at different values of R_0 not only allows us to probe the functional dependence of the gravitational potential with the distance but also to improve the constraints on G and Λ.

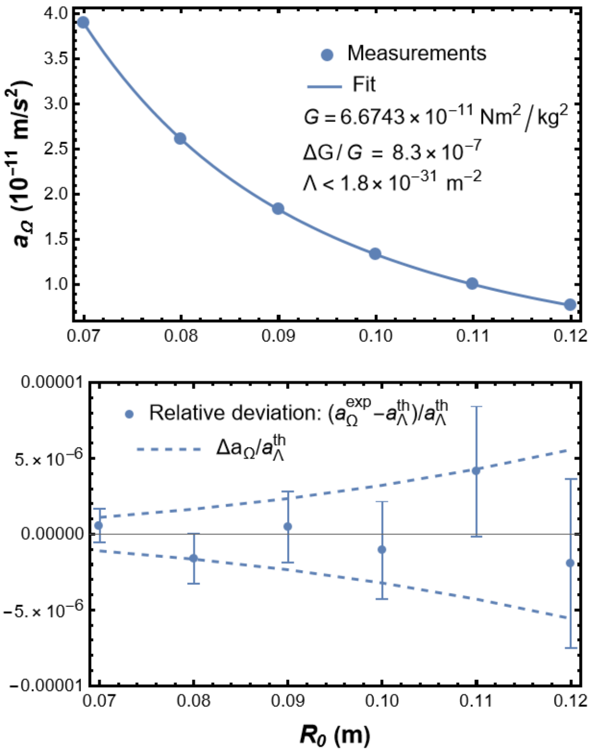

Figure 7.2: Simulated Experiment to Test Lambda-gravity. Top: Simulated measurements of a_Ω at different R_0 values (blue circles). The fitted curve of the measurements (solid blue line) is used to estimate G, indicating the relative precision $\Delta G/G$, and to set an upper bound on Λ. Bottom: Relative deviation of the simulated experimental measurements $a_\Omega^{\rm exp}$ from the theoretical prediction $a_\Lambda^{\rm th}$ (blue circles), along with the relative precision $\Delta a_\Omega / a_\Lambda^{\rm th}$ (blue dashed line). The precision $\Delta a_\Omega = 4.3 \times 10^{-17}$ m/s^2 is assumed, along with a massive sphere of mass $M = 100$ g, with an oscillating amplitude $\delta_R = 1$ mm.

To ensure that the uncertainties ΔG and $\Delta\Lambda$ are primarily determined by Δa_Ω, we assume that the relative experimental precision for measuring δ_R, R_0, and M is better than 10^{-6}. These precision levels are achievable for the parameters considered in our experimental setup, as suggested by CODATA information [204], with the particular caveat that the oscillating mass must be placed in a vacuum to minimize systematic uncertainties in determining M. Given these conditions, it is reasonable to assume that the uncertainties in δ_R, R_0, and M do not introduce significant noise that could limit the precision set by Δa_Ω.

Regarding the measurement of the cosmological constant, our results indicate that the expected precision for estimating Λ is of the order of 10^{-31} m^{-2}, as shown in Figure 7.2. It is important to emphasize that this value should be regarded as an upper limit on Λ. This limit is approximately 20 orders of magnitude below the current best estimation from the Planck experiment, $\Lambda = (1.09 \pm 0.028) \times 10^{-52}$ m^{-2} [188]. Nevertheless, setting such a bound represents an unprecedented level of precision for Λ in Earth-based experiments.

Our analysis demonstrates that the proposed BEC-based experiment provides a promising tool for probing gravity through the estimation of fundamental gravitational parameters, enabling precise measurements of G and imposing constraints on Λ. The improvement in the precision for determining G by two orders of magnitude compared to current methods suggests that this approach could contribute to resolving persistent discrepancies in its experimental determination [205]. Additionally, although our estimated upper limit on Λ remains far above cosmological observations, achieving such a constraint in a laboratory setting is an unprecedented milestone.

These results highlight the potential of quantum systems to improve the precision for performing gravity tests, opening new avenues not only for conducting fundamental research but also for implementing this progress in more practical applications. In the next chapter, we explore how the experimental proposal presented in this thesis—based on the BEC phonons—could be translated into a technological device for gravity measurements, creating new opportunities for commercial applications.

Chapter 8

Technological Implementation & Commercialization Roadmap

The proposal to use the phonons of a Bose-Einstein Condensate to probe gravity, as extensively discussed in this thesis, is highly promising for fundamental research and practical applications. Given its potential, it is essential to consider the technological implementation of this idea and its eventual commercialisation.

Historically, the often unintended impact of theoretical physics research on technological progress has significantly driven scientific progress. Therefore, the translation of theoretical and experimental research into the generation of intellectual property and then into commercially viable technology plays an important role in scientific endeavour.

In this chapter, we present a patent closely related to the proposal constructed in this thesis, as both rely on the same physical principles and share the core ideas and purposes. A Market Analysis of the patent was conducted to explore the transition from a laboratory-based tabletop experiment to a commercially viable technological product. Although the market analysis was conducted for a different experimental setup, the fundamental similarities with the proposal in this thesis allow the straightforward extrapolation of its conclusions.

8.1 USA Patent

During the period dedicated to creating this thesis, the author collaborated with Prof. Ivette Fuentes by supporting the submission process of the USA Patent

Application US20220171089A1 [206], which was successfully granted.

The patent describes a method for measuring the acceleration and gravitational gradient associated with a gravitational field by employing at least two atomic modes within one or more trapped BECs. The density distribution of one atomic mode is altered by the gravitational field, whereas the second remains unchanged. This distinction can be achieved by positioning one BEC along an axis parallel to the gravitational field and the other BEC along an axis perpendicular to it. By analysing the different evolutions of each atomic mode under the influence of the gravitational field, specifically by measuring the difference in the frequencies of the modes, the acceleration and gravitational gradient can be inferred.

While the method described in the patent differs from the approach proposed in this thesis, both proposals are founded on the same physical system: the BEC, and the same physical principle: the phonon evolution under the influence of an external gravitational field. The main distinction between both approaches lies in the fact that the patent is based on the comparison of the frequencies of two phonon modes, one affected by gravity while the other remains unchanged. In contrast, this thesis explores the resonant processes between the phonons and gravity, which may involve the analysis of only one phonon mode. Despite these differences, both proposals share a common path towards developing into a technological product with the potential for commercialization. The following section outlines the roadmap towards accomplishing this objective.

8.2 Market Analysis

In conjunction with the patent application, the author of this thesis also contributed to the realization of a market analysis for the patent, which was led by Dr. Jesus Rogel and Prof. Ivette Fuentes.

This market analysis outlines a commercialization strategy for the patented method for measuring accelerations and gravitational gradients. It addresses the key aspects required to accomplish the goal of transitioning from an experimental proposal—a detector concept—to a commercially available technological device. The analysis evaluates the key industries, the fabrication scalability of the product, the regulatory laws involved, the generation and protection of intellectual property, and the marketing strategy. This section summarizes the findings and conclusions derived from the market analysis.

8.2.1 Target Industries and Markets

The patent's technological application of high-precision gravimetry and gradiometry covers a broad spectrum across multiple industrial sectors that can benefit from the enhancement of gravitational and non-inertial motion sensing. The main target industries, along with the corresponding applications, are summarized below.

Subterranean Exploration. High-resolution gravitational measurements allow non-invasive detection and identification of underground resources, including oil, gas, water, and mineral deposits. This significantly improves the exploration efficiency and reduces environmental impact.

Automotive and Transportation. Enhanced acceleration sensors improve safety features such as automatic braking and stability control, contributing to the development of safer and more reliable transportation systems.

Aerospace. Precise gravimetry provides reliable navigational data in environments where GPS is unavailable, such as deep-sea exploration and space missions. This information is essential for trajectory correction and advanced inertial guidance systems.

Geophysical Research and Environmental Monitoring. Accurate mapping of Earth's gravitational field supports research in tectonics, volcanology, and seismology, contributing to improved earthquake prediction, for instance. Additionally, gravitational monitoring helps track environmental changes, such as glacier melting and groundwater levels.

Entertainment. High-precision motion tracking can enhance the responsiveness and realism of virtual- and augmented-reality gaming experiences.

8.2.2 Value Proposition

Accelerometers and gradiometers developed from BECs based on the patent offer significant advantages, making them an appealing and viable technology.

Precision and Sensitivity. The precision for detecting minute variations in gravitational fields is significantly enhanced by exploiting the quantum properties of the BEC, which include the advantage of producing entangled phonon states.

Miniaturisation. A beneficial feature of the phonon-based gravimeters is their ability to maintain precision when miniaturised, which contrasts with the gravimeters based on atom interferometry, whose precision is lost when their size is decreased.

Cost-Competitive Production. The production cost is expected to be competitive with respect to the existing atom-interferometry gravimeters by taking advantage of the materials and manufacturing techniques currently in use by the industry.

Versatility. The wide range of applications across industries increases the commercial potential of the technology and allows the possibility of tailoring and optimizing it for specific cases.

8.2.3 Regulations and Certifications

Technological inventions are subject to a complex regulatory landscape, which includes compliance with safety standards, quality certifications, and export controls. These factors must be considered for the successful commercial exploitation of the product.

Safety Regulations. Working with BECs involves manipulating atomic samples, which is generally a safe procedure. However, it is crucial to consider safety regulations regarding toxicity, flammability, and volatility. Additionally, regulatory standards for safe BEC operation must be met to prevent accidents in processes such as cooling systems and vacuum chambers, which are essential for achieving Bose-Einstein condensation.

Quality Certifications. To ensure that the manufacturing processes and the final products meet industry standards and perform consistently, it is vital to obtain ISO certifications and establish rigorous product testing procedures.

8.2.4 Intellectual Property Strategy

The successful commercialisation of a product requires a strong intellectual property (IP) strategy for protecting the core inventions and expanding the patent portfolio.

IP Protection. For the gravimetry proposed by the patent, it is important to secure and safeguard the measuring techniques, the application spectrum and any associated hardware or software innovation involved in the gravimeter implementation. This can be achieved by proper management and protection of the patent, ensuring the proper filing, maintenance and enforcement of the initial patent.

Patent Expansion. It is crucial to expand the patent portfolio by filing any improvements, innovations, or new applications that emerge as the commercialisation process progresses. Important areas for further patenting may include miniaturisation techniques, software algorithms, and innovations for specialised applications.

Licensing and Monetisation. To increase the commercial impact of the invention, different licensing models can be considered. For instance, exclusive licensing could be pursued for highly specialised industries holding the infrastructure necessary to fully commercialise the technology; non-exclusive licensing may be advantageous for mass-market applications where several companies could benefit from the invention.

Revenue Streams. To ensure that the invention is financially sustainable in the long term, various revenue streams can be explored. These include generating royalties implemented as a percentage of sales, entering joint ventures with established companies that share both risks and rewards, and facilitating technology transfers that permit the sale or licensing of the invention's construction and operational processes.

8.2.5 Production and Scalability

To accomplish the transition from a laboratory setting to a market product, it is necessary to address the production scalability process and the technical challenges involved in manufacturing quantum gravimeters.

Manufacturing Scalability. The continuous BEC technology replaces the traditional method of using BECS for metrology, which requires interrupting the Bose-Einstein condensation to take a measurement. This technology enables the feasible production of BECs for quantum gravimetry. Moreover, maintaining optimal levels of Bose-Einstein condensation necessitates real-time monitoring of atomic density, temperature stability, vacuum integrity, and trapping potential control.

Ventures with Established Companies. Creating joint ventures with industry leaders and established companies could provide a great opportunity to take advantage of their existing infrastructure, production capabilities, and market access, thereby minimising the time and costs needed to launch the technology.

Technology Developers. Strategic partnerships with technology developers specialising in specific procedures can accelerate technological development and contribute to the generation of further intellectual property, thanks to innovations arising from the manufacturing process or hardware optimizations.

8.2.6 Marketing and Outreach

To establish the invention in the marketplace, it is important to settle an extensive marketing and outreach strategy.

Industry Engagement. The most effective way to market the product is by attending leading quantum technology conferences and summits. This not only showcases the product to potential partners and industry experts but also enables the development of a network through strong relationships with key investors and industry leaders.

Online Presence. Nowadays, the Internet's impact cannot be underestimated. Therefore, to expand visibility and engage with broader audiences, it is fundamental to have a strong social media presence and dedicate a website showcasing the invention's features, applications, and impact across industries.

Educational Initiatives. Workshops and webinars help to educate and demonstrate to potential investors and customers the invention's applications and impact. Collaborating with academic institutions on joint research projects is also an effective strategy for boosting the visibility of the technology.

8.2.7 Risk Analysis and Mitigation

There are inherent risks associated with any cutting-edge technology, ranging from the technical to the more commercial aspects. It is crucial to identify these risks and develop strategies for mitigating or avoiding them.

Technical Risks. BECs are highly sensitive to environmental conditions such as temperature fluctuations, mechanical vibrations and electromagnetic signals, which can compromise the accuracy and reliability of the inventions in situations outside the laboratory. The design of environmental controls plays a key role in ensuring the proper functioning of the invention.

Market Risks. Competing devices from other companies are likely to emerge, compromising the impact of the invention. To remain at the forefront of the market, highlighting the advantages of the invention and pursuing continuous innovation will maintain its competitiveness.

Regulatory Risks. Quantum technologies represent an emerging industry, and unexpected changes in legislation could affect the commercialisation of this technology. Therefore, it is a good practice to engage legal and policy advisors and to keep a continuous watch on legislative developments.

8.2.8 Implementation Plan

Short-Term (0-2 years). The primary objective in the initial phase of development is to establish the proof of concept for the invention, which involves the experimental validation of the theoretical predictions concerning the precision and functionality of the gravimeter.

Mid-Term (2-5 years). The next step focuses on developing initial prototypes for real-world testing and demonstration, in addition to obtaining the required certifications for safety procedures, environmental compliance, and quality standards. During this period, it is essential to raise awareness and generate demand for the product as part of the objectives.

Long-Term (5-10 years). At this stage, as the technology becomes established, the objective lies, first, in scaling the manufacturing process to meet market demands while maintaining the product quality and reliability and, second, in expanding the product into new markets to achieve a global reach.

8.2.9 Conclusion

The market analysis provides a comprehensive roadmap for commercialising quantum gravimeters based on BEC's phonons. It addresses and analyses a wide range of key factors, including targeting potential markets, evaluating regulatory requirements, production scalability, managing risk, and developing a strategic growth plan. By following the recommendations and steps outlined, quantum gravimeters possess significant potential to transition from a laboratory environment to an impactful commercial product.

Chapter 9

Conclusions and Outlook

9.1 Closing Remarks

This thesis presents a novel approach to high-precision gravity measurement, taking advantage of quantum metrology techniques applied to the phonon states within a Bose-Einstein condensate (BEC). The proposed quantum interferometry scheme provides an alternative to standard atom interferometry and offers new opportunities to probe gravitational interactions at cutting-edge levels of precision. We employed this framework in modified gravity models, such as Modified Newtonian Dynamics (MOND) and Lambda gravity, to explore its potential for testing deviations from Newtonian gravity and constraining fundamental gravitational parameters.

Our experimental proposal combined several research areas. At its core lies the physics of the BEC, a cloud of trapped bosonic particles cooled to almost absolute zero, where most particles transition into a collective ground state while the remaining ones behave as collective mode excitations. Under specific conditions, these collective excitations correspond to phonons, which can be used to prepare quantum states. In particular, we focused on Gaussian states because they are easily implemented in the laboratory and have a well-developed theoretical framework. Furthermore, when examining the interaction of the BEC with an external gravitational field, we demonstrated that gravity drives phonon evolution through Gaussian transformations. Since gravity changes the quantum state of the phonons, we employed quantum metrology to quantify these changes and estimate a physical parameter characterizing the external gravitational field, e.g. the induced acceleration, thereby achieving gravity measurements. This framework can be naturally extended for exploring relativistic effects through the study of the relativistic BEC.

The essential material required for constructing this framework was comprehensively reviewed. In Chapter 2, we studied bosonic quantum fields in flat spacetime, which provided us with insights into quantum fields for later application to the non-relativistic and relativistic BECs. Next, in Chapter 3, we explored Gaussian states and Gaussian transformations using the covariance matrix, which helped us to create highly sensitive phonon states and to characterize their evolution in the presence of an external gravitational potential. Chapter 4 introduced quantum metrology to establish a rigorous methodology for estimating the parameters driving changes in a quantum system such as the BEC. Following this, Chapter 5 offered a thorough review of the physics of the BEC, including an analysis of the relativistic BEC. In Chapter 6, this material was finally combined to establish our experimental proposal of placing an oscillating massive sphere near a BEC to induce a resonant gravitational signal that can be detected using phonon dynamics. Finally, in Chapter 7, we applied this proposal to test modified theories of gravity, deriving the predictions of MOND and Lambda-gravity for the gravitational potential of the oscillating mass and evaluating the feasibility of distinguishing these effects from standard Newtonian gravity.

The primary achievement of this thesis is establishing a novel experimental framework for measuring gravity with high precision. By employing BEC phonons within a frequency interferometry scheme, we demonstrated the framework's potential for testing modified theories of gravity motivated by the problems of dark matter and dark energy. In particular, we examined the MOND and Lambda-gravity models. Our findings indicate that our proposal enhances the precision for testing MOND by three orders of magnitude compared to existing Earth-based experiments, thereby opening new avenues for testing MOND even in the presence of the external field effect. In the case of Lambda-gravity, our results demonstrate that our method improves current measurements of Newton's gravitational constant G by two orders of magnitude and establishes the first tabletop experiment constraining the value of the cosmological constant Λ.

Additionally, this thesis achieves the first implementation of the tritter operator for measuring the gravitational potential. The inclusion of the tritter enhances the precision of the experimental setup by two orders of magnitude, reinforcing the feasibility of quantum techniques for high-precision tests of gravity. In this thesis, we have also laid the groundwork for extending our experimental proposal to test modified theories of gravity within the relativistic regime and, more generally, relativistic effects in the weak-gravity regime. Finally, in addition to fundamental research, we have also considered the potential generation of new technology by summarizing a market analysis dedicated to the commercialisation of quantum gravimeters, which are founded on the exploitation of BEC phonons.

Despite the promising results obtained, we must address certain issues before proceeding with the practical implementation of our proposal. One of the primary challenges is the ability to generate squeezed phonon states in the laboratory, which remains an area of research under development. The squeezing of phonons is a key ingredient in this proposal, as these states provide the highest sensitivity for gravitational measurements. Furthermore, since this is a theoretical proposal, an essential next step is to conduct a proof-of-principle experiment to demonstrate its feasibility. Such an experiment could confirm the levels of precision predicted by our derivations and ensure that all the relevant experimental factors have been correctly considered. Additionally, it would provide valuable feedback to refine the proposal and enhance our understanding of its implementation.

9.2 Outlook

Several exploration routes remain for future research within this project. A further refinement of the Lambda-gravity test can be conducted, which involves modifying the experimental setup to isolate the measurement of the cosmological constant. By placing a BEC inside a spherical hollow massive shell that oscillates in resonance with the BEC phonons, we can take advantage of a corollary of the Gurzadyan theorem that drops he second statement of Newton's shell theorem. This corollary implies the existence of a gravitational force inside the shell that originates exclusively from the Λ term as the contribution of the G term vanishes. Detecting a signal in this setup would provide a direct measurement of Λ through a tabletop experiment.

Another avenue of exploration is to investigate modifications of gravity induced by Yukawa interactions. This project is currently under development. Additionally, our experiment can be adapted to consider BECs trapped in harmonic potentials, which are commonly used to create BECs in the laboratory, in contrast to the uniform potential examined in this thesis. This would help us evaluate how different trapping potentials affect the precision of BECs in measuring gravity. While BECs in harmonic potentials also exhibit phononic excitations—which have been observed to transition into a one-dimensional regime—a systematic study is needed to quantify their impact on measuring gravity.

Finally, by extending this framework to relativistic regimes, this thesis established the foundation for future research aimed at implementing our proposal for testing modifications of gravity within these regimes and measuring relativistic effects in the weak-gravity limit, with potential implications for fundamental physics and high-precision gravimetry.

In conclusion, our findings highlight the remarkable potential of Bose-Einstein condensates for measuring and testing gravity. Along with the progress of technology and experimental techniques, we anticipate that BEC-based gravimetry will play an increasingly significant role in expanding the frontiers of fundamental physics and the innovation of technology.

Appendix A

Summary of Gaussian Transformations and Gaussian States in the CMF

Following the covariance matrix formalism introduced in Section 3.3 and Section 3.4, where the Phase space description of Gaussian states and Gaussian transformations was established, we now provide a general characterization of all Gaussian transformations in terms of the matrix W introduced in Eq. (3.22). This is done for one-mode and two-mode bosonic systems ($N = 1, 2$).

For the sake of clarity, we recall the general form of a Gaussian state in Hilbert space, expressed as the unitary transformation

$$\hat{U} = e^{\frac{i}{2}\hat{\boldsymbol{A}}^{\dagger} W \hat{\boldsymbol{A}} + \hat{\boldsymbol{A}}^{\dagger} K \boldsymbol{\gamma}},$$

and its corresponding Phase space representation, determined by the symplectic matrix S and the displacement vector $\boldsymbol{b}$

$$S = e^{iKW}, \qquad \boldsymbol{b} = \left(\int_0^1 e^{iKWt} dt \right) \gamma \, .$$

As previously stated, these two expressions provide the dictionary that translates Gaussian transformations in Hilbert space to their counterparts in Phase space.

A.1 One-mode Gaussian Transformations

In Hilbert space, all the single-mode ($N = 1$) Gaussian transformations can be conveniently parameterized as

$$W = \begin{pmatrix} -\theta & ire^{i\chi} \\ -ire^{-i\chi} & -\theta \end{pmatrix}, \qquad \gamma = \begin{pmatrix} \alpha \\ \alpha^* \end{pmatrix}, \tag{A.1}$$

where $\theta, r, \chi \in \mathbb{R}$ and $\alpha \in \mathbb{C}$. This leads to the unitary Gaussian transformation:

$$\begin{aligned} \hat{U}_{\text{1-mode}} &= e^{-i\theta\hat{a}^\dagger\hat{a}}\, e^{-\frac{r}{2}(e^{i\chi}\hat{a}^{\dagger 2} - e^{-i\chi}\hat{a}^2)}\, e^{\alpha\hat{a}^\dagger - \alpha^*\hat{a}} \\ &\equiv \hat{R}(\theta) \cdot \hat{S}_{\text{1-sq}}(r, \chi) \cdot \hat{D}(\alpha)\,. \end{aligned} \tag{A.2}$$

$\hat{R}(\theta)$ is the phase-shifting or rotation operator,
$\hat{S}_{\text{1-sq}}(r, \chi)$ is the one-mode squeezing operator and
$\hat{D}(\alpha)$ is the Weyl displacement operator.

A.1.1 Displacement Operator

The displacement operator $\hat{D}(\alpha)$ can be singled out by taking

$$W = 0, \qquad \gamma = \begin{pmatrix} \alpha \\ \alpha^* \end{pmatrix}.$$

• Transformation:
In Hilbert space, the operator $\hat{D}(\alpha)$ is given by the unitary transformation

$$\hat{D}(\alpha) = e^{\alpha\hat{a}^\dagger - \alpha^*\hat{a}}. \tag{A.3}$$

In Phase space, the displacement transformation is given by the pair:

$$\mathbf{b}_{\hat{D}} = \begin{pmatrix} \alpha \\ \alpha^* \end{pmatrix}, \qquad S_{\hat{D}} = \mathbb{I}. \tag{A.4}$$

• State:
Applying the transformation to the vacuum $|0\rangle$, we generate a *coherent state.*

$$|\alpha\rangle = \hat{D}(\alpha)\,|0\rangle\,. \tag{A.5}$$

In Phase space, the state is expressed as

$$\mathbf{d}_{\text{coh}} = \begin{pmatrix} \alpha \\ \alpha^* \end{pmatrix}, \qquad \Gamma_{\text{coh}} = \mathbb{I}. \tag{A.6}$$

A.1.2 Phase-shifting or Rotation Operator

The phase-shifting operator $\hat{R}(\theta)$ can be singled out by taking

$$W = \begin{pmatrix} -\theta & 0 \\ 0 & -\theta \end{pmatrix}, \qquad \gamma = 0.$$

• Transformation

In Hilbert space, the operator $\hat{R}(\theta)$ is given by the unitary transformation

$$\hat{R}(\theta) = e^{-i\theta\hat{a}^\dagger\hat{a}}. \tag{A.7}$$

In Phase space, the phase-shifting transformation is given by the pair:

$$\mathbf{b}_{\hat{R}} = 0, \qquad S_{\hat{R}} = \begin{pmatrix} e^{-i\theta} & 0 \\ 0 & e^{i\theta} \end{pmatrix}. \tag{A.8}$$

• State:

Applying the transformation to the vacuum $|0\rangle$, we get a trivial transformation.

$$\hat{R}(\theta)\,|0\rangle = |0\rangle\,. \tag{A.9}$$

In Phase space, the state is expressed as

$$\mathbf{d}_{\hat{R}} = 0, \qquad \Gamma_{\hat{R}} = \mathbb{I}.$$

The phase-shifting transformation is a passive transformation that does not change the particle content or energy of the state. Then, if we start with a vacuum state, we remain in the vacuum.

A.1.3 One-mode Squeezing Operator

The one-mode squeezing operator $\hat{S}_{\text{1-sq}}(r,\chi)$ can be singled out by taking

$$W = \begin{pmatrix} 0 & ire^{i\chi} \\ -ire^{-i\chi} & 0 \end{pmatrix}, \qquad \gamma = 0.$$

• Transformation:

In Hilbert space, the operator $\hat{S}_{\text{1-sq}}(r,\chi)$ is given by the unitary transformation

$$\hat{S}_{\text{1-sq}}(r,\chi) = e^{-\frac{r}{2}(e^{i\chi}\hat{a}^{\dagger 2} - e^{-i\chi}\hat{a}^2)}. \tag{A.10}$$

In Phase space, the one-mode squeezing transformation is given by the pair:

$$\mathbf{b}_{\text{1-sq}} = 0, \qquad S_{\text{1-sq}}(r,\chi) = \begin{pmatrix} \cosh r & -e^{i\chi}\sinh r \\ -e^{-i\chi}\sinh r & \cosh r \end{pmatrix}. \tag{A.11}$$

• State:

Applying the transformation to the vacuum $|0\rangle$, we get a *one-mode squeezed state.*

$$|S_{\text{1-sq}}(r,\chi)\rangle = \hat{S}_{\text{1-sq}}(r,\chi)\,|0\rangle\,. \tag{A.12}$$

In Phase space, the state is expressed as

$$\mathbf{d}_{\text{1-sq}} = 0, \qquad \Gamma_{\text{1-sq}}(r,\chi) = \begin{pmatrix} \cosh 2r & -e^{i\chi}\sinh 2r \\ -e^{-i\chi}\sinh 2r & \cosh 2r \end{pmatrix}. \tag{A.13}$$

A.2 Two-mode Gaussian Transformations

In Hilbert space, all the two-mode ($N = 2$) Gaussian transformations can be conveniently parameterized as

$$W = \begin{pmatrix} -\theta_1 & -i\theta_B e^{i\chi_B} & ir_1 e^{i\chi_1} & ir_T e^{i\chi_T} \\ i\theta_B e^{-i\chi_B} & -\theta_2 & ir_T e^{i\chi_T} & ir_2 e^{i\chi_2} \\ -ir_1 e^{-i\chi_1} & -ir_T e^{-i\chi_T} & -\theta_1 & i\theta_B e^{-i\chi_B} \\ -ir_T e^{-i\chi_T} & -ir_2 e^{-i\chi_2} & -i\theta_B e^{i\chi_B} & -\theta_2 \end{pmatrix}, \qquad \gamma = \begin{pmatrix} \alpha_1 \\ \alpha_2 \\ \alpha_1^* \\ \alpha_2^* \end{pmatrix}, \tag{A.14}$$

where the different $\theta, r, \chi \in \mathbb{R}$ and α_1, $\alpha_2 \in \mathbb{C}$. This leads to the unitary Gaussian transformation:

$$\begin{aligned}\hat{U}_{\text{2-mode}} &= e^{-i\theta_1 \hat{a}_1^\dagger \hat{a}_1 - i\theta_2 \hat{a}_2^\dagger \hat{a}_2} \cdot e^{-\frac{r_1}{2}(e^{i\chi_1}\hat{a}_1^{\dagger 2} - e^{-i\chi_1}\hat{a}_1^2) - \frac{r_2}{2}(e^{i\chi_2}\hat{a}_2^{\dagger 2} - e^{-i\chi_2}\hat{a}_2^2)} \\ &\quad \cdot e^{-r_T(e^{i\chi_T}\hat{a}_1^\dagger \hat{a}_2^\dagger - e^{-i\chi_T}\hat{a}_1\hat{a}_2)} \cdot e^{\theta_B(e^{i\chi_B}\hat{a}_1^\dagger \hat{a}_2 - e^{-i\chi_B}\hat{a}_1\hat{a}_2^\dagger)} \\ &\quad \cdot e^{\alpha_1 \hat{a}_1^\dagger - \alpha_1^* \hat{a}_1 + \alpha_2 \hat{a}_2^\dagger - \alpha_2^* \hat{a}_2} \\ &\equiv \hat{R}(\theta_1, \theta_2) \cdot \hat{S}_{\text{1-sq}}(r_1, \chi_1; r_2, \chi_2) \cdot \hat{S}_{\text{2-sq}}(r_T, \chi_T) \\ &\quad \cdot \hat{B}(\theta_B, \chi_B) \cdot \hat{D}(\alpha_1, \alpha_2)\,. \end{aligned} \tag{A.15}$$

$\hat{R}(\cdot)$, $\hat{S}_{\text{1-sq}}(\cdot)$ and $\hat{D}(\cdot)$ keep the same definition from the previous section,
$\hat{S}_{\text{2-sq}}(r_T, \chi_T)$ is the two-mode squeezing operator and
$\hat{B}(\theta_B, \chi_B)$ is the mode-mixing operator.

A.2.1 Displacement Operator

The displacement operator $\hat{D}(\alpha_1, \alpha_2)$ can be singled out by taking

$$W = 0, \qquad \gamma = \begin{pmatrix} \alpha_1 \\ \alpha_2 \\ \alpha_1^* \\ \alpha_2^* \end{pmatrix}.$$

- **Transformation:**

In Hilbert space, the operator $\hat{D}(\alpha_1, \alpha_2)$ is given by the unitary transformation

$$\hat{D}(\alpha) = e^{\alpha_1 \hat{a}_1^\dagger - \alpha_1^* \hat{a}_1 + \alpha_2 \hat{a}_2^\dagger - \alpha_2^* \hat{a}_2}. \tag{A.16}$$

In Phase space, the displacement transformation is given by the pair:

$$\mathbf{b}_{\hat{D}} = \begin{pmatrix} \alpha_1 \\ \alpha_2 \\ \alpha_1^* \\ \alpha_2^* \end{pmatrix}, \qquad S_{\hat{D}} = \mathbb{I}. \tag{A.17}$$

- **State:**

Applying the transformation to the vacuum $|0\,0\rangle$, we generate a *coherent state.*

$$|\alpha_1\,\alpha_2\rangle = \hat{D}(\alpha_1,\alpha_2)\,|0\,0\rangle\,. \tag{A.18}$$

In Phase space, the state is expressed as

$$\mathbf{d}_{\text{coh}} = \begin{pmatrix} \alpha_1 \\ \alpha_2 \\ \alpha_1^* \\ \alpha_2^* \end{pmatrix} \qquad \Gamma_{\text{coh}} = \mathbb{I}. \tag{A.19}$$

A.2.2 Phase-shifting or Rotation Operator

The phase-shifting operator $\hat{R}(\theta_1,\theta_2)$ can be singled out by taking

$$W = \begin{pmatrix} -\theta_1 & 0 & 0 & 0 \\ 0 & -\theta_2 & 0 & 0 \\ 0 & 0 & -\theta_1 & 0 \\ 0 & 0 & 0 & -\theta_2 \end{pmatrix}, \qquad \gamma = 0.$$

• **Transformation:**
In Hilbert space, the operator $\hat{R}(\theta_1,\theta_2)$ is given by the unitary transformation

$$\hat{R}(\theta) = e^{-i\theta_1 \hat{a}_1^\dagger \hat{a}_1 - i\theta_2 \hat{a}_2^\dagger \hat{a}_2}. \tag{A.20}$$

In Phase space, the phase-shifting transformation is given by the pair:

$$\mathbf{b}_{\hat{R}} = 0, \qquad S_{\hat{R}} = \begin{pmatrix} e^{-i\theta_1} & 0 & 0 & 0 \\ 0 & e^{-i\theta_2} & 0 & 0 \\ 0 & 0 & e^{i\theta_1} & 0 \\ 0 & 0 & 0 & e^{i\theta_2} \end{pmatrix}. \tag{A.21}$$

• **State:**
Applying the transformation to the vacuum $|0\,0\rangle$, we get a trivial transformation.

$$\hat{R}(\theta_1,\theta_2)\,|0\,0\rangle = |0\,0\rangle\,. \tag{A.22}$$

In Phase space, the state is expressed as

$$\mathbf{d}_{\hat{R}} = 0, \qquad \Gamma_{\hat{R}} = \mathbb{I}.$$

A.2.3 One-mode Squeezing Operator

The one-mode squeezing operator $\hat{S}_{\text{1-sq}}(r_1, \chi_1; r_2, \chi_2)$ can be singled out by taking

$$W = \begin{pmatrix} 0 & 0 & ir_1 e^{i\chi_1} & 0 \\ 0 & 0 & 0 & ir_2 e^{i\chi_2} \\ -ir_1 e^{-i\chi_1} & 0 & 0 & 0 \\ 0 & -ir_2 e^{-i\chi_2} & 0 & 0 \end{pmatrix}, \qquad \gamma = 0.$$

• **Transformation:**

In Hilbert space, the operator $\hat{S}_{\text{1-sq}}(r_1, \chi_1; r_2, \chi_2)$ is given by the unitary transformation

$$\hat{S}_{\text{1-sq}}(r_1, \chi_1; r_2, \chi_2) = e^{-\frac{r_1}{2}(e^{i\chi_1}\hat{a}_1^{\dagger 2} - e^{-i\chi_1}\hat{a}_1^2) - \frac{r_2}{2}(e^{i\chi_2}\hat{a}_2^{\dagger 2} - e^{-i\chi_2}\hat{a}_2^2)}. \tag{A.23}$$

In Phase space, the one-mode squeezing transformation is given by the pair:

$$\mathbf{b}_{\text{1-sq}} = 0, \tag{A.24}$$

$$S_{\text{1-sq}}(r_1, \chi_1; r_2, \chi_2) =$$

$$\begin{pmatrix} \cosh r_1 & 0 & -e^{i\chi_1}\sinh r_1 & 0 \\ 0 & \cosh r_2 & 0 & -e^{i\chi_2}\sinh r_2 \\ -e^{-i\chi_1}\sinh r_1 & 0 & \cosh r_1 & 0 \\ 0 & -e^{-i\chi_2}\sinh r_2 & 0 & \cosh r_2 \end{pmatrix}.$$

• **State:**

Applying the transformation to the vacuum $|0\,0\rangle$, we get a *one-mode squeezed state.*

$$|S_{\text{1-sq}}\rangle = \hat{S}_{\text{1-sq}}(r_1, \chi_1; r_2, \chi_2)\,|0\,0\rangle\,. \tag{A.25}$$

In Phase space, the state is expressed as

$$\mathbf{d}_{\text{1-sq}} = 0, \tag{A.26}$$

$$\Gamma_{\text{1-sq}}(r_1, \chi_1; r_2, \chi_2) =$$

$$\begin{pmatrix} \cosh 2r_1 & 0 & -e^{i\chi_1}\sinh 2r_1 & 0 \\ 0 & \cosh 2r_2 & 0 & -e^{i\chi_2}\sinh 2r_2 \\ -e^{-i\chi_1}\sinh 2r_1 & 0 & \cosh 2r_1 & 0 \\ 0 & -e^{-i\chi_2}\sinh 2r_2 & 0 & \cosh 2r_2 \end{pmatrix}.$$

A.2.4 Two-mode Squeezing Operator

The two-mode squeezing operator $\hat{S}_{\text{2-sq}}(r_T, \chi_T)$ can be singled out by taking

$$W = \begin{pmatrix} 0 & 0 & 0 & ir_T e^{i\chi_T} \\ 0 & 0 & ir_T e^{i\chi_T} & 0 \\ 0 & -ir_T e^{-i\chi_T} & 0 & 0 \\ -ir_T e^{-i\chi_T} & 0 & 0 & 0 \end{pmatrix}, \qquad \gamma = 0.$$

• **Transformation:**
In Hilbert space, the operator $\hat{S}_{\text{2-sq}}(r_T, \chi_T)$ is given by the unitary transformation

$$\hat{S}_{\text{2-sq}}(r_T, \chi_T) = e^{-r_T(e^{i\chi_T}\hat{a}_1^\dagger \hat{a}_2^\dagger - e^{-i\chi_T}\hat{a}_1\hat{a}_2)}. \tag{A.27}$$

In Phase space, the two-mode squeezing transformation is given by the pair:

$$\mathbf{b}_{\text{2-sq}} = 0, \tag{A.28}$$

$$S_{\text{2-sq}}(r_T, \chi_T) =$$

$$\begin{pmatrix} \cosh r_T & 0 & 0 & -e^{i\chi_T}\sinh r_T \\ 0 & \cosh r_T & -e^{i\chi_T}\sinh r_T & 0 \\ 0 & -e^{-i\chi_T}\sinh r_T & \cosh r_T & 0 \\ -e^{-i\chi_T}\sinh r_T & 0 & 0 & \cosh r_T \end{pmatrix}.$$

- **State:**

Applying the transformation to the vacuum $|0\,0\rangle$, we get a *two-mode squeezed state.*

$$|S_{\text{2-sq}}\rangle = \hat{S}_{\text{2-sq}}(r_T, \chi_T)\,|0\,0\rangle\,. \tag{A.29}$$

In Phase space, the state is expressed as

$$\mathbf{d}_{\text{2-sq}} = 0, \tag{A.30}$$

$$\Gamma_{\text{2-sq}}(r_T, \chi_T) =$$

$$\begin{pmatrix} \cosh 2r_T & 0 & 0 & -e^{i\chi_T}\sinh 2r_T \\ 0 & \cosh 2r_T & -e^{i\chi_T}\sinh 2r_T & 0 \\ 0 & -e^{-i\chi_T}\sinh 2r_T & \cosh 2r_T & 0 \\ -e^{-i\chi_T}\sinh 2r_T & 0 & 0 & \cosh 2r_T \end{pmatrix}.$$

A.2.5 Mode-mixing Operator

The mode-mixing operator $\hat{B}(\theta_B, \chi_B)$ can be singled out by taking

$$W = \begin{pmatrix} 0 & -i\theta_B e^{i\chi_B} & 0 & 0 \\ i\theta_B e^{-i\chi_B} & 0 & 0 & 0 \\ 0 & 0 & 0 & i\theta_B e^{-i\chi_B} \\ 0 & 0 & -i\theta_B e^{i\chi_B} & 0 \end{pmatrix}, \qquad \gamma = 0.$$

- **Transformation:**

In Hilbert space, the operator $\hat{B}(\theta_B, \chi_B)$ is given by the unitary transformation

$$\hat{B}(\theta_B, \chi_B) = e^{\theta_B(e^{i\chi_B}\hat{a}_1^\dagger \hat{a}_2 - e^{-i\chi_B}\hat{a}_1\hat{a}_2^\dagger)}. \tag{A.31}$$

In Phase space, the mode-mixing transformation is given by the pair:

$$\mathbf{b}_{\text{M-M}} = 0, \tag{A.32}$$

$$S_{\text{M-M}}(\theta_B, \chi_B) =$$

$$\begin{pmatrix} \cos\theta_B & e^{i\chi_B}\sin\theta_B & 0 & 0 \\ -e^{-i\chi_B}\sin\theta_B & \cos\theta_B & 0 & 0 \\ 0 & 0 & \cos\theta_B & e^{-i\chi_B}\sin\theta_B \\ 0 & 0 & -e^{i\chi_B}\sin\theta_B & \cos\theta_B \end{pmatrix}.$$

- **State:**

Applying the transformation to the vacuum $|0\,0\rangle$, in Phase space, the state is expressed as

$$\mathbf{d}_{\text{M-M}} = 0 \qquad \Gamma_{\text{M-M}} = \mathbb{I}.$$

A mode-mixing transformation does not change the number of particles in the system. This can be seen clearly from the creation and annihilation operators of the transformation in Hilbert space. While the mode-mixing operator creates a particle in one of the modes, it destroys another particle in the other mode.

Appendix B

Mean Number of Particles

The mean number of particles of a Gaussian state is a useful quantity that can be straightforwardly calculated using the covariance matrix formalism. We define the mean number of particles in the mode i as

$$n_i := \mathrm{Tr}[\hat{a}_i^\dagger \hat{a}_i \hat{\rho}], \tag{B.1}$$

where $0 \leq i \leq N$. Using the commutation relations (3.15) and the definitions of the first and second moments (3.18), the particle number in the mode i for the state $(\boldsymbol{d}, \Gamma)$ can be expressed as [44],

$$n_i = \frac{1}{2}(\Gamma_{ii} + d_i^* d_i - 1). \tag{B.2}$$

Thus, the mean total number of particles in the Gaussian state is

$$n := \sum_{i=1}^{N} = \frac{1}{2}\left(\frac{1}{2}\mathrm{tr}[\Gamma] + \boldsymbol{d}^\dagger \boldsymbol{d} - N\right). \tag{B.3}$$

Below, we list the mean total number of particles for some representative Gaussian states.

a) Coherent state: $|\alpha\rangle$

Considering the state (A.5), the number of particles in a coherent state is:

$$n = |\alpha|^2. \tag{B.4}$$

b) One-mode squeezed state: $|S_{\text{1-sq}}(r, \chi)\rangle$

Considering the state (A.12), the number of particles in a coherent state is:

$$n = \sinh^2 r. \tag{B.5}$$

c) Two-mode squeezed state: $|S_{\text{2-sq}}(r_T, \chi_T)\rangle$

Considering the state (A.29), the number of particles in a coherent state is:

$$n = 2\sinh^2 r_T. \tag{B.6}$$

d) Mode-mixed state: $\hat{M}(\theta_B, \chi_B)\,|0\rangle$

Considering the state generated by (A.31), the number of particles in a coherent state is:

$$n = 0. \tag{B.7}$$

e) Displaced squeezed state: $\hat{D}_\alpha \hat{S}_{\text{1-sq}}(r, \chi)\,|0\rangle$

$$n = \sinh^2 r + |\alpha|^2. \tag{B.8}$$

f) Squeezed displaced state: $\hat{S}_{\text{1-sq}}(r, 0)\hat{D}_\alpha\,|0\rangle$

$$n = \sinh^2 r + |\beta|^2, \tag{B.9}$$

where $|\beta|^2 = |\alpha^* \cosh r - \alpha \sinh r|^2$.

g) Squeezed-squeezed state: $\hat{S}_{\text{1-sq}}(r', 0)\hat{S}_{\text{1-sq}}(r, 0)\,|0\rangle$

$$n = \sinh^2(r + r'). \tag{B.10}$$

Appendix C

Quantum Fisher Information's Computation

The Mathematica file used to compute the quantum Fisher information in (6.32) from Chapter 6 is attached. Some of the calculated matrices are too large to be fully displayed. However, they can be reproduced readily with the information provided and access to Wolfram Mathematica software. The file refers the reader to the relevant equations and sections. While some notation has been changed, every effort has been made to maintain consistency.

Quantum Frequency Interferometry

Here, we calculate the Quantum Fisher Information for estimating $\epsilon = a_\Omega$ associated to the oscillating sphere's gravitational influence on the phonons of the BEC.

1. Quantum Fisher Information (QFI)

Consider a probe state $(\boldsymbol{d}_0, \Gamma_0)$ undergoing a change driven by a symplectic transformation $S(\epsilon)$, which results in the state $(\boldsymbol{d}, \Gamma)$. Then, the QFI for estimating the parameter ϵ is given by:

$$F(\epsilon) = \sum_{k,l=1}^{N} 2\,\mathrm{Re}\left[\overline{Q}^{k\,l}(\epsilon)\, Q^{k\,l}(\epsilon)\right] + 2\,\partial_\epsilon \boldsymbol{d}^\dagger(\epsilon)\,\Gamma^{-1}(\epsilon)\,\partial_\epsilon \boldsymbol{d}(\epsilon), \qquad \text{(D.1) or}$$

see (4.16)
where

$$P = \begin{pmatrix} R & Q \\ \overline{Q} & \overline{R} \end{pmatrix}, \qquad \mathrm{PK} + K\,P^\dagger = 0, \qquad \text{with } P = S^{-1}\,\partial S, \qquad R = \alpha^\dagger\,\partial\alpha - \overline{\beta^\dagger\,\partial\beta}$$

and $\quad Q = \alpha^\dagger\,\partial\beta - \overline{\beta^\dagger\,\partial\alpha}\,. \qquad$ (D.2)

We can split the symplectic transformation as $\quad S = S_\epsilon\, S_0, \quad$ such that
$P = S_0^{-1}\, S_\epsilon^{-1}\, \dot{S}_\epsilon\, S_0 := S_0^{-1}\, P_\epsilon\, S_0 \quad$ that is $\quad P_\epsilon := S_\epsilon^{-1}\, \dot{S}_\epsilon\,.$
Also, let us remember that $\quad \boldsymbol{d} = S_\epsilon\, \boldsymbol{d}_0 + \boldsymbol{b}_\epsilon\,.$ With these ingredients, we can simplify the last term in QFI as:

$$\partial_\epsilon \boldsymbol{d}^\dagger\, \Gamma^{-1}\, \partial_\epsilon \boldsymbol{d} = \left(P_\epsilon\, d_0 + S_\epsilon^{-1}\, \dot{b}_\epsilon\right)^\dagger \Gamma_0^{-1} \left(P_\epsilon\, d_0 + S_\epsilon^{-1}\, \dot{b}_\epsilon\right).$$

As we are working with a three-mode scheme, $i = \{1, 2, 3\}$, and given that for a two-mode squeezing $b_\epsilon = 0$, the QFI reads:

$$F(\epsilon) = \sum_{k,l=1}^{3} 2\,\mathrm{Re}\left[\overline{Q}^{k\,l}\, Q^{k\,l}\right] + 2\,(P_\epsilon\, d_0)^\dagger\, \sigma_0^{-1}\,(P_\epsilon\, d_0).$$

We need to calculate: $d_0,\ S_0,\ \Gamma_0,\ S_\epsilon^{-1},\ \dot{S}_\epsilon,\ P,\ P_\epsilon$.

2. Interferometric Scheme

We are considering a three-mode system exclusively described by Gaussian states and Gaussian transformations.

2.1 Initial state

The BEC's atoms in the ground state are considered to be a coherent state and the phonon modes l and n are assumed to be in the vacuum. In the covariance matrix formalism, the state of the BEC at this point is given by the pair:

d_{coh} =

In[1]:= $$\mathbf{d}_{\mathbf{coh}} = \begin{pmatrix} \alpha \\ 0 \\ 0 \\ \mathtt{Conjugate}[\alpha] \\ 0 \\ 0 \end{pmatrix};$$

Γ_{coh} =

$$\Gamma_{\mathbf{coh}} = \begin{pmatrix} 1 & 0 & 0 & 0 & 0 & 0 \\ 0 & 1 & 0 & 0 & 0 & 0 \\ 0 & 0 & 1 & 0 & 0 & 0 \\ 0 & 0 & 0 & 1 & 0 & 0 \\ 0 & 0 & 0 & 0 & 1 & 0 \\ 0 & 0 & 0 & 0 & 0 & 1 \end{pmatrix};$$

Cf. Section 3.7.

2.2 Probe state

Cf. Section 6.4.1

- Step 1:

We act on the initial state, first, using a two-mode squeezing unitary transformation

$$\hat{U}_{2\,\mathrm{sq}}(r) = \exp\left(\chi\, \hat{b}_l^\dagger\, \hat{b}_n^\dagger + \chi^*\, \hat{b}_l\, \hat{b}_n\right)$$

to parametrically populate the phonon modes, where $\chi = r\, e^{i\vartheta_{\mathrm{sq}}}$ (cf. eq. (6.22)). The symplectic matrix associated to the transformation is:

$S_{2\,\mathrm{sq}}$ =

In[ ]:= $$\mathbf{S}_{\mathbf{2\,sq}} = \begin{pmatrix} 1 & 0 & 0 & 0 & 0 & 0 \\ 0 & \mathtt{Cosh}[r] & 0 & 0 & 0 & -e^{i\,\vartheta_{sq}}\,\mathtt{Sinh}[r] \\ 0 & 0 & \mathtt{Cosh}[r] & 0 & -e^{i\,\vartheta_{sq}}\,\mathtt{Sinh}[r] & 0 \\ 0 & 0 & 0 & 1 & 0 & 0 \\ 0 & 0 & -e^{-i\,\vartheta_{sq}}\,\mathtt{Sinh}[r] & 0 & \mathtt{Cosh}[r] & 0 \\ 0 & -e^{-i\,\vartheta_{sq}}\,\mathtt{Sinh}[r] & 0 & 0 & 0 & \mathtt{Cosh}[r] \end{pmatrix};$$

- Step 2:

Next we apply a tritter to mix the two squeezed phonon modes with the atoms in the ground state (cf. eq. (6.23)). The symplectic matrix associated with the tritter is

S_{tr} =

In[ ]:=

$$\mathrm{S_{tr}} = \begin{pmatrix} \mathrm{Cos}[\theta] & \frac{\mathrm{i}\, e^{\mathrm{i}\vartheta}\,\mathrm{Sin}[\theta]}{\sqrt{2}} & \frac{\mathrm{i}\, e^{\mathrm{i}\vartheta}\,\mathrm{Sin}[\theta]}{\sqrt{2}} & 0 & 0 & 0 \\ \frac{\mathrm{i}\, e^{-\mathrm{i}\vartheta}\,\mathrm{Sin}[\theta]}{\sqrt{2}} & \mathrm{Cos}\left[\frac{\theta}{2}\right]^2 & -\mathrm{Sin}\left[\frac{\theta}{2}\right]^2 & 0 & 0 & 0 \\ \frac{\mathrm{i}\, e^{-\mathrm{i}\vartheta}\,\mathrm{Sin}[\theta]}{\sqrt{2}} & -\mathrm{Sin}\left[\frac{\theta}{2}\right]^2 & \mathrm{Cos}\left[\frac{\theta}{2}\right]^2 & 0 & 0 & 0 \\ 0 & 0 & 0 & \mathrm{Cos}[\theta] & \frac{-\mathrm{i}\, e^{-\mathrm{i}\vartheta}\,\mathrm{Sin}[\theta]}{\sqrt{2}} & \frac{-\mathrm{i}\, e^{-\mathrm{i}\vartheta}\,\mathrm{Sin}[\theta]}{\sqrt{2}} \\ 0 & 0 & 0 & \frac{-\mathrm{i}\, e^{\mathrm{i}\vartheta}\,\mathrm{Sin}[\theta]}{\sqrt{2}} & \mathrm{Cos}\left[\frac{\theta}{2}\right]^2 & -\mathrm{Sin}\left[\frac{\theta}{2}\right]^2 \\ 0 & 0 & 0 & \frac{-\mathrm{i}\, e^{\mathrm{i}\vartheta}\,\mathrm{Sin}[\theta]}{\sqrt{2}} & -\mathrm{Sin}\left[\frac{\theta}{2}\right]^2 & \mathrm{Cos}\left[\frac{\theta}{2}\right]^2 \end{pmatrix};$$

Then, the complete symplectic transformation of the probe state is

$S_0 =$

In[ ]:=

```
MatrixForm[FullSimplify[Str.S2 sq]]
```

In[2]:=

$$\mathrm{S_0} = \begin{pmatrix} \mathrm{Cos}[\theta] & \frac{\mathrm{i}\, e^{\mathrm{i}\vartheta}\,\mathrm{Cosh}[r]\,\mathrm{Sin}[\theta]}{\sqrt{2}} & \frac{\mathrm{i}\, e^{\mathrm{i}\vartheta}\,\mathrm{Cosh}[r]\,\mathrm{Sin}[\theta]}{\sqrt{2}} & 0 & -\frac{\mathrm{i}\, e^{\mathrm{i}(\vartheta+\vartheta_{sq})}\,\mathrm{Sin}[\theta]\ \mathrm{S}}{\sqrt{2}} \\ \frac{\mathrm{i}\, e^{-\mathrm{i}\vartheta}\,\mathrm{Sin}[\theta]}{\sqrt{2}} & \mathrm{Cos}\left[\frac{\theta}{2}\right]^2 \mathrm{Cosh}[r] & -\mathrm{Cosh}[r]\,\mathrm{Sin}\left[\frac{\theta}{2}\right]^2 & 0 & e^{\mathrm{i}\vartheta_{sq}}\,\mathrm{Sin}\left[\frac{\theta}{2}\right]^2 \mathrm{Si} \\ \frac{\mathrm{i}\, e^{-\mathrm{i}\vartheta}\,\mathrm{Sin}[\theta]}{\sqrt{2}} & -\mathrm{Cosh}[r]\,\mathrm{Sin}\left[\frac{\theta}{2}\right]^2 & \mathrm{Cos}\left[\frac{\theta}{2}\right]^2 \mathrm{Cosh}[r] & 0 & -e^{\mathrm{i}\vartheta_{sq}}\,\mathrm{Cos}\left[\frac{\theta}{2}\right]^2 \mathrm{S} \\ 0 & \frac{\mathrm{i}\, e^{-\mathrm{i}(\vartheta+\vartheta_{sq})}\,\mathrm{Sin}[\theta]\,\mathrm{Sinh}[r]}{\sqrt{2}} & \frac{\mathrm{i}\, e^{-\mathrm{i}(\vartheta+\vartheta_{sq})}\,\mathrm{Sin}[\theta]\,\mathrm{Sinh}[r]}{\sqrt{2}} & \mathrm{Cos}[\theta] & -\frac{\mathrm{i}\, e^{-\mathrm{i}\vartheta}\,\mathrm{Cosh}[r]\ \mathrm{Si}}{\sqrt{2}} \\ 0 & e^{-\mathrm{i}\vartheta_{sq}}\,\mathrm{Sin}\left[\frac{\theta}{2}\right]^2 \mathrm{Sinh}[r] & -e^{-\mathrm{i}\vartheta_{sq}}\,\mathrm{Cos}\left[\frac{\theta}{2}\right]^2 \mathrm{Sinh}[r] & \frac{-\mathrm{i}\, e^{\mathrm{i}\vartheta}\,\mathrm{Sin}[\theta]}{\sqrt{2}} & \mathrm{Cos}\left[\frac{\theta}{2}\right]^2 \mathrm{Cosh} \\ 0 & -e^{-\mathrm{i}\vartheta_{sq}}\,\mathrm{Cos}\left[\frac{\theta}{2}\right]^2 \mathrm{Sinh}[r] & e^{-\mathrm{i}\vartheta_{sq}}\,\mathrm{Sin}\left[\frac{\theta}{2}\right]^2 \mathrm{Sinh}[r] & \frac{-\mathrm{i}\, e^{\mathrm{i}\vartheta}\,\mathrm{Sin}[\theta]}{\sqrt{2}} & -\mathrm{Cosh}[r]\ \mathrm{Sin} \end{pmatrix}$$

Thus, the probe state is described by the displacement vector

$d_0 =$

In[5]:=

```
MatrixForm[FullSimplify[S0.dcoh]]
```

In[7]:=

$$\mathrm{d_0} = \begin{pmatrix} \alpha\,\mathrm{Cos}[\theta] \\ \frac{\alpha\,\mathrm{Sin}[\theta]\ (\mathrm{i}\,\mathrm{Cos}[\vartheta]+\mathrm{Sin}[\vartheta])}{\sqrt{2}} \\ \frac{\alpha\,\mathrm{Sin}[\theta]\ (\mathrm{i}\,\mathrm{Cos}[\vartheta]+\mathrm{Sin}[\vartheta])}{\sqrt{2}} \\ \mathrm{Conjugate}[\alpha]\ \mathrm{Cos}[\theta] \\ \frac{\mathrm{Conjugate}[\alpha]\ \mathrm{Sin}[\theta]\ (-\mathrm{i}\,\mathrm{Cos}[\vartheta]+\mathrm{Sin}[\vartheta])}{\sqrt{2}} \\ \frac{\mathrm{Conjugate}[\alpha]\ \mathrm{Sin}[\theta]\ (-\mathrm{i}\,\mathrm{Cos}[\vartheta]+\mathrm{Sin}[\vartheta])}{\sqrt{2}} \end{pmatrix};$$

and covariance matrix

$\Gamma_0 =$

In[ ]:=

```
MatrixForm[
 FullSimplify[S0.ConjugateTranspose[S0], Assumptions → Element[{θ, ϑ, r, ϑsq}, Reals]]]
```

In[ ]:=

$$\Gamma_\theta = \left(\begin{array}{cc}
\text{Cosh}[r]^2 - \text{Cos}[2\,\theta]\,\text{Sinh}[r]^2 & i\,\sqrt{2}\,e^{i\,\vartheta}\,\text{Cos}[\theta]\,\text{Sin}[\theta]\,\text{Sinh}[r]^2 \\
-i\,\sqrt{2}\,e^{-i\,\vartheta}\,\text{Cos}[\theta]\,\text{Sin}[\theta]\,\text{Sinh}[r]^2 & \frac{1}{4}\left(1+3\,\text{Cosh}[2\,r]+2\,\text{Cos}[2\,\theta]\,\text{Sinh}[r]^2\right) \\
-i\,\sqrt{2}\,e^{-i\,\vartheta}\,\text{Cos}[\theta]\,\text{Sin}[\theta]\,\text{Sinh}[r]^2 & -\text{Sin}[\theta]^2\,\text{Sinh}[r]^2 \\
e^{-i\,(2\,\vartheta+\vartheta_{sq})}\,\text{Sin}[\theta]^2\,\text{Sinh}[2\,r] & i\,\sqrt{2}\,e^{-i\,(\vartheta+\vartheta_{sq})}\,\text{Cos}[\theta]\,\text{Cosh}[r]\,\text{Sin}[\theta]\,\text{Sinh} \\
i\,\sqrt{2}\,e^{-i\,(\vartheta+\vartheta_{sq})}\,\text{Cos}[\theta]\,\text{Cosh}[r]\,\text{Sin}[\theta]\,\text{Sinh}[r] & e^{-i\,\vartheta_{sq}}\,\text{Cosh}[r]\,\text{Sin}[\theta]^2\,\text{Sinh}[r] \\
i\,\sqrt{2}\,e^{-i\,(\vartheta+\vartheta_{sq})}\,\text{Cos}[\theta]\,\text{Cosh}[r]\,\text{Sin}[\theta]\,\text{Sinh}[r] & -\frac{1}{4}\,e^{-i\,\vartheta_{sq}}\,(3+\text{Cos}[2\,\theta])\,\text{Sinh}[2\,r]
\end{array}\right.$$

2.3 Gravity-induced transformation

The time-evolution operator (cf. eq. (6.20)) involves three transformations on the phonons: displacement, two-mode squeezing and mode-mixing. In particular, we consider the two-mode squeezing transformation induced by the oscillating sphere under the resonant condition $\Omega = \omega_l + \omega_n$:

$$\hat{U}_g(\xi) = \exp\left(\xi\,\hat{b}_l^\dagger\,\hat{b}_n^\dagger + \xi^*\,\hat{b}_l\,\hat{b}_n\right),$$

where $\xi = s\,e^{i\phi_B}$ (cf. eq. (6.23)). The associated symplectic transformation, denoted S_ϵ , carry the physical parameter we are interested in measuring: $\epsilon\, = a_\Omega$.

2.4 Interferometric Closure

Subsequently, the 'beams' are 'brought together' making the reverse operations corresponding to the tritter and the two-mode squeezing. The state of the full interferometer is defined as

$$\begin{aligned} d &:= S.\,d_0 \\ &= S_{\text{tr}}(-\theta)\;\; S_{2\,\text{sq}}(-r)\;\; S(\epsilon)\;\; S_{\text{tr}}(\theta)\;\; S_{2\,\text{sq}}(r)\;\; d_0 \end{aligned}$$

$$\begin{aligned} \Gamma &:= S.\Gamma_0.S^\dagger \\ &= \;S_{\text{tr}}(-\theta)\; S_{2\,\text{sq}}(-r)\;\; S(\epsilon)\;\; S_{\text{tr}}(\theta)\; S_{2\,\text{sq}}(r)\; \Gamma_0\; \left[S_{\text{tr}}(-\theta)\; S_{2\,\text{sq}}(-r)\; S(\epsilon)\;\; S_{\text{tr}}(\theta)\; S_{2\,\text{sq}}(r)\;\right]^\dagger \end{aligned}$$

However, since the QFI is independent of the particular measurement scheme used, we only need to consider:

$$\begin{aligned} d &= S(\epsilon)\;\; S_{\text{tr}}(\theta)\;\; S_{2\,\text{sq}}(r)\;\; d_0 \\ &= S_\epsilon\, S_0\;\; d_0 \end{aligned}$$

$$\begin{aligned} \Gamma &= \;S(\epsilon)\;\; S_{\text{tr}}(\theta)\;\; S_{2\,\text{sq}}(r)\;\; \Gamma_{\text{vac}}\;\left[S(\epsilon)\;\; S_{\text{tr}}(\theta)\;\; S_{2\,\text{sq}}(r)\right]^\dagger \\ &= S_\epsilon\, \Gamma_0\, {S_\epsilon}^\dagger \end{aligned}$$

3. Preliminary computations

Gravitational-induced two-mode squeezing:

If the squeezing transformation is chosen, the symplectic matrix of the transformation associated to the unitary transformation $\hat{U}_g$ is:

In[ ]:=

$$\mathrm{S}_\epsilon = \begin{pmatrix} 1 & 0 & 0 & 0 & 0 & 0 \\ 0 & \mathrm{Cosh}[s] & 0 & 0 & 0 & -e^{i\,\phi_B}\,\mathrm{Sinh}[s] \\ 0 & 0 & \mathrm{Cosh}[s] & 0 & -e^{i\,\phi_B}\,\mathrm{Sinh}[s] & 0 \\ 0 & 0 & 0 & 1 & 0 & 0 \\ 0 & 0 & -e^{-i\,\phi_B}\,\mathrm{Sinh}[s] & 0 & \mathrm{Cosh}[s] & 0 \\ 0 & -e^{-i\,\phi_B}\,\mathrm{Sinh}[s] & 0 & 0 & 0 & \mathrm{Cosh}[s] \end{pmatrix};$$

We start by calculating $P_\epsilon = S_\epsilon^{-1}\,\dot{S}_\epsilon$.

$P_\epsilon =$

In[ ]:=

```
MatrixForm[FullSimplify[Inverse[Sϵ].D[Sϵ, s]]]
```

In[6]:=

$$\mathrm{P}_\epsilon = \begin{pmatrix} 0 & 0 & 0 & 0 & 0 & 0 \\ 0 & 0 & 0 & 0 & 0 & -e^{i\,\phi_B} \\ 0 & 0 & 0 & 0 & -e^{i\,\phi_B} & 0 \\ 0 & 0 & 0 & 0 & 0 & 0 \\ 0 & 0 & -e^{-i\,\phi_B} & 0 & 0 & 0 \\ 0 & -e^{-i\,\phi_B} & 0 & 0 & 0 & 0 \end{pmatrix};$$

And now, we calculate $P = S_0^{-1}\,P_\epsilon\,S_0$.

$P =$

In[ ]:=

```
MatrixForm[FullSimplify[Inverse[S0].Pϵ.S0]]
```

In[ ]:=

$$\mathrm{P} = \begin{pmatrix} 0 & -\frac{i\,e^{i\,(\vartheta-\vartheta_{sq}+\phi_B)}\,\mathrm{Cos}[\theta]\,\mathrm{Sin}[\theta]\,\mathrm{Sinh}[r]}{\sqrt{2}} \\ -\frac{i\,e^{-i\,(\vartheta-\vartheta_{sq}+\phi_B)}\,\mathrm{Cos}[\theta]\,\mathrm{Sin}[\theta]\,\mathrm{Sinh}[r]}{\sqrt{2}} & -\frac{1}{4}\,i\,(3+\mathrm{Cos}[2\,\theta])\,\mathrm{Sin}\left[\vartheta_{sq}-\phi_B\right]\,\mathrm{Sinh}[2\,r] \\ -\frac{i\,e^{-i\,(\vartheta-\vartheta_{sq}+\phi_B)}\,\mathrm{Cos}[\theta]\,\mathrm{Sin}[\theta]\,\mathrm{Sinh}[r]}{\sqrt{2}} & \frac{1}{2}\,i\,\mathrm{Sin}[\theta]^2\,\mathrm{Sin}\left[\vartheta_{sq}-\phi_B\right]\,\mathrm{Sinh}[2\,r] \\ e^{-i\,(2\,\vartheta+\phi_B)}\,\mathrm{Sin}[\theta]^2 & -\frac{i\,e^{-i\,(\vartheta+\phi_B)}\,\mathrm{Cos}[\theta]\,\mathrm{Cosh}[r]\,\mathrm{Sin}[\theta]}{\sqrt{2}} \\ -\frac{i\,e^{-i\,(\vartheta+\phi_B)}\,\mathrm{Cos}[\theta]\,\mathrm{Cosh}[r]\,\mathrm{Sin}[\theta]}{\sqrt{2}} & \frac{1}{2}\,e^{-i\,\phi_B}\,\mathrm{Sin}[\theta]^2\left(\mathrm{Cosh}[r]^2-e^{-2\,i\,(\vartheta_{sq}-\phi_B)}\,\mathrm{Sinh}[r]^2\right) \\ -\frac{i\,e^{-i\,(\vartheta+\phi_B)}\,\mathrm{Cos}[\theta]\,\mathrm{Cosh}[r]\,\mathrm{Sin}[\theta]}{\sqrt{2}} & \frac{1}{4}\,e^{-i\,(2\,\vartheta_{sq}+\phi_B)}\,(3+\mathrm{Cos}[2\,\theta])\left(-e^{2\,i\,\vartheta_{sq}}\,\mathrm{Cosh}[r]^2+e^{2\,i\,\phi_B}\,\mathrm{Sinh}[r]^2\right) \end{pmatrix}$$

4. QFI computation

Having calculated the state of the phonons under the gravitational influence of the oscillating sphere, given by the displacement vector ***d***, the covariance matrix Γ, and the derived matrix P, the QFI given by (D.1) can be readily computed.

4.1 First term

We calculate the first term for the QFI

```
In[ ]:= FullSimplify[
 2 (P[[1, 4]] × P[[4, 1]] + P[[2, 5]] × P[[5, 2]] + P[[3, 6]] × P[[6, 3]] + P[[1, 5]] × P[[4, 2]] + P[[2, 4]] ×
      P[[5, 1]] + P[[1, 6]] × P[[4, 3]] + P[[3, 4]] × P[[6, 1]] + P[[2, 6]] × P[[5, 3]] + P[[3, 5]] × P[[6, 2]])]
```

Out[ ]=

$$\frac{1}{4}\Big((11+4\,\mathrm{Cos}[2\,\theta]+\mathrm{Cos}[4\,\theta])\,\mathrm{Cosh}[r]^4+8\,\mathrm{Sin}[\theta]^4+(11+4\,\mathrm{Cos}[2\,\theta]+\mathrm{Cos}[4\,\theta])\,\mathrm{Sinh}[r]^4+\mathrm{Cosh}[r]^2\left(4\,\mathrm{Sin}[2\,\theta]^2-2\,(11+4\,\mathrm{Cos}[2\,\theta]+\mathrm{Cos}[4\,\theta])\,\mathrm{Cos}\left[2\left(\vartheta_{\mathrm{sq}}-\phi_{\mathrm{B}}\right)\right]\mathrm{Sinh}[r]^2\right)\Big)$$

Which can be equivalently re-expressed
as:

$$= 2\left(1-\mathrm{Cos}^4[\theta]\right) + \mathrm{Sin}^2[2\,\theta]\,\mathrm{Sinh}^2[r] + 2\left(1+\mathrm{Cos}^4[\theta]\right)\mathrm{Sin}^2\left[\vartheta_{\mathrm{sq}}-\phi_B\right]\mathrm{Sinh}^2[2\,r]$$
$$= 4-2\left(1+\mathrm{Cos}^4[\theta]\right) + \mathrm{Sin}^2[2\,\theta]\,\mathrm{Sinh}^2[r] + 2\left(1+\mathrm{Cos}^4[\theta]\right)\mathrm{Sin}^2\left[\vartheta_{\mathrm{sq}}-\phi_B\right]\mathrm{Sinh}^2[2\,r]\,.$$

4.2 Second term

Let’s calculate the second term which reads: $2\,(P_\epsilon\, d_0)^\dagger\, \Gamma_0^{-1}\,(P_\epsilon\, d_0)$. We start computing

```
In[20]:= MatrixForm[FullSimplify[Pϵ.S0.dcoh]]
```

Out[20]//MatrixForm=

$$\begin{pmatrix} 0 \\ \frac{\mathbb{i}\, e^{\mathbb{i}\,(\vartheta+\phi_{\mathrm{B}})}\,\mathrm{Conjugate}[\alpha]\,\mathrm{Sin}[\theta]}{\sqrt{2}} \\ \frac{\mathbb{i}\, e^{\mathbb{i}\,(\vartheta+\phi_{\mathrm{B}})}\,\mathrm{Conjugate}[\alpha]\,\mathrm{Sin}[\theta]}{\sqrt{2}} \\ 0 \\ -\frac{\mathbb{i}\, e^{-\mathbb{i}\,(\vartheta+\phi_{\mathrm{B}})}\,\alpha\,\mathrm{Sin}[\theta]}{\sqrt{2}} \\ -\frac{\mathbb{i}\, e^{-\mathbb{i}\,(\vartheta+\phi_{\mathrm{B}})}\,\alpha\,\mathrm{Sin}[\theta]}{\sqrt{2}} \end{pmatrix}$$

```
In[ ]:= MatrixForm[FullSimplify[Inverse[Γ0]]]
```

In[ ]:=

$$\mathrm{I}\Gamma_0 = \left(\begin{array}{ccc}
\mathrm{Cosh}[r]^2-\mathrm{Cos}[2\,\theta]\,\mathrm{Sinh}[r]^2 & \mathbb{i}\,\sqrt{2}\,e^{\mathbb{i}\,\vartheta}\,\mathrm{Cos}[\theta]\,\mathrm{Sin}[\theta]\,\mathrm{Sinh}[r]^2 & \mathbb{i}\,\sqrt{2}\,e^{\mathbb{i}} \\
-\mathbb{i}\,\sqrt{2}\,e^{-\mathbb{i}\,\vartheta}\,\mathrm{Cos}[\theta]\,\mathrm{Sin}[\theta]\,\mathrm{Sinh}[r]^2 & \frac{1}{4}\left(1+3\,\mathrm{Cosh}[2\,r]+2\,\mathrm{Cos}[2\,\theta]\,\mathrm{Sinh}[r]^2\right) & \\
-\mathbb{i}\,\sqrt{2}\,e^{-\mathbb{i}\,\vartheta}\,\mathrm{Cos}[\theta]\,\mathrm{Sin}[\theta]\,\mathrm{Sinh}[r]^2 & -\mathrm{Sin}[\theta]^2\,\mathrm{Sinh}[r]^2 & \frac{1}{4}\,(1+3\,\mathrm{Cos} \\
-e^{-\mathbb{i}\,(2\,\vartheta+\vartheta_{\mathrm{sq}})}\,\mathrm{Sin}[\theta]^2\,\mathrm{Sinh}[2\,r] & -\frac{\mathbb{i}\,e^{-\mathbb{i}\,(\vartheta+\vartheta_{\mathrm{sq}})}\,\mathrm{Sin}[2\,\theta]\,\mathrm{Sinh}[2\,r]}{2\,\sqrt{2}} & -\mathbb{i} \\
-\frac{\mathbb{i}\,e^{-\mathbb{i}\,(\vartheta+\vartheta_{\mathrm{sq}})}\,\mathrm{Sin}[2\,\theta]\,\mathrm{Sinh}[2\,r]}{2\,\sqrt{2}} & -e^{-\mathbb{i}\,\vartheta_{\mathrm{sq}}}\,\mathrm{Cosh}[r]\,\mathrm{Sin}[\theta]^2\,\mathrm{Sinh}[r] & \frac{1}{4}\,e^{-\mathbb{i}\,\vartheta_{\mathrm{s}}} \\
-\frac{\mathbb{i}\,e^{-\mathbb{i}\,(\vartheta+\vartheta_{\mathrm{sq}})}\,\mathrm{Sin}[2\,\theta]\,\mathrm{Sinh}[2\,r]}{2\,\sqrt{2}} & \frac{1}{4}\,e^{-\mathbb{i}\,\vartheta_{\mathrm{sq}}}\,(3+\mathrm{Cos}[2\,\theta])\,\mathrm{Sinh}[2\,r] & -e^{-\mathbb{i}\,\vartheta_{\mathrm{sq}}}
\end{array}\right.$$

Setting $\alpha = \left|\alpha\right| e^{\mathrm{i}\vartheta_0}$, we get for the second term in the QFI:

In[ ]:=

$$\mathbf{FullSimplify}\Big[\, 2\left(0\;\; -\frac{i\,e^{-i\,(\vartheta+\phi_B-\vartheta_0)}\,\alpha\,\mathrm{Sin}[\theta]}{\sqrt{2}}\;\; -\frac{i\,e^{-i\,(\vartheta+\phi_B-\vartheta_0)}\,\alpha\,\mathrm{Sin}[\theta]}{\sqrt{2}}\;\; 0\;\; \frac{i\,e^{i\,(\vartheta+\phi_B-\vartheta_0)}\,\alpha\,\mathrm{Sin}[\theta]}{\sqrt{2}}\;\; \frac{i\,e^{i\,(\vartheta+\phi_B-\vartheta_0)}\,\alpha\,\mathrm{Sin}[\theta]}{\sqrt{2}}\right).\mathrm{I}\Gamma_0. \begin{pmatrix} 0 \\ \frac{i\,e^{i\,(\vartheta+\phi_B-\vartheta_0)}\,\alpha\,\mathrm{Sin}[\theta]}{\sqrt{2}} \\ \frac{i\,e^{i\,(\vartheta+\phi_B-\vartheta_0)}\,\alpha\,\mathrm{Sin}[\theta]}{\sqrt{2}} \\ 0 \\ -\frac{i\,e^{-i\,(\vartheta+\phi_B-\vartheta_0)}\,\alpha\,\mathrm{Sin}[\theta]}{\sqrt{2}} \\ -\frac{i\,e^{-i\,(\vartheta+\phi_B-\vartheta_0)}\,\alpha\,\mathrm{Sin}[\theta]}{\sqrt{2}} \end{pmatrix}\Big]$$

Out[ ]=

$$\left\{\left\{4\,\alpha^2\,\mathrm{Sin}[\theta]^2\,\left(\mathrm{Cosh}[r]^2+\mathrm{Cos}[2\,\theta]\,\mathrm{Sinh}[r]^2-\mathrm{Cos}[\theta]^2\,\mathrm{Cos}\left[2\,\vartheta_0+\vartheta_{sq}-2\,(\vartheta+\phi_B)\right]\,\mathrm{Sinh}[2\,r]\right)\right\}\right\}$$

Which can be equivalently re-expressed
as:

$$=\;|\;\alpha_0\;|^2\left\{4\,\mathrm{Sin}^4[\theta]-\mathrm{Sinh}[2\,r]\,\mathrm{Cos}\left[2\,\vartheta_0+\vartheta_{sq}-2\,(\vartheta+\phi_B)\right]\mathrm{Sin}^2[2\,\theta]\;+\;\mathrm{Cosh}[2\,r]\,\mathrm{Sin}^2[2\,\theta]\right\}.$$

Putting both results together, we obtain that the QFI is proportional to:

$$4-2\left(1+\mathrm{Cos}^4[\theta]\right)\;+\;\mathrm{Sin}^2[2\,\theta]\,\mathrm{Sinh}^2[r]\;+\;2\left(1+\mathrm{Cos}^4[\theta]\right)\mathrm{Sin}^2\left[\vartheta_{sq}-\phi_B\right]\mathrm{Sinh}^2[2\,r]\,+$$
$$|\;\alpha_0\;|^2\left\{4\,\mathrm{Sin}^4[\theta]-\mathrm{Sinh}[2\,r]\,\mathrm{Cos}\left[2\,\vartheta_0+\vartheta_{sq}-2\,(\vartheta+\phi_B)\right]\mathrm{Sin}^2[2\,\theta]\;+\;\mathrm{Cosh}[2\,r]\,\mathrm{Sin}^2[2\,\theta]\right\},$$

where he have left out the factors involving the ϵ derivative of $\hat{U}_g$ as here we left the squeezing parameter s undetermined, but is corresponds to the factor $r_{l\,n}$ appearing in (6.21).

Appendix D

Precision Evaluation

The Mathematica file used to calculate the precision for measuring a_Ω in (6.37) and to check the consistency with respect to the experimental constraints is attached.

Precision to measure acceleration amplitude

Numerical evaluation of the precision for measuring the acceleration amplitude a_Ω.

Fundamental constants

```
In[65]:=  r = 5.2917 × 10^-11;        (* Bohr radius, m *)
          ℏ = 1.055 × 10^-34;         (* Reduced Planck's constant, kg.m^2.s^-1 *)
          k_B = 1.3806 × 10^-23;      (* Boltzmann constant, m^2.kg.s^-2.K^-1 *)
```

Experimental parameters

```
In[68]:=  m = 1.44 × 10^-25;          (* Rubidium mass, kg *)
          a = 99 r;                   (* Rubidium scattering length, m *)
          d = 5.8 × 10^-42;           (* Rubidium decay constant , m^6/s *)

          L = 500 × 10^-6;            (* Length of the BEC, m *)
          N_a = 4 × 10^6;             (* Number of atoms *)
          ρ = 1 × 10^20;              (* BEC density, m^-3 *)
          α = √(N_a/(π ρ L^3));       (* BEC's length-to-radius ratio *)
          N_p = 1100;                 (* Number of phonons *)

          n = 1;                      (* Phonon's number modes (l+n=odd)   *)
          l = 2;
          t = 1;
          texp = 0.1 × 3/(2 d ρ^2);
          (* Single-experiment time (0.1 times the BEC half-life), s *)

          T = 10^-9;                  (* Temperature, K *)
          θ = 0.31;                   (* Tritter angle *)
          τ = 2 592 000;
          (* Total time of estimation (3 153 600 ~ 36 days ), s *)
          γ = 10^-2;                  (* Damping rate, s^-1 *)

          Print["α = ", N[α, 4]]
          (* N[] avoids value displaying in terms of π *)
          Print["Time of experiment: ", texp, " s"]
```

```
α = 0.01009

Time of experiment: 2.58621 s
```

Derived parameters

In[86]:=

$$c = \sqrt{\frac{4\,\pi\,\hbar^2\,a}{m^2} \times \frac{N_a}{\pi\,\alpha^2\,L^3}}; \qquad \text{(* Speed of sound, m/s *)}$$

$$\text{Rep} = \frac{\tau}{t}; \qquad \text{(* Number of repetitions *)}$$

$$\Omega = \frac{c\,\pi}{L}\,(n + l); \qquad \text{(* Resonant frequency, s}^{-1}\text{ *)}$$

$$\omega_n = \frac{c\,\pi}{L}\,n; \qquad \text{(* Modes frequency, s}^{-1}\text{ *)}$$

$$\omega_l = \frac{c\,\pi}{L}\,l;$$

$$Q = \frac{\Omega}{\gamma}; \qquad \text{(* Quality factor *)}$$

$$\text{Print}\left[\text{"Speed of sound: "},\ 10^3\,c,\ \text{" mm/s"}\right]$$

```
Print["Frequency: ", Ω, " Hz"]
```

```
Speed of sound: 1.87979 mm/s

Frequency: 35.4333 Hz
```

Precision

In[96]:=

$$\Delta a_\Omega = \frac{\alpha\,\hbar\,\pi^3\,\sqrt{2\,n\,l}\,\left(l^2 - n^2\right)^2}{16\,N_a\,m\,\theta\,\sqrt{L\,a\,\tau\,t\,N_p}\,\left(l^2 + n^2\right)};$$

```
Print["Sensitivity: ", ΔaΩ, " m/s"]
```

Sensitivity: 4.81378×10^{-16} m/s

Constraints

1) Condition for dilute regime, $\frac{N_0\,a^3}{V} << 1$

In[102]:=

$$\frac{N_a\,a^3}{\pi\,\alpha^2\,L^3}$$

$$\text{TrueQ}\left[\frac{N_a\,a^3}{\pi\,\alpha^2\,L^3} \le 0.1\right]$$

Out[102]=

```
0.0000143778
```

Out[103]=

```
True
```

2) Condition for Bogoliubov approximation, number of excited atoms << number of atoms in the condensate ($N_{\text{exc}} << N_0$)

In[107]:=

$$\frac{m\,c^2}{\hbar\,(\omega_n+\omega_1)}\,N_p$$

$$N_a$$

$$\text{TrueQ}\left[\frac{m\,c^2}{\hbar\,(\omega_n+\omega_1)}\,N_p \le 0.1\,N_a\right]$$

Out[107]=

```
149 731.
```

Out[108]=

```
4 000 000
```

Out[109]=

```
True
```

3) Condition for phonon regime, $\hbar\omega_n << \mathrm{m}\,c^2$

In[110]:=

$$\hbar\,\omega_1$$

$$m\,c^2$$

$$\text{TrueQ}\left[\hbar\,\omega_1 \le 0.1\,m\,c^2\right]$$

Out[110]=

$$2.49214\times10^{-33}$$

Out[111]=

$$5.08842\times10^{-31}$$

Out[112]=

```
True
```

5) Condition for low-temperature regime, $k_B\,T << \mu = m\,c^2$

In[113]:=

$$k_B\,T$$

$$m\,c^2$$

$$\text{TrueQ}\left[k_B\,T \le 0.1\,m\,c^2\right]$$

Out[113]=

$$1.3806\times10^{-32}$$

Out[114]=

$$5.08842\times10^{-31}$$

Out[115]=

```
True
```

6) We need to bound the density from above to extend the life-time t_{hl} of the BEC

In[116]:=

$$\frac{3}{2\,d\,\rho^2}$$

Out[116]=

```
25.8621
```

7) In order to keep the ratio α small, we have to make the density as big as possible.

$$\alpha = \sqrt{\frac{N_0}{\pi\,\rho\,L^3}}$$

The optimal density is the one that allows us enough time for doing the experiment while keeping α small.

Dampings

Landau damping ($\hbar\omega_n << k_B T << \mu = m c^2$):

In[117]:=

$$\Gamma_L = \frac{3\pi^3}{40} \times \frac{(k_B T)^4 \omega_1}{m \rho \hbar^3 c^5}$$

Out[117]=

$$5.02842 \times 10^{-6}$$

Beliaev damping ($\hbar\omega_n << k_B T << \mu = m c^2$):

In[118]:=

$$\Gamma_B = \frac{3}{640\pi} \times \frac{\hbar (\omega_1)^5}{m \rho c^5}$$

Out[118]=

$$3.42555 \times 10^{-12}$$

Decoherence time:

```
(* γ corresponds to the dominating damping process, r0 is the squeezing parameter *)
```

$$t_{min} = \frac{1}{\gamma} \text{Log}\left[\frac{1 - 2 \text{Cosh}[2 r_0]}{1 - \text{Cosh}[r_0]}\right];$$

$$t_{min} = 10\, t\, \text{Log}\left[\frac{1 - 2 \text{Cosh}[2 (0.001)]}{1 - \text{Cosh}[0.001]}\right]$$

Out[ ]=

$$369.827$$

Others

Squeezing parameter (linear term, without potential factor):

$$\frac{2 m^2 c^2 L^2 (l^2 + n^2)}{\sqrt{2 n l} (l^2 - n^2)^2 \pi^2 \hbar^2}$$

$$s = \frac{m^2 c^3 L (l^2 + n^2)\, t}{2 \sqrt{n l} (l - n)^2 \hbar^2}$$

Out[ ]=

$$50427.7$$

Number of phonons:

In[ ]:= $2\, \text{Sinh}[4.8]^2$

Out[ ]=

$$7381.39$$

Bibliography

[1] Ashby, N. (2003) ‘Relativity in the Global Positioning System’ *Living Rev. Relativity* 6, 1.

[2] Ursin, R. et al. (2009) ‘Space-quest, experiments with quantum entanglement in space’ *Europhysics News* 40, 26.

[3] S. Schiller et al. (2012) ‘The space optical clocks project: Development of high-performance transportable and breadboard optical clocks and advanced subsystems’ *2012 European Frequency and Time Forum* pp. 412-418

[4] Ahmadi, M. et al. (2014) ‘Relativistic Quantum Metrology: Exploiting relativity to improve quantum measurement technologies’ *Sci Rep* 4, 4996.

[5] Birrell, N. and Davies, P. (1982) *Quantum Fields in Curved Space.* Cambridge University Press.

[6] Abbott, B.P. et al. (LIGO Scientific Collaboration and Virgo Collaboration) (2016) ‘Observation of Gravitational Waves from a Binary Black Hole Merger’ *Phys. Rev. Lett.* 116, 061102.

[7] Alsing, P. M. and Fuentes, I. (2012) ‘Observer dependent entanglement’ *Class. Quantum Grav.* 29, 224001.

[8] Aspachs, M.; Adesso, G. and Fuentes, I. (2010) ‘Optimal quantum estimation of the Unruh-Hawking effect’ *Phys. Rev. Lett.* 105, 151301.

[9] Hosler, D. (2013) ‘Relativistic Quantum Communication’, PhD thesis, University of Sheffield, Sheffield.

[10] Downes, T. G.; Milburn, G. J. and Caves, C. M. (2012) ‘Optimal Quantum Estimation for Gravitation’ *e-print* arXiv:1108.5220[gr-qc].

[11] Hartley, D.; Käding, C.; Howl, R. and Fuentes, I. (2024) ‘Quantum-enhanced screened dark energy detection’ *Eur. Phys. J. C* 84, 49.

[12] Wolf, P.; Bordé, C.J.; Clairon, A. et al. (2009) ‘Quantum physics exploring gravity in the outer solar system: the SAGAS project’ *Exp Astron* 23, 651.

[13] Dimopoulos, S. et al. (2008) ‘Atomic gravitational wave interferometric sensor’ *Phys. Rev. D* 78, 122002.

[14] Moore, G. (1970) ‘Quantum Theory of the Electromagnetic Field in a Variable-Length One-Dimensional Cavity’ *J. Math. Phys.* 11, 269.

[15] Wilson, C.; Johansson, G.; Pourkabirian, A. et al. (2011) ‘Observation of the dynamical Casimir effect in a superconducting circuit’ *Nature* 479, 376.

[16] Lock, M. and Fuentes, I. (2017) ‘Dynamical Casimir effect in curved spacetime’ *New J. Phys.* 19, 073005.

[17] Howl, R. and Fuentes, I. (2023) ‘Quantum Frequency Interferometry: with applications ranging from gravitational wave detection to dark matter searches’ *AVS Quantum Sci.* 5, 014402.

[18] Sabin C.; Bruschi D.; Ahmadi M. and Fuentes I. (2014) ‘Phonon creation by gravitational waves’ *New J. Phys.* 16, 085003.

[19] Bravo, T.; Rätzel, D. and Fuentes, I. (2020) ‘Phononic gravity gradiometry with Bose-Einstein condensates’ *e-print* arXiv:2001.10104[quant-ph].

[20] Perlmutter, S. *et al.* (1999) ‘Measurements of Ω and Λ from 42 High-Redshift Supernovae’ *Astrophys. J.* 517, 565.

[21] Riess, A. G. *et al.* (1998) ‘Observational Evidence from Supernovae for an Accelerating Universe and a Cosmological Constant’ *Astron. J.* 116, 1009.

[22] Rubin, V. (1983) ‘Dark matter in spiral galaxies’ *Scientific American* 248, 96.

[23] Arbey, A. and Mahmoudi, F. (2021) ‘Dark matter and the early Universe: A review’ *Progress in Particle and Nuclear Physics* 119, 103865.

[24] Buchdahl, H. (1970) ‘Non-Linear Lagrangians and Cosmological Theory’ *Mon.Not.Roy.Astron.Soc.* 150, 1.

[25] Hawking, S. (1974) ‘Black hole explosions?’ *Nature* 248, 30.

[26] Hawking, S. (1975) ‘Particle creation by black-holes’ *Comm. Math. Phys.* 43, 199.

[27] Parker, L. (1968) ‘Particle Creation in Expanding Universes’ *Phys. Rev. Lett.* 21, 19.

[28] Parker, L. (1969) ‘Quantized Fields and Particle Creation in Expanding Universes. I’ *Phys. Rev.* 183, 1057.

[29] Howl, R.; Hackermüller, L.; Bruschi, D. and Fuentes, I. (2018) ‘Gravity in the quantum lab’ *Advances in Physics: X* 3, 1383184.

[30] Carroll, S. (2019) *Spacetime and Geometry: An Introduction to General Relativity.* Cambridge University Press.

[31] Wald, Robert M. (2010) *General Relativity.* University of Chicago Press.

[32] Greiner, W. and Reinhardt, J. (1996) *Field Quantization.* Springer Science & Business Media.

[33] Davis, H.T. and Thomson, K.T. (2000) *Linear Algebra and Linear Operators in Engineering.* Academic Press.

[34] Serafini, A. (2017) *Quantum Continuous Variables: A Primer of Theoretical Methods.* CRC Press.

[35] Weedbrook, Christian et al. (2012) ‘Gaussian Quantum Information’ *Rev. Mod. Phys.* 80, 621.

[36] Ferraro, A.; Olivares, S and Paris, M (2005) *Gaussian states in continuous variable quantum information.* Napoli Series on Physics and Astrophysics, Bibliopolis.

[37] Adesso, G.; Ragy, S. and Lee, A. (2014) ‘Continuous Variable Quantum Information: Gaussian States and Beyond’ *Open systems and information dynamics* 21, 1440001.

[38] Andersen, U. et al. (2016) ‘30 years of squeezed light generation’ *Physica Scripta* 91, 053001.

[39] Adesso, G. and Illuminati, F. (2007) ‘Entanglement in continuous-variable systems: recent advances and current perspectives’ *J. Phys. A: Math. Theor.* 40, 7821.

[40] Wald, R. (1994) *Quantum Field Theory in Curved Spacetime and Black Hole Thermodynamics*. University of Chicago Press.

[41] Mandl, F. and Shaw, G. (2010) *Quantum Field Theory*. Wiley.

[42] Roman, S. (2007) *Advanced Linear Algebra*. Graduate Texts in Mathematics. Springer.

[43] Simon, R.; Mukunda, N. and Dutta, B. (1994) ‘Quantum-noise matrix for multimode systems: U(n) invariance, squeezing, and normal forms’ *Phys. Rev. A* 49, 1567.

[44] Safranek, D. (2016) ‘Gaussian quantum metrology and space-time probes’, PhD thesis, University of Nottingham, Nottingham.

[45] Safranek, D. and Fuentes, I. (2016) ‘Optimal probe states for the estimation of Gaussian unitary channels’ *Phys. Rev. A* 94, 062313.

[46] Hall, B. (2003) *Lie Groups, Lie Algebras, and Representations: An Elementary Introduction*. Springer Science & Business Media.

[47] Arvind; Dutta, B.; Mukunda, N. and Simon, R. (1995) ‘The real symplectic groups in quantum mechanics and optics’ *Pramana* 45, 471.

[48] Williamson, j. (1936) ‘On the Algebraic Problem Concerning the Normal Forms of Linear Dynamical Systems’ *Am. J. Math.* 58, 141.

[49] Scully, M. and Zubairy, M. (1997) *Quantum Optics*. Cambridge University Press.

[50] Leroux, I.; Schleier-Smith, M. and Vuletić, V. (2010) ‘Orientation-Dependent Entanglement Lifetime in a Squeezed Atomic Clock’ *Phys.Rev.Lett.* 104, 250801.

[51] Louchet-Chauvet, A. et al. (2010) ‘Entanglement-assisted atomic clock beyond the projection noise limit’ *New J. Phys.* 12, 065032.

[52] Okano, M. et al. (2015) '0.54 μm resolution two-photon interference with dispersion cancellation for quantum optical coherence tomography' *Sci. Rep.* 5, 18042.

[53] Arai, K. et al. (2018) 'Geometric phase magnetometry using a solid-state spin' *Nat. Commun.* 9, 4996.

[54] Tse, M. et al. (2019) 'Quantum-Enhanced Advanced LIGO Detectors in the Era of Gravitational-Wave Astronomy' *Phys. Rev. Lett.* 123, 231107.

[55] Polino, E. et al. (2020) 'Photonic quantum metrology' *AVS Quantum Sci.* 2, 024703.

[56] Giovannetti, V.; Lloyd, S. and Maccone, L. (2006) 'Quantum metrology' *Phys. Rev. Lett.* 96, 010401.

[57] Helstrom, C. (1976) *Quantum Detection and Estimation Theory.* Academic Press.

[58] Holevo, A. (2011) *Probabilistic and Statistical Aspects of Quantum Theory.* Springer Science & Business Media.

[59] Kok, P. and Lovett, B.W. (2010) *Introduction to Optical Quantum Information Processing.* Cambridge University Press.

[60] Braunstein, S. L. and Caves, C. M. (1994) 'Statistical distance and the geometry of quantum states' *Phys. Rev. Lett.* 72, 3439.

[61] Cramér, H. (1946) *Mathematical methods of statistics.* Princeton University Press.

[62] Paris, M. (2009) 'Quantum estimation for quantum technology' *Int. J. Quant. Inf.* 7, 125.

[63] Bures, D. (1969) 'An Extension of Kakutani's Theorem on Infinite Product Measures to the Tensor Product of Semifinite w*-Algebras' *Trans. Amer. Math. Soc.* 135, 199.

[64] Ulhman, A. (1976) 'The "transition probability" in the state space of a $*$-algebra' *Rep. Math. Phys.* 9, 273.

[65] Sidhu, J. and Kok, P. (2020) ‘Geometric perspective on quantum parameter estimation’ *AVS Quantum Sci.* 2, 014701.

[66] Safranek, D.; Lee, A. and Fuentes, I. (2015) ‘Quantum parameter estimation using multi-mode Gaussian states’ *New J. Phys.* 17, 073016.

[67] Monras, A. (2013) ‘Phase space formalism for quantum estimation of Gaussian states’ *e-print* arXiv:1303.3682[quant-ph].

[68] Pinel, O. et al. (2013) ‘Quantum parameter estimation using general single-mode Gaussian states’ *Phys. Rev. A* 88, 040102.

[69] Sabín, C.; Kohlrus, J.; Bruschi, D. and Fuentes, I. (2016) ‘Thermal noise in BEC-phononic gravitational wave detectors’ *EPJ Quantum Technology* 3, 8.

[70] Giovannetti, V.; Lloyd, S. and Maccone, L. (2011) ‘Advances in quantum metrology’ *Nature Photonics* 5, 222.

[71] Lindkvist, J. et al. (2015) ‘Motion and gravity effects in the precision of quantum clocks’ *Sci. Rep.* 5, 10070.

[72] Bruschi, D. et al. (2014) ‘Quantum estimation of the Schwarzschild spacetime parameters of the Earth’ *Phys. Rev. D* 90, 124001.

[73] Pethick, C. and Smith, H. (2001) *Bose-Einstein Condensation in Dilute Gases.* Cambridge University Press.

[74] Bose, S. N. (1924) ‘Plancks Gesetz und Lichtquantenhypothese’ *Z. Physik* 26, 178.

[75] Einstein, A. (2005). ‘Quantentheorie des einatomigen idealen Gases’ *Sitzungsberichte der Preussischen Akademie der Wissenschaften* (in German) 1, 3.

[76] London, F. (1938) ‘The λ-Phenomenon of Liquid Helium and the Bose-Einstein Degeneracy’ *Nature* 141, 643-644.

[77] Landau, L. (1941) ‘Theory of the Superfluidity of Helium II’ *Phys. Rev.* 60, 356.

[78] Bogoliubov, N. (1947) ‘On the theory of superfluidity’ *J. Phys. (USSR)* 11, 23.

[79] Landau, L. and Lifshitz, E. (1951) *Statisticheskai Fizika* (in Russian). Fizmatgiz, Moscow.

[80] Penrose, O. (1951) 'CXXXVI. On the quantum mechanics of helium II' *The London, Edinburgh, and Dublin Philosophical Magazine and Journal of Science* 42, 1373.

[81] Penrose, O. and Onsager, L. (1956) 'Bose-Einstein Condensation and Liquid Helium' *Phys. Rev.* 104, 576

[82] E. P. Gross (1961) 'Structure of a quantized vortex in boson systems' *Nuovo Cim.* 20, 454.

[83] Pitaevskii, L. 'Vortex lines in an imperfect Bose gas' *Sov. Phys. JETP* 13, 451.

[84] Anderson, M. H. et al. (1995) 'Observation of Bose-Einstein Condensation in a Dilute Atomic Vapor' *Science* 269, 198.

[85] Davis, K. B. et al. (1995) 'Bose-Einstein Condensation in a Gas of Sodium Atoms' *Phys. Rev. Lett.* 75, 3969.

[86] Pitaevskii, L. and Stringari, S. (2016) *Bose-Einstein condensation and Superfluidity* Oxford University Press.

[87] Landau L. D. and Lifshitz, E. M. (1987) *Quantum Mechanics.* Pergamon Press.

[88] Fagnocchi, S. (2010) 'Relativistic Bose-Einstein condensates: a new system for analogue models of gravity' *New J.Phys.* 12, 095012.

[89] Bruschi, D. et al. (2014) 'Testing the effects of gravity and motion on quantum entanglement in space-based experiments' *New J. Phys.* 16, 053041.

[90] Visser, M. and Molina-Paris, C. (2010) 'Acoustic geometry for general relativistic barotropic irrotational fluid flow' *New J.Phys.* 12, 095014.

[91] Hartley, D.; Bravo, T.; Ratzel, D.; Howl, R. and Fuentes, I. (2018) 'Analogue simulation of gravitational waves in a $3+1$-dimensional Bose-Einstein condensate' *Phys. Rev. D* 98, 025011.

[92] Belenchia, A. et al. (2022) 'Quantum physics in space' *Physics Reports* 951, 1.

[93] Frye, K. et al. (2021) 'The Bose-Einstein Condensate and Cold Atom Laboratory' *EPJ Quant. Tech.* 8, 1.

[94] Kasevich, M. and Chu, S. (1991) 'Atomic interferometry using stimulated Raman transitions' *Phys. Rev. Lett.* 67, 181.

[95] Kasevich, M. and Chu, S. (1992) 'Measurement of the gravitational acceleration of an atom with a light-pulse atom interferometer' *Appl. Phys. B* 54, 321.

[96] Halkyard, P.; Jones, M. and Gardiner, S. (2010) 'Rotational response of two-component Bose-Einstein condensates in ring traps' *Phys. Rev. A* 81, 061602.

[97] Marti, G.; Olf, R. and Stamper-Kurn, D. (2015) 'Collective excitation interferometry with a toroidal Bose-Einstein condensate' *Phys. Rev. A* 91, 013602.

[98] Debs, J. E. et al. (2011) 'Cold-atom gravimetry with a Bose-Einstein condensate' *Phys. Rev. A* 84, 033610.

[99] Baumgärtner, F. et al. (2010) 'Measuring Energy Differences by BEC Interferometry on a Chip' *Phys. Rev. Lett.* 105, 243003.

[100] Wang, Y. et al. (2005) 'Atom Michelson Interferometer on a Chip Using a Bose-Einstein Condensate' *Phys. Rev. Lett.* 94, 090405.

[101] Kruse, I. et al. (2016) 'Improvement of an Atomic Clock using Squeezed Vacuum' *Phys. Rev. Lett.* 117, 143004.

[102] Kovachy, T. et al. (2015) 'Quantum superposition at the half-metre scale' *Nature* 528, 530.

[103] Tsarev, D.; Ngo, T.; Lee, R. and Alodjants, A. (2019) 'Nonlinear quantum metrology with moving matter-wave solitons' *New J. Phys.* 21, 083041.

[104] Gabbrielli, M.; Pezze, L. and Smerzi, A. (2015) 'Spin-Mixing Interferometry with Bose-Einstein Condensates' *Phys. Rev. Lett.* 115, 163002.

[105] Pelegrí, G.; Mompart, J. and Ahufinger, V. (2018) 'Quantum sensing using imbalanced counter-rotating Bose-Einstein condensate modes' *New J. Phys.* 20, 103001.

[106] Szigeti, S.; Nolan, S.; Close, J. and Haine, S. (2020) ‘High-Precision Quantum-Enhanced Gravimetry with a Bose-Einstein Condensate’ *Phys. Rev. Lett.* 125, 100402.

[107] Müntinga, H. et al. (2013) ‘Interferometry with Bose-Einstein Condensates in Microgravity’ *Phys. Rev. Lett.* 110, 093602.

[108] Lotz, C.; Piest, B.; Rasel, E. and Overmeyer, L. (2023) ‘The Einstein Elevator - Space Experiments at the new Hannover Center for Microgravity Research’ *Europhys. News* 54, 9.

[109] Becker, D. et al. (2018) ‘Space-borne Bose-Einstein condensation for precision interferometry’ *Nature* 562, 391.

[110] Aveline, D. et al. (2020) ‘Observation of Bose-Einstein condensates in an Earth-orbiting research lab’ *Nature* 582, 193.

[111] Hardman, K. et al. (2016) ‘Simultaneous Precision Gravimetry and Magnetic Gradiometry with a Bose-Einstein Condensate: A High Precision, Quantum Sensor’ *Phys. Rev. Lett.* 117, 138501.

[112] Bruschi, D.; Fuentes, I. and Louko, J. (2012) ‘Voyage to Alpha Centauri: Entanglement degradation of cavity modes due to motion’ *Phys. Rev. D* 85, 061701.

[113] Ahmadi, M; Bruschi, D. and Fuentes, I. (2014) ‘Quantum metrology for relativistic quantum fields’ *Phys. Rev. D* 89, 065028.

[114] Rätzel, D.; Howl, R.; Lindkvist, J. and Fuentes, I. (2018) ‘Dynamical response of Bose-Einstein condensates to oscillating gravitational fields’ *New J. Phys.* 20, 073044.

[115] Báez-Camargo, A.; Hartley, D.; Käding, C. and Fuentes, I. (2024) ‘Dynamical Casimir effect with screened scalar fields’ *AVS Quantum Sci.* 6, 045001.

[116] Bravo, T.; Dennis, R.; Bruschi, D. and Fuentes, I. (2020) *Quantum gravimeters and gradiometers.* European Patent EP3983829A1.

[117] Barbado, L.; Báez-Camargo, A. and Fuentes, I. (2020) ‘Evolution of confined quantum scalar fields in curved spacetime. Part I’ *Eur. Phys. J. C* 80, 796.

[118] Barbado, L.; Báez-Camargo, A. and Fuentes, I. (2021) 'Evolution of confined quantum scalar fields in curved spacetime. Part II' *Eur. Phys. J. C* 81, 953.

[119] Rätzel, D. and Fuentes, I. (2019) 'Testing small scale gravitational wave detectors with dynamical mass distributions' *J. Phys. Commun.* 3 025009.

[120] Gaunt, A. et al. (2013) 'Bose-Einstein Condensation of Atoms in a Uniform Potential' *Phys. Rev. Lett.* 110, 200406.

[121] Shammass, I.; Rinott, S.; Berkovitz, A.; Schley, R. and Steinhauer, J. (2012) 'Phonon Dispersion Relation of an Atomic Bose-Einstein Condensate' *Phys. Rev. Lett.* 109, 195301.

[122] Olshanii, M. (1998) 'Atomic Scattering in the Presence of an External Confinement and a Gas of Impenetrable Bosons' *Phys. Rev. Lett.* 81, 938.

[123] Batchelor, M.; Guan, X.; Oelkers, N. and Lee, C. (2005) 'The 1D interacting Bose gas in a hard wall box' *J. Phys. A: Math. Gen.* 38 7787.

[124] Monras, A. (2006) 'Monras, A. (2006) 'Optimal phase measurements with pure Gaussian states' *Phys. Rev. A* 73, 033821.

[125] Szigeti, S.; Lewis-Swan, R. and Haine, S. (2017) 'Pumped-Up $SU(1,1)$ Interferometry' *Phys. Rev. Lett.* 118, 150401.

[126] Barnett, S.; Burnett, K. and Vaccaro, J. (1996) 'Why a condensate can be thought of as having a definite phase' *J. Res. Natl. Inst. Stand. Technol* 101, 593.

[127] Chernyak, V.; Choi, S. and Mukamel, S. (2003) 'Generalized coherent state representation of Bose-Einstein condensates' *Phys. Rev. A* 67, 053604.

[128] Jaskula, J. et al. (2012) 'Acoustic Analog to the Dynamical Casimir Effect in a Bose-Einstein Condensate' *Phys. Rev. Lett.* 109, 220401.

[129] Steinhauer, J. (2016) 'Observation of quantum Hawking radiation and its entanglement in an analogue black hole' *Nature Phys.* 12, 959.

[130] Katz, N. et al. (2004) 'High Sensitivity Phonon Spectroscopy of Bose-Einstein Condensates using Matter-Wave Interference' *Phys. Rev. Lett.* 93, 220403.

[131] Szigeti, S.; Debs, J.; Hope, J.; Robins, N. and Close, J. (2012) ‘Why momentum width matters for atom interferometry with Bragg pulses’ *New J. Phys.* 14, 023009.

[132] Stenger, J. et al. (1999) ‘Bragg Spectroscopy of a Bose-Einstein Condensate’ *Phys. Rev. Lett.* 82, 4569.

[133] Linnemann, D. et al. (2016) ‘Quantum-Enhanced Sensing Based on Time Reversal of Nonlinear Dynamics’ *Phys. Rev. Lett.* 117, 013001.

[134] Burd, S. et al. (2024) ‘Experimental Speedup of Quantum Dynamics through Squeezing’ *PRX Quantum* 5, 020314.

[135] Schley, R. et al. (2013) ‘Planck Distribution of Phonons in a Bose-Einstein Condensate’ *Phys. Rev. Lett.* 111, 055301.

[136] Steinhauer, J. (2014) ‘Observation of self-amplifying Hawking radiation in an analogue black-hole laser’ *Nature Phys.* 10, 864.

[137] Pinel, O. et al. (2012) ‘Ultimate sensitivity of precision measurements with intense Gaussian quantum light: A multimodal approach’ *Phys. Rev. A* 85, 010101.

[138] Bressanini, G.; Genoni, M.; Kim, M. and Paris, M. (2024) ‘Multi-parameter quantum estimation of single- and two-mode pure Gaussian states’ *J. Phys. A: Math. Theor.* 57, 315305.

[139] Stellmer, S.; Pasquiou, B.; Grimm, R. and Schreck, F. (2013) ‘Laser Cooling to Quantum Degeneracy’ *Phys. Rev. Lett.* 110, 263003.

[140] Barrett, M.; Sauer, J. and Chapman, M. (2001) ‘All-Optical Formation of an Atomic Bose-Einstein Condensate’ *Phys. Rev. Lett.* 87, 010404.

[141] Egorov, M. et al. (2013) ‘Measurement of s-wave scattering lengths in a two-component Bose-Einstein condensate’ *Phys. Rev. A* 87, 053614.

[142] Kraemer, T. et al. (2004) ‘Optimized production of a cesium Bose-Einstein condensate’ *Appl. Phys. B* 79, 1013.

[143] van der Stam, K. et al. (2007) ‘Large atom number Bose-Einstein condensate of sodium’ *Rev. Sci. Instrum.* 78, 013102.

[144] Hänsel, W.; Hommelhoff, P.; Hänsch, T. W. and Reichel, J. (2001) 'Bose-Einstein condensation on a microelectronic chip' *Nature* 413, 498.

[145] Meppelink, R. et al. (2010) 'Thermodynamics of Bose-Einstein-condensed clouds using phase-contrast imaging' *Phys. Rev. A* 81, 053632.

[146] Fried, D. G. et al. (1998) 'Bose-Einstein Condensation of Atomic Hydrogen' *Phys. Rev. Lett.* 81, 3811.

[147] Moerdijk, A.; Boesten, H. and Verhaar, B. (1996) 'Decay of trapped ultracold alkali atoms by recombination' *Phys. Rev. A* 53, 916.

[148] Burt, E. et al. (1997) 'Coherence, Correlations, and Collisions: What One Learns about Bose-Einstein Condensates from Their Decay' *Phys. Rev. Lett.* 79, 337.

[149] Pitaevskii, L. P. and Stringari, S. (1997) 'Landau damping in dilute Bose gases' *Phys. Lett. A* 235, 398.

[150] Giorgini, S. (1998) 'Damping in dilute Bose gases: A mean-field approach' *Phys. Rev. A* 57, 2949.

[151] Howl, R.; Sabín, C.; Hackermüller, L. and Fuentes, I. (2017) 'Quantum decoherence of phonons in Bose-Einstein condensates' *J. Phys. B: At. Mol. Opt. Phys.* 51, 015303.

[152] Rätzel, D. and Schützhold, R. (2021) 'Decay of quantum sensitivity due to three-body loss in Bose-Einstein condensates' *Phys. Rev. A* 103, 063321.

[153] Juschitz, P. (2021) 'Two-mode Phonon Squeezing in Bose-Einstein Condensates for Gravitational Wave Detection' *e-print* arXiv:2101.05051[cond-mat.quant-gas].

[154] Dowling, J. and Seshadreesan, K. (2015) 'Quantum Optical Technologies for Metrology, Sensing, and Imaging' *Journal of Lightwave Technology* 33, 2359.

[155] Nunnenkamp, A.; Børkje, K.; Harris, J. G. E. and Girvin, S. M. (2010) 'Cooling and squeezing via quadratic optomechanical coupling' *Phys. Rev. A* 82, 021806.

[156] Meystre, P. (2013) 'A short walk through quantum optomechanics' *Annalen der Physik* 525, 215.

[157] Gross, C. (2012) ‘Spin squeezing, entanglement and quantum metrology with Bose-Einstein condensates’ *J. Phys. B: At. Mol. Opt. Phys.* 45, 103001.

[158] Tufarelli, T. et al. (2012) ‘Input–output Gaussian channels: theory and application’ *New J. Phys.* 14, 093046.

[159] Xin, L.; Barrios, M.; Cohen, J. and Chapman, M. (2023) ‘Long-Lived Squeezed Ground States in a Quantum Spin Ensemble’ *Phys. Rev. Lett.* 131, 133402.

[160] Chin, C.; Grimm, R.; Julienne, P. and Tiesinga, E. (2010) ‘Feshbach resonances in ultracold gases’ *Rev. Mod. Phys.* 82, 1225.

[161] Wagner, T.; Schlamminger, S.; Gundlach, J. and Adelberger, E. (2012) ‘Torsion-balance tests of the weak equivalence principle’ *Class. Quantum Grav.* 29, 184002.

[162] Gundlach, J. et al. (2007) ‘Laboratory Test of Newton’s Second Law for Small Accelerations’ *Phys. Rev. Lett.* 98, 150801.

[163] Little, S.; Little, M. (2014) ‘Laboratory test of Newton’s law of gravity for small accelerations’ *Class. Quantum Grav.* 31, 195008.

[164] Timberlake, C. et al. (2021) ‘Probing modified gravity with magnetically levitated resonators’ *Phys. Rev. D* 104, L101101.

[165] Rubin, V. and Ford, W. (1970) ‘Rotation of the Andromeda Nebula from a Spectroscopic Survey of Emission Regions’ *Astrophys. J.* 159, 379.

[166] Rubin, V.; Ford, W. and Thonnard, N. (1980) ‘Rotational properties of 21 SC galaxies with a large range of luminosities and radii, from NGC 4605 (R=4kpc) to UGC 2885 (R=122kpc).’ *Astrophys. J.* 238, 471.

[167] Zwicky, F. (1933) ‘Die Rotverschiebung von extragalaktischen Nebeln’ *Helvetica Physica Acta* 6, 110.

[168] Wu, X.; Chiueh, T.; Fang, L. and Xue, Y. (1998) ‘A comparison of different cluster mass estimates: consistency or discrepancy?’ *Mon. Not. R. Astron. Soc.* 301, 861.

[169] Refregier, A. (2003) ‘Weak Gravitational Lensing by Large-Scale Structure’ *Annu. Rev. Astron. Astrophys.* 41, 645.

[170] Bennett, C. et al. (2013) ‘Nine-year Wilkinson Microwave Anisotropy Probe (WMAP) Observations: Final Maps and Results’ *Astrophys. J.s* 208, 20.

[171] Ade, P. et al. (2014) ‘Planck 2013 results. I. Overview of products and scientific results’ *A&A* 571, A1.

[172] Fukugita, M.; Hogan, C. and Peebles, P. (1998) ‘The Cosmic Baryon Budget’ *Astrophys. J.* 503, 518.

[173] Martens, N. and Lehmkuhl, D. (2020) ‘Dark matter = modified gravity? Scrutinising the spacetime–matter distinction through the modified gravity/dark matter lens’ *Stud. Hist. Philos. Sci. B* 72, 237.

[174] McGaugh, S. (2020) ‘Predictions and Outcomes for the Dynamics of Rotating Galaxies’ *Galaxies* 8, 35.

[175] Baudis, L. (2018) ‘The Search for Dark Matter’ *Eur. Rev.* 26, 70.

[176] Milgrom, M. (1983) ‘A modification of the Newtonian dynamics as a possible alternative to the hidden mass hypothesis.’ *Astrophys. J.* 270, 365.

[177] Chae, K. et al. (2020) ‘Testing the Strong Equivalence Principle: Detection of the External Field Effect in Rotationally Supported Galaxies’ *Astrophys. J.* 904, 51.

[178] Famaey, B. and McGaugh, S. (2012) ‘Modified Newtonian Dynamics (MOND): Observational Phenomenology and Relativistic Extensions’ *Living Rev. Relativity* 15, 10.

[179] Chan, M. and Del Popolo, A. (2020) ‘The radial acceleration relation in galaxy clusters’ *Mon. Not. R. Astron. Soc.* 492, 5865.

[180] McGaugh, S. S. (2015) ‘A tale of two paradigms: the mutual incommensurability of ΛCDM and MOND’ *Can. J. Phys.* 93, 250.

[181] Chae, K. (2022) ‘Distinguishing Dark Matter, Modified Gravity, and Modified Inertia with the Inner and Outer Parts of Galactic Rotation Curves’ *Astrophys. J.* 941, 55.

[182] Hernandez, X. et al. (2023) ‘Statistical analysis of the gravitational anomaly in Gaia wide binaries’ *Mon. Not. R. Astron. Soc.* 528, 4720.

[183] Berezhiani, L. and Khoury, J. (2015) ‘Theory of dark matter superfluidity’ *Phys. Rev. D* 92, 103510.

[184] Berezhiani, L. and Khoury, J. (2016) ‘Dark matter superfluidity and galactic dynamics’ *Phys. Lett. B* 753, 639.

[185] Carney, D. et al. (2021) ‘Mechanical quantum sensing in the search for dark matter’ *Quantum Science and Technology* 6, 024002.

[186] Graham, P. W.; Kaplan, D. E.; Mardon, J.; Rajendran, S.; Terrano, W. A. (2016) ‘Dark matter direct detection with accelerometers’ *Phys. Rev. D* 93, 075029.

[187] Peebles, P. (2024) ‘Status of the ΛCDM theory: supporting evidence and anomalies’ *e-print* arXiv:2405.18307[astro-ph].

[188] Aghanim, N. et al. (2020) ‘Planck 2018 results. VI. Cosmological parameters’ *Astron. Astrophys.* 641, A6. [Erratum: *Astron. Astrophys.* 652, C4 (2021)].

[189] Gurzadyan, V. (1985) ‘The cosmological constant in the McCrea-Milne cosmological scheme’ *The Observatory* 105, 42.

[190] Gurzadyan, V. and Stepanian, A. (2019) ‘The cosmological constant derived via galaxy groups and clusters’ *Eur. Phys. J. C* 79, 169.

[191] Milgrom, M. (2015) ‘MOND theory’ *Canadian Journal of Physics* 93, 107.

[192] Famaey, B. and Binney, J. (2005) ‘Modified Newtonian dynamics in the Milky Way’ *Monthly Notices of the Royal Astronomical Society* 363, 603.

[193] Gurzadyan, V. (2019) ‘On the common nature of dark matter and dark energy: Galaxy groups’ *Eur. Phys. J. Plus* 134, 14.

[194] Gurzadyan, V. and Stepanian, A. (2018) ‘Two fundamental constants of gravity unifying dark matter and dark energy’ *Eur. Phys. J. C* 78, 632.

[195] McCrea, W. and Milne, E. (1934) ‘Newtonian Universes and the curvature of space’ *Q. J. Math.* 5, 73.

[196] Gurzadyan, V. and Stepanian, A. (2019) ‘Cosmological constant as a fundamental constant’ *Eur. Phys. J. Plus* 134, 98.

[197] Gurzadyan, V. and Stepanian, A. (2019) ‘H_0 tension: clue to common nature of dark sector?’ *Eur. Phys. J. C* 79, 568.

[198] Riess, A. (2019) ‘Large Magellanic Cloud Cepheid Standards Provide a 1% Foundation for the Determination of the Hubble Constant and Stronger Evidence for Physics beyond ΛCDM’ *Astrophys. J.* 876, 85.

[199] Riess, A. (2019) ‘The expansion of the Universe is faster than expected’ *Nat. Rev. Phys.* 2, 10.

[200] Riess, A. G. et al. (2024) ‘JWST Observations Reject Unrecognized Crowding of Cepheid Photometry as an Explanation for the Hubble Tension at 8σ Confidence’ *Astrophys. J. Lett.* 962, L17.

[201] Gurzadyan, V. and Stepanian, A. (2021) ‘Hubble tension vs two flows’ *Eur. Phys. J. Plus* 136, 235.

[202] Gurzadyan, V. G. and Stepanian, A. (2021) ‘Hubble tension and absolute constraints on the local Hubble parameter’ *Astron. Astrophys.* 653, A145.

[203] Kravtsov, A. (2013) ‘The Size–Virial Radius Relation of Galaxies’ *Astrophys. J.* 764, L31.

[204] Mohr, P.; Newell, D.; Taylor, B. and Tiesinga, E. (2024) ‘CODATA Recommended Values of the Fundamental Physical Constants: 2022’ *e-print* arXiv:2409.03787[hep-ph].

[205] Rothleitner, C. and Schlamminger, S. (2017) ‘Invited Review Article: Measurements of the Newtonian constant of gravitation, G’ *Rev. Sci. Instrum.* 88, 111101.

[206] Bravo, T.; Dennis, R.; Bruschi, D. and Fuentes, I. (2024) *Quantum gravimeters and gradiometers.* United States Patent US20220171089A1.